STUDY OF ELECTRONIC STRUCTURES AND CORRELATIONS IN GRAPHENE USING OPTICAL SPECTROSCOPIES

PRANJAL KUMAR GOGOI

NATIONAL UNIVERSITY OF SINGAPORE

2013

STUDY OF ELECTRONIC STRUCTURES AND CORRELATIONS IN GRAPHENE USING OPTICAL SPECTROSCOPIES

PRANJAL KUMAR GOGOI

(M.Sc., PHYSICS, TEZPUR UNIVERSITY;

M.Tech., ENERGY TECHNOLOGY, TEZPUR UNIVERSITY)

A THESIS SUBMITTED

FOR THE DEGREE OF DOCTOR OF PHILOSOPHY

DEPARTMENT OF PHYSICS

NATIONAL UNIVERSITY OF SINGAPORE

2013

Declaration

I hereby declare that the thesis is my original work and it has been written by me in its entirety. I have duly acknowledged all the sources of information which have been used in the thesis.

This thesis has also not been submitted for any degree in any university previously.

Pranjal Kumar Gogoi
March 28, 2013

Acknowledgements

Hereby I express my sincere gratitude to everyone who has helped me directly and indirectly during my PhD work. Particularly I would like to thank my supervisor Asst Prof. Andrivo Rusydi for his constant encouragement, instructions, support and patience while guiding me during my PhD. It has been a great and invaluable learning experience for me working under his supervision. Similarly I am thankful to my co-supervisors Prof. Thirumalai Venky Venkatesan and Prof. Loh Kian Ping for their invaluable inputs and guidance.

I would like to thank Dr. Iman Santoso specially for his constant help and for his time during the last four years. We had many fruitful discussions which have been important building blocks on which this thesis work rests.

Similarly I would take the opportunity to thank all my lab members, NanoCore members, SSLS members and my friends from the physics department of NUS for their numerous help and also for making my stay in NUS enjoyable and memorable.

Finally I would like to thank my family members back for their love and support during all these years. This thesis work would not have been possible without their care and understanding.

Table of Contents

Abstract

Graphene is a unique two-dimensional (2D) material with extra ordinary as well as superlative electronic, optical, mechanical and thermal properties. In this thesis we have explored graphene optical properties using various experimental techniques namely spectroscopic ellipsometry, vacuum ultraviolet reflectivity and ultrafast pump-probe technique. The main emphasis has been to study the optical conductivity (from infrared to vacuum ultraviolet) which gives information about graphene electronic structures as well as correlation effects present. It is remarkable that the 2D structure as well as relatively straightforward transfer process to various substrates make it possible to manipulate the dielectric environment to finally control the correlation strengths in graphene. Keeping these in mind graphene samples on different substrates with varying dielectric constants as well as band-gaps are measured using the techniques mentioned. Our results show anomalous screening of many-body effects in graphene on a metal substrate as compared to the case on quartz. Another new and intriguing observation has been the near perfect transparency of graphene in ultraviolet region due to Fano anti-resonance between the continuum and resonant excitonic states residing in the new hybrid bands supported by the low band gap insulating substrate $SrTiO_3$. Similarly observation of a high energy resonant exciton in epitaxial graphene is another highlight which underlies the crucial role many-body effects play in graphene optical properties. Furthermore in the case when treated with mild oxygen plasma graphene shows tunable optical absorption which could be an important step forward for future applications.

List of Tables

List of Figures

List of important Symbols and Abbreviations

Symbol	Description
σ_1	Real part of the complex optical sheet (bulk) conductivity
ε_1	Real part of the complex dielectric function
ε_2	Imaginary part of the complex dielectric function
α_g	Fine-structure constant
α_g^*	Effective fine-structure constant
v_F	Fermi velocity
Ψ	Amplitude ratio of the p- and s- polarized light waves
Δ	Phase difference between the p- and s- polarized light waves

Abbreviation	Description
2DEG	Two dimensional electron gas
CVD	Chemical vapour deposition/deposited
QHE	Quamtum hall effect
UV	Ultraviolet
IR	Infra-red
STM	Scanning tunneling microscope/microscopy
HEMT	High electron mobility transistors
SE	Spectroscopic ellipsometer/ellipsometry
LED	Light emitting diode
TEM	Transmission electron microscope
VUV	Vacuum ultraviolet
DFT	Density functional theory
LDA	Local density approximation
BSE	Bethe-Salpeter Equation
PL	Photoluminescence
UDR	Ultrafast differential reflectivity
GOQ	Graphene on quartz
GOC	Graphene on copper
PMT	Photo-multiplier tube
UHV	Ultrahigh vacuum
SWNT	Single-walled nanotube
RAE	Rotating analyzer ellipsometer

Chapter 1

Introduction

In this introductory chapter we give a brief overview of the importance, excitement and current trends in graphene research. Graphene research, both theoretically and experimentally, has thrived at a tremendous pace in recent years despite being a very new field in relative terms. Extraordinary physical properties coupled with immense potential for applications in the near future have fueled a huge surge of fundamental as well as applied research efforts in graphene. After highlighting these features the particular motivations and directions of this thesis are described in brief. An outline of the organization of the thesis is given at the end as a guideline for the rest of the thesis.

1.1 Graphene: importance, excitement and relevance

Just within nine years of its successful isolation [1,2] graphene has established itself firmly as a field of great importance with wide spread and immense current research efforts. It possesses unique and superlative properties which excite both physicists with penchant for deeper principles of nature and applied scientists. Incidentally its isolation was no less dramatic as it involved an amazingly simple yet ingenious method of using a scotch tape to exfoliate layers of graphite. The real innovation was the use of a 300nm thick SiO_2 on silicon which made the single graphene layer visible to the eye due to the constructive interference. The importance of graphene in physics as well as science in general and also the fast maturity of the research activities have been recognized by the award of the Nobel prize for physics to the discoverers and pioneers A Geim and K.S. Novoselov in 2010 [3].

Graphene is a two-dimensional (2D) sheet of carbon atoms arranged in hexagonal structure. It was studies theoretically for a long time before its experimental discovery as a building block of other carbon based materials [4-6], mainly graphite. Carbon, due to its ability to form various kinds of bonds, can be found in numerous different forms in nature with even more diverse properties. For example, among allotropes of carbon there are zero-dimensional fullerene [7], one-dimensional (1D) carbon nanotubes [8,9], 2D graphene and three dimensional (3D) graphite. Interestingly graphene could be thought of as the building block of all these materials of other dimensions structurally as well as from the point of view of understanding the electronic properties. For example fullerenes could be derived from graphene by folding it and introducing pentagons, carbon nanotubes could be thought of as the effect of rolling graphene and joining the carbon atoms in the edges, graphite is stacked up graphene sheets on top of each other in a certain order etc.

In 1987 S. Mouras and coworkers first mentioned the term ‘graphene’ [10]. However it was predicted that 2D materials could not exist in nature due to the thermodynamic instabilities at finite temperatures [11-15]. So immediately after the successful isolation of graphene from bulk graphite it created a lot of curiosity and excitement from these fundamental aspects. However this excitement was literally the precursor to an avalanche only. Almost immediately numerous reports showed that graphene has unique and superlative properties, particularly massless carriers mimicking relativistic physics, supreme electronic quality etc. [16-19]. It attracted huge interest as a hot-bed for

fundamental physics experiments which otherwise require extreme experimental sophistication such as particle colliders. Similarly its 2D nature, with unprecedented mechanical properties, opened up possibilities (with exciting results) for various application oriented research. Unlike conventional heterostructures which carry the two dimensional electron gas (2DEG) layer buried deep inside, graphene is essentially a single sheet of charge carrier accessible immediately. Coupled with its superlative electronic quality even in ambient, the easily accessible 2D surface geometry have made the graphene community dream seriously of a day when graphene will be the material replacing silicon in electronics [2, 18, 20-22].

The spread of graphene research (even to disciplines other than physics and chemistry) has been also facilitated by the success in producing good quality samples on a large scale. Epitaxial growth on SiC [23], chemical vapour deposition (CVD) on metal catalysts [24], chemical exfoliation [25, 26] etc. have been successful techniques to different extents but also with their own limitations. Large area samples (even 30 inch × 30 inch) using CVD technique [27] have been already demonstrated which is a major step towards commercialization of graphene in numerous applications. But CVD grown samples do not possess the same high electronic quality of exfoliated samples and still for fundamental physics experiments the smaller (typically few 10s of micron) but electronically high quality single crystals prepared by the original micromechanical exfoliation technique are used mostly.

While graphene itself is an extraordinary 2D material, it has also naturally encouraged and guided physicists and material scientists to look for similar 2D materials [22] and this class of material has been one of the most important focus of recent interest. Materials like boron nitride (BN) [2], molybdenum disulphide (MoS_2) [28] have been studied with interesting results. Also recently graphene heterostructures with these materials have been shown to be very promising with novel functionalities as well as rich new physics not easily accessible in other condensed matter systems [29-31].

1.2 Extraordinary properties

Perhaps the following words from Nobel Laureate K. S. Novoselov from his Nobel lecture [3] best describe how special graphene is -

".. The major draw to people in the field, though, is graphene's unique properties, each of which seems to be superior to its rivals. This material is the first 2D atomic crystal ever known to us [1,2]; the thinnest object ever obtained; the world's strongest material [32]; its charge carriers are massless Dirac fermions [16-18]; it is extremely electrically [33] and thermally conductive [34]; very elastic; and impermeable to any molecules [35]—the list goes on. Even a simple inventory of graphene's superlative qualities would require several pages, and new entries are being added on a monthly basis…"

Here some of the important such properties and their reports are discussed very briefly.

1.2.1 Electrical Properties

The most striking feature of graphene is its electronic property. It has linear bandstructure and the valence and conduction bands touch at the K and K' points of the Brillouin zone [5, 18, 19, 36]. Therefore it is a zero gap semimetal and the charge carriers behave like massless Dirac Fermions [16-18]. This gapless nature, which is a consequence of the honeycomb structure, has unique implications manifested in its properties. Furthermore charge carriers in graphene obey chiral symmetry akin to what is seen in quantum electrodynamics (QED) for particles and antiparticles [19]. These similarities between quasi-particles in graphene and particles in relativistic QED have led to some of the most interesting theoretical predictions [19, 37-42] as well as experiments confirmations [16, 17, 43, 44] which address deeper fundamental physics questions. One of the first such results is the observation of half integer quantum hall effect (QHE) [16, 17]. Charge conjugation symmetry guarantees that in presence of magnetic field there will be Landau levels $E_n = \pm\sqrt{2e\hbar v_F^2 B\left(n+\frac{1}{2}\pm\frac{1}{2}\right)}$, where *e,* $\hbar$, v_F, *B, n* are electronic charge, Plank constant, Fermi velocity, magnetic field, n = 0,1,2,3.. respectively. This is remarkably different from other systems where the charge carriers are not massless. The plateaus of the Hall conductivity are seen as $\pm\frac{1}{2}(4e^2/\mathrm{h})$ at filling factor of ± 2. Moreover low broadening of the Landau levels, large separation of the zeroth and first Landau level (which is a result of relatively high Fermi velocity and linear dispersion) make it possible to observe this QHE even at room temperature. This is not only very remarkable from fundamental physics point of view but it also opens the

door for possible use of this observation as a relatively easily available resistance standard [45,46].

Klein tunneling is another very interesting manifestation of the chiral symmetry of the charge carriers of graphene and it has been predicted and observed experimentally [43,44]. Klein paradox refers to perfect transmission probability of the charge carriers through an energy barrier when the barrier height is more than $2m_0c^2$, where m_0 is electron rest mass and c is the speed of light.. Similarly strong coulomb interaction effects in graphene have been observed using very high quality suspended graphene in strong magnetic field in the form of fractional QHE [47]. This also emboldens the prevailing notion that improvement of graphene electronic quality could further lead to some very fundamental results and findings in the near future particularly in the direction of electronic correlation effects in graphene. Very recent report of observation of Hofstadter's butterfly pattern [48] in graphene on BN is a step in such directions [31].

Graphene has remarkably high mobility (~ 15000 $cm^2\ V^{-1}\ s^{-1}$) even at ambient conditions which weakly depends on temperature and stays high even when the carrier density is high (> 10^{12} cm^{-2}) [1,18]. There has been report of extremely high mobilities of 200,000 $cm^2\ V^{-1}\ s^{-1}$ at electron densities of 2×10^{12} cm^{-2} in suspended graphene [49]. Similarly more recent efforts in using substrates like BN has resulted in an almost 10 fold increase in the mobilities of graphene samples [50]. These last reports have attracted tremendous interest due to the potential of such very high mobility samples for fundamental studies as well as application in areas like spintronics [51], high frequency devices etc. [21].

Mobility values are generally lower for (~ 10000 cm^2 V^{-1} s^{-1}) CVD graphene than exfoliated samples [52].

As mentioned before graphene heterostructures with other 2D materials could lead to some exciting new functionality such as the recent report of high on-off ratio in a vertical structure using graphene-BN as well as graphene-MoS_2 layers [29]. This could be a very important step towards large scale integrated circuits using graphene which has a finite undesirable metallic conductivity even at the charge neutrality point. A similar recent report of [30] strong localization and metal - to- insulator transition in ultra high quality graphene monolayers sandwiched between BN layers is an indication of the prospects this field has in enabling the exploration of a whole new paradigm previously unexplored in condensed matter physics.

1.2.2 Optical properties

Naively a one atom thick material like graphene would be thought of as not very interesting from the point of view of optics as it would absorb very little light, as the interaction area is small and increasing the layer numbers would automatically prohibit us from studying the unique single layer regime. But totally against this intuitive assumption graphene absorbs significantly large amount of light (~ 2.3 %) and this absorbance is defined by the most fundamental constant of nature - the fine structure constant [53-56]. To give a comparative figure, a 20 nm layer of InGaAs would be required to absorb the

same amount of light at wavelength 1.55 μm [21]. So, overall it signifies the strong interaction of graphene with light. Incidentally it can be said that the whole graphene revolution is thankful to this remarkable property of graphene (high absorption in the visible range) which makes graphene visible to the naked eye despite being a monolayer and every time we see graphene basically we are "seeing" the most fundamental constant of nature [3].

This universal absorption of graphene in the infrared to visible gradually increases to ~10% in the ultraviolet (UV) range where the transitions near the van Hove singularity gives rise to a peak [57-59]. Excitonic effect red shifts this peak and also gives it an asymmetric shape. This is remarkable because graphene as a semimetal is expected to show strong screening and signatures of many-body effects should be small in it if at all they exist. But on the contrary the red shift is rather large and also the renormalization of the peak is quite robust as seen in numerous reports [57-61].

A few theoretical studies have shown the importance of many-body effects in graphene for optical properties beyond the UV range till higher energy of ~20 eV [62,63]. These show significant signatures of renormalization of the optical conductivity of graphene in the high energy range. However experimental investigations of graphene optical response in this range is scarce [64, 65] and more research efforts in this direction would definitely be needed for better understanding of graphene electronic structures as well as correlation effects in graphene.

Graphene optics in the infrared (mid to far IR) energy range has also elucidated some interesting aspects of electronic structure of graphene and multilayers [54, 66, 67]. Perhaps the most interesting results in this range is the gate tunability of the Pauli blocking in graphene [54,66]. One of the most intriguing unsolved issues in this field is the finite residual conductivity in the blocking region, the origin of which may be due to many-body effects or impurities. The biggest challenge in these experimental efforts is the requirement of very high quality large area graphene samples which could be gated effectively (which is another challenge due to leakage through the gate dielectric.)

Plasmonics is another exciting recent area which is relevant in this infrared spectral range and which uses the unique electronic properties of graphene with its 2D geometry and also lithographically patterned graphene [68-71]. Gate tunability of these plasmon waves opens up another capability which could be crucial for future applications.

1.2.3 Mechanical, chemical and other properties

Among many superlative qualities of graphene a key one is that it is the strongest material known in the world [32]. Atomic force microscopy study using nano-indentation of free-standing mono-layer graphene has revealed that it has a Young's modulus of E = 1.0 terapascals, third-order elastic stiffness of D = –2.0 terapascals which are far above any other known material. Similarly graphene has extremely high thermal conductivity (in the range ~$(4.84 \pm 0.44) \times 10^3$ to $(5.30 \pm 0.48) \times 10^3$ W/mK) as reported measured

using free-standing monolayer graphene [34]. These values are even better than carbon nanotubes.

As its very malleable, strain and deformations can alter graphene electronic, optical and phonon properties locally [72]. Observations of huge pseudo magnetic fields of 300T in graphene has been reported using STM studies on highly strained graphene nanobubles [73]. This is a result of the unique band dispersion of graphene, where the carriers are massless, as well as the particular lattice symmetry. These huge local pseudo magnetic fields in graphene may lead to the possibility of study of the behaviour of charge carriers in such unprecedented conditions.

There are many such reports which show the superlative properties of graphene could be found elsewhere as well. One particular aspect which needs special mention is that the unique 2D structure of graphene (with surface only but no volume) immediately makes it an exciting candidate for functionalization unlike any other known material. Hydrogenation [74] and fluorination [75] have been two such approaches which could prove to be two important ways of tailoring graphene properties.

1.3 Tremendous potential for applications

With all the unique and superior properties described above (and many which have not been even mentioned) graphene offers unlimited application avenues. In fact it is a firm belief that its application potential would create whole new technology frontiers beyond the conventional areas [3, 22].

First and foremost application of graphene is envisaged to be in making superior commercial transistors utilizing its excellent electronic quality and easy gate tunability [3, 18-22]. Extremely high carrier mobility even in ambient conditions is of great advantage here. Although the origin and limiting factors of mobility are still unresolved issues [33], it is predicted that ambient mobility of above $\sim 10^5$ cm^2 V^{-1} s^{-1} could be achieved. Using alternative substrates like BN has been another direction of focus with the observation of some very high values of mobilites therein [22, 50].

High frequency transistors could be a possibility with graphene with its high mobility and high Fermi velocity which might be an alternative to current GaAs based high-electron-mobility-transistors (HEMTs) [21, 76] in the near future. However low on/off ratio is a big bottleneck in potential graphene applications when integration to integrated circuits is considered [3,20]. Opening a bandgap using lithographic techniques [77], using chemical routes (like self assembly) for designed nanostructures [78], using chemically modified graphene [74, 75] etc. are currently explored directions in this regards. One of the most exciting and recent developments has been in using graphene hetorstructures with other 2D materials to achieve higher on-off ratios [29] as mentioned previously.

The discovery of methods to successfully prepare very large area CVD graphene with reasonable quality has opened up tremendous opportunities in the field of optoelectronics by using graphene as a transparent conducting electrode [26,27]. Excellent electronic conductivity, considerable absorption of visible light, robust mechanical strength and very high chemical stability underlie this potential [3, 18-21]. Transparent conductive

electrodes have widespread application in numerous conventional applications like solar cells, photodetectors, liquid crystal displayes, LEDs etc. where mainly conductive indium tin oxide is used. However the rising cost as well as relative chemical instability of indium tin oxide is detrimental for such applications. With the additional property of flexibility of graphene there has been a huge surge of research efforts particularly in this direction and flexible displays using graphene could be a commercial reality very soon [21, 27,79].

Composite materials using graphene is another lively area of research which exploits all the superlative electrical, chemical, optical and mechanical properties of graphene [80]. Possible chemical routes like direct exfoliation in organic solvents or first oxidation and then exfoliation in water make such approaches relatively easily accessible and more commercially viable. Here the extraordinary mechanical strength of graphene could be the biggest advantage with the realization of high-performance composites [81]. Some chemical derivatives like flourographene still retain these superlative mechanical properties of graphene while other properties could be tuned to achieve different functionalities [75]. Similarly controlled strain engineering could be another way to manipulate graphene properties with applications in mind [72].

Niche application like using graphene membranes as support in TEM studies has become a commercial reality already [3,82]. Many such applications could be mentioned such as ultrasensitive gas detectors [83], ultrafast photodetectors [84], very efficient mode lockers [85], variable quantum capacitors [86] etc. which have been realized recently.

In summary, graphene seems to offer unlimited opportunities for applications with its unique and superlative properties. Further combining these properties new application frontiers could be explored which were not accessible previously.

1.4 Motivation of this thesis

As has been described in the previous sections of this chapter, graphene presents itself as a melting pot of both deep physics as well as a potential workhorse for future applications. In this thesis we investigate the optical properties of graphene using various spectroscopic techniques with primary focus on the electronic structure and correlation effects which address fundamental physical principles. It is implicit that a better understanding of graphene electronic structure and correlations effects is also crucial for future applications.

Graphene has optical properties (to be described more specifically and with details in chapter 2) which are not only unique in themselves but representative of the rich physics graphene manifests. There has been considerable progress in this field in the direction of elucidating fundamental physics as well as with more focus in applications. But it has to be said that comparatively optical properties, particularly from fundamental physics point of view, is still less explored in comparison to numerous transport studies.

Optical spectroscopic techniques are powerful tools to study the electronic structure of materials in general and these could probe different regions of the energy dispersion of the material under study depending on the spectral range of measurement. We have used

spectroscopic ellipsometry (SE), vacuum ultraviolet reflectivity (VUV) as well as optical pump-probe techniques in this thesis to explore graphene optical properties (or optical conductivity to be more specific) from near infrared to VUV range (~ 0.5 eV to 35 eV).

The basic aim is to better understand the electronic structures of graphene and also electronic correlations therein which have been shown to be the cause of remarkable renormalization of the optical properties in many theoretical as well as some experimental reports [53-60, 62,63].

Graphene with its unique low energy dispersion, 2D nature as well as semi metallic character offers itself as a very interesting playground for correlation effect. Intuitively it should be weakly interacting as it is semi-metallic, but low density of state near the Dirac point leads to deviations from this picture. Moreover in general in reduced dimensions electronic correlation effects are more prominent and with its strictly 2D nature graphene is an ideal candidate in the search for such effects [87]. Indeed there have been reports of strong electronic correlation effects in the form of fractional QHE [47], broken symmetry states in quantum hall regime [88], renormalization of Fermi velocity [89], nonlinear spectrum near the Dirac point [90], similarity to marginal Fermi liquid theory [91] etc. which explore the low energy spectrum of graphene. Yet it is still an open field with no consensus whether graphene is weakly or strongly interacting in a general sense. However, quite surprisingly most of the observed infrared to visible response of graphene could be explained in a non-interacting picture. But it turns out that there are signatures of robust correlation effects in the UV range as well as beyond. In fact it has been

predicted that a closer look at the visible to lower far infrared energy range of the spectrum could answer some of the fundamental questions in this field [62, 92-94].

Graphene with its 2D nature also offers the possibility of tuning its dielectric environments easily. This essentially affects the interaction strengths in it. A major effort in this thesis has been in this direction to study the optical conductivity in different screening regimes with some fundamental insight into the correlation effects in it.

Probing optical properties till higher energies (~35 eV) is vital for understanding the electronic structure encompassing various regions of the Brillouin zone. Moreover graphene is predicted [62, 63] to show considerable many-body effects in these regime and we explore this regime experimentally in this thesis.

Optical conductivity measurement of graphene on low band-gap insulators (or wide band-gap semiconductor) substrates is a completely new system of study not explored before with the possibility of interesting electronic coupling and interference effects due to the interaction of the bands of graphene, which is the thinnest material known, with the substrate bands. As will be described in detail later it gives us some very new, interesting and exciting physics at this interface.

Another motivation of this thesis is to study the effects of controlled chemical modification of graphene on the electronic as well as optical properties of graphene. Controlled treatment with very low power oxygen plasma has been used to chemically modify graphene and it is studied with SE.

The advantages and limitations of our techniques are explained in detail in later chapters in appropriate places. Various challenges in the studies have been highlighted wherever needed.

It has to be mentioned that although the primary motive is to study graphene using optical spectroscopic techniques to understand its physics, a thorough grasp of the experimental aspects in each case is simultaneously necessary for such an effort (also keeping in mind further studies in this field) like any other experimental study in science. So, considerable effort in this thesis is motivated towards a deep and involved understanding of the various experimental techniques used. At the end particular mention has to be made of the training in the sample preparation techniques of various graphene types as well as lithographic techniques. Understanding and implementing various aspects of preparing high quality graphene samples is one of the keys to successful experiments in this field (like in many other fields).

1.5 Organization of materials

In this introductory chapter we have given a general overview of graphene research highlighting its unique and superlative properties. Brief discussion on the application potentials thereafter puts it in the right perspective in the backdrop of the huge current research efforts in graphene. The particular motivations and general problems undertaken for this thesis have been described after that.

In the second chapter graphene physics has been dealt with in greater detail. Particular emphasis has been given to the general optical properties of graphene from far infrared to VUV keeping in mind the particular aspects we study in this thesis. Physical principles involved for the optical processes in different situations of interest are discussed separately in adequate detail (also keeping in mind the space constraints).

The third chapter describes various experimental techniques used- spectroscopic ellipsometry (SE), VUV reflectivity etc. with particular focus on the physical principles involved.

In the fourth chapter various data analysis strategies and procedures are described. The main focus is on analysis procedures of SE data not only because it is the central technique used but also because in itself use of SE requires a thorough understanding of the data analysis procedure for reliable extraction of the final optical properties under study.

In the fifth chapter we describe our results and findings of study of high energy excitonic effects in epitaxial graphene using both SE and VUV reflectivity.

In the sixth chapter we report the results of our study of screening of many body effects in graphene on metallic substrate. We use SE for this comparative study where optical conductivity is also measured for graphene on quartz substrate.

In the seventh chapter we describe our results of combined SE as well as pump-probe study of graphene on $SrTiO_3$ and graphene on SiO_2.

In chapter eight, which is the fourth and final of the results chapters, we describe the SE study of graphene exposed to controlled low power oxygen plasma.

In chapter nine we summarize all the important findings of this thesis. A few important future directions, which could be explored immediately as important further studies related to this thesis, are explained in short detail.

Chapter 2

Basic physics and background

In this chapter we start with the description of the main features of graphene crystal structure as well as its band structure from the tight-binding approach and later on correlate various features of the optical conductivity to unique band dispersions of graphene. With detailed theoretical considerations of the various features in the optical conductivity starting from far infrared to vacuum ultraviolet, the role of many-body effects is emphasized in all spectral ranges as the cause of remarkable renormalizations of the optical conductivity. This is the primary reason behind the motivation of this thesis to use optical conductivity measurement as a means to probe and understand the electronic structures of graphene in a broad energy range. Further recent experimental and theoretical studies have been brought into focus related to substrate effects such as-dielectric screening manipulation, charge transfer, hybridization etc. which are also investigated experimentally to different extents in this thesis. Finally discussion of light emission from graphene is discussed as it underlies our new findings in this direction.

2.1 Graphene band structure

Graphene is a two-dimensional sheet of carbon atoms arranged in a honeycomb lattice structure as shown in Figure 2.1(a). Here we will briefly describe the crystal structure and band structure of graphene emphasizing aspects which are crucial for optical properties.

The Bravais lattice could be chosen such that the lattice vectors are given by $\mathbf{a_1}$, $\mathbf{a_2}$ as shown in Figure 2.1 (a) with

$$\boldsymbol{a_1} = \frac{a}{2}(3, \sqrt{3}) \text{ and } \boldsymbol{a_2} = \frac{a}{2}(3, -\sqrt{3}) \qquad (2.1)$$

Where the nearest neighbour carbon-carbon distance is given by $a = 1.42\,\mathring{A}$. We get the reciprocal lattice vectors $\boldsymbol{b_1}, \boldsymbol{b_2}$ from the conditions $\boldsymbol{a_i} \cdot \boldsymbol{b_j} = 2\pi\delta_{ij}$ to be

$$\boldsymbol{b_1} = \frac{2\pi}{3a}(1, \sqrt{3}), \quad \boldsymbol{b_2} = \frac{2\pi}{3a}(1, -\sqrt{3}). \qquad (2.2)$$

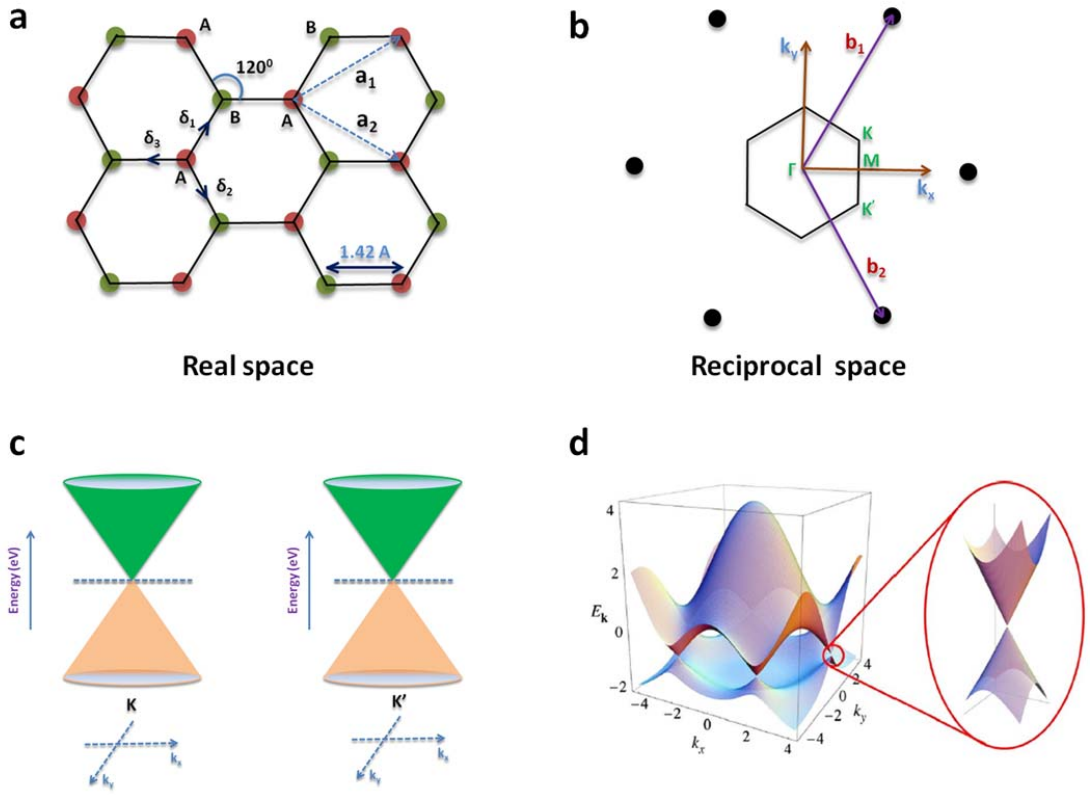

Figure 2.1 (a) Hexagonal lattice of graphene. (b) Reciprocal lattice of graphene with the first Brillouin zone. (c) Dirac cones at the K and K' points in the reciprocal lattice. (d) Energy dispersion for graphene with finite t and t'. Here t = 2.7 eV and t' = 0.02 eV respectively. Zoomed in dispersion near the Dirac point is shown in the right. (Figures are adapted after modifications from [19])

The first Brillouin zone is given by a hexagon as shown in Figure 2.1 (b) rotated by an angle of $\frac{\pi}{2}$ with respect to the original real space hexagon. In particular the equivalent points K and K' in the corners of the first Brillouin zone are very important for graphene physics, whose coordinates are given by

$$\boldsymbol{K} = (\frac{2\pi}{3a}, \frac{2\pi}{3a\sqrt{3}}) \text{ and } \boldsymbol{K'} = (\frac{2\pi}{3a}, -\frac{2\pi}{3a\sqrt{3}}) \quad (2.3)$$

The nearest neighbour vectors in real space are given by

$$\boldsymbol{\delta_1} = \frac{a}{2}(1, \sqrt{3}), \quad \boldsymbol{\delta_2} = \frac{a}{2}(1, -\sqrt{3}), \quad \boldsymbol{\delta_3} = -a(1, 0). \quad (2.4)$$

If the orbital in site $\boldsymbol{R_i}$ with spin $\boldsymbol{s}$ is given by (i, s) and the corresponding creation operator by $a_{s,i}^{\dagger}\left(b_{s,i}^{\dagger}\right)$ for an atom on the A (B) sublattice, then including nearest-neighbour and next-nearest-neighbour hopping terms, the Hamiltonian for the graphene electrons can be written as

$$H = -t\sum_{<i,j>,s}\left(a_{s,i}^{\dagger}b_{s,j} + H.c.\right) - t'\sum_{\ll i,j\gg,s}\left(a_{s,i}^{\dagger}a_{s,i} + b_{s,i}^{\dagger}b_{s,i} + H.c.\right) \quad (2.5)$$

Here t ($\approx$ 2.7 eV) is the nearest neighbour hopping term which represents hopping between different sublattices. Similarly t' is the next-nearest-neighbour hopping term which represents hopping in the same sublattice.

The eigenvalues derived from this Hamiltonian are given by [5]

$$E_{\pm}(\boldsymbol{k}) = \pm t\sqrt{3 + f(\boldsymbol{k})} - t'f(\boldsymbol{k}), \quad (2.6)$$

where $f(\boldsymbol{k}) = 2\cos(\sqrt{3}\,k_y a) + 4\cos(\frac{\sqrt{3}}{2}k_y a)\cos\frac{3}{2}(k_x a)$, *(2.7)*

Here $\pi^*$and π band energies are given by the plus and minus signs respectively in the above expression *(2.6)*. Figure 2.1(d) shows the full band structure in the case when both t and t' are nonzero. A nonzero t' leads to asymmetric bands. If we concentrate on the band structure very near to the K (or K') point then we get the following from the expressions *(2.6)* and *(2.7)* above as $\boldsymbol{k} = \boldsymbol{K} + \boldsymbol{q}$ for $|\boldsymbol{q}| \ll |\boldsymbol{K}|$,

$$E_{\pm}(\boldsymbol{q}) \approx \pm v_F|\boldsymbol{q}| + \mathcal{O}[(q/K)^2] \qquad (2.8)$$

Here $\boldsymbol{q}$ is the momentum measured from the K (K') point and v_F represents the Fermi velocity given by $v_F = 3ta/2$ with a value $v_F \cong 10^6$ m/s. This expression for energy dispersion (ignoring terms of higher order in (q/K))

$$E_{\pm}(\boldsymbol{q}) = \pm v_F|\boldsymbol{q}| \qquad (2.9)$$

is exactly like that of an ultra-relativistic massless particle of spin (**s**) ½ , but with speed 300 times smaller than the speed of light and given by the Fermi velocity v_F. This unique band dispersion of graphene is responsible for most of its fascinating properties and because of this behaviour akin to relativistic particles the equivalent reciprocal lattice points K and K' are known as Dirac points. Figure 2.1 (c) above shows the linear dispersion of graphene near to the Dirac points K and K' and also the so called Dirac cones.

Now if we take into account the expansion of the energy term *(2.6)* including terms in t' till second order in (q/K), we get

$$E_{\pm}(\boldsymbol{q}) \simeq 3t' \pm v_F|\boldsymbol{q}| - \left(\frac{9t'a^2}{4} \pm \frac{3ta^2}{8}\sin(3\theta_{\boldsymbol{q}})\right)|\boldsymbol{q}|^2 \qquad (2.10)$$

Where $\theta_{\boldsymbol{q}} = \tan^{-1}\left(\frac{q_x}{q_y}\right)$ gives the angle in the momentum space. The basic conclusion that can be derived from this expression is that a nonzero t' breaks the electron-hole

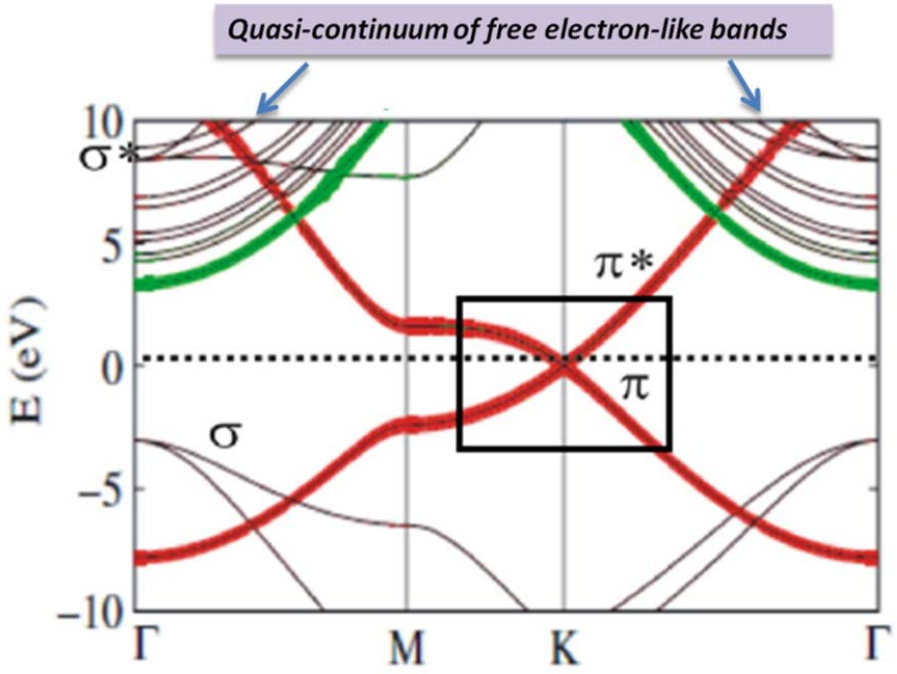

Figure 2.2 Graphene dispersion along different directions in the Brillouin using ab-initio density functional theory (DFT) calculations. (Figure is adapted from [183])

symmetry and also shifts the position of the Dirac point. There is trigonal wrapping (or threefold symmetry) [95] of the band dispersion when terms up to second order in (q/K) are taken into account. Also the band dispersion is direction dependent in the reciprocal space (Fig 2.1(d)).

Figure 2.2 above shows results of band structure calculations using the density functional theory (DFT) [96, 97] within the local density approximation (LDA) approach [183]. These band dispersions along different directions in the Brillouin zone tell us about characteristics far away from the Dirac point. As can be seen, the energy gap between the conduction band edge and the valence band edge is of the order of 20 eV at the Γ point. Also the dispersion is parabolic near Γ point unlike the K (K') points.

In this thesis we explore the graphene optical properties in a broad energy range (~ 0.5 eV to 35 eV) and therefore graphene band dispersion encompassing points far away from the Dirac point is of immediate relevance to our understandings.

2.2 Optical response of graphene

The optical conductivity of graphene shows features characteristic of intraband and interband transitions depending on the energy range of interest [53-61, 98-101]. Here we will discuss the optical response (predicted and observed real part of the optical conductivity (σ_1), absorbance, transmittance etc.) of graphene for a broad energy range starting from far infrared to vacuum ultraviolet (VUV) (~ 35 eV). Free carrier (intraband)

absorption dominates the far-infrared σ_1 of graphene. Basic Drude model can account for most of these responses. Also one recent emerging area of study is plasmonic effects in graphene [69-71,102] which can be observed in the far infrared (IR) spectral range exploring and utilizing unique geometry and excitations in graphene (and nanostructured graphene) different from conventional metal and 2DEG systems. In the mid IR to near IR region σ_1 is dominated by interband transitions leading to the now famous universal constant conductance defined by the fine structure constant [53-56]. The Fermi level can also be tuned in this range using controlled field effect (gating) resulting in the so called Pauli blocking where the transitions below $2|\varepsilon_F|$ are suppressed [54, 66], where ε_F represents the Fermi energy with respect to the Dirac point. Beyond this, in the ultraviolet (UV) region σ_1 rises from the constant value till the van-Hove peak which is renormalized by excitonic effects [57-61]. Significantly, σ_1 beyond this spectral range has not been explored as much as it has been for the lower energy ranges. In this thesis we have experimentally determined σ_1 of graphene not only for the conventional range of IR to UV [61] but from IR till unprecedented VUV range (0.5 – 35 eV) [64] with some very interesting observations obtained regarding the electronic structure and also about the important roles of many-body effects present in different cases.

2.2.1 Intraband absorption: Drude response

Free-carrier absorption in graphene involves scattering with phonons or defects to conserve momentum [66]. This is shown schematically in the Figure 2.3 (a) below.

Overall, Drude model can explain the absorption characteristics given by the frequency dependent sheet conductivity,

$$\sigma(\omega) = \frac{\sigma_0}{1+i\omega\tau} \qquad (2.11)$$

here ω, τ, σ_0 represent the angular frequency of light, electron scattering time and dc conductivity respectively. The expression for Drude weight (integrated oscillator strength) for massless Dirac fermions in graphene is $D = e^2 v_F \sqrt{\pi n}$ which is different from that for conventional metals or semiconductors (with $D = \pi n e^2/m$) [104, 105]. Of

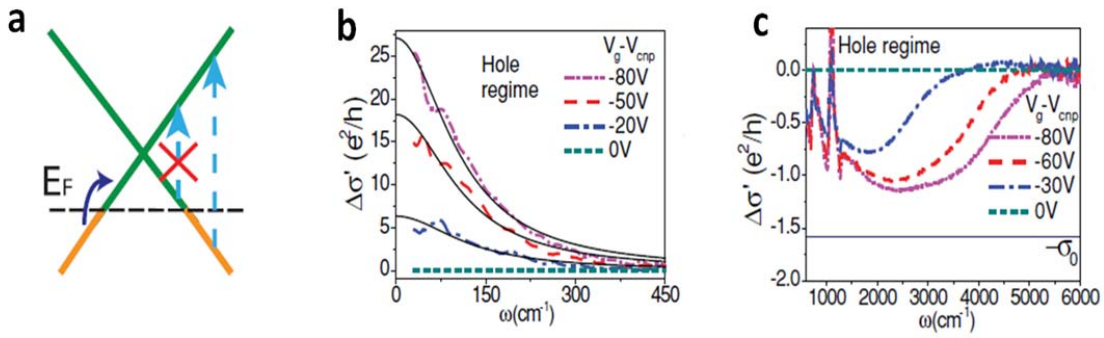

Figure 2.3 (a) Schematic of intraband and interband absorption in hole doped graphene. (b) Gate dependent change in σ_1 in hole doped graphene in the spectral range 30<ω<450 cm^{-1}. (c) Gate induced change in the interband σ_1 in the spectral range 600<ω<6000 cm^{-1}. (Figures are adapted from [66])

particular relevance here is a recent study of CVD graphene [24] in the far and mid-IR regions with field effect tuning of the carrier concentration [54, 66]. The results of σ_1 measurement [66] as shown in Figure 2.3(b) can be fitted well with the Drude model in

the formalism of Kubo formula ignoring many-body effects [92, 106]. Figure 2.3 (c) also shows the Pauli blocking ($\approx 2|\varepsilon_F|$) effect (described schematically in Figure 2.3 (a)). From the inferred Fermi energy ε_F the Drude weight for interband transition could be calculated as $D_{inter} = e^2 v_F \sqrt{\pi n} = (e^2/\hbar)\varepsilon_F$. Strictly speaking Pauli blocking is associated with interband transitions and will be discussed further in the next section. The findings show that the D_{intra} is lower than D_{inter} against the expectations from optical sum rule. This is explained by the incomplete Pauli blocking below ε_F whose origin is still not very clear. It could be due to impurity in the sample or many-body effects [107].

2.2.2 Interband absorption

Beyond far IR range direct transitions from the valence band to the conduction band take place and these are called inter band transitions. Tight-binding model can be used to calculate the optical sheet conductivity of graphene due to interband transitions with reasonable success [98-101, 108].

2.2.2.1 Infrared and visible absorption

One of the most fascinating and unique manifestation of the linear band structure of graphene is found in the optical signatures in the range from about 0.5 eV to 1.2 eV as the frequency independent universal absorption (or equivalently σ_1) [53-56, 98-101, 102, 108]. This universal absorption can be interpreted from the structure of the expression of σ_1

$$\sigma_1(\omega) = \frac{\pi e^2}{\omega} |\boldsymbol{v}(\boldsymbol{\omega})|^2 D(\omega) \left[f\left(-\frac{\hbar\omega}{2}\right) - f\left(\frac{\hbar\omega}{2}\right) \right] \quad (2.12)$$

Where $\boldsymbol{v}(\boldsymbol{\omega})$ is the velocity matrix element between the initial state to the final state; $D(\omega)$ is the 2D joint density of state and $f(\epsilon) = [\exp\left(\frac{\epsilon}{T}\right) + 1]^{-1}$ is the Fermi Dirac distribution. Now with only nearest neighbour hopping possible $D(\omega) \propto \hbar\omega/t^2a^2$; $|\boldsymbol{v}(\boldsymbol{\omega})|^2 \propto v_F \propto ta/\hbar$, here *a* is the carbon inter-atomic distance etc. [53,56]. If we use these expressions in the above equation *(2.12)* we see that the final expression for σ_1 is independent of *a*, *t* and *ω*. At zero temperature σ_1 is found to be proportional to $e^2/\hbar$. Using Fresnel equations in the thin film limit the optical transmission of a monolayer graphene can be immediately calculated from this to be

$$T_{opt} = (1 + \frac{\pi\alpha}{2})^{-2} \approx 1 - \pi\alpha \approx 0.977 \quad (2.13)$$

Using reflectivity measurements Mak et. al, [55] have obtained similar results as shown in Figure 2.4 (d,e). Different samples were measured which show similar results [54, 58,59,66]. The decrease of σ_1 for the low energy range as shown in the Figure 2.4 (e) can be explained by the unintentional doping effect as well as temperature broadening according to the expression

$$\sigma_1(\omega) = \frac{\pi e^2}{4h} \left[tanh\left(\frac{\hbar\omega + 2\epsilon_F}{4k_BT}\right) + \tanh\left(\frac{\hbar\omega - 2\epsilon_F}{4k_BT}\right) \right] \quad (2.14)$$

Here the symbols have their usual meaning as before [92,109].

One important aspect of interband absorptions in the far IR region is the Pauli blocking as mentioned in the previous section and also schematically shown in Figure 2.3 (a) and also shown in the data of Figure 2.3 (c). Transitions are forbidden up to an energy $2|\varepsilon_F|$ due to doping of graphene till energy ε_F as the Fermi level is away from the Dirac point in this

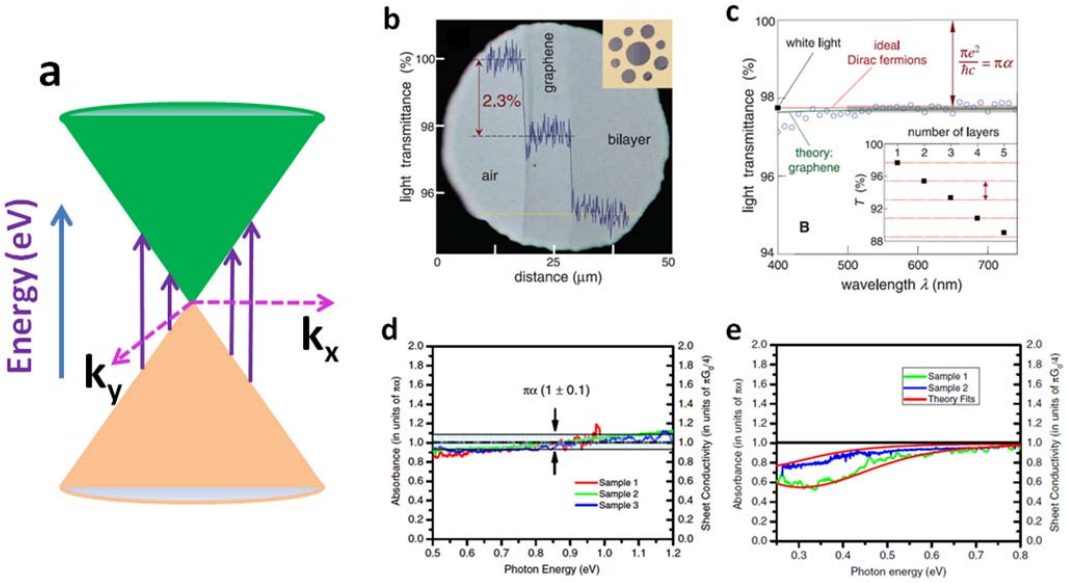

Figure 2.4 Optical response of graphene in the infrared region defined by the fine structure constant. (a) Schematic of interband transitions in undoped graphene. (b) Optical image of single layer graphene and bilayer graphene covering a 50 μm aperture. (c) Transmittance of single layer graphene and as a function of the number of layers (inset). (Figures (b) and (c) are adapted from [56]). (d) Graphene absorbance for three different monolayer samples on SiO_2/Si substrates measured between photon energies 0.5 eV to 1.2 eV. (e) Absorbance for two samples in the photon energy range 0.25 to 0.8 eV. (Figures (d) and (e) are adapted from [55])

case. However the blocking is broadened by finite temperature effect as well as carrier lifetimes. As mentioned, studies of σ_1 with electrostatic gate tuning of the carrier

concentration in this spectral range show a systematic shift in the Pauli blocking with applied gate voltage [54,66]. This tunability of σ_1 as well as capability of graphene to be doped highly with other techniques (most common is electrolytic doping [110]) may lead to many applications in the near future [111,112].

2.2.2.2 Ultra-violet (UV) absorption and beyond

Theoretical studies using GW calculations (which take into account band to band and

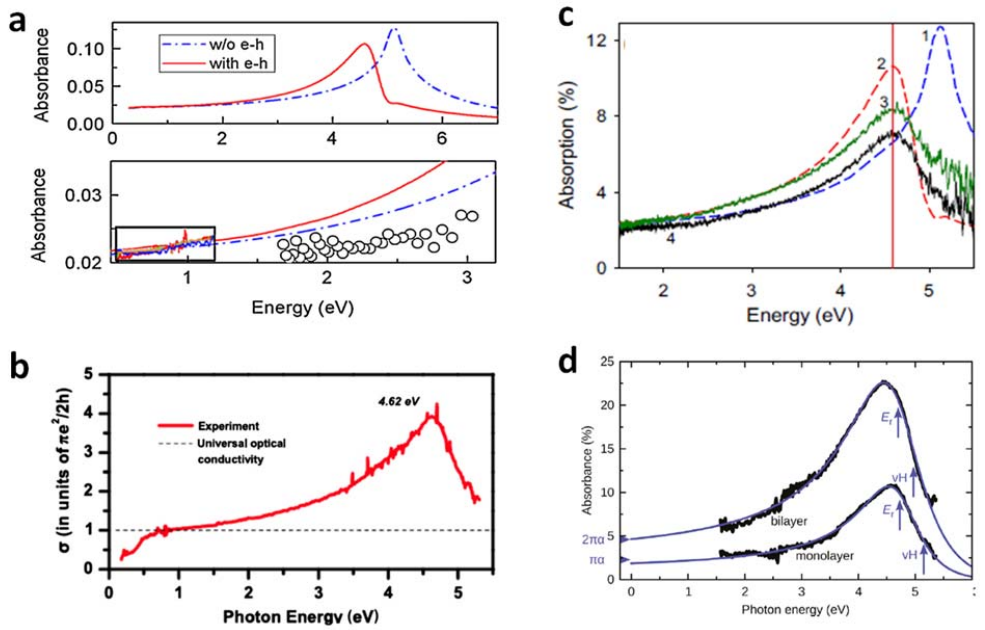

Figure 2.5 Optical response of graphene in the spectral range from 0.3 eV to 5.3 eV. (a) Absorbance of graphene calculated with and without taking into account excitonic effect (upper panel) and comparison with experiment [55,59] (lower panel) (Figure is adapted from [57]). (b) σ_1 of graphene obtained using reflectivity measurements (Figure is adapted from [59]). (c) Absorbance obtained using ellipsometry measurement; also showing results (dashed lines) from theoretical calculations with (red) and without (blue) excitonic effect (Figure is adapted from [58]). (d) Absorbance by transmission measurement on free standing graphene for monolayer and bilayer. (Figure is adapted from [60]).

electron- electron (e-e) interactions) show that σ_1 of graphene should increase gradually beyond the universal value in the visible range and there should be a peak due to band to band transitions in the saddle point singularity in the M point of the graphene Brillouin zone at the deep UV region [62]. However with the incorporation of electron-hole (e-h) interactions using GW and Bethe-Salpeter Equation (GW-BSE) approach [184] it has been seen that there is a pronounced red shift in the peak position of the order of 600 meV from 5.2 eV to 4.6 eV [62]. The details are explained briefly in the next section. There have been few experimental reports [58-61], recently confirming this predictions, which use techniques like reflectivity (Fig 2.5 (b)), SE (Fig 2.5 (c)) and transmission through free standing graphene (Fig 2.5 (d)).

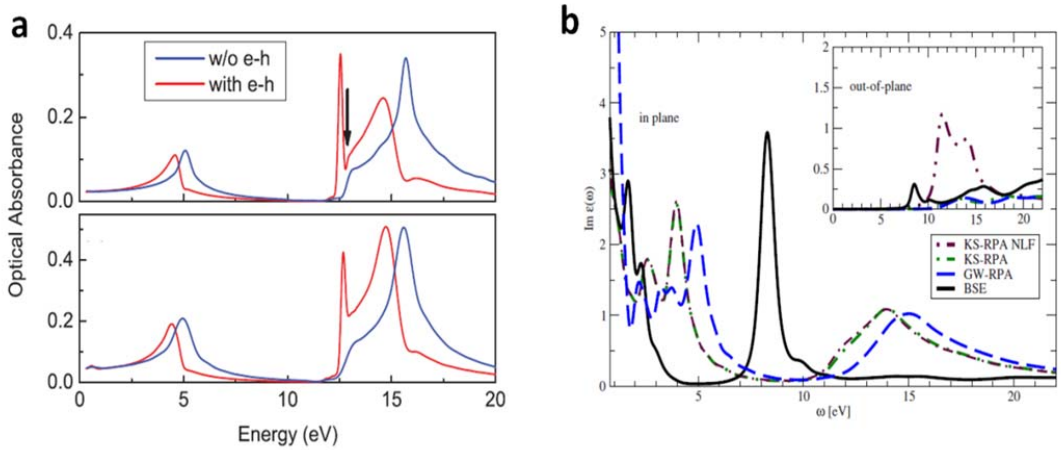

Figure 2.6 Optical response of graphene for VUV range. (a) absorbance of graphene with and without excitonic effect for monolayer (top) and bilayer (bottom) graphene. (Figure is adapted from [62]) (b) In plane optical absorption of graphene (out of plane absorption is shown in the inset). (Figures is adapted from [63]).

The σ_1 shows an asymmetric peak at around 4.6 eV in all these experimental studies. Moreover it has been observed that the sheet conductivity increases linearly with layer number [59]. However there have been relatively very few studies both theoretically [62,63] and experimentally [65] which explores σ_1 beyond about 5.3 eV. In the Figure 2.6 below we have plotted the predicted σ_1 from two reports [62, 63] where ab-initio calculations have been performed till 20 eV and 22 eV respectively. Both results show very prominent renormalization of the σ_1 when e-h interactions are taken into account beyond the GW result (which only takes e-e interactions and band to band transitions into account). Measurement of σ_1 in this high energy range is very important from the point of view of probing the electronic structure of graphene far beyond the Dirac point. Also as we have seen from these reports (and explained briefly in the next section) it gives us valuable information about many-body effects in graphene.

In this thesis we have for the first time [64] experimentally determined σ_1 of epitaxial graphene in the broad range from 0.5 eV to 35 eV using combined SE and reflectivity measurements. The details will be explained in the results section.

2.2.3 Role of many-body effects in the optical response

Despite being a semi metal, because of its 2-dimensional nature and vanishing density of state at the Dirac point, graphene shows reduced screening [19,182]. Signature of reduced screening and considerable many-body effects are in fact present in all the spectral ranges of interest and discussed till now [93,94,113,114]. Although there have been many

interesting and crucial reports about many –body effects in graphene still it is a very open field with lots of unanswered or partially answered questions. Particularly a straightforward answer to the question whether graphene is strongly interacting or weakly interacting system has not been found yet [19, 115, 116, 182]. It appears that a safe approach would be to ask more specific questions with respect to the energy scales of interest [116].

For the mid IR region as shown in the Figure 2.3(c) the Pauli blocking is not perfect and there is a threshold below the edge and σ_1 does not go to zero here [54]. The threshold may be due to either impurity and defect states or due to many-body effects [107] as predicted in some recent theoretical studies [93,113,114]. The broadening of the edge of the blocking, Fermi edge singularities and increase of the conductivity just next to the edge have been predicted in these calculations and some of these have been confirmed by experiments [54]. Controlled experiments with high quality gated samples are required for better understanding of the many body effects and its contribution to the final conductivity in this spectral range.

A robust signature of many-body effects in graphene can be seen in the red shift of the band to band peak at 5.2 eV to 4.6 eV [57- 60]. Both theoretical predictions and many experimental reports confirm this finding [57-61]. The joint density of state (JDOS) which is proportional to $-\log|1-(\omega/\omega_0)|$ determine the final line shape of the optical conductivity for a 2D saddle point [117]. As this function is symmetric, the line shape of σ_1 is predicted to be symmetric in this picture. Ab-initio GW calculations predict such a

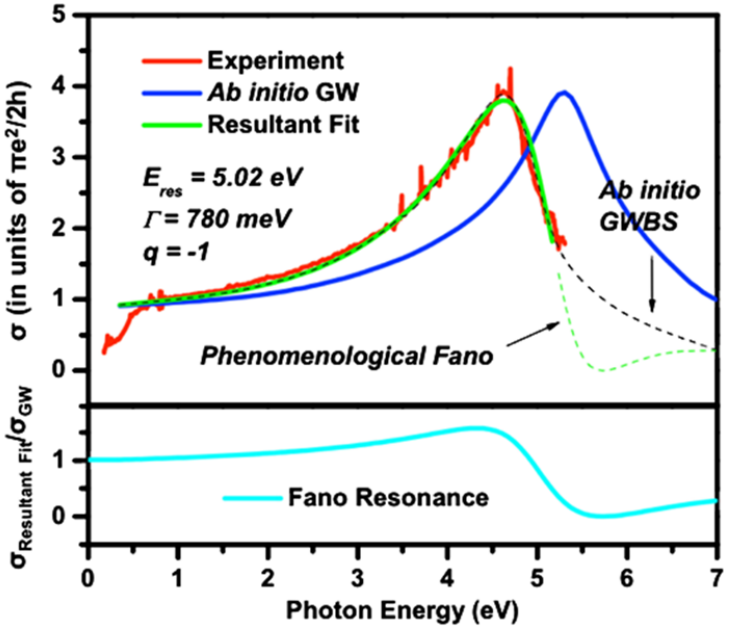

Figure 2.7 Experimental data fit of σ_1 using the Fano model starting with result from GW calculations. The black dashed line represents calculations using GW-BSE approach which shows excellent agreement with the Fano fit as well as with the experimental data within the experimental spectrum range. (Figure is adapted from [59])

symmetric line shape as shown in the Figure 2.7 [57]. But introduction of e-h interactions using GW-BSE approach leads to two very prominent effects in the final σ_1 - asymmetry and red shift of the peak by 600 meV from 5.2 to 4.62 eV. This can also be interpreted using phenomenological Fano line- shape analysis [118-121]. As graphene has no band-gap there can be no bound excitons in graphene [57,62]. However discrete excitonic states below the saddle point singularity can couple with the continuum of states and this leads to redistribution of the oscillator strength. This is the essence of the Fano resonance. In this case the relationship for the final optical conductivity can be written as

$$\frac{\sigma_1}{\sigma_{1,\mathrm{cont}}} = C\frac{(q+\varepsilon)^2}{1+\varepsilon^2} \qquad (2.15)$$

Here $\boldsymbol{\varepsilon} = (\omega - \omega_{\boldsymbol{res}})/(\Gamma/2)$ is the normalized energy by width, Γ relative to the excitonic resonance energy $\omega_{\boldsymbol{res}}$. The magnitude of q^2 quantifies the ratio of the strength of the e-h coupling to the band to band transition, whereas the asymmetry of the line-shape is determined by the sign of q.

Using this phenomenological Fano model the observed asymmetry and red shift in σ_1 can be very satisfactorily reproduced as shown in the Figure 2.7 above [59]. This also agrees very well with the ab-initio GW-BSE calculation results. Overall these results shows that graphene carries very prominent signatures of many-body effects in the σ_1 in the UV range in the form of excitonic effect.

In this thesis we have performed extensive studies of σ_1 of graphene in this spectral range using different substrates [61, 185]. These studies reveal interesting aspects of unequal screening of e-e and e-h interactions in the different systems which will be described in detail in the result section.

For energies in the range above 5 eV and till about 20 eV there have been theoretical reports of similar considerable as well as dramatic many-body effects as shown in Figure 2.6 above [62,63]. The Figures 2.6 (a) shows the effect of incorporating e-h interactions by GW- BSE approach in the calculations of σ_1 in the energy range till 20 eV for both single layer (top) and bilayer (bottom) free-standing graphene [62]. Here a weakly resonant (with a relatively longer lifetime) exciton has been predicted just below the

absorption edge at about 12.5 eV. This weak resonant characteristic is explained with the help of the fact that the bands responsible for the transitions - σ and π^* are almost parallel. The position of the excitonic peak is almost same for both monolayer and bilayer graphene.

In a similar study by Trevisanutto et. al, [63] a more dramatic manifestation of a resonant excitonic peak has been predicted at an energy 8.3 eV for monolayer graphene for in-plane optical response [63]. Figure 2.6 (b) shows the result for the imaginary part of the in plane dielectric function of monolayer graphene. For bilayer graphene the peak is blue-shifted to 9.6 eV. This excitonic resonance has resulted from a background continuum of dipole forbidden transitions. The Figure 2.6(b) also shows the dramatic shift of almost all spectral weight to the excitonic peak position area when e-h interactions are taken into account in the calculations.

In this thesis we have measured σ_1 of epitaxial graphene in a broad energy range (0.5 eV 35 eV) [64]. We find some very prominent and important signatures of many-body effects in our results which are explained in detail later.

Overall it can be said that despite being a semi metal graphene shows rich manifestation of many-body effects in all the different spectral ranges of interest. Therefore σ_1 (or absorbance etc.) investigations could be a very powerful approach to elucidate the role and significance of these interactions. Most of the efforts in this thesis have been in this direction with some interesting as well as important results.

2.3 Substrate effects

In graphene, because of its 2D nature, many-body interactions can be tailored externally by varying the substrate dielectric functions [93]. A low density of state near the Dirac point helps in this regard. Moreover substrates can contribute charge impurity scatterers as well as affect the flexural phonon modes of graphene, affecting both transport as well as optical properties. Numerous substrate dependent (also for free-standing case) transport studies have revealed [19,49,50,122,123] such effects but in comparison such optical studies [50] are scarce. There has been predictions of considerable charge transfer as well as hybridization of bands of graphene with various substrates [126,127]. These hybridizations (or 'mixing') and considerable charge transfer will affect the σ_1 of graphene. Below we discuss these effects briefly.

2.3.1 Tailoring the dielectric screening

Structurally graphene is unique in the sense that it is a true 2D material and hence the substrate can affect its strength of interactions directly (depending on the graphene – substrate interface quality and coupling). A relevant parameter for the strength of these interactions is the effective fine structure (α_g^*) constant as highlighted by recent transport measurements [125]. In case of free standing graphene the effective fine structure constant (α_g) is purely the ratio of the potential energy to kinetic energy of electron given by $e^2/\hbar v_F$, where v_F is the renormalized Fermi velocity near Dirac point [115].

But in case of graphene sandwiched between two different media, the effective fine structure constant can be written as

$$\alpha_g^* = \frac{2e^2}{(\varepsilon^1 + \varepsilon^2)\hbar v_F} \qquad (2.16)$$

where ε^1 and ε^2 are the complex dielectric functions of the two media respectively. For the free standing case the fine structure constant is given by the nominal value 2.2 and this value indicates that graphene is a strongly interacting system (near the Dirac point) [19, 116]. However a recent study on highly oriented pyrolytic graphene [115] has

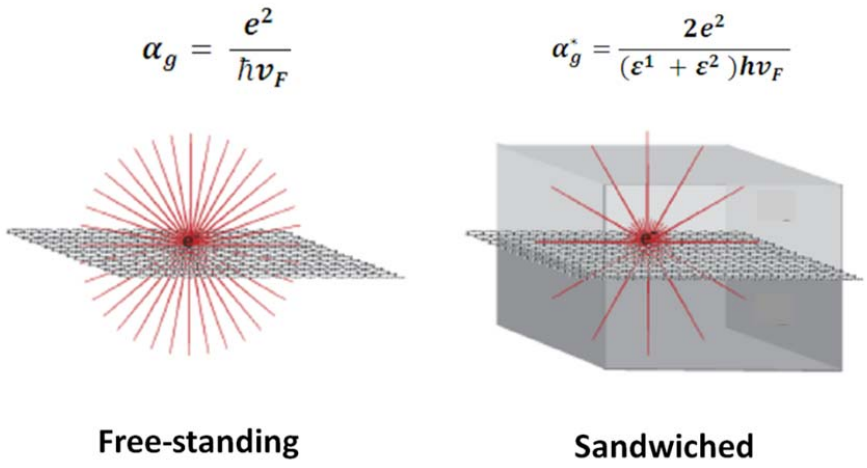

Figure 2.8 Schematic of dielectric screening environment of free-standing graphene (left) and graphene sandwiched between two mediums (right) with complex dielectric constants ε^1 and ε^2. (Figure is adapted from [125])

revealed that the value of the effective fine structure constant (which is evaluated as a function of momentum and energy) can be far lower than the nominal value indicating

that graphene might be a weakly interacting system even near the Dirac point. However it is still debated whether graphene is a weakly interacting or a strongly interacting system. In this thesis we have measured σ_1 by varying the substrate environments using extreme cases of dielectric screening- one substrate being a wide band gap insulator (quartz) which gives a nominal effective fine structure constant of ~ 0.81 in ambient, while one substrate being a metal contributing energy dependent and far lower effective fine structure constant. The details of the interesting finding are explained in the results section [61].

2.3.2 Charge transfer and hybridization

In recent studies it has been found that graphene-substrate systems show considerable charge transfer as well as band structure modification (for the graphene layer) for different kind of substrates [125-129]. Particularly detailed DFT calculations for graphene on metallic hybrid systems has revealed that metals can be broadly divided into two categories depending on the coupling strengths between the p_z orbital of the carbon atoms and d_{z^2} orbital of the metal (for example Cu, Ni etc.) atoms [126,127]. In case of the first class of atoms (Ni, Co etc.) the coupling is strong and it perturbs the unique bandstructure of graphene strongly making the band more graphene –metal hybrid type. On the other hand in the second class (Cu, Al etc) the perturbation is weak and the graphene layer still retains its characteristics to a large extent. Figure 2.9(a) show the band structure of a graphene on Cu (111) hybrid system with the distance between the graphene and Cu layer as 3.26 Å [126]. In this case the Fermi level is in the conduction

band slightly above the Dirac point. The charge transfer is due to the work function difference between the graphene layer and the metallic substrate. Moreover the charge transfer is a strong function of the spacing between graphene and the substrate as shown in Figure 2.9 (b) [127].

In similar studies there have been predictions of similar strong substrate induced charge transfer and also band structure renormalization (or hybridizations) for wide band gap semiconductor substrates like TiO_2 [128]. Ab-initio DFT calculations for graphene- TiO_2 (110) hybrid system shows considerable charge transfer as shown in the Figure 2.10 (a). Similar studies on graphene- graphitic carbon nitride (g-C_3N_4) hybrid system shows a band gap opening as well as 'mixed' bandstructure far away from the Dirac point as shown in the Figure 2.10 (b) [129].

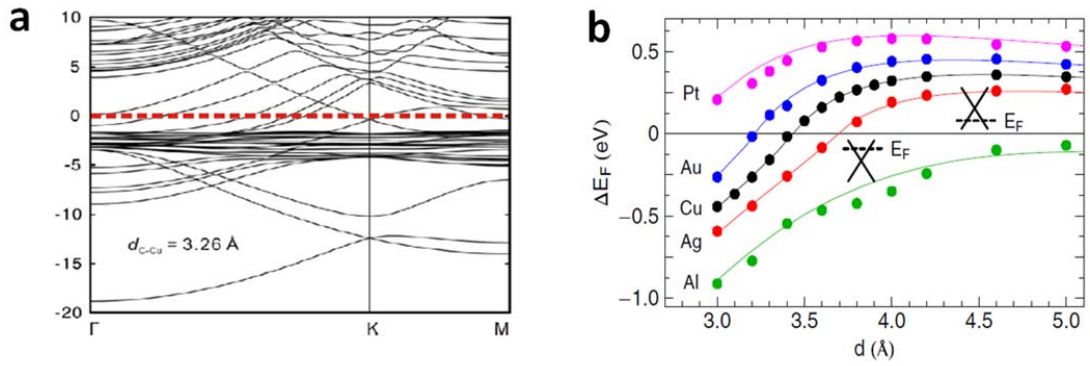

Figure 2.9 (a) Electronic band structure of graphene-copper hybrid system with the distance between graphene and copper 3.26 Å.(Figure is adapted from [126]). (b) Shift of the graphene Fermi-level as a function of the interface distance. The dots represents DFT calculation results while the lines represent the model outputs used in [127]. (Figure is adapted from [127]).

These charge transfer effects as well as hybridizations for graphene-substrate systems will have immediate manifestations on σ_1. For example relatively huge predicted Fermi level shift of around 0.65 eV for graphene-TiO_2(110) hybrid systems as predicted [128] can be measured as a Pauli blocking in σ_1. Also it can be expected that the huge supply of holes will lead to more screening of many-body effects in the graphene layer. Therefore those features which are characteristics of many-body effects will be affected in these systems as compared to free-standing graphene. Another manifestation may be due to the band structure renormalization in the hybrid system. The overall shape of σ_1 might be affected due to the deviation of the graphene band structure from the pristine case.

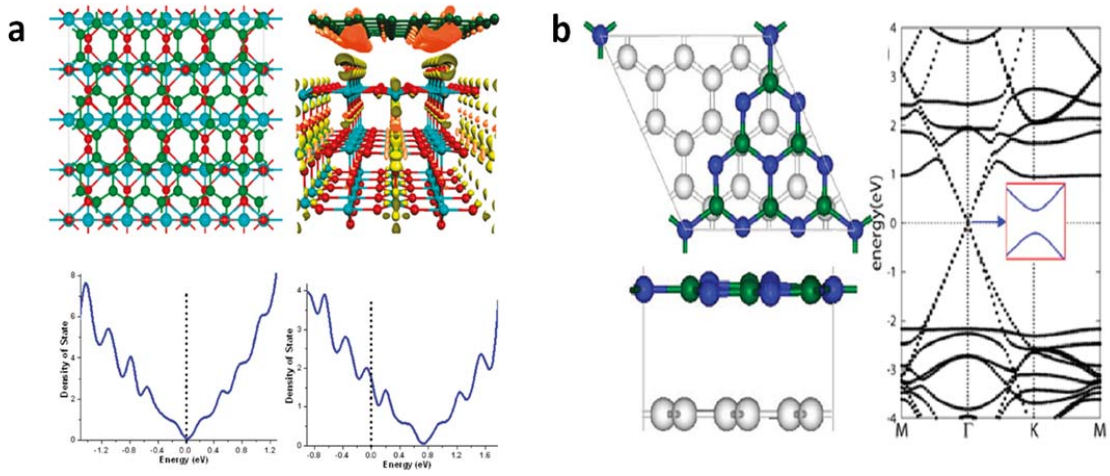

Figure 2.10 (a) Top**:** Model for simulation and 3D charge density for graphene –rutile TiO_2(110) interface; bottom: Density of state for freestanding (left) and rutile TiO_2 (110) supported graphene. The black dashed line represents the Fermi level position. (Figure is adapted from [126]). (b) Left: top view (top) and side view (bottom) of graphene/g-C_3N_4 interface model. Right: Resultant band structure of graphene supported on g-C_3N_4. (Figure is adapted from [127]).

In our results [61] we find some relevant insights in these directions as discussed in the results section. It may be mentioned that in real cases- the graphene –substrate interface is not ideal as used in the calculations. As seen in the calculations the charge transfer and hybridizations are strong functions of the graphene substrate distance and with no other material between those two. Hence a very clean interface is an absolute requirement to observe such effects. This is the main challenge in these efforts along-with the fact that extracting the contribution from only the graphene layer in absorption, reflectivity or ellipsometric studies is another challenge as its generally very small in comparison to the substrate contribution.

2.4 Photo-induced effects

Graphene-substrate systems as well as graphene interfaces with other materials can show photo-induced effects like charge transfer between the graphene layer and substrate [128, 131,132]. This is another way of introducing charge carriers in graphene and changing its conductivity. Fundamentally the study of these charge transfer may reveal the underlying interesting physical processes like charge carrier transfer process and the dynamics, extent of hybridization etc. Also understanding and exploring these photo-induced charge transfer may lead to applications in solar cell technologies, photodetectors, photocatalysis etc. [130-134]. Below we will briefly describe some of these aspects.

2.4.1 Light induced doping

The large work function difference between graphene and its substrate may lead to considerable charge transfer as shown in Figure 2.10 (a) for the case of graphene/titania where graphene becomes hole-doped [128]. Another result from this DFT study is that direct transition from the valence band of graphene to the conduction band of titania is possible with light illumination of the right wavelength (Fig 2.11 (a)). In another study using molecular dynamics simulation in the framework of time domain DFT reveals

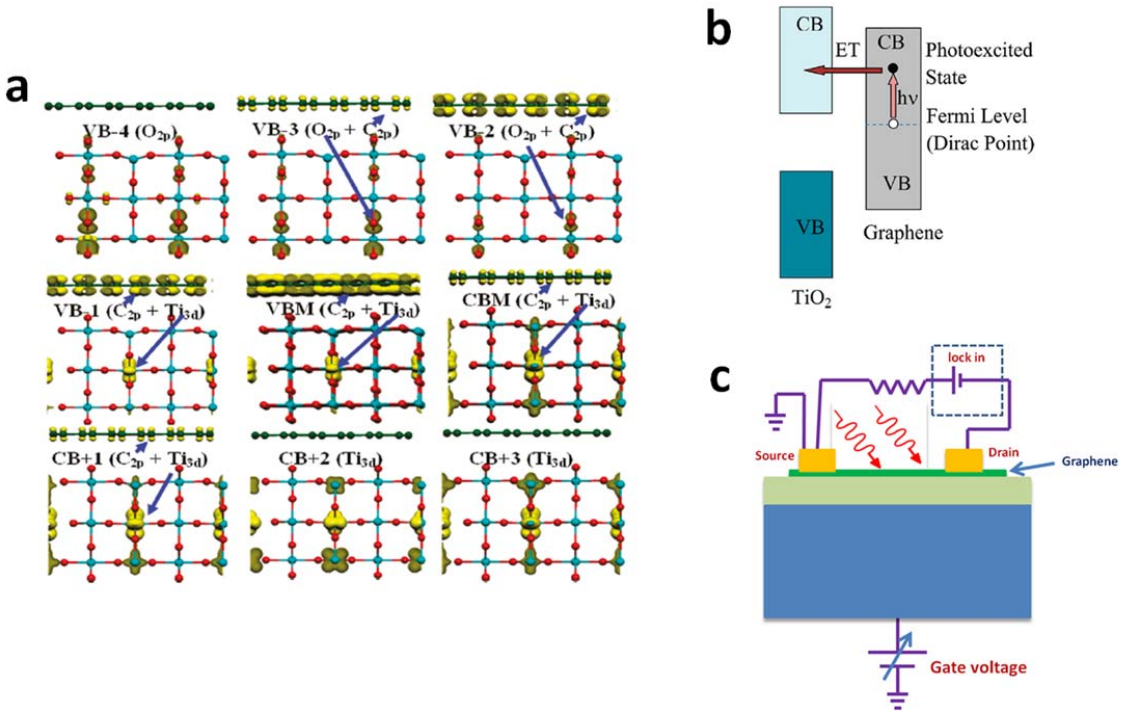

Figure 2.11 (a) Electron and hole density distributions for the valence band and conduction states in the graphene-rutile TiO_2(110) hybrid system. The green, blue and red balls represent C, Ti, O atoms respectively. (Figure is adapted from [128]). (b) Schematic representation of the light induced electron injection in the graphene-rutile TiO_2(110) hybrid system (Figure is adapted from [135]). (c) Schematic circuit of the proposed illuminated FET transport measurement system.

[135] that for this system the time scale of charge transfer is faster than electron-phonon relaxation. This is very interesting both from theoretical as well as application point of view. Carriers are assumed to be relaxing and recombining faster before they are separated as graphene shows semi-metallic characteristics. But this result shows that in fact the charge separation is efficient enough for application purpose. These kind of systems can be used in photovoltaics, photodetectors etc.

We propose an illuminated field effect measurement set up with planner geometry between graphene and substrate mimicking the geometrical structures used in the theoretical calculations [128, 129, 135] to find out the amount of charge transfer which leads to change in dc conductivity of graphene. We have tried to fabricate field effect devices on graphene /300 nm $SrTiO_3$/Nb-$SrTiO_3$ for this kind of studies. As $SrTiO_3$ has similar 3d bands for transitions to be possible like rutile TiO_2(110), the results could lead to the quantification of this charge transfer during illumination and also it may reveal other fundamental aspects of the hybrid system. The aim is to fabricate similar devices on graphene on TiO_2(110) films later.

Our results of measurements of σ_1 in graphene on $SrTiO_3$ (100) substrates have reveled that in fact under illumination there are transitions possible from graphene valence band to low lying 3d conduction bands of $SrTiO_3$. Simultaneously the hybrid nature of the bands leads to new excitonic states in graphene near the band-gap energy of $SrTiO_3$ resulting in a huge renormalization of the optical response of the graphene layer [185] due to Fano resonance. Essentially this shows that graphene on $SrTiO_3$ behaves more like a composite or hybrid system than in the case of wide band gap substrates like SiO_2/Si

and the optical properties of the graphene layer changes drastically in the former case. The details are explained in the results (Chapter 7).

2.5 Light emission

As graphene does not have a band gap the excited carriers relax fast and hence there is no efficient light emission from graphene [136-139]. Under continuous-wave laser excitation graphene shows no measureable photoluminescence (PL) spectra. However it has been seen that when excited with 30-fs pulsed light from a Ti:sapphire laser it shows measureable PL spectra [136]. As shown in the Figure 2.12 (a) the PL spectra is of wide

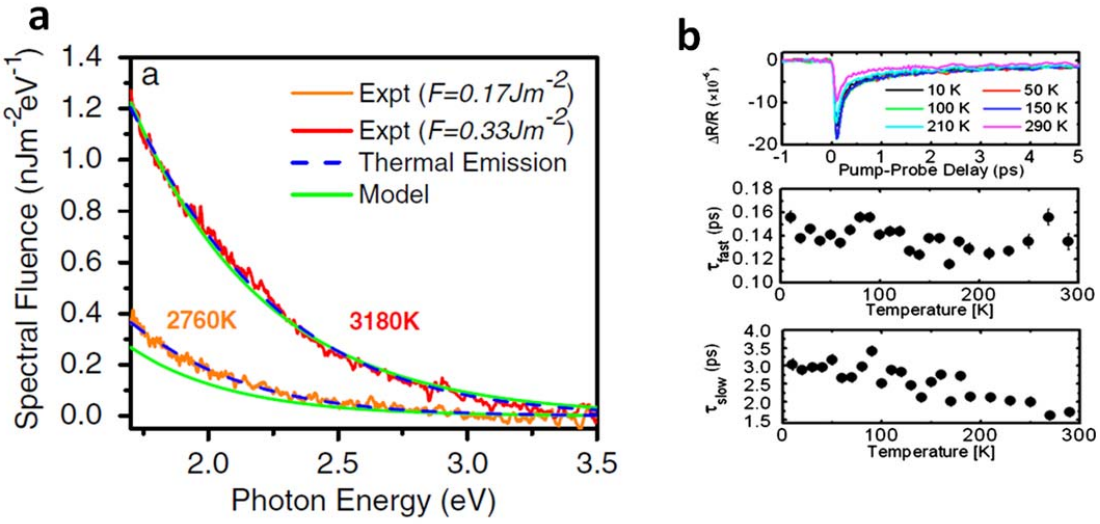

Figure 2.12 (a) Data and fit (using thermal emission and model introduced in [136]) of Spectral fluence of light emission from graphene for excitation with 30-fs pulses of absorbed fluences of F = 0.17 and 0.33 Jm^{-2}. (Figure is adapted from [136]) (b) Temperature dependence of the transient differential reflectivity $\Delta R/R$ vs pump probe delay for bilayer graphene. The panels below shows the time constants for fast (τ_{fast}) and slow (τ_{slow}) exponential decay as functions of temperature. (Figure is adapted from [140])

spectral range and there is light emission even above the excitation wavelength. These spectra can be explained using a thermal emission model using the Plank's law as

$$\mathcal{F}(\hbar\omega) = \tau_{em}\, \varepsilon(\hbar\omega) \frac{\omega^3}{2\pi^2\, c^2} \left[\exp(\frac{\hbar\omega}{k_B T_{em}})\right]^{-1} \qquad (2.17)$$

here $\varepsilon(\hbar\omega)$, τ_{em} denotes the emissivity, obtained from the measured absorption spectrum of graphene and the effective emission time for each excitation pulse respectively. It can be inferred from this study that the electrons thermalize rapidly to a Fermi-Dirac distribution achieving a high emission temperature during the short laser pulse duration of ~ 30 fs.

Figure 2.12 (b) shows the results of time resolved transient differential reflectance spectra of bilayer graphene on SiO_2/Si substrate at different temperatures [140]. These results can be fitted with a bi-exponential model

$$\frac{\Delta R}{R} = A_{fast} \exp(-t/\tau_{fast}) + A_{slow} \exp(-t/\tau_{slow}). \qquad (2.18)$$

The τ_{fast} (<160 fs) and τ_{slow} (1.5-3.4 ps) can be associated with processes of optical phonon emission and optical phonon-acoustic phonon coupling respectively. In this report [140] a comparison of the time resolved transient differential reflectance spectra of $FeCl_3$ intercalated graphene with the pristine bilayer graphene has been made and it

reveals different mechanism and process of energy relaxation as well as charge carrier dynamics in these systems. Overall these kind of ultrafast dynamical studies are crucial for understanding different kinds of radiative recombination processes in graphene as well as the energy relaxation pathways.

In this thesis we have also performed such a time resolved comparative transient differential reflectance spectra study for graphene on SiO_2/Si and graphene on $SrTiO_3$ with interesting and important results. The details are described in the results.

Chapter 3

Experimental techniques

In this chapter we discuss all the relevant experimental and sample fabrication techniques used in our work. As spectroscopic ellipsometry is the central measurement technique used, the principles of ellipsometry are explained in detail starting from Fresnel equations and using Stokes vectors representation finally. It is followed by the description of features of the lab ellipsometer system as well the reflectivity set-up in the SUPERLUMI beamline at DESY. Sample preparation and characterization for both epitaxial as well as Chemical Vapour Deposited graphene have been described in detail in the next section. As considerable preliminary work has been performed for studies like gate dependent optical conductivity study, light induced charge transfer etc. the relevant electrode deposition techniques, electron beam lithography process are also touched upon. We conclude with a concise description of the transport measurement set up details for those studies.

3.1 Spectroscopic ellipsometry (SE)

The main measurement technique used in this thesis is spectroscopic ellipsometry (SE) [141-144]. Ellipsometry is a relatively old technique first developed by Drude [145] in 1887. But it only started gaining widespread use from 1970's due to automation of the measurement technique and also use of computers for fast data processing. Ellipsometry gives the complex reflection coefficients (Ψ, Δ) spectra, from which the optical constants and thickness of the thin film layers in a samples can be extracted using optical modeling. Moreover it is a very surface sensitive technique and the measurement is even sensitive to a thickness change of the order of ~1Å. Unlike reflectivity and transmission

measurements it can provide both the real and imaginary parts of the dielectric functions simultaneously which is another major advantage of this technique. These features make SE an ideal system for a wide range of applications in research and industry.

3.1.1 Introduction to spectroscopic ellipsometry

In ellipsometry, change in polarized light is measured upon reflection on (or transmission through) a sample. In almost all cases two quantities are measured - (Ψ, Δ) , where Ψ represents the amplitude ratio and Δ represent the phase difference between the p- and s-polarized light waves. When the measurement is performed over an energy range it is

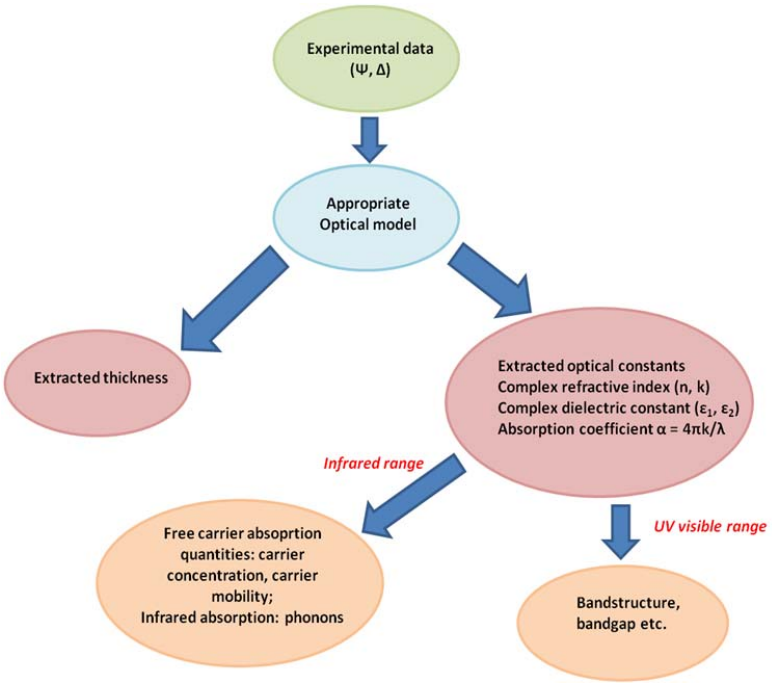

Figure 3.1: Ellipsometry technique workflow schematic.

called SE. The most commonly used energy range for SE is the ultraviolet-visible (UV-VIS) range.

However it should be mentioned that although it is a fast, nondestructive and very surface sensitive technique, the analysis and interpretation of the (Ψ, Δ) data to extract the optical constants finally (or additionally thickness also) is not trivial (Fig. 3.1). In fact only when the sample under study is homogenous, isotropic, and thick enough - the (Ψ, Δ) values can be analytically converted to the optical constants. In any other case an optical model with associated numerical approximation techniques are required for extraction of meaningful results.

3.1.2 p- and s- polarized light and Fresnel coefficients

As ellipsometry is exclusively about polarization change upon reflection on a sample (or transmission through a sample), to understand the principles involved we start with the Fresnel equations which give the reflection (transmission) amplitude coefficients for p- and s- polarized light [146,147].

When a linearly polarized light wave travels in the *x* direction it's electric and magnetic field vectors can be expressed as

$$E = E_0 \, exp[i(\omega t - Kx + \delta)], \qquad (3.1a)$$

$$B = B_0 \, exp[i(\omega t - Kx + \delta)]. \qquad (3.1b)$$

Here K is the propagation number, ω is the angular frequency and δ is the initial phase.

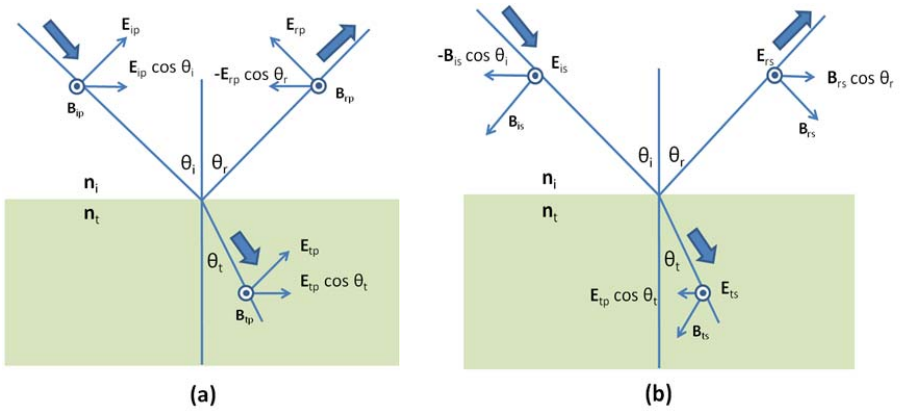

Figure 3.2: Electric filed (**E**) and magnetic field (**B**) for (a) p-polarization and (b) s-polarization of light (Figures are adapted after modifications from [144]).

In the case of light being reflected or transmitted by a sample in oblique incidence, the wave can be treated as composed of two components— p- polarized where the electric field vector is in plane (plane of incidence) and the other is s- polarized where the electric field is perpendicular to the plane.

In case of a medium with refractive index *n*, using Maxwell's equations and boundary conditions we finally get amplitude reflection coefficient for p-polarized light

$$r_p \equiv \frac{E_{rp}}{E_{ip}} = \frac{n_t \cos\theta_i - n_i \cos\theta_t}{n_t \cos\theta_i + n_i \cos\theta_t} \qquad (3.2)$$

Similarly the amplitude transmission coefficient for p-polarized light is

$$t_p \equiv \frac{E_{tp}}{E_{ip}} = \frac{2\, n_i \cos\theta_i}{n_t \cos\theta_i + n_i \cos\theta_t} \qquad (3.3)$$

and amplitude reflection and transmission coefficients for s- polarized light respectively are

$$r_s \equiv \frac{E_{rs}}{E_{is}} = \frac{n_i \cos\theta_i - n_t \cos\theta_t}{n_i \cos\theta_i + n_t \cos\theta_t} \quad (3.4)$$

and $$t_s \equiv \frac{E_{ts}}{E_{is}} = \frac{2\, n_i \cos\theta_i}{n_i \cos\theta_i + n_t \cos\theta_t} \quad (3.5)$$

The above four relations *(3.2- 3.5)* are known as Fresnel equations. When the refractive index is complex, these equations can be further generalized to obtain the following Fresnel relations for reflection

$$r_p = \frac{N_{ti}^2 \cos\theta_i - \left(N_{ti}^2 - (\sin\theta_i)^2\right)^{\frac{1}{2}}}{N_{ti}^2 \cos\theta_i + \left(N_{ti}^2 - (\sin\theta_i)^2\right)^{\frac{1}{2}}} \quad (3.6)$$

and $$r_s = \frac{\cos\theta_i - \left(N_{ti}^2 - (\sin\theta_i)^2\right)^{\frac{1}{2}}}{\cos\theta_i + \left(N_{ti}^2 - (\sin\theta_i)^2\right)^{\frac{1}{2}}} \quad (3.7)$$

here *N* is the complex refractive index and $N_{ti} = \frac{N_t}{N_i}$.

In case of multilayer systems the resultant amplitude reflection coefficients can be expressed as a sum of individual appropriate combinations of the amplitude reflection and transmission coefficients of each interface and also taking into account the phase differences of each wave.

3.1.3 Representation of polarized light

An electromagnetic wave travelling in the z direction can be expressed as a vector sum of electric fields $\boldsymbol{E}_x$ and $\boldsymbol{E}_y$:

$$\boldsymbol{E}\,(z,t) = \boldsymbol{E}_x\,(z,t) + \boldsymbol{E}_y\,(z,t)$$

$$= \{\,E_{x0}\,exp[i(\omega t - Kx + \delta_x)]\}\hat{\boldsymbol{x}} + \{E_{y0}\,exp\big[i\big(\omega t - Kx + \delta_y\big)\big]\}\hat{\boldsymbol{y}} \qquad (3.8)$$

Here $\hat{\boldsymbol{x}}$ and $\hat{\boldsymbol{y}}$ represent the unit vectors along the respective directions. The relative phase difference $\big(\delta_y - \delta_x\big)$ is the most important quantity which determines the state of polarization of the resultant wave. A neat and elegant way to mathematically represent polarization states and also analyze the effect of optical components in a real system is the use of *Jones vectors* and *Jones matrices* respectively [141-144].

A complete representation of the polarization state of a wave can be given by

$$\boldsymbol{E}(z,t) = \begin{bmatrix} E_{x0}\ exp(i\delta_x) \\ E_{y0}\ exp(i\delta_y) \end{bmatrix} \qquad (3.9)$$

It can be written further simply as

$$\boldsymbol{E}(z,t) = \begin{bmatrix} E_x \\ E_y \end{bmatrix} \qquad (3.10)$$

Where $E_x = E_{x0}\ exp(i\delta_x)$ and $E_y = E_{y0}\ exp(i\delta_y)$.

In ellipsometry, relative changes in amplitude and phase are of importance. Therefore Jones vectors are generally expressed in terms of normalized intensities. So, linearly polarized wave in x and y directions would be given by $E_{linear,x} = \begin{bmatrix} 1 \\ 0 \end{bmatrix}$ and $E_{linear,y} = \begin{bmatrix} 0 \\ 1 \end{bmatrix}$ respectively.

Similarly, linearly polarized light oriented at 45^0 is written as $E_{+45^0} = \frac{1}{\sqrt{2}}\begin{bmatrix}1\\1\end{bmatrix}$ etc. In this formalism, optical components are described by 2×2 matrices called Jones matrices. Using Jones matrices each ellipsometric components like a polarizer, analyzer, compensator etc. can be represented as a 2×2 matrix and on mathematical terms pre-multiplication of the Jones vector of the wave with the respective matrix will represent the result of the wave going through (or 'interacting' with) the component. As an example we can take the case of a linear polarizer whose azimuth angle is α with respect to the x-y coordinates of a linearly polarized light $\boldsymbol{E}_i$. This can be represented by the following

$$\boldsymbol{E}_0 = \begin{bmatrix}\cos\alpha & 0\\ 0 & \sin\alpha\end{bmatrix}\boldsymbol{E}_i \qquad (3.11)$$

This process can be used sequentially when more optical components are present keeping in mind the proper order of matrix multiplication.

Another way of representing polarization states is the Stokes parameters (or vectors). Unlike Jones vectors Stokes vectors can be used for un-polarized as well as partially polarized waves. These Stokes parameters have direct relevance in ellipsometry measurements as those are measured in ellipsometry and they appear in the final measured quantities as explained in the next section.

The four components of the Stokes vector are as follows:

$$S_o = I_x + I_y = E_x E_x^* + E_y E_y^* \qquad (3.12a)$$

$$S_1 = I_x - I_y = E_x E_x^* - E_y E_y^* \quad (3.12b)$$

$$S_2 = I_{+45^0} + I_{-45^0} = 2E_{x0}E_{y0}\cos\Delta \quad (3.12c)$$

$$S_3 = I_R - I_L = -2E_{x0}E_{y0}\sin\Delta \quad (3.12d)$$

here I_x and I_y represent the light intensity of linear polarization in the x and y directions respectively. Similarly I_{+45^0} represent the light intensity at $+45^0$ polarization etc. I_R and I_L represent the light intensity for right-circular and left-circular polarization. Also $\Delta = \delta_x - \delta_y$. In vector form Stokes vector is represented as

$$S = \begin{bmatrix} S_0 \\ S_1 \\ S_2 \\ S_3 \end{bmatrix} \quad (3.13)$$

The transformation of a Stokes vector is represented by a Mueller matrix which is a 4×4 matrix. Therefore optical elements in this representation are given by Mueller matrices. For example when a linearly polarized light wave which is at 45^0 passes through a polarizer whose transmission axis is along the x direction, the output light wave can be obtained as

$$\frac{1}{2}\begin{bmatrix} 1 & 1 & 0 & 0 \\ 1 & 1 & 0 & 0 \\ 0 & 0 & 0 & 0 \\ 0 & 0 & 0 & 0 \end{bmatrix}\begin{bmatrix} 1 \\ 0 \\ 1 \\ 0 \end{bmatrix} = \begin{bmatrix} 1/2 \\ 1/2 \\ 0 \\ 0 \end{bmatrix} \quad (3.14)$$

Here the 4×4 matrix on the left hand side is the Mueller matrix for the polarizer.

3.1.4 Principles of ellipsometric measurement

When light is reflected (or transmitted through) a sample, the p- and s- polarized components of the light wave undergo different changes in amplitude and phase. Ellipsometry is a technique in which these changes are measured. The fundamental quantities measured in ellipsometry are (Ψ, Δ) which express the amplitude ratio and phase difference between the p- and s- polarized waves. They are related to the (complex) amplitude reflection coefficients as follows:

$$\rho \equiv \tan \Psi \, exp\,(i\Delta) \equiv \frac{r_p}{r_s} \qquad (3.15)$$

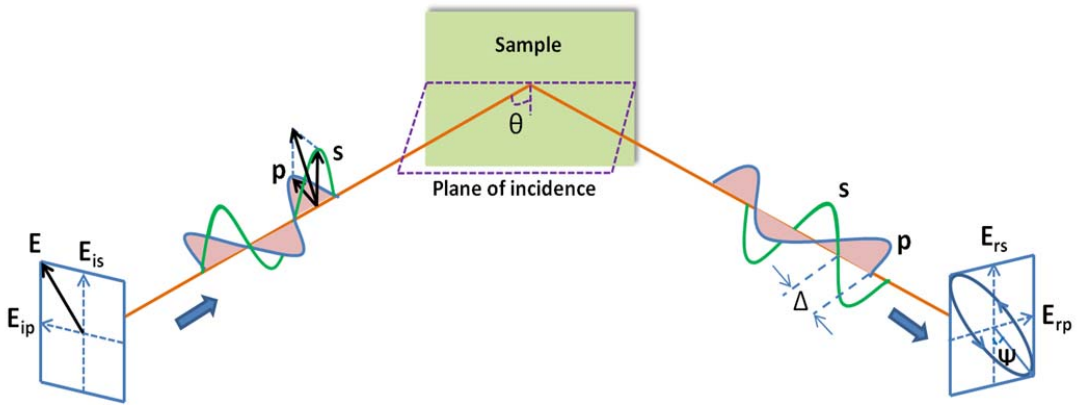

Figure 3.3: Schematic of the measurement principle of ellipsometry (Figure is adapted after modifications from [144]).

In case of transmission, the amplitude reflection coefficients are replaced by amplitude transmission coefficients. As r_p and r_s are defined in terms of ratios of reflected electric fields to incident electric fields the above expression *(3.15)* can be further written as

$$\rho \equiv \tan\Psi \, exp\,(i\Delta) \equiv \frac{r_p}{r_s} \equiv \frac{\left(\frac{E_{rp}}{E_{ip}}\right)}{\left(\frac{E_{rs}}{E_{is}}\right)} \qquad (3.16)$$

In the Figure 3.3 above E_{is} and E_{ip} are equal (which is not always the case). In such a case

$$\tan\Psi \, exp\,(i\Delta) \equiv \frac{r_p}{r_s} = \frac{E_{rp}}{E_{rs}} \qquad (3.17)$$

and Ψ can be interpreted as the angle between the reflected p- and s- polarization. Similarly Δ is given by the phase difference between these two waves as shown in Figure 3.3.

In general while considering ellipsometric configurations proper care should be taken for the coordinate systems used. These considerations are not explained here and can be found in other references [141- 144].

There are various kinds of ellipsometry set-ups depending on the ways of measurement of (Ψ, Δ). Till around 1970 only null ellipsometry was used. But nowadays most ellipsometric systems are of different kinds which can be broadly divided into two major categories – with rotating optical elements and those using photoelastic modulators. For our studies an ellipsometer with rotating optical elements (more specifically rotating

analyzer with compensator) is used. The working principle is briefly explained in the next section for such an ellipsometer.

3.1.4.1 Rotating analyzer ellipsometry

A rotating analyzer ellipsometer is one of the various kinds of ellipsometer set-ups used and it can be symbolically represented as PSA_R, where P, S and A_R stand for polarizer, sample and (rotating) analyzer respectively. In SE systems, generally the wavelength of the incident light is selectively changed using a monochromator. But this essentially slows down the speed of operation. Therefore in many SE systems, particularly used in real time monitoring, a grating spectrometer is used in the detector side and the incident light is white light. The system used in the current thesis is of the later kind.

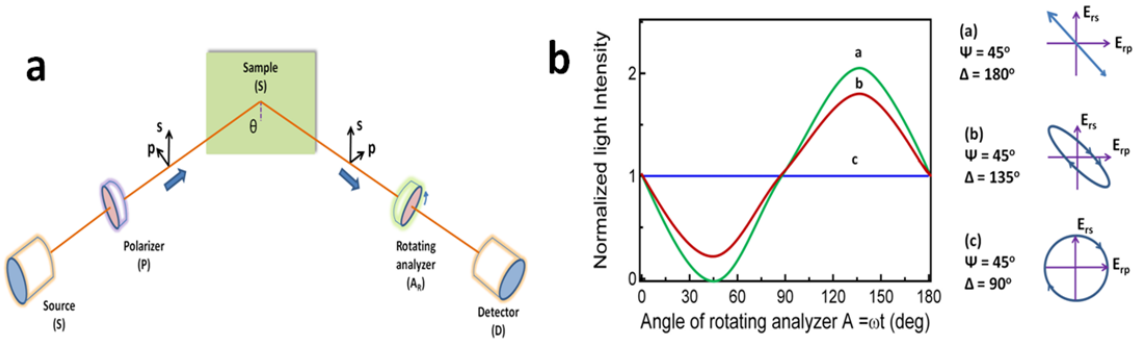

Figure 3.4: (a) Schematic of rotating analyzer configuration; (b) Normalized light intensity in rotating analyzer configuration. (Figures are adapted after modifications from [144])

Applying Jones vectors and Mueller matrices the output of this PSA_R configuration can be expressed as

$$\boldsymbol{L}_{out} = \boldsymbol{AR}(A)\boldsymbol{SR}(-P)\boldsymbol{PL}_{in} \quad (3.18)$$

Here $\boldsymbol{L}_{out}$ is the Jones vector for the wave at the detector and can be expressed as $\begin{bmatrix} E_A \\ 0 \end{bmatrix}$.

$\boldsymbol{L}_{in}$ is the input Jones vector incident from the source given by $\begin{bmatrix} 1 \\ 0 \end{bmatrix}$. The '*A*' of the rotation matrix $\boldsymbol{R}(A)$ represents a rotation angle of the analyzer. Similarly *P* is a rotation angle of the polarizer. If written explicitly in matrix form the above expression becomes

$$\begin{bmatrix} E_A \\ 0 \end{bmatrix} = \begin{bmatrix} 1 & 0 \\ 0 & 0 \end{bmatrix}\begin{bmatrix} \cos A & \sin A \\ -\sin A & \cos A \end{bmatrix}\begin{bmatrix} \sin\Psi\, exp(i\Delta) & 0 \\ 0 & \cos\psi \end{bmatrix}\begin{bmatrix} \cos P & -\sin P \\ \sin P & \cos P \end{bmatrix}\begin{bmatrix} 1 & 0 \\ 0 & 0 \end{bmatrix}\begin{bmatrix} 1 \\ 0 \end{bmatrix} \quad (3.19)$$

Here $\boldsymbol{S}$ is the Jones matrix that corresponds to the light reflection from the sample.

When $P = 45^0$ the above equation takes the form

$$\begin{bmatrix} E_A \\ 0 \end{bmatrix} = \begin{bmatrix} 1 & 0 \\ 0 & 0 \end{bmatrix}\begin{bmatrix} \cos A & \sin A \\ -\sin A & \cos A \end{bmatrix}\begin{bmatrix} \sin\Psi\, exp(i\Delta) \\ \cos\psi \end{bmatrix} \quad (3.20)$$

We get $E_A = \cos A \sin\psi exp(i\Delta) + \sin A \cos\psi$. The light intensity at the detector can be expressed as the square of the modulus of E_A. So,

$$I = |E_A|^2 = I_o\ (1 - \cos 2\psi \cos 2A + \sin 2\psi \cos\Delta \sin 2A)$$

$$= I_o\ (1 + S_1 \cos 2A + S_2\ \sin 2A\ ) \quad (3.21)$$

I_o in the expression above represents the proportional constant of the reflected light whose intensity is again proportional to the intensity of the incident light intensity from the source. As can be seen from the above expression the measured intensity varies as a function of the angle *2A*. Therefore the period of this variation is 180 degrees. In general in a rotating analyzer ellipsometer (RAE) the Stokes parameters S_1 and S_2 are measured as the Fourier coefficients of $\cos 2A$ and $\sin 2A$ respectively. When the analyzer rotates at a speed of ωt the general expression for the detector intensity can be expressed as

$$I(t) = I_o\ (1 + \alpha \cos 2\omega t + \beta\ \sin 2\omega t\ ) \qquad (3.22)$$

The normalized light intensity at the detector calculated from this expression *(3.22)* is plotted in Figure 3.4(b) above.

In the most general case where polarizer angle is not restricted to 45^0 the expression for E_A becomes

$$E_A = \cos P \cos A \sin\psi \exp(i\Delta) + \sin P\ \sin A \cos\psi \qquad (3.23)$$

In this case the normalized Fourier coefficients are

$$\alpha = \frac{\cos 2P - \cos 2\psi}{1 - \cos 2P \cos 2\psi} \quad \text{and} \quad \beta = \frac{2 \sin 2\Psi \cos\Delta \sin 2P}{1 - \cos 2P \cos 2\Psi} \qquad (3.24)$$

Trigonometric manipulations give us the following familiar expressions

$$\alpha = \frac{(\tan\Psi)^2 - (\tan P)^2}{(\tan\Psi)^2 + (\tan P)^2} \quad \text{and} \quad \beta = \frac{2 \tan\psi \cos\Delta \tan P}{(\tan\Psi)^2 + (\tan P)^2} \qquad (3.25)$$

These expressions can be inverted to give (Ψ,Δ) as follows

$$\tan\Psi = \sqrt{\frac{1+\alpha}{1-\alpha}}|\tan P| \quad \text{and} \quad \cos\Delta = \frac{\beta}{\sqrt{1-\alpha^2}} \tag{3.26}$$

In general case of rotating analyzer ellipsometers (α, β) are extracted as the Fourier coefficients of the measured intensities in the detector. Then the above expressions *(3.26)* are used to get (Ψ, Δ) from those.

Introduction of a compensator in the RAE system enables the measurement of the Stokes parameter $\boldsymbol{S_3}$, which is otherwise not possible in case of RAE system with no compensators. This increases the accuracy of measurement when $\Delta \cong 0^o \; or \; 180^o$. In the presence of a compensator (for the case of $PSCA_R$ system) the Jones vector at the detector can be written as

$$\boldsymbol{L}_{out} = \boldsymbol{AR}(A)\boldsymbol{CSR}(-P)\boldsymbol{PL}_{in} \tag{3.27}$$

Where $\boldsymbol{C}$ is given by

$$\boldsymbol{C} = \begin{bmatrix} \exp(i\delta) & 0 \\ 0 & 1 \end{bmatrix}. \tag{3.28}$$

This is the Jones matrix for a compensator whose fast axis is in the direction of s-polarization. If we proceed with the analysis as in the case without a compensator above we finally see that the introduction of the compensator only shifts the Δ value without any change of Ψ. Physically it means that the compensator does not affect the amplitude of p- and s-polarized light but only changes the relative phase. So, in this case the final

results obtained above *(3.24 – 3.26)* are still valid with only a replacement of Δ by $\Delta' = \Delta - \delta$.

3.1.5 Experimental set-up in the laboratory

For this thesis a spectroscopic ellipsometer SE850 manufactured by SENTECH GmbH is

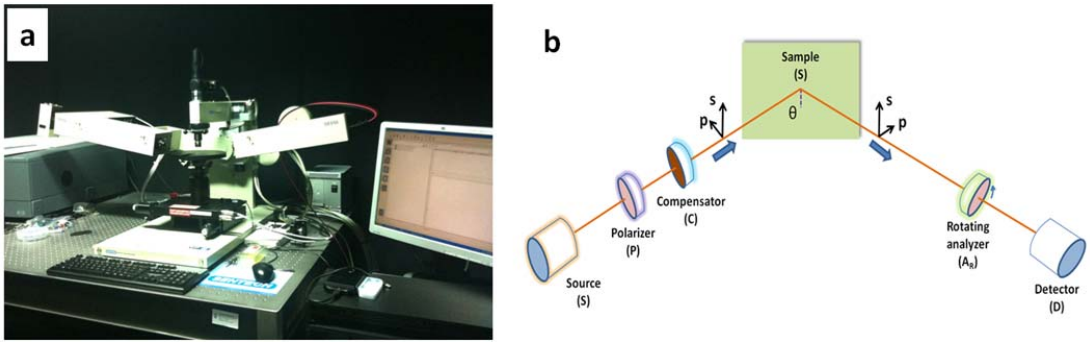

Figure 3.5: (a) Image of the lab ellipsometer SE850. (b) Schematic of the lab ellipsometer system with a compensator.

used. It has a rotating analyzer configuration with a compensator fitted on the polarizer arm after the polarizer. It has a spectral range of 0.5 eV (2500 nm)to 6.3 eV(195 nm).

Three different light sources — deep UV(deuterium), UV-VIS source (Xe-lamp) and the near infra-red (NIR) source (Halogen lamp of the Fouier transform infra-red spectrometer (FTIR)) are used for different regions of the spectrum. Grating spectrometer is used for all the three different energy ranges in the detector side for spectroscopic (wavelength variation) measurement. This results in a fast data acquisition.

The spot size or diameter of the typically used beam is of the range of few millimeters. But there are additional detachable micro-focus optical elements which can be used to focus the spot diameter to about ~200 micron. This small spot size is desirable in case of smaller samples and also to reduce back reflection issues in certain transparent samples where other corrective measures are not possible. However these micro-focus elements cannot be used for the whole spectral range of the ellipsometer. From various studies using different samples, reproducibility consideration and reliability estimation from those – it has been found that with those micro-focus elements 0.5 to 5.3 eV range is the useful one and hence for almost all studies in this thesis SE data have been reported for this range.

3.2 Reflectivity measurement- SUPERLUMI beamline

A considerable part of this thesis also involves investigating the electronic structure of graphene in vacuum ultraviolet (VUV) range using reflectivity measurements up to 35 eV (and starting at 3.8 eV). For this the SUPERLUMI beamline at HASYLAB/DESY, Hamburg is used.

The end station for the reflectivity measurement at the SUPERLUMI beam line is shown in Figure 3.6 [160]. The two mirrors M_1 and M_2 focus the incoming beam at the entrance slit of the primary monochromator vertically and horizontally respectively. A gold mesh is placed in the sample chamber such that the beam meets the gold mesh before the respective samples. For reflectivity measurement the angle of incidence and reflection is

17.5° (path shown in red in Figure 3.6). Luminescence at 45° incidence angle can be recorded by another PMT detector (path shown in blue in Figure 3.6) besides the first one used for reflectivity measurement.

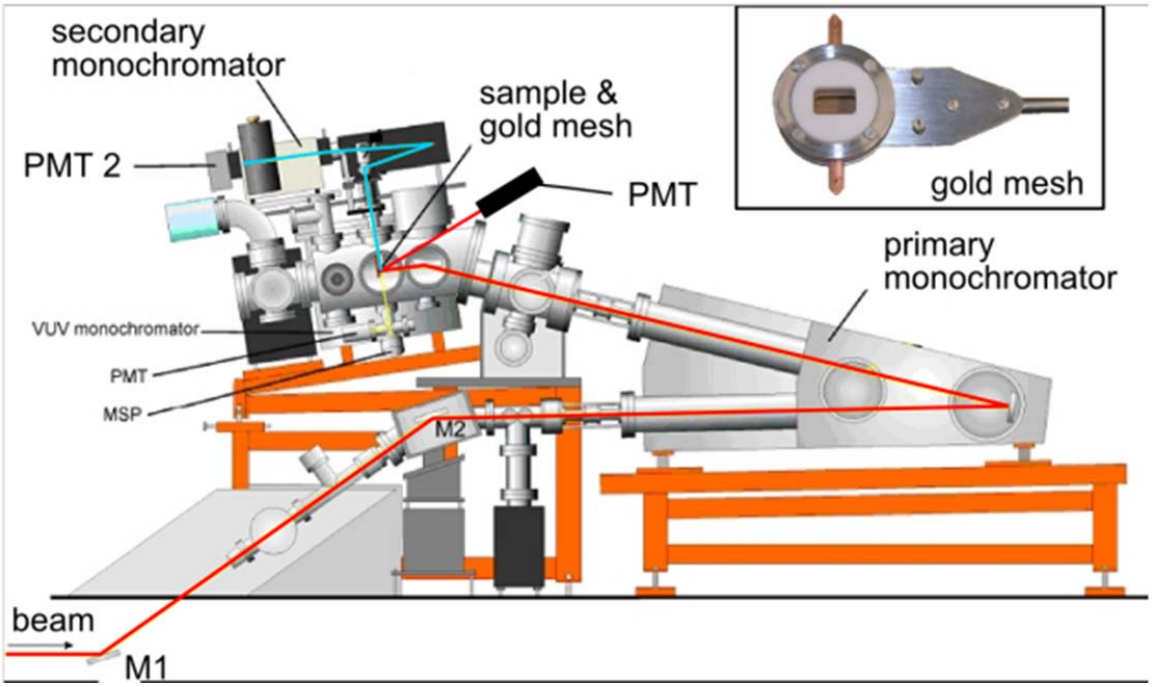

Figure 3.6: Schematic of SUPERLUMI beamline at HASYLAB/DESY.

The primary 2 m normal-incidence monochromator in 15° McPherson mounting is equipped with two holographic concave gratings (1200 groves/mm; Al&MgF_2 coating) and defines the impinging energy on the sample. The energy range is from 3.8 eV to 40 eV with an energy resolution up to 0.02 nm with proper exit slit configuration. The

incidence angle is measured from the surface normal and all reflectivity measurements are performed at 17.5^{o} incidence angle. As a coating of sodium salicylate ($NaC_7H_5O_3$) is used to detect the reflection, the primary photomultiplier (PMT) has to be calibrated with respect to the incoming reflected light. The primary PMT is VALVO PMT XP2230 B. To calibrate this PMT the reference spectra of sodium salicylate were taken for the whole energy range from 3.8 eV to 40 eV. This measurement was taken while a second monochromator (ARC 0.3m Czenery-Turner: "Spectral Pro 300i" (f/4)) which is set to 420 nm excitation energy and a HAMAMATSU R6358P photomultiplier was employed. The measurement is performed at 45^{o} incidence angle and a representative luminescence spectra is plotted below in Figure 3.7.

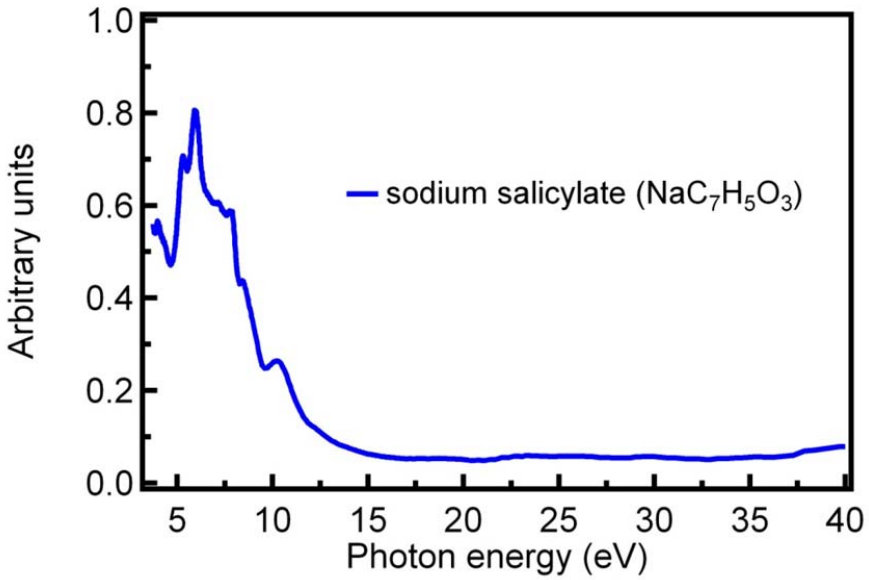

Figure 3.7: Luminescence spectra of sodium salicylate ($NaC_7H_5O_3$) divided by the DORIS current.

The sample holder is made of copper and samples are attached to the holder using silver paste. Samples can be attached to both sides of the flat holder and the choice of sample for measurement can be controlled by rotational and vertical motion of the holder.

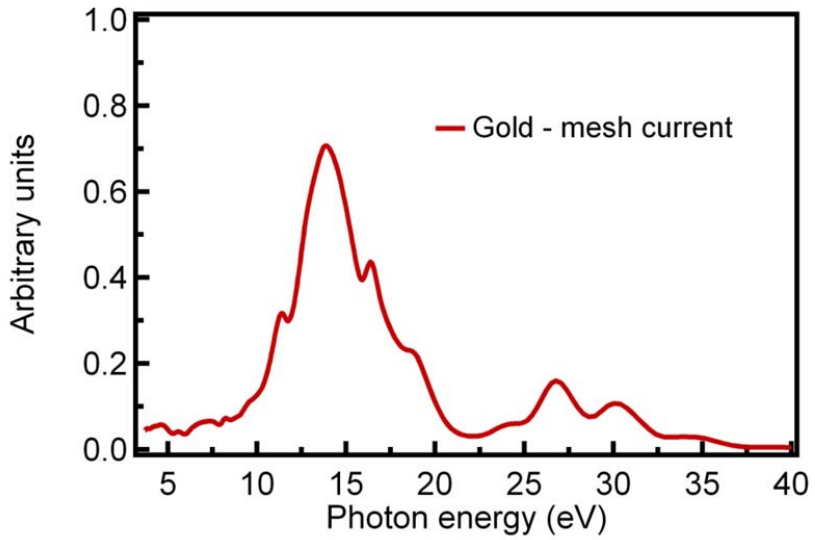

Figure 3.8: Gold current spectra divided by the DORIS current.

The system can be cooled down to 10 K using a He-flow CRYOVAC KONTI cryostat via a cold finger attached to the sample holder.

The function of the gold mesh is to take care of the fluctuations in the beam intensity as well as the gradual decay of storage ring (DORIS) current. Therefore the gold mesh current is used for normalizing each raw reflectivity spectra. There are further steps in the normalization process. The first step as mentioned is to divide the raw reflectivity

$R_{raw}(\omega)$ by the simultaneous gold mesh current $I_{Au}^{raw}(\omega)$. The next step is to take care of the contributions from the primary monochromator. That is to divide the intensity-normalized data by the reference spectrum $R_{ref}(\omega)$. If we denote this intermediate reflectivity as $R'(\omega)$ we get

$$R'(\omega) = \frac{R_{raw}(\omega)}{I_{Au}^{raw}(\omega)} \times \frac{1}{R_{ref}(\omega)} \qquad (3.29)$$

Again the photo-absorption of gold is energy dependent. Therefore this expression has to be further multiplied by the reference gold-mesh current $I_{Au}^{ref}(\omega)$ recorded when the reference sodium salicylate spectra was recorded. This cancels the contribution from the variation of photo-absorption of gold-mesh with wavelength. Therefore the final reflectivity $R(\omega)$ is given by

$$R(\omega) = R'(\omega) I_{Au}^{ref}(\omega) = \frac{R_{raw}(\omega)}{R_{ref}(\omega)} \times \frac{I_{Au}^{ref}(\omega)}{I_{Au}^{raw}(\omega)} = c \times \frac{R_{raw}(\omega)}{R_{ref}(\omega)} \qquad (3.30)$$

where c is a constant. So we see that finally we get a normalized reflectivity spectra (with the arbitrary constant factor). This constant can be different for each injection and each particular measurement. As we will see in the next chapter one way to get the actual reflectivity without this factor is to use reflectivity extracted from SE data to normalize at the proper low energy region (around 5 eV).

3.3 Sample preparation

In this thesis epitaxial graphene grown on 6H-SiC(0001) and also graphene grown by chemical vapour deposition (CVD) on copper and then transferred to other substrates are used. These two kinds of graphene are used primarily because of their large lateral dimensions. The spot size of ~200 micron (using microspot elements) for SE is adequate for optical measurements on these graphene samples. For reflectivity measurements also the large lateral dimension (~1 mm) is required.

3.3.1 Epitaxial graphene

Ultrathin epitaxial graphene grown thermally on SiC has been shown to be a promising material for fundamental studies as well as applications [23, 148- 151]. For studies in this thesis epitaxial graphene films were prepared on 6H-SiC(0001) as reported in many previous works [23, 148- 151]. Two sequential steps are needed to grow these epitaxial graphene samples. First- annealing the SiC in presence of Si flux (at ~1100^{o} C). This starts decomposition of SiC and it initiates desorption of Si. The process creates a carbon rich layer which is known conventionally as a buffer layer. Typically this layer can be seen as a 6×6 superstructure in STM images. Secondly annealing at still higher temperatures without the Si flux creates monolayer (~1200^{o} C, 2 min), bilayer (~1250^{o} C, 2 min) and trilayer and above (above 1300^{o} C, 2 min) on top of the buffer layer. The annealing pressures are generally below 5×10^{-9} mbar.

3.3.1.1 Preparation

In our case n-type Si-terminated 6H-SiC(0001) (obtained from CREE Research Inc.) is first chemically treated with 10% HF solution. Then it is annealed in UHV at ~ 850^{o} C resulting in 3×3 reconstruction of carbon rich surface. The sample is subsequently annealed at different higher temperatures (> 1200^{o} C) for certain times with slow cooling afterwards. As mentioned above epitaxial graphene films of different layer numbers (1 to several layer numbers) form in this way depending on the temperature of annealing, time of annealing and also cooling rate. An optical pyrometer is used to measure the temperature of the sample stage during the annealing.

The author prepared these graphene samples together with Dr. Iman Santoso. Raman as well as Atomic Force Microscopy (AFM) characterizations were also performed by the author together with Dr. Iman Santoso. Scanning tunneling microscopy (STM) characterizations were performed by collaborators from Prof. A. T. S. Wee's group.

3.3.1.2 Layer number determination: Scanning Tunneling Microscopy (STM) and Raman spectra

For monolayer and bilayer samples (as expected from growth conditions) STM measurements are performed in UHV conditions. The results show characteristic monolayer and bilayer features as reported in similar previous studies [23, 148- 151]. The monolayer sample shows distinctive characteristic hexagonal symmetry as shown in Figure 3.9(a). The bilayer sample shows [Figure 3.9(b)] triangular symmetry (which is a

result of stacking of two layers) which is also a characteristic signature of bilayer graphene.

Raman measurements were performed using a commercial system (Renishaw inVia) at a wavelength of 514 nm (Argon laser) for samples with layer numbers greater than two.

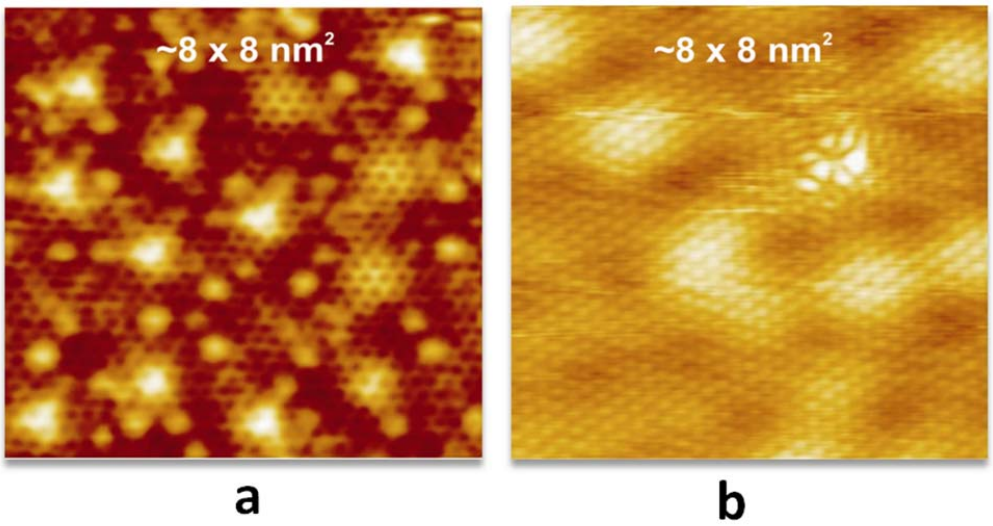

Figure 3.9: STM image of (a) monolayer and (b) bilayer epitaxial graphene.

Highly ordered pyrolytic graphite (HOPG), 6H-SiC substrate and a 6H-SiC substrate with buffer layer are also measured and the Raman shift results are plotted together in Figure 3.10. Graphene has characteristic Raman peaks at 1585 cm^{-1} (G) and around 2720 cm^{-1} (2D) which originate from in-plane vibrations and from a double resonant process [153]. The 6H-SiC has a peak at around 1516 cm^{-1} which is considered to be an overtone of the L point optical phonon.

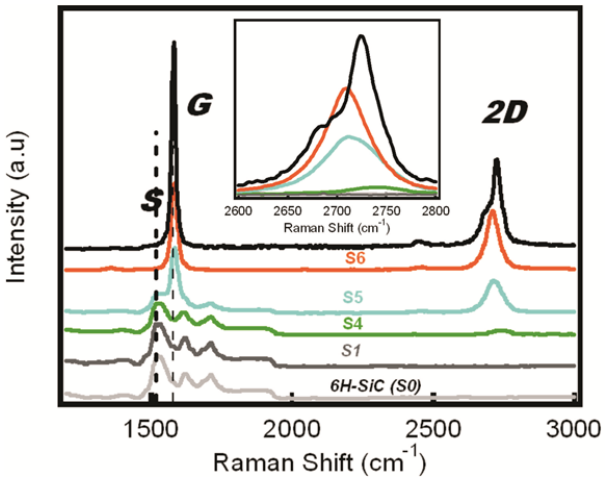

Figure 3.10: Raman shift signal of bare 6H-SiC (S0), S1 ("buffer layer" on top of 6H-SiC), multilayers graphene (S4, S5, S6), and Graphite (HOPG).

Shivaraman *et. al,* [152] have reported a technique which can be used for determination of layer thickness of epitaxial graphene. They utilized the fact that the substrate Raman peak is attenuated gradually when the graphene layer thickness increases on top of it. The

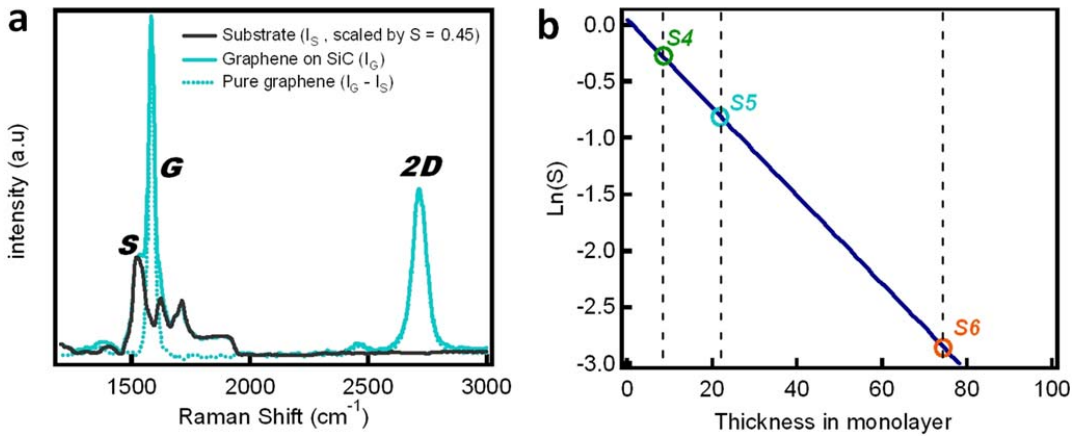

Figure 3.11: Determination of *N* using attenuated 6H-SiC peak (S). *(a)* Extracting N for sample S5 using attenuated 6H-SiC peak S method. *(b)* Calibration curve from [85] that is used for obtaining N for sample S4, S5, and S6.

three samples S4, S5, S6 are prepared using increasingly higher temperatures. Therefore it is expected that they will have the same increasing order of layer number. As can be seen from Figure 3.10 the S peak is attenuated more for increasing layer numbers.

Now the S peak intensity for the bare 6H-SiC should be scaled down by a number less than 1 to match (Figure 3.11(a)) with the corresponding peak strength for a particular sample (with a certain layer number). In Figure 3.11(a) the 'S' in the vertical axis represents this number. If the natural logarithm of these numbers for different samples are taken and they are put on the 'calibration curve' from the report of Shivaraman *et al.* [152] we get the required layer numbers as shown in Figure 3.11 (b) above. In this particular case the layer numbers are found to be 8, 22 and 75 for S4, S5 and S6 respectively.

3.3.2 Chemical Vapour Deposited (CVD) graphene

Monolayer graphene samples, which were prepared by CVD method on copper foil as reported by Li et al. [24], procured from Graphene Square Inc. are used for the studies in this thesis (besides epitaxial graphene described above). The thickness of the copper foil is 25 micron on which the graphene layer is grown by the low pressure CVD technique.

The author performed the graphene transfer as well as Raman characterization himself. The whole transfer process is carried out in a class 1000 clean-room inside Singapore Synchrotron Light Source (SSLS) facility.

3.3.2.1 Wet transfer process

There are various steps involved in the transfer process and every step is crucial for the final quality of the graphene. The steps involved can be broadly divided into three [27]:

(a) Spin-coating an approximately 300 nm layer of Poly(methyl methacrylate) (PMMA) on the copper foil with graphene. This is for supporting the graphene layer in the subsequent processes as well as protection from oxygen plasma treatment later. After heat treatment, the foil is treated in oxygen plasma chamber in 20 sccm oxygen flow with an RF power of 20 watt for 2 minutes. The foil is kept upside down to make sure that the bottom layer of graphene (which is unwanted) is etched away.

(b) The foil is then cut to smaller pieces according to requirement (e.g., $5\ mm \times 5\ mm$ or $2.5\ mm \times 2.5\ mm$ and then kept floating with the PMMA side up for a few hours in a 0.1 M ammonium persulphate ($(NH_4)_2S_2O_5$) solution in water. This etches away the copper and only the graphene films with PMMA coating floats in the solution. When the etching is complete the films are transferred carefully to beakers with deionized water (DI) water with the help of glass slides.

(c) After few hours of floating in DI water the films are now transferred to individual substrates carefully. The substrates with the films are then kept on a hot plate at 60 degrees and then 100 degrees subsequently evaporate the water. These dry substrates with films are then put into acetone. The PMMA gets dissolved in acetone and only the graphene layer stays on the substrate. The substrates with graphene are then dipped in

isopropyl alcohol (IPA) for some time and then blown with dry nitrogen carefully and gently.

Typically for optical measurements the graphene layer is placed on the substrate (Figure 3.12) such that it occupies one part of the substrate leaving enough bare substrate area for a measurement of the substrate alone to be possible on the same sample. This is to make

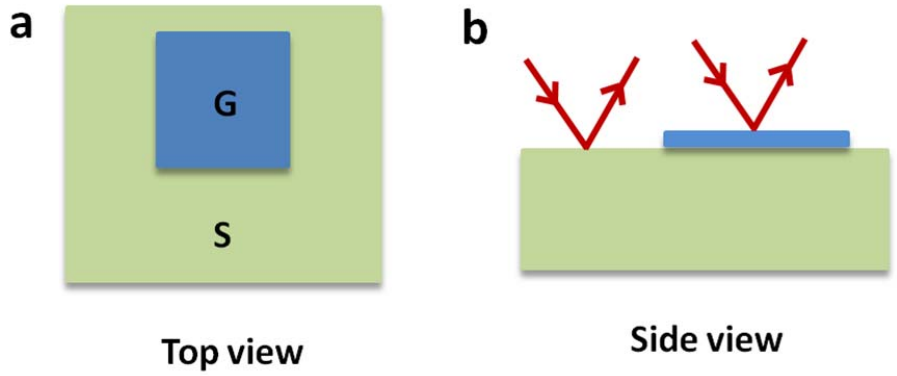

Figure 3.12: Schematic of (a) top view and (b) side view of a substrate with graphene for optical measurements to show the positioning of the graphene layer.

sure that in optical data analysis later, differences in data due to measurements on different substrates or substrates with different treatment history are eliminated. Also all the above steps should be performed very carefully keeping particularly in mind that no copper residue is left (without etched), PMMA should be fully removed, and the substrates should be cleaned properly before transfer of graphene.

Monolayer graphene is transferred to various substrates- namely, amorphous quartz, SiO_2/Si, $SrTiO_3$ (100) etc. for various studies using the techniques described above.

3.3.2.2 Characterization using Raman spectra

In case of transfer to 300 nm SiO_2/Si substrates, monolayer graphene is visible under the microscope at different magnifications. Most of the samples are found to be uniform with very small bilayer parts and with no PMMA residue. For other substrates the graphene layer is not visible under the microscope, but it can be inferred from the SiO_2/Si case that these samples are also of good quality as these are transferred exactly in the same ways

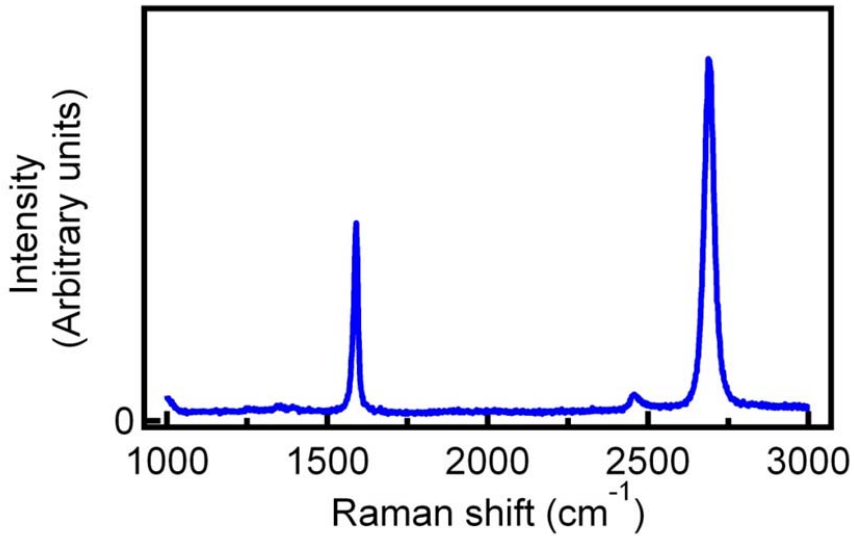

Figure 3.13: Raman Spectra of graphene on SiO_2/Si with 514.5 nm laser.

too. However Raman shift measurements are performed as in the case of epitaxial graphene case above for all substrates with graphene. As shown in Figure 3.13 (in the case of 300 nm SiO_2/Si substrate) it shows strong monolayer characteristic with negligible defect contributions [153]. This confirms high quality of the graphene samples prepared. For other substrates generally there are Raman peaks present in the range of

measurement for the bare substrate itself. But when the substrate contribution is taken out using proper normalization from the 'graphene + substrate' data, finally we get very similar plots like the above (Figure 3.13).Which again reconfirms the good quality of graphene samples on all substrates.

3.3.3 Electrode deposition for gating experiments

One of the directions in this thesis is to investigate the gate dependent σ_1 of graphene on SiO_2/Si substrates. Electrodes have to be deposited on the graphene layer for proper electrical connection. The schematic of the electrical circuit is presented in Figure 3.14.

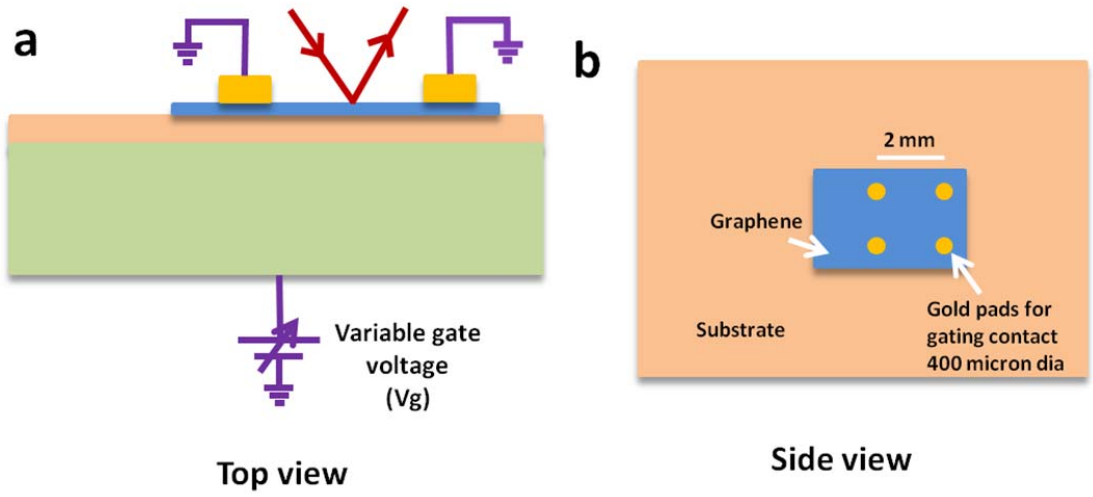

Figure 3.14: (a) Schematic device configuration for gate dependent σ_1 study (side view). (b) Top view with dimensions for the same configuration.

The electrodes (circular patches) are deposited using a stencil mask with four holes of 400 micron diameter in a square pattern. There are more holes in the mask but all others

are covered (using a vacuum compatible tape) except four of those forming a square (Fig. 3.15(b) and (d)). Before placing the stencil mask the graphene layer uniformity and continuity is checked under the microscope and the stencil mask is placed in the best position while keeping it under the microscope on top of the sample. The electrodes are deposited using a thermal evaporator at a base pressure of $\sim 2 \times 10^{-6}$ mbar. A 5 nm chromium layer is first deposited for better adhesion. On top of that 35 nm gold is evaporated subsequently. The substrate with the graphene layer with the contacts is

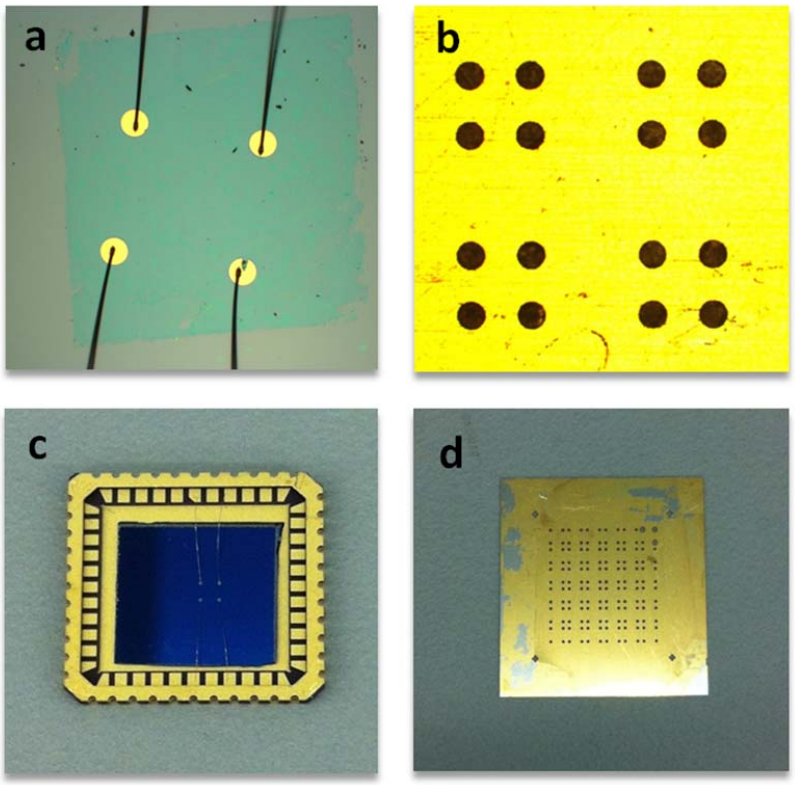

Figure 3.15: (a) Optical micrograph of the real sample showing the deposited electrodes after wire bonding; (b) optical micrograph of the stencil mask. (c) Image of the wire-bonded sample on a 44 pin chip carrier (LCC04420). (d) Image of the stencil mask.

then glued to a 44 pin chip carrier (LCC04420) using conducting silver paste in the bottom (Fig. 3.15(c)). Later on wire bonding is performed from these deposited contacts to the chip carrier contact pads (Fig. 3.15(a)).

3.3.4 Electron beam lithography (EBL)

One of the directions of this thesis is the understanding of optical processes in a 'graphene + substrate' system. As electric transport measurements in graphene shows that its chemical potential can be tuned easily using a gate voltage its desirable to study the simultaneous interplay of gate induced doping and the light induced charge transfer doping (if there is any) for graphene on various substrates. The final aim is to study the transport behaviour when light shines on these devices. Particularly, preliminary field-effect device fabrications on graphene samples on 300 nm SiO_2 /n-Si substrates as well as on 300nm $SrTiO_3$ (100)/Nb-$SrTiO_3$ (100) are performed using EBL facility in Graphene Research Center. The various steps involved in the field-effect device fabrication using EBL is explained above in Figure 3.16 using schematics.

All these steps are carried out in a class 10000 clean room in the Graphene Research Center. The Scanning electron microscope (SEM) used for EBL is further inside a class 1000 room. Typically for CVD grown graphene and transferred to SiO_2/Si substrates, all the steps described in Figure 3.16 can be used as the graphene layer is visible under the microscope. So, finding out a defect free and residue free region is easier there.

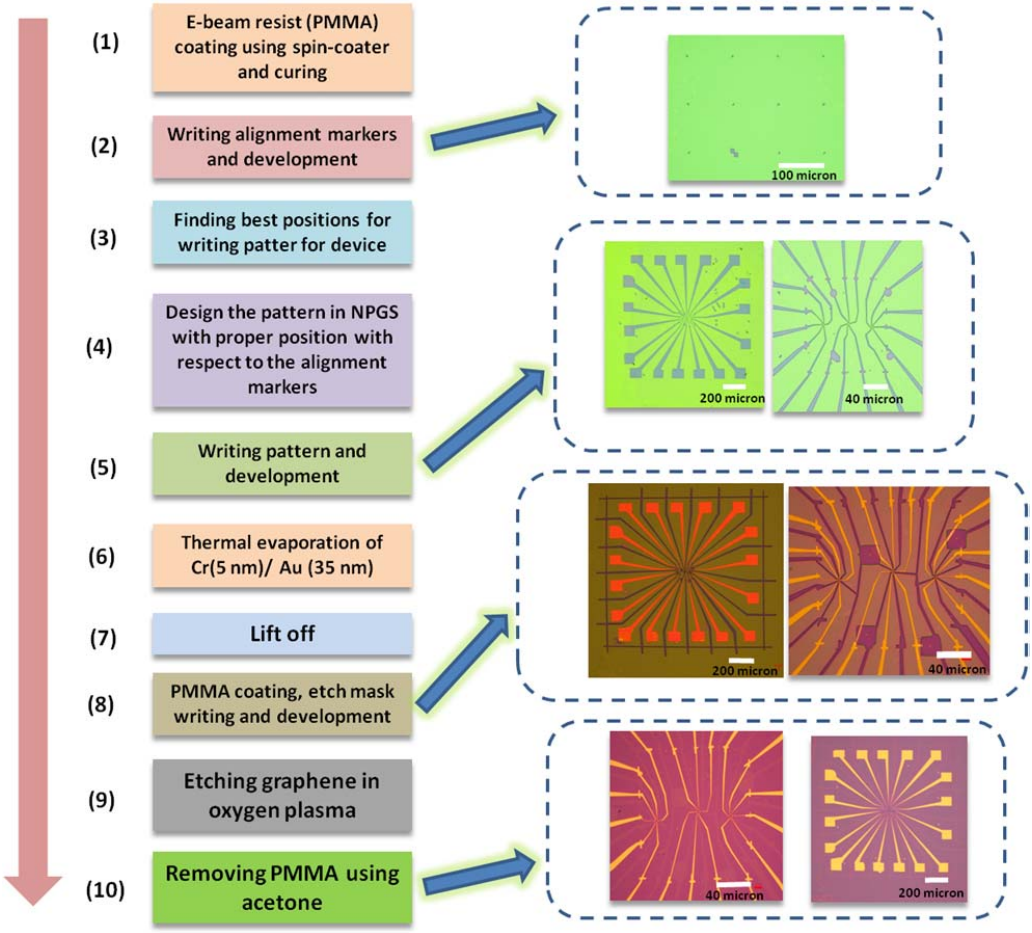

Figure 3.16: Electron beam lithography steps. The images in the right are from various stages in the process taken from real samples. The arrows correspond to the step when the image was taken.

But for CVD graphene generally, irrespective of the substrate writing the alignment markers (steps (2) and (3)) is not necessary. Moreover for substrates other than SiO_2/Si, graphene layer is not visible under the microscope; so the steps (2) and (3) mentioned above could be skipped. Instead many patterns are written at all the possible good areas

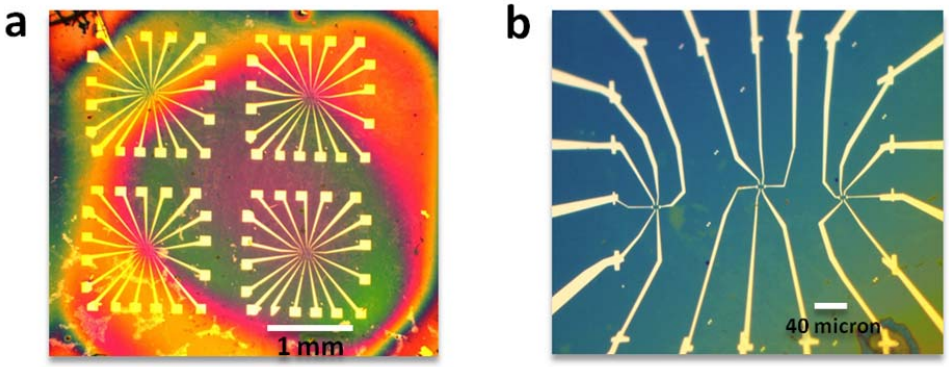

Figure 3.17: (a) 4 patters written each with 3 devices on 'graphene on 300nm $SrTiO_3$ (100)/Nb-$SrTiO_3$'; (b) zoomed in image of one single pattern.

with the expectation of a good final yield (i.e., the number of working devices). Figure 3.17 shows a typical graphene on 300nm $SrTiO_3$ (100)/Nb-$SrTiO_3$ (100) sample with 12 devices fabricated (4X3) on it. The images are taken after a PMMA layer is coated (for graphene etching of steps (8) and (9)) and therefore those look coloured.

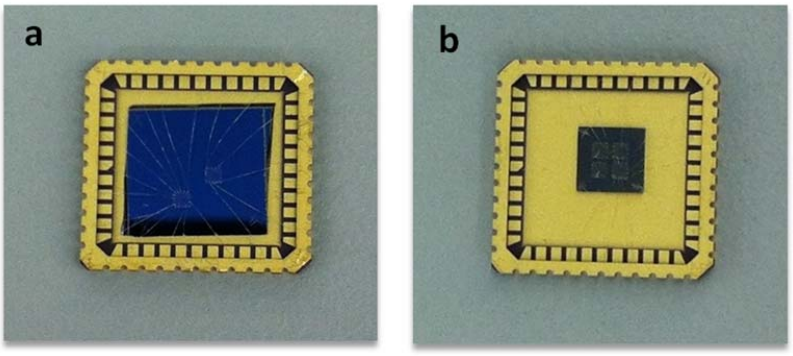

Figure 3.18: (a) Final image of graphene on SiO2/n-Si devices after wire-bonding; (b) Final image of graphene on STO/Nb-STO devices after wirebonding

After EBL the samples are glued with conducting silver paste to Chip carriers. Wire bonding is used to connect the device electrodes to the chip carrier bonding pads. Figure 3.18 shows the images of the final devices in this stage.

3.4 Transport measurement

As we want to study how the dc conductivity of graphene (on different substrates) change when illuminated with light of different wavelengths, field effect devices were fabricated on monolayer graphene using EBL method described in the previous section. Here we will very briefly discuss the (transport) measurement technique for these devices.

The devices are fabricated in the Hall bar geometry as shown in Figure 3.19 (a) below. Basically we use four probe method using two of the middle electrodes as voltage terminals as shown in Figure 3.19 (a). A lock-in amplifier (SR380) is used to source current and measure voltage across the terminals. A 13.3 Hz AC sinusoidal voltage is applied from the Lock-in. As shown in the schematic diagram of Figure 3.19 (b) a 10 MΩ resistor is used in series in the source-drain circuit to limit the current. Typically a voltage of amplitude 0.1 V is applied which results in a current of 10 nA flowing through the circuit with graphene in series. A sourcemeter (Keithley 6430) is used to apply the gate voltage. This gate voltage is also applied with a high resistance of 100 MΩ in series. The resistance of the gate dielectric (SiO_2 or STO) is far higher than this. Therefore the gate voltage sourced by the sourcemeter appears almost fully across the gate dielectric

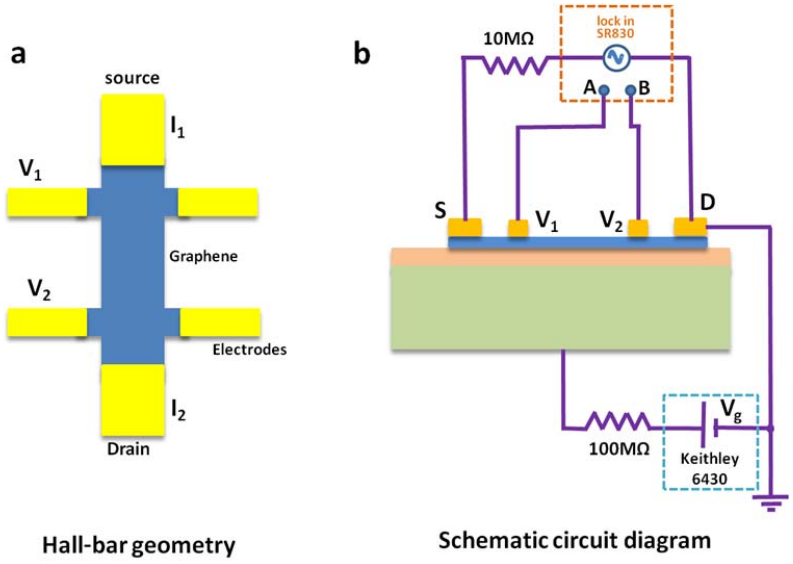

Figure 3.19: (a) Schematic of Hall-bar geometry of graphene with electrodes; (b) schematic circuit diagram for field-effect measurement.

effectively. The 100 MΩ resistor is used for current limiting purpose for safety in case when the gate dielectric is leaky and it does not affect the normal operations. In this configuration, when the gate voltage sweeping tunes the chemical potential of graphene we get transport results for both hole and electron doped regimes. To observe the effect of illumination on the dc conductivity of graphene (on different substrates) we propose a measurement set-up with the same configuration with an additional light source (with monochromator) illuminating the sample during measurement (Fig. 2.11(c)).

Chapter 4

Data analysis procedures

As proper modeling and fitting of data is of utmost importance in ellipsometric studies for reliable extraction of optical constants, in this chapter we have explained the underlying principles of modeling and fitting ellipsometric data in general as well as for specific cases relevant to our work. We start with an example of ellipsometric data for a multilayer system and describe the general strategy of employing proper optical model, dielectric function model and fitting subsequently. Fundamental aspects of Drude-Lorentz oscillator model is explained in detail as this dielectric function model is used for all the fitting in this thesis. Use of various graphical software tools, normalization procedure for high energy reflectivity data and Fano analysis techniques have been described briefly as these comprise important common practical aspects of this thesis.

4.1 Ellipsometric data for ambient/thin film/substrate system

As the measured quantities Ψ and Δ in ellipsometry are the amplitude ratio of and phase difference between p-polarized and s-polarized light respectively, depending on the sample optical properties and the structure (Ψ, Δ) will show variations which are not so trivial [141- 144]. Particularly, one of the most commonly encountered sample structure is ambient/thin-film/substrate structure. For this system the amplitude reflection (transmission) coefficients can be written as

$$r_{012,p} = \frac{r_{01,p} + r_{12,p}\exp(-i2\beta)}{1 + r_{01,p}r_{12,p}\exp(-i2\beta)} \qquad r_{012,s} = \frac{r_{01,s} + r_{12,s}\exp(-i2\beta)}{1 + r_{01,s}r_{12,s}\exp(-i2\beta)} \qquad (4.1)$$

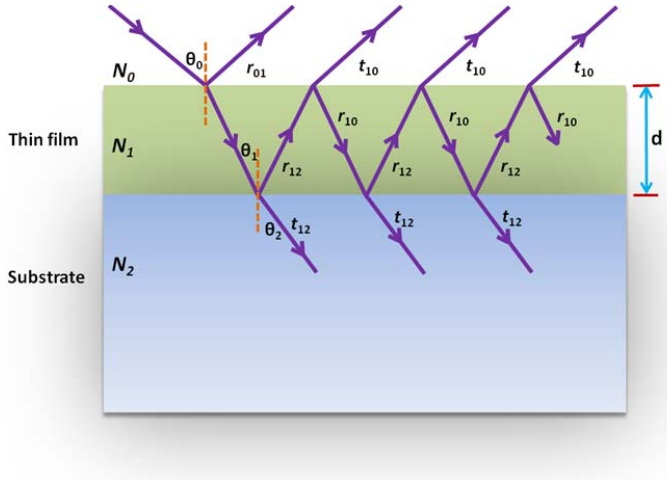

Figure 4.1 Amplitude reflection and transmission coefficients for a ambient/thin-film/substrate structure

$$t_{012,p} = \frac{t_{01,p} + t_{12,p}\exp(-i\beta)}{1 + r_{01,p}r_{12,p}\exp(-i2\beta)} \qquad t_{012,s} = \frac{t_{01,s} + t_{12,s}\exp(-i\beta)}{1 + r_{01,s}r_{12,s}\exp(-i2\beta)} \qquad (4.2)$$

Here d is the thickness of the thin film [143,144,146]. The phase thickness is given by

$$\beta = 2\pi d N_1 \cos\theta_1/\lambda. \qquad (4.3)$$

Using these- the fundamental ellipsometric equation can be expressed as

$$\rho = \tan\Psi\, exp\,(i\Delta) = \frac{r_p}{r_s} \qquad (4.4)$$

$$= \left[\frac{r_{01,p} + r_{12,p}\exp(-i2\beta)}{1 + r_{01,p}r_{12,p}\exp(-i2\beta)}\right] \Big/ \left[\frac{r_{01,s} + r_{12,s}\exp(-i2\beta)}{1 + r_{01,s}r_{12,s}\exp(-i2\beta)}\right]$$

Now as an example of such a sample we can take the case of air/300 nm amorphous SiO_2/ c-Si.

Figure 4.2 (a) shows the (Ψ, Δ) plots for the measurements at 70^0 incident angle. Here the thin film is 300 nm amorphous SiO_2 which has negligible absorption in the measurement range. On the other hand the substrate layer (c-Si) has nonzero ε_1 and ε_2 for the measurement range as shown in Figure 4.2(b).

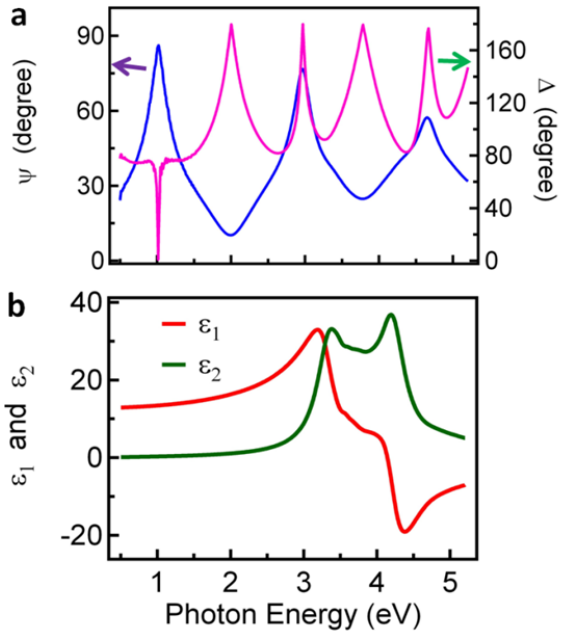

Figure 4.2 (a) (Ψ, Δ) data for air/300 nm amorphous SiO_2/ c-Si; **(b)** (ε_1,ε_2) for the c-Si substrate taken from literature.

Figure 4.2 (a) is an example of typical ellipsometry measurement (i.e. (Ψ, Δ) data) for a air/ transparent thin film/substrate system. It may be mentioned that the Δ data is plotted in the range 0 to 180^0 instead of 0 to 360^0, as physically the same information is carried by the former. For the same substrate if the thickness of the film is varied or the real part

of the dielectric constant (ε_1) changes the (Ψ, Δ) data will vary accordingly. In general the thin film may be absorbing too ($\varepsilon_2 > 0$). In such a case the resultant (Ψ, Δ) values would change accordingly as required by equation *(4.4)* above.

In this thesis we deal with monolayer graphene on different substrates. For substrates like amorphous quartz, $SrTiO_3$ etc. the 'graphene on substrate' structures fall into this category of (air/absorbing film/substrate) as the substrate is bulk. On the other hand for graphene on a layered substrate like amorphous SiO_2/Si the overall system has one additional layer (or may be more if we consider interfacial layers in the optical model). In such a case the ellipsometric equation [143,144,146] will be given by

$$\rho = \tan\Psi \, exp\,(i\Delta) = \frac{r_p}{r_s}$$

$$= \frac{\left[\frac{r_{01,p} + r_{12,p}\exp(-i2\beta) + [r_{01,p}r_{12,p} + \exp(-i2\beta)]r_{23,p}exp(-i2\beta)}{1 + r_{01,p}r_{12,p}\exp(-i2\beta) + [r_{12,p} + r_{01,p}\exp(-i2\beta)]r_{23,p}exp(-i2\beta)}\right]}{\left[\frac{r_{01,s} + r_{12,s}\exp(-i2\beta) + [r_{01,s}r_{12,s} + \exp(-i2\beta)]r_{23,s}exp(-i2\beta)}{1 + r_{01,s}r_{12,s}\exp(-i2\beta) + [r_{12,s} + r_{01,s}\exp(-i2\beta)]r_{23,s}exp(-i2\beta)}\right]} \qquad (4.5)$$

4.2 Strategy for extraction of optical constants and thickness

The basic strategy for extraction of optical constants and thickness of material layers consisting the sample can be divided into three parts –(1) choosing a dielectric function to represent the optical properties; (2) construction of an optical model and (3) fitting measured (Ψ, Δ). The first two steps may not be in that order strictly. Depending on the

sample structure and requirements there may be simplifications or additional auxiliary steps involved in such an analysis but in general the above three steps are always employed.

4.2.1 Dielectric function models

One of the most commonly used dielectric function model is the Lorentz oscillator model. It can be derived using classical theories as explained in the next section. This classical model has quantum mechanical analogs with the same final mathematical expressions but with reinterpretation of the terms. Lorentz and Drude oscillator models are often used as a starting point in combination to 'completely' describe the ellipsometric data of solids covering a broad energy range. In short Lorentz oscillator model applies to insulators and semiconductors whereas Drude oscillator model is applicable to free electron metals. In this thesis we have used Drude-Lorentz oscillators exclusively as our dielectric function models. In the following sections these are explained.

4.2.1.1 Lorentz oscillator model

In the classical picture the negatively charged electron can be imagined to be attached to the nucleus by a 'spring' force as shown in Figure 4.3 (c) below [141-144, 146,147]. When ac field of the impinging light reaches the sample, the equation of motion can be written as

$$m_e \frac{d^2x}{dt^2} = -m_e \Gamma \frac{dx}{dt} - m_e \omega_0 x - eE_0 \exp(i\omega t) \qquad (4.6)$$

Here m_e and e are the mass and charge of the electron respectively; $E_0 \exp(i\omega t)$ is the ac electric field of the light; Γ is the damping coefficient; ω_0 is the natural frequency of the spring given by $\sqrt{k_f/m}$. The above equation is for a forced vibration.

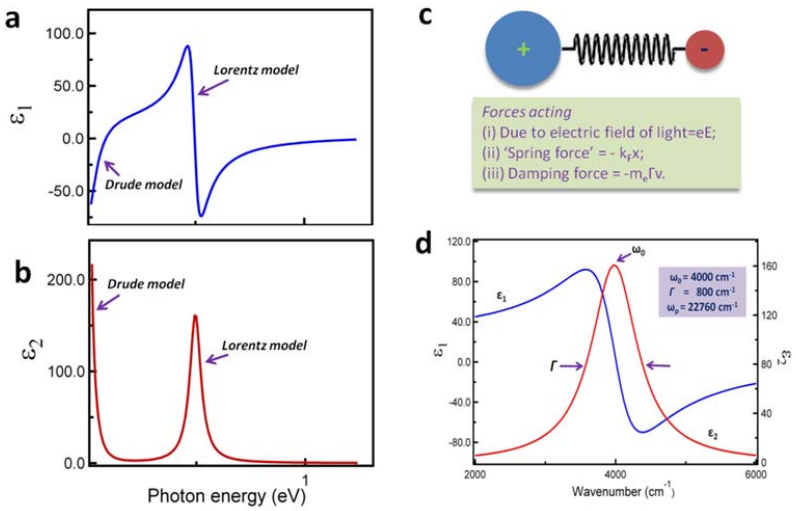

Figure 4.3 (a) ε_1 from Drude-Lorentz oscillator model; **(b)** ε_2 from Drude-Lorentz oscillator model; **(c)** schematic of electron motion when light falls on a sample; **(d)** dielectric function calculated using one oscillator.

In the steady state if we assume a solution of the form

$$x(t) = A\, exp\,(i\omega t) \qquad (4.7)$$

Then we get

$$A = -\frac{eE_o}{m_e} \frac{1}{(\omega_0^2 - \omega^2) + i\Gamma\omega} \qquad (4.8)$$

In the case when the volume concentration of electrons is given by N_e, the electrical polarization can be expressed as $P = -e\,N_e\,x(t) = = -e\,N_e A\,exp\,(i\omega t)$. Now for a linear dielectric the dielectric constant ε can be written as

$$\varepsilon = 1 + \frac{P}{\varepsilon_0 E} = 1 + \chi \qquad (4.9)$$

Substituting the expressions for P and E from above to this we get

$$\varepsilon = 1 + \frac{e^2 N_e}{\varepsilon_0 m_e} \frac{1}{(\omega_0^2 - \omega^2) + i\Gamma\omega} \qquad (4.10)$$

The real and imaginary parts are given (using the plasma frequency expression $\omega_p^2 = \frac{e^2 N_e}{\varepsilon_0 m_e}$)

$$\varepsilon_1 = 1 + \frac{e^2 N_e}{\varepsilon_0 m_e} \frac{(\omega_0^2 - \omega^2)}{(\omega_0^2 - \omega^2)^2 + \Gamma^2\omega^2} = 1 + \omega_p^2 \frac{(\omega_0^2 - \omega^2)}{(\omega_0^2 - \omega^2)^2 + \Gamma^2\omega^2} \qquad (4.11)$$

$$\varepsilon_2 = \frac{e^2 N_e}{\varepsilon_0 m_e} \frac{\Gamma\omega}{(\omega_0^2 - \omega^2)^2 + \Gamma^2\omega^2} = \omega_p^2 \frac{\Gamma\omega}{(\omega_0^2 - \omega^2)^2 + \Gamma^2\omega^2} \qquad (4.12)$$

The above three expressions (4.10-12) represent the Lorentz oscillator model. In Figure 4.3(d) above we have plotted ε_1 and ε_2 against wavenumber (in units of cm^{-1}) for a natural frequency, $\omega_0 = 4000\ cm^{-1}$, $\Gamma = 800\ cm^{-1}$ and $\omega_p = 22760\ cm^{-1}$. In general when there are more than one natural frequency present the final total dielectric constant is given by

$$\varepsilon_1 = 1 + \sum \frac{\omega_{p,n}^2(\omega_n^2-\omega^2)}{\left(\omega_n^2-\omega^2\right)^2+\Gamma_n^2\omega^2} \quad (4.13)$$

and $$\varepsilon_2 = \sum \frac{\omega_{p,n}^2\Gamma_n\omega}{\left(\omega_n^2-\omega^2\right)^2+\Gamma_n^2\omega^2} \quad (4.14)$$

4.2.1.2 Drude model

Metals and semiconductors with free electrons and free carriers respectively show optical response given by the so called Drude model [142,143,147, 154,155]. This model can be in principle derived directly from the expression for the Lorentz oscillator model explained in the previous section. This can be performed by setting $\omega_n = 0$ for all oscillators in expressions *(4.13)* and *(4.14)* which means that all electrons (or carriers) are free to move. Also assuming that all electrons are subjected to the same frictional force constant $\Gamma_n = \Gamma_f$, we get

$$\varepsilon_1 = 1 + \frac{\omega_p^2}{\omega^2+\Gamma_f^2} \quad (4.15)$$

and $$\varepsilon_2 = \frac{\omega_p^2\Gamma_f}{\omega(\omega^2+\Gamma_f^2)} \quad (4.16)$$

Where the plasma frequency is given by the expression which uses the total free electron concentration $\omega_p = \left(e^2N_{ef}/\varepsilon_0 m_e\right)^{1/2}$.

In the Drude model the damping term can be interpreted in times of the scattering rate of electrons. If the mean scattering rate is given by $\langle\tau\rangle$ the rate of change of the average velocity $\langle v\rangle$ is given by

$$\frac{d\langle v\rangle}{dt} = -\frac{\langle v\rangle}{\langle\tau\rangle} - \frac{eE}{m} \qquad (4.17)$$

Using $E = E_0 \exp(i\omega t)$ and looking for a steady state solution of the form $\langle v\rangle = \langle v_0\rangle \exp(i\omega t)$ we get

$$\langle v\rangle = \frac{eE/m}{\frac{1}{\langle\tau\rangle} - i\omega} \qquad (4.18)$$

Now the complex conduction current can be expressed as

$$J_c = -N_{ef} e\langle v\rangle = \sigma E. \qquad (4.19)$$

Therefore we get

$$\sigma = \sigma_1 + i\,\sigma_2 = \frac{N_{ef} e^2\langle\tau\rangle/4\pi\varepsilon_0 m}{1 - i\omega\langle\tau\rangle} = \frac{\sigma_0/4\pi\varepsilon_0}{1 - i\omega\langle\tau\rangle} \qquad (4.20)$$

Here $\sigma_0 = \frac{N_{ef} e^2\langle\tau\rangle}{m} = 4\pi\varepsilon_0\sigma(\omega = 0)$ in SI units gives the dc conductivity.

So the real and imaginary parts are given by

$$\sigma_1 = \frac{(\sigma_0/4\pi\varepsilon_0)}{1 + \omega^2\langle\tau\rangle^2} \qquad (4.21)$$

and $$\sigma_2 = \frac{(\sigma_0\omega\langle\tau\rangle/4\pi\varepsilon_0)}{1 + \omega^2\langle\tau\rangle^2} \qquad (4.22)$$

But optical conductivity and dielectric constants are related by

$$\sigma = \frac{i\omega}{4\pi}(1-\varepsilon) \qquad (4.23)$$

If we make the substitutions using *(4.21)* and *(4.22)* to *(4.23)* we see that equations *(4.21)* and *(4.22)* above are equivalent to those obtained from Lorentz oscillator model *(4.11)* and *(4.12)* with the condition that

$$\Gamma_f = \frac{1}{\langle\tau\rangle}. \qquad (4.24)$$

4.2.1.3 Other models

Occasionally other models are also used depending on the material under study and also on the energy range of measurement. Typically when the band gap of the material is well beyond the upper limit of the energy range of measurement, dielectric models such as Sellmeier, Cauchy etc. are used.

The Sellmeier model can be derived by setting $\varepsilon_2 \backsim 0$, in the Lorentz model. If we put $\Gamma \to 0$ and also write the Lorentz equations using wavelength λ such that $\frac{\omega}{c} = \frac{2\pi}{\lambda}$ we get

$$\varepsilon_1 = 1 + \frac{e^2 N_e}{\varepsilon_0 m_e (2\pi c)^2} \frac{\lambda_0^2 \lambda^2}{\lambda^2 - \lambda_0^2}; \qquad \varepsilon_2 = 0 \qquad (4.25)$$

Normally these are written as

$$\varepsilon_1 = n^2 = A' + \sum \frac{B_j \lambda^2}{\lambda^2 - \lambda_{0j}^2}, \quad \varepsilon_2 = 0 \qquad (4.26)$$

Similarly a series expansion of the expression *(4.25)* above gives the familiar Cauchy model

$$n = A + \frac{B}{\lambda^2} + \frac{C}{\lambda^4} + \ ..., k = 0 \qquad (4.27)$$

Another model which can be used for amorphous materials and where there is a band gap present is the Tauc-Lorentz model [143]. The basic idea is to model the ε_2 as a product of a unique bandgap term and the Lorentz term. This takes care of the asymmetric shape of the ε_2. The ε_1 is found from the Kramers-Kronig (KK) transformation (explained in section 4.2.1.4 next) of ε_2. As we have only used Drude-Lorentz oscillator models exclusively for this thesis we will not go to the details of this and other models further.

4.2.1.4 Kramers-Kronig relationship

Kramers – Kronig (KK) relation follows causality [147]. This basically implies that ε_1 and ε_2 are not independent but interrelated. Mathematically if we know either ε_1 or ε_2 for the whole range $\omega_0 = 0$ to $\omega_0 = \infty$ then the other can be calculated using one of the following:

$$\varepsilon_1(\omega) = 1 + \frac{2}{\pi} P \int_0^\infty \frac{\omega' \varepsilon_1(\omega')}{\omega'^2 - \omega^2} d\omega' \qquad (4.28)$$

and $$\varepsilon_2(\omega) = \frac{2\omega}{\pi} P \int_0^{\infty} \frac{\varepsilon_1(\omega')-1}{\omega'^2-\omega^2} d\omega' \quad (4.29)$$

P represents the principal value of the complex integral give by:

$$P\int_0^{\infty} d\omega' \equiv \lim_{\delta\to 0}\left(\int_0^{\omega-\delta} d\omega' + \int_{\omega+\delta}^{0} d\omega'\right) \quad (4.30)$$

A physically correct dielectric model should satisfy the KK relationship. Dielectric functions such as Drude-Lorentz, Tauc-Lorentz etc. follow KK relations. But dielectric models such as Sellmeier and Cauchy do not strictly obey KK relationship as in both of those ε_2 = 0 and ε_1 is non zero, which can not satisfy the KK relations above. Nevertheless they are physically meaningful.

In normal reflectivity measurement and subsequent data analysis KK relationship is used extensively to get the phase information of the reflectivity from the amplitude measurement. So, it is an inherent requirement of these measurements to be performed in a large enough energy range for the KK transformations to be meaningful. In ellipsometric data analysis both ε_1 and ε_2 information can be obtained simultaneously without any KK transformation. In case of bulk isotropic substrates the direct conversion of (Ψ,Δ) to $(\varepsilon_1, \varepsilon_2)$ is possible. On the other hand while fitting multilayer data, KK constrained models such as Drude-Lorentz can be used which can finally give $(\varepsilon_1, \varepsilon_2)$ information simultaneously. However depending on the range of measurement sometimes it makes more sense to use dielectric function models which are non-KK constrained.

4.2.2 Optical models

An optical model takes into account the geometrical structure of the sample with the most reasonable representation of the shape and size of the constituent parts. It is a very crucial

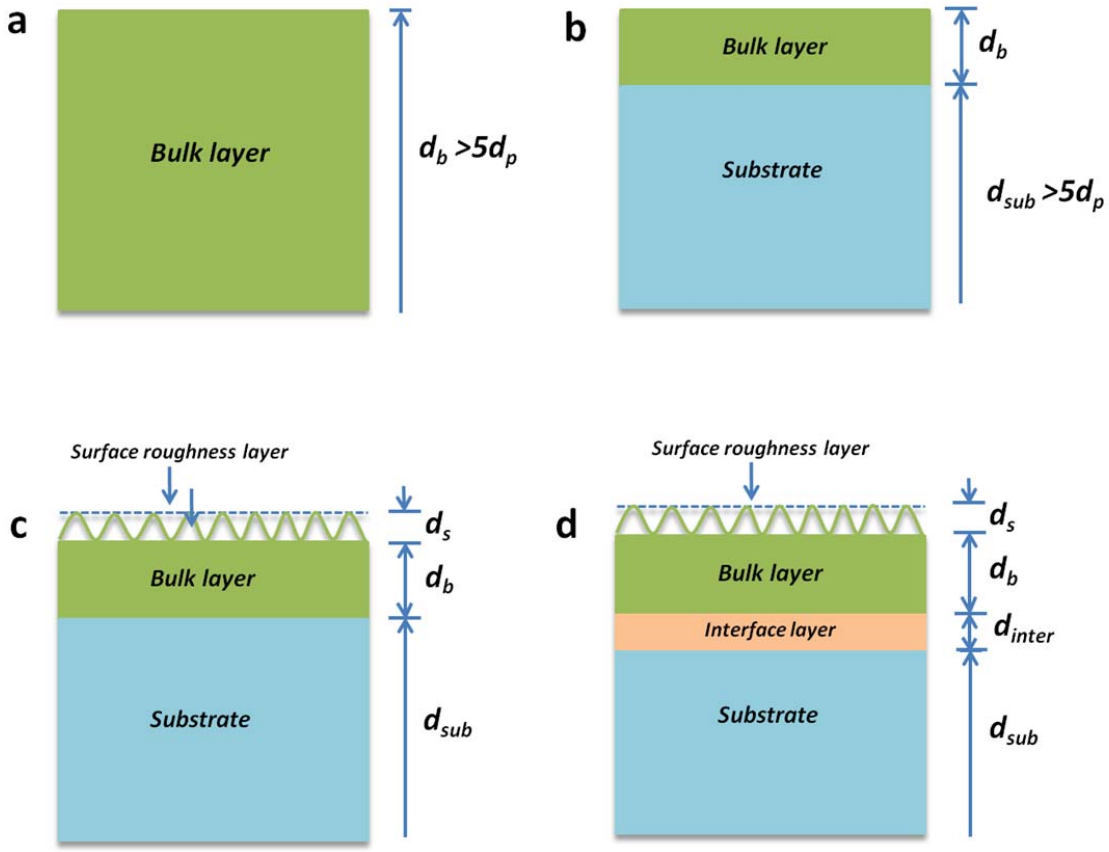

Figure 4.4 Various optical models for ellipsometric data analysis. (Figures are adapted after modifications from [144])

step in ellipsometric data analysis and often the model has to be optimized through iteration. In Figure 4.4 a few commonly used optical models are shown. Intuitively the analysis procedure becomes rather mathematically complicated in the order of (a) to (d).

Generally if the dielectric constants are known for each layer then determining the thickness of layers is relatively straightforward. But the opposite is not true even for say model (c) onwards. The model of Figure 4.4 (a) is applicable when the sample under measurement is an ambient/bulk system. Here the bulk material should be such that its thickness is at least 5 times bigger than the penetration depth (d_p) of light. Also the surface should be flat. In this case the dielectric function ε can be evaluated directly from the measured (Ψ, Δ) by direct analytical manipulations. In figure 4.4 (b) an ambient/thin film/substrate system is shown. Here again the substrate thickness should be greater than at least 5 times the penetration depth (d_p) of light. This model is less complicated to handle mathematically from the measured data when the dielectric constant of the bulk layer and the substrate are not very similar.

In this thesis we have mainly used these two simple models (or one with an additional bulk layer) for most analysis as our substrates are thick enough and also the layers (substrate and films on top) are atomically smooth as confirmed by Atomic force microscopy (AFM) results.

The models shown in Figure 4.4 (c) and 4.4 (d) represent realistic situations where the top surface is rough and also there is one interfacial layer in between the substrate and the bulk layer respectively.

4.2.3 Summary and schematic

Linear regression analysis is generally used for ellipsometric data analysis, where an error function is calculated optimizing the optical constants as well as thickness of layers and the minimum error is found out. The schematic workflow of the procedure is plotted below in Figure 4.5.

Here an optical model corresponding to the sample structure is first constructed. Thereafter dielectric functions for each layer is taken if known or else a model dielectric function is employed. Now using analytical parameters in the model (for example layer thickness, dielectric model parameters) the values of (Ψ, Δ) are calculated for each data point and fitted against the experimental data. From these the error is calculated subsequently. This error is minimized using optimization of the models and going through the same steps. Finally when the error is within acceptable limits we get the required optical constants and (or thickness) of layers.

In practice an optical model is just an approximation to the real structure of the sample and the obtained results may not be correct despite the fitting being good. In such cases an independent estimation of the sample structure using other techniques like AFM, Transmission Electron Microscope (TEM) etc. is desirable to check the validity of the optical models used. Once that is confirmed the ellipsometry method can be used as a robust technique in a quick, nondestructive way for effective determination of optical constants (and thicknesses).

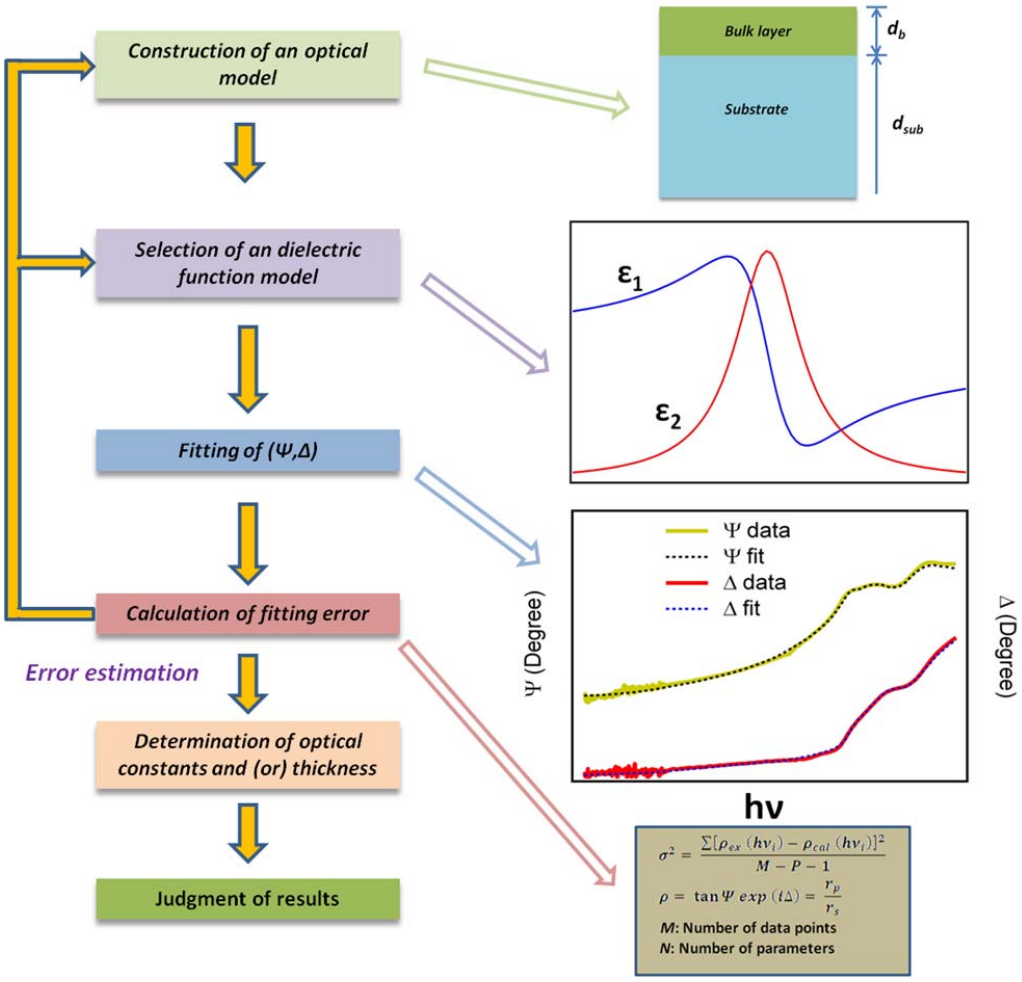

Figure 4.5 Schematic workflow of data analysis steps in ellipsometry. (Figure is adapted after modifications from [144])

In this thesis we have used manual fitting of our experimental data using Drude-Lorentz oscillator models. The number of oscillators used (although in some cases it is around 60 for the spectral range from 0.5 eV to 35 eV) is still manageable in all the cases for such a manual fitting. The error is estimated for different apparently small number of 'good fits'

and the fit corresponding to the minimum error one gives us the required dielectric constants.

As an alternative to this approach mathematical inversion can also be used if we know say the thickness information of the layers beforehand accurately enough. As an example Kravets et al. [58] have used this mathematical inversion technique for graphene on various substrates.

It may be mentioned that effective medium approximations (EMA) are employed extensively in ellipsometric data analysis which take into account microscopic aspects of surface and interface structure (or geometrical irregularities deviating from an exact flat surface or interface). But it involves very detailed mathematical considerations and the complexity of analysis increases manifold. In case of graphene it has been seen that ellipsometric studies without taking EMA approximations are fairly good enough to elucidate the important and interesting aspects of the dielectric function [158]. Also our graphene samples are monolayer with reliable flatness. Therefore we have not considered EMA analysis in this thesis.

4.2.4 Error estimation

Different error functions have been used for estimations of errors in ellipsometric analysis [140-143]. The most basic and commonly used ones are

$$\eta = \frac{1}{\sqrt{M-P-1}}\left\{\sum_{j=1}^{M}\left[\rho_{ex}(h\nu_i) - \rho_{cal}(h\nu_j)\right]^2\right\}^{1/2} \quad (4.31)$$

$$\eta = \frac{1}{\sqrt{M-P-1}}\left\{\sum_{j=1}^{M}\left(\left[\tan\Psi_{ex}\ (h\nu_j) - \tan\Psi_{cal}\ (h\nu_j)\right]^2 + \left[\cos\Delta_{ex}(h\nu_j) - \cos\Delta_{cal}(h\nu_j)\ \right]^2\right)\right\}^{1/2} \quad (4.32)$$

Here 'ex' and 'cal' represent experimental and calculated values; M, P represents the number of measurement points and number of parameters respectively. η is commonly called the unbiased estimator or the mean squared error (MSE).

Another fitting error function used can be written as

$$\chi = \frac{1}{\sqrt{M-P-1}}\left\{\sum_{j=1}^{M}\left[\frac{\rho_{ex}(h\nu_i) - \rho_{cal}(h\nu_j)}{\delta\rho(h\nu_i)}\right]^2\right\}^{1/2} \quad (4.33)$$

Here, χ is known as the biased estimator and $\delta\rho$ is the measurement error for ellipsometry instrument.

We have used *(4.32)* above to estimate the errors in our ellipsometric fitting in this thesis. As we use an ellipsometer with a retarder, the possible experimental errors when Δ is near 0^0 and 180^0 are reduced and therefore it makes MSE a reliable estimate of the fitting error [143,144]. In all the individual fittings we try to look for the minimum MSE also keeping in mind the limits of the experimental error. As an example the MSE is 0. 017 degree for the case of our (Ψ, Δ) best fit for graphene on copper in Figure 6.6. As the experimental error in the Ψ measurement is 0.1 degree and that of Δ is 0.2 degree the

MSE represents a good fit in this example. We used similar considerations to estimate the 'goodness of fit' in all ellipsometric data analysis in this thesis.

4.3 Graphical data fitting

In this thesis a powerful graphical software Reffit [156]) as well as other custom made in-house graphical programs [using Igor platform] have been used to fit the experimental data. In this section the main aspects of these tools will be described very briefly keeping in mind the physical aspects of the built models etc.

Reffit is designed to fit almost all optical spectra namely, reflectivity R(ω), transmission, ellipsometry output etc. The basic assumption underlying this approach of Reffit is that all the optical properties that are dealt with are determined solely by the complex dielectric function $\varepsilon(\omega) = \varepsilon_1(\omega) + \varepsilon_2(\omega)$ of the material under study. So, in short the basic aim of Reffit is to get information of the dielectric function of the material based on optical spectra. To accomplish the fitting of these experimental spectra a suitable model of the dielectric function which has certain number of adjustable parameters is used. Optimizing these parameters the best fit is obtained which gives the desired dielectric function.

There can be two approaches to fit optical spectra. One uses formula defined dielectric functions with limited number of parameters. This approach is straightforward and most of the parameters can be given immediate physical significance. On the other hand there is another approach called variational (or 'free shape' approach) [157] where any

function can be used as the 'basis' in principle and by superposition of a large number of such functions a final fitting can be achieved. In this approach the individual parameters are hard to associate with immediate physical significance but this approach is definitely valid. Depending on what kind of optical spectra is analyzed and the data range- the variational fitting can be either Kramers-Kronig constrained or not-Kramers-Kronig constrained.

In our case we use manual fitting as opposed to automated fitting approach capable in Reffit. We use Drude-Lorentz oscillator models as our individual oscillators but the number of such oscillators could be relatively large. So it may be said that our approach is intermediate between the two approaches mentioned above. We try to fit ellipsometry data using KK constrained Drude-Lorentz oscillators and finally extract the dielectric functions of layers from the best fit. It may be mentioned that Reffit uses Lavenberg – Marquardt (LM) algorithm for minimizing the error in fitting in its automated case.

For the best fit it is desirable to do fitting of different spectra simultaneously. For example its ideal to fit simultaneously say ellipsometry and reflectivity data measured on the same sample if possible. In our case we have used a similar approach by trying to fit ellipsometry data measured at different angles (3 or 4) simultaneously. This put further constraints on the fitting parameters and it can be expected that it leads to accurate final results possible.

Some of the physical requirements of the modeling of dielectric functions used in Reffit are (which are generally true):

(1) $\varepsilon_1(\omega) = \varepsilon_1(-\omega)$ and $\varepsilon_2(\omega) = \varepsilon_2(-\omega)$ and therefore its sufficient to model the ε(ω) only for ω ≥ 0 only.

(2) $\varepsilon_2(\omega > 0) \geq 0$.

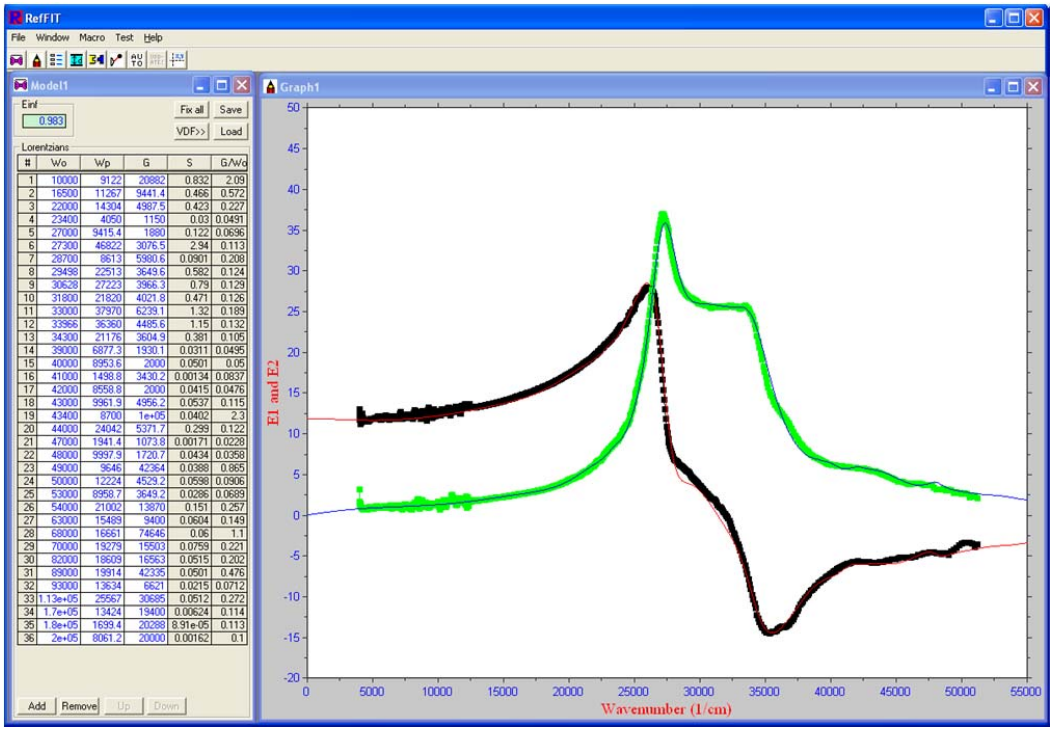

Figure 4.6 Screenshot of Reffit window for fitting $(\varepsilon_1, \varepsilon_2)$ of Si.

(3) At very high frequencies the optical properties of light are similar to that of vacuum: $\varepsilon_1(\omega \to \infty) = 1$ and $\varepsilon_2(\omega \to \infty) = 0$.

(4) The real and imaginary parts of all physically possible dielectric functions are coupled via Kramers –Kronig relationship.

In Figure 4.6 we have shown a screenshot of a typical fitting session for the dielectric function of Si substrate. Here actually we already have the dielectric function for the Si substrate from direct conversion of (Ψ, Δ) data. But the final dielectric function ε (or $\varepsilon_1(\omega)$ and $\varepsilon_2(\omega)$) are fitted using many Drude-Lorentz oscillators (36 in total) with the

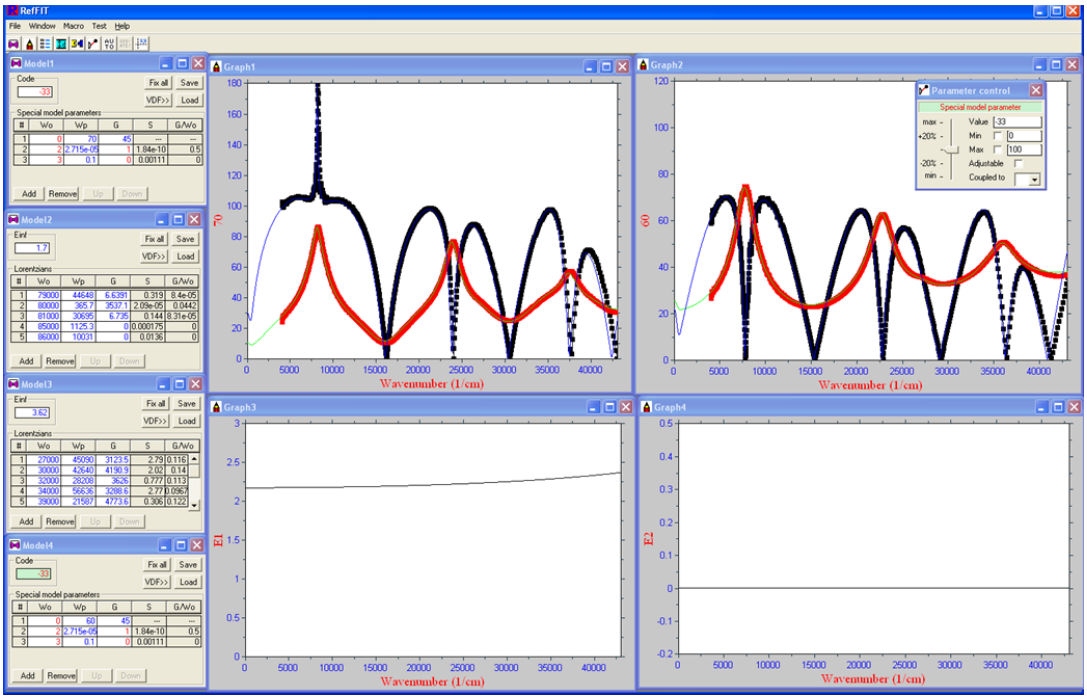

Figure 4.7 Screenshot of Reffit window for fitting (Ψ,Δ) data for 'SiO_2/Si' using built-in model -33.

procedure as explained earlier. This is to facilitate the later fitting of (Ψ, Δ) data for 'SiO_2/Si' as well as 'Graphene/ SiO_2/Si' in a multilayer model approach.

Reffit has some built-in models which can be used for commonly encountered sample structures for reflectivity, transmission and ellipsometry etc. spectra analysis. We use

such a model (model -33 in the Reffit program). We will not go to the details of the intricacies of the implementation of this method but the basic idea is to make a composite model 'combining' the individual dielectric function of each layer. Here the composite

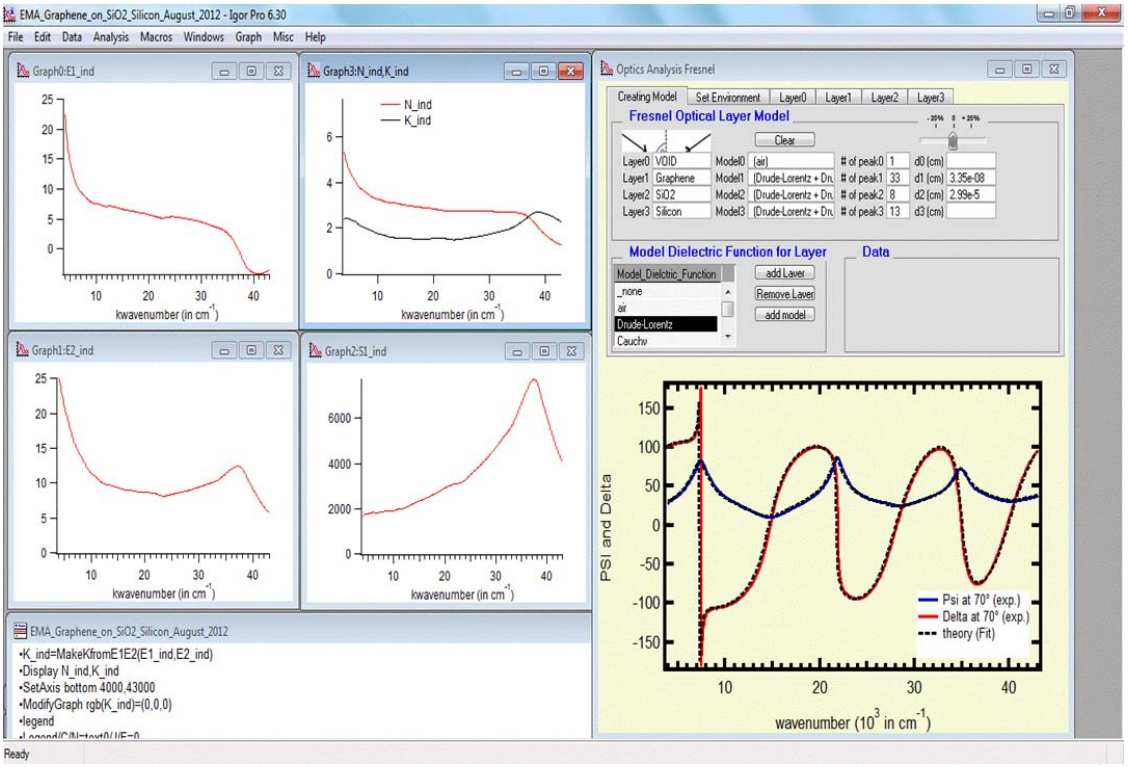

Figure 4.8 Screenshot of the in-house graphical data fitting program.

model, as shown in the screenshot in Figure 4.7, is more like the replica of the optical model constructed. Model 1 and model 4 in the figure works as the 'composite model' for 70 degree and 60 degree incidence angle data respectively. Model 2 and model 3 are for dielectric functions of thin SiO_2 layer and Si substrate layer respectively. The output (Ψ, Δ) of the fitting is plotted against the data for different incidence angle as shown in graph

1 and graph 2 of Figure 4.7 . We basically play with the SiO_2 layer dielectric function in this case to fit the final (Ψ, Δ). The Si substrate layer dielectric function is used from the previous fitting session as described in Fig 4.6 without multilayer approach and this dielectric function is not changed during the current fitting. The resultant $\varepsilon_1(\omega)$ and $\varepsilon_2(\omega)$ for the SiO_2 layer are plotted in graph 3 and graph 4 respectively of Figure 4.7.

A very similar in-house graphical program is also used for some data fitting in this thesis. A screenshot of such a fitting session is shown in Fig. 4.8. This program is written in the Igor pro platform.

4.4 Normalization of high energy reflectivity data with ellipsometry data

As mentioned in the previous chapter one part of the study in this thesis involves finding out the optical properties of graphene in the broad energy range from 0.5 eV to 35 eV. For this reflectivity measurements were performed from 3.8 eV to 40 eV (although we only consider data till 35 eV in our analysis) in the SUPERLUMI beamline in DESY Hamburg. But this reflectivity data has to be normalized as explained in section 3.2 of the previous chapter. This is performed by using the ellipsometry data and the extracted optical dielectric functions of the layers [64,159]. Basically the combined reflectivity (for the ellipsometry range) can be calculated for any incident angle once we have extracted the dielectric functions of all the layers. In this case we have used Reffit itself to give us the reflectivity of the sample at 17.5^o incident angle. Now this reflectivity is plotted along

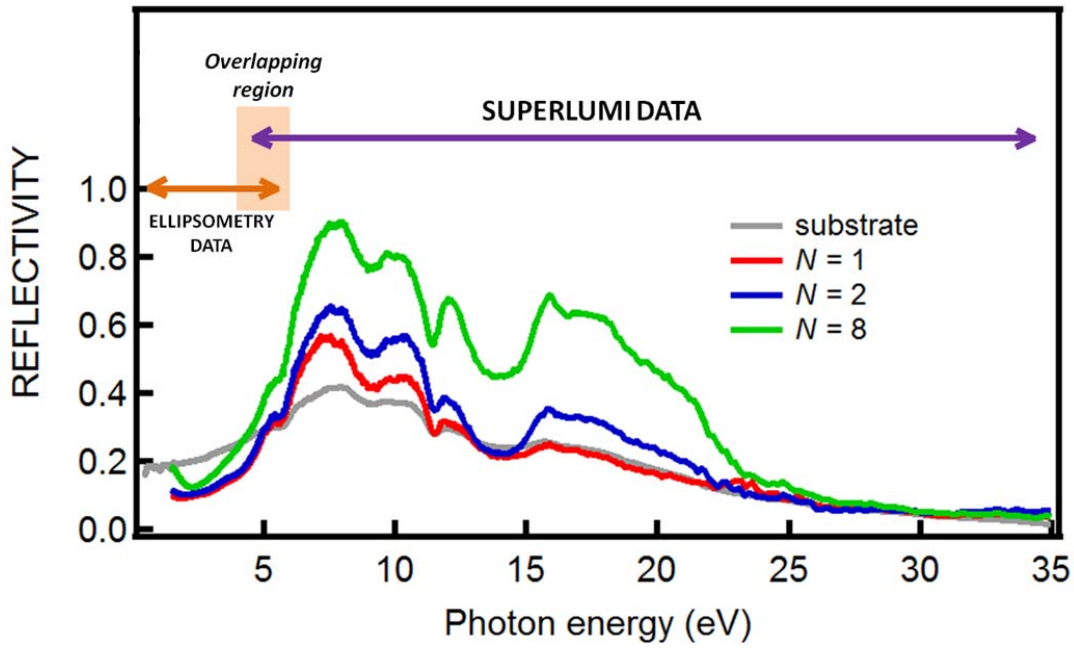

Figure 4.9 Normalized reflectivity and the 'normalization range' for reflectivity data.

with the SUPERLUMI reflectivity. As the reflectivity obtained from ellipsometry data is self normalized we can multiply the SUPELUMI data by appropriate constants to bring it to overlap with the ellipsometry data in the range from about 3.8 eV to 5.3 eV. Then the two parts of the data are combined at a suitable point (approximately 4.8 eV) to give us the final overall normalized reflectivity. The final reflectivity obtained for the case of epitaxial graphene with layer numbers 1, 2 and 8 are shown above in Figure 4.9. The overlapping region is also indicated there. Finally graphical fitting using Reffit is used to extract the overall dielectric functions for graphene layer from these reflectivity data for the whole range.

4.5 Fano analysis

Fano line shape analysis [118- 121, 193] is a central technique used for all our results except for the one described in Chapter 5. The basic relationship between the final optical conductivity σ_1 and the unperturbed $\sigma_{1,\mathrm{cont}}$ can be expressed as

$$\frac{\sigma_1}{\sigma_{1,\mathrm{cont}}} = \frac{(q+\varepsilon)^2}{1+\varepsilon^2} \qquad (4.34)$$

Here $\boldsymbol{\varepsilon} = (\omega - \omega_{\boldsymbol{res}})/(\Gamma/2)$ is the normalized energy by width, Γ relative to the excitonic resonance energy $\omega_{\boldsymbol{res}}$. Here the width of resonance, Γ further gives an estimate of the auto-ionization time when used in conjunction with the Heisenberg's uncertainty principle. The magnitude of q^2 quantifies the ratio of the strength of the e-h coupling to the band to band transition, whereas the asymmetry of the line-shape is determined by the sign of q.

We use a band to band σ_1 of the form

$$\sigma_{1,\mathrm{cont}}(\omega) = \mathrm{A} \times \left[\exp\left[-\frac{(\omega-\omega_0)^2}{\gamma^2}\right] \otimes \left[-\log\left|1-\frac{\omega}{\omega_0}\right|\right]\right] + \mathrm{B} \qquad (4.35)$$

where the constant B is to account for the constant universal conductivity in the infrared and the logarithmic term comes from the expression for optical transitions near a saddle point singularity [117]. The Gaussian broadening of γ is to account for the experimental width.

We fit the experimental optical conductivity graphically using Igor macro programming as shown in the screenshot of Figure 4.10. As seen in the screenshot q, G (or Γ), E_r, E_0, determine the Fano function. And when this function is used to convolute the unperturbed

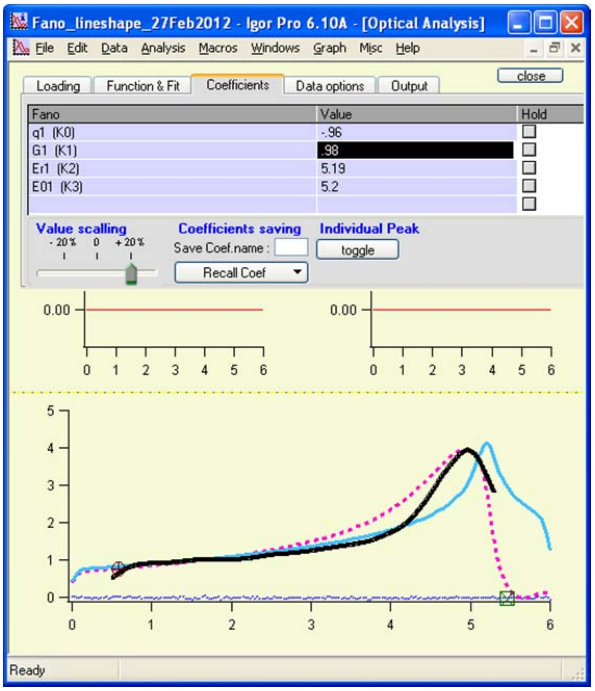

Figure 4.10 Screenshot of Fano line-shape analysis macro using Igor.

$\sigma_{1,cont}$ it finally gives us the fitting curve shown in pink dashed line in the screenshot. Here the fitting does not look good because we are trying to fit graphene on copper data (shown in black line) which can not be fitted using Fano approach due to different physical reasons (explained in detail in chapter 6) [61]. The cyan line represents $\sigma_{1,cont}$. The particular details can be found in the results chapter for this case. The Fano fitting routine used in this thesis is given in Appendix B.

Chapter 5

High-Energy Resonant Excitonic Effects in Graphene

Using a combination of ultraviolet-vacuum ultraviolet reflectivity and spectroscopic ellipsometry, we observe a resonant exciton at an unusually high energy of 6.3 eV in epitaxial graphene. Surprisingly, the resonant exciton occurs at room temperature and for a very large number of graphene layers N ≈ 75, thus suggesting a poor screening in graphene. The σ_1 of a resonant exciton scales linearly with the number of graphene layers (up to at least 8 layers), implying the quantum character of electrons in graphene. Furthermore, a prominent excitation at 5.4 eV, which is a mixture of interband transitions from π to π^* at the M point and a π plasmonic excitation, is observed. In contrast, for graphite the resonant exciton is not observed but strong interband transitions are seen instead. Supported by theoretical calculations for $N \leq 28$ the σ_1 is dominated by the resonant exciton, while for N >28 it is a mixture between exitonic and interband transitions. The latter is characteristic of graphite, indicating a crossover in the electronic structure from stacked graphene to graphite. Our study shows that important elementary excitations in graphene occur at high binding energies and elucidate the differences in the way electrons interact in graphene and graphite.

My main contributions in this work are in sample preparation, data taking and analysis. Theoretical calculations were performed by Dr. Y. Lu and Prof Yuan Ping Feng in close collaboration with our group.

5.1 Introduction

As described in detail in chapter 2, σ_1 of graphene carries very distinct signatures of many-body effects in the different spectral ranges. Moreover measurement of σ_1 to higher energies beyond the conventional range (near infrared to UV-VIS) is crucial to understand graphene electronic structure and the resultant optical transitions and

processes. This work is an attempt to study the optical properties of epitaxial graphene addressing both of the above aspects particularly.

5.1.1 Motivation

Recent theoretical studies based on the *ab initio GW* and Bethe-Salpeter equation (BSE) approach by Yang *et al.*[57, 62] and Trevisanutto *et al.*[63] have predicted the existence and have highlighted the importance of resonant excitonic effects in the optical absorption of graphene. As described in Figure 2.6 particularly, the two different reports [62, 63] show the effects of electron-hole interactions in the optical absorption till energies of 20 eV and 22 eV respectively. However, as evident from Figure 2.6 there is disagreement as to the origin and position of the exciton. In reports by Yang et. al, [57, 62] the optical conductivity carries signatures of the prominent resonant excitonic effects in the region of spectra where transitions near the saddle point singularity dominates (~5 eV). Also their calculations [62] reveal contributions from a narrow resonant excitonic effect resulting from the nearly parallel σ and π^* bands in the higher energy region (~ 12.5 eV) just below the absorption contiuum. In Ref. 63, however, the resonant exciton was predicted to appear at 8.3 eV due the background single-particle continuum of dipole forbidden transition at the the Γ point. Despite their disagreement, these reports concur upon the fact that resonant excitons play an important role in elementary excitations in graphene and thus its understanding is crucial. Experimental study of σ_1 is further

necessary to resolve these differences and also for better understanding of the graphene electronic structure. Although there have been some reports of σ_1 till the deep UV range (~ 5.3 eV) there is no reliable σ_1 data in the higher energy range beyond 9 eV [65]. This makes it a more compelling motivation for the current study.

5.2 Experimental technique and data analysis

In this work σ_1 of epitaxial graphene on a 6H-SiC(0001)/buffer layer substrate is measured in an unprecedented wide photon energy range from 0.5 to 35 eV using a combination of SE and UV-VUV reflectrometry. The combination of these two techniques enables a stabilized Kramers- Kronig transformation [159], which is crucial to resolve precisely the dielectric function. We mainly study the evolution of σ_1 as a function of the number of layers *N* (hence forth $\sigma_{1,N}$) including graphite.

5.2.1. Sample preparation and characterization

Epitaxial graphene samples on 6H-SiC(0001) were prepared by a Si desorption process in Si flux as described in previous studies [148, 149]. This process was found to lead to multilayer graphene with ordered stacking [149]. The thickness was determined using Scanning Tunneling Microscope (STM) and Raman spectroscopy [149, 152]. The reproducibility was checked by fabricating and repeating individual measurements on three different samples which were grown under identical conditions, with at least three different locations on each sample yielding reproducible results. The sample preparation and characterization processes are explained in detail in section 3.3.1 of this thesis.

5.2.2 Measurement and Data analysis

SE is a self-normalizing technique to determine the complex elements of dielectric tensor from a single measurement without performing Kramers-Kronig transformation [141-144]. From SE, we extract reflectivity (R) and use this to normalize the UV-VUV-reflectance data. Using this method, we are able to achieve a stabilized Kramers-Kronig transformation that yields the σ_1 and reveals changes in the optical spectral weight up to 35 eV [159]. The UV-VUV reflectance measurements were carried out at the Beamline I of HASYLAB [160] using linearly polarized light with the normal incident angle of ~17.5^{o}. The details of the SUPERLUMI set-up and the interpretation and analysis of the reflectivity data can be found in the section 3.2 of this thesis. The measurements were done at room temperature at an ultra high vacuum pressure better than 10^{-9} mbar.

Since our graphene samples are made epitaxially on top of 6H-SiC and those are of sub nanometer to few nanometer thickness it is necessary to eliminate the background signal from 6H-SiC and in additional from "buffer layer". Later on we treat the buffer layer and 6H-SiC as a substrate. As can be seen from Fig. 5.1 (a) below, the reflectivity spectra consist of the signal from graphene (layer A) and substrate (layer B). To do so we take the reflectivity spectrum of substrate as a reference and do the fitting (using Reffit) with the phenomenological oscillators constrained with Kramers-Kronig transformation. One can see that, for example, from substrate to $N = 1$ graphene, the reflectivity is similar in the region between 12 and 35 eV but they differ in the region 0 to 5 eV where the

reflectivity is suppressed and in the region 5 to 10 eV where the reflectivity is increased. The complex dielectric function of graphene (N = 1) then can be obtained by fitting the reflectivity of graphene with parameters gained from the substrate (these parameters result should be fixed now) and altering only the oscillator parameters from graphene.

5.3 Results and discussions

Figure 5.1(a) shows room-temperature reflectivity data for N-dependent epitaxial

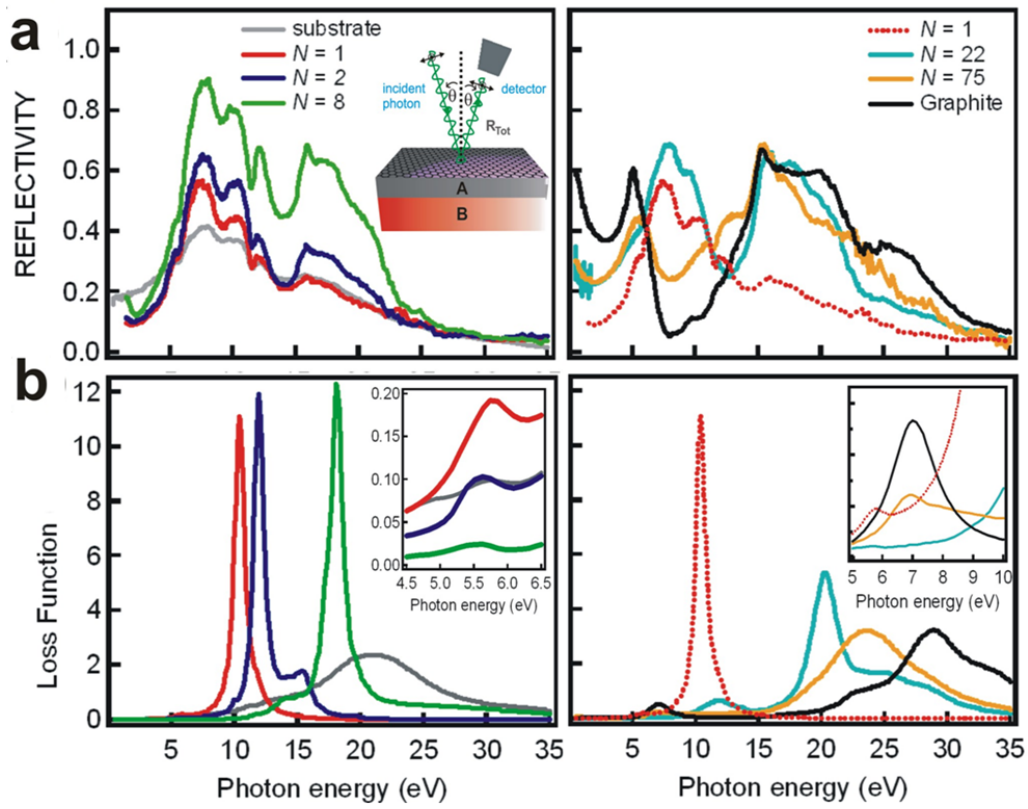

Figure 5.1 (Color online) Room-temperature experimental results of (a) reflectivity and (b) loss function, Im (ε^{-1}). The inset of (a) shows the experimental geometry while the insets of (b) shows (ε^{-1}) on an expanded scale from 4.5 to 6.5 eV and from 5 to 10 eV [64].

graphene, graphite and the substrate. One can immediately see that the reflectivity of epitaxial graphene is very much dependent on N and very much distinct from that of graphite. The reflectivity has rich and distinct structures especially in the range from 5 to 8 eV for N = 1, 2, and 8 while additional structures occur around 14 to 20 eV for N = 22 and 75. On the other hand, the reflectivity of graphite shows strong structures below 0.5

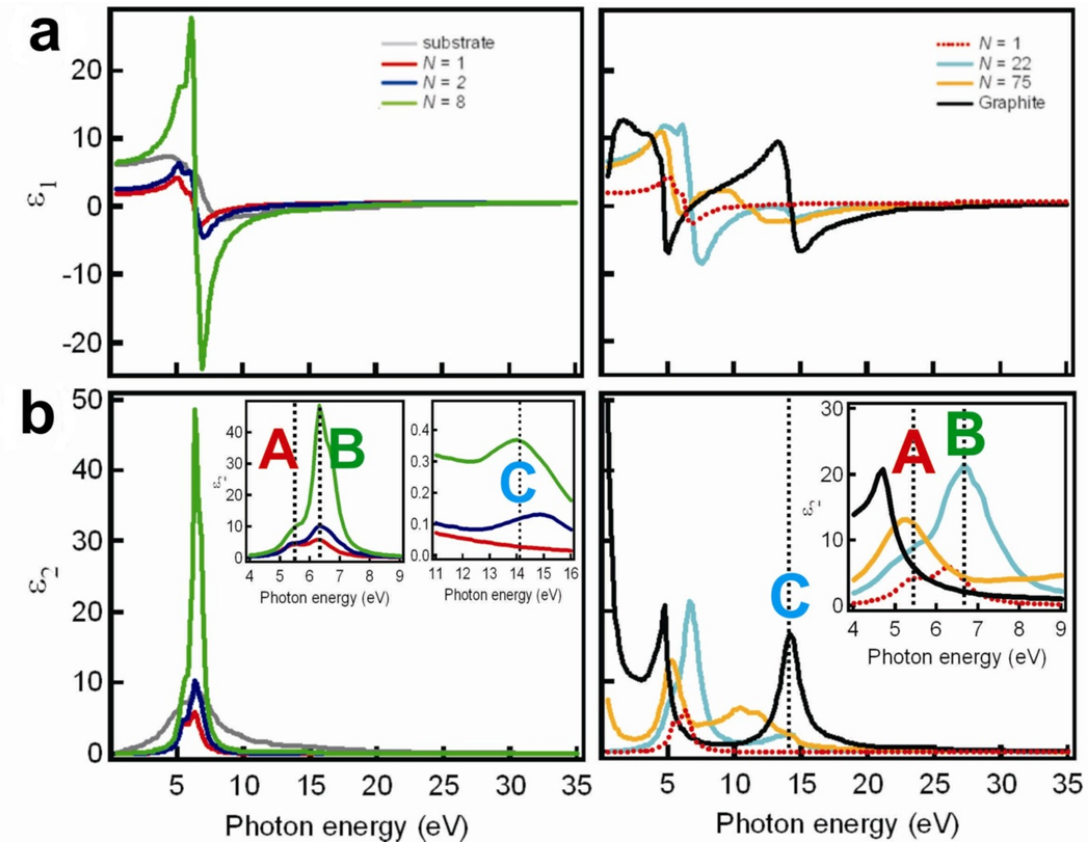

Figure 5.2 The complex dielectric function ε(ω) for graphene, substrate and graphite. (a) real part, ε_1 and (b) imaginary part, ε_2. Insets show the zoom-in of the ε_2 for various energy ranges [64].

eV and ~5 eV and around 14 to 20 eV which are similar to published result [161]. The same situation is true for the complex dielectric functions, ε_1 and ε_2 (Figs. 5.2 (a) and 5.2 (b)), which are proportionally related to the refractive index and absorption coefficient. The complex dielectric function (ε) is extracted from the reflectivity data by fitting to the Drude-Lorentz (DL) oscillators graphically using the Reffit software as described in section 4.2.1 and 4.3. The reflectivity *R* is related to this dielectric constant ε through,

$$R = \left|\frac{1-\sqrt{\varepsilon}}{1+\sqrt{\varepsilon}}\right| \qquad (5.1)$$

It is also obvious that most structures in ε_1 and ε_2 in figure 5.2 (a) and 5.2 (b) are revealed in the same region as in reflectivity data. Further rigorous discussion will be achieved by analyzing σ_1. The σ_1 has been obtained through the complex dielectric function

$$\varepsilon(\omega) = \varepsilon_1(\omega) + \varepsilon_2(\omega) \qquad (5.2)$$

$$\varepsilon_2(\omega) = \frac{i\,4\pi\sigma_1(\omega)}{\omega} \qquad (5.3)$$

The $\sigma_{1,N}$ shows striking results [Figs. 5.3(a) and 5.3(b)]. For $N = 1$, the $\sigma_{1,1}$ is dominated by two well-defined peaks, one very pronounced at 6.3 eV (peak B) and the other less pronounced at 5.4 eV (peak A), with almost equal full width at half maximum (FWHM) of ~0.8 eV. These structures, especially peak B, are considerably sharp for this high-energy range.

Now we focus our discussion on peak B as it shows an interesting dependence on *N* [Fig. 5.3(c)]. The $\sigma_{1,N}$ (B) increases rapidly toward $N = 8$, while it's FWHM and peak position

remain independent of *N*. For *N* >8, $\sigma_{1,N}$ (B) decreases while the peak position shifts toward higher energy (6.7 and 11 eV for *N* = 22 and *N* = 75, respectively). For graphite, peak B disappears and our result is similar to the published data [161].

To find out the origin of peak B, we have directly compared our experimental data with theoretical calculations [57, 62, 63]. As shown in inset 1 of Fig. 5.3(a), the line shape and the $\sigma_{1,1}$ (B) between experimental data and theoretical calculations from Ref. 63 are surprisingly very similar. This comparison shows decisive evidence of the high-energy resonant exciton in epitaxial graphene. The resonant exciton arises from dipole transitions of the single-particle continuum. However, the observed resonant exciton peak occurs *red shifted* compared to the calculations. Our calculations show that the red shifted exciton could result from film-substrate interactions, which are not included in the previous calculations (with details below). Thus, the origin of peak B is the high-energy resonant exciton as predicted.

Furthermore, our detailed study rules out the interband transitions and plasmonic excitations as the origin of peak B. Based on Density Functional Theory (DFT), we have calculated optical conductivity for *N* = 1 and 2 and found that peak B does not originate from interband transitions [Fig. 5.4 (a)]. Second, one may argue that we have to consider contributions from a plasmonic excitation. To address this issue, we have studied in detail an energy-loss function Im(ε^{-1}) which can reveal collective excitations such as plasmonic excitations [162, 163]. As shown in Fig. 5.1(b), there is no feature that can be attributed to a plasmonic excitation. For *N* = 1, Im(ε^{-1}) is dominated by a strong

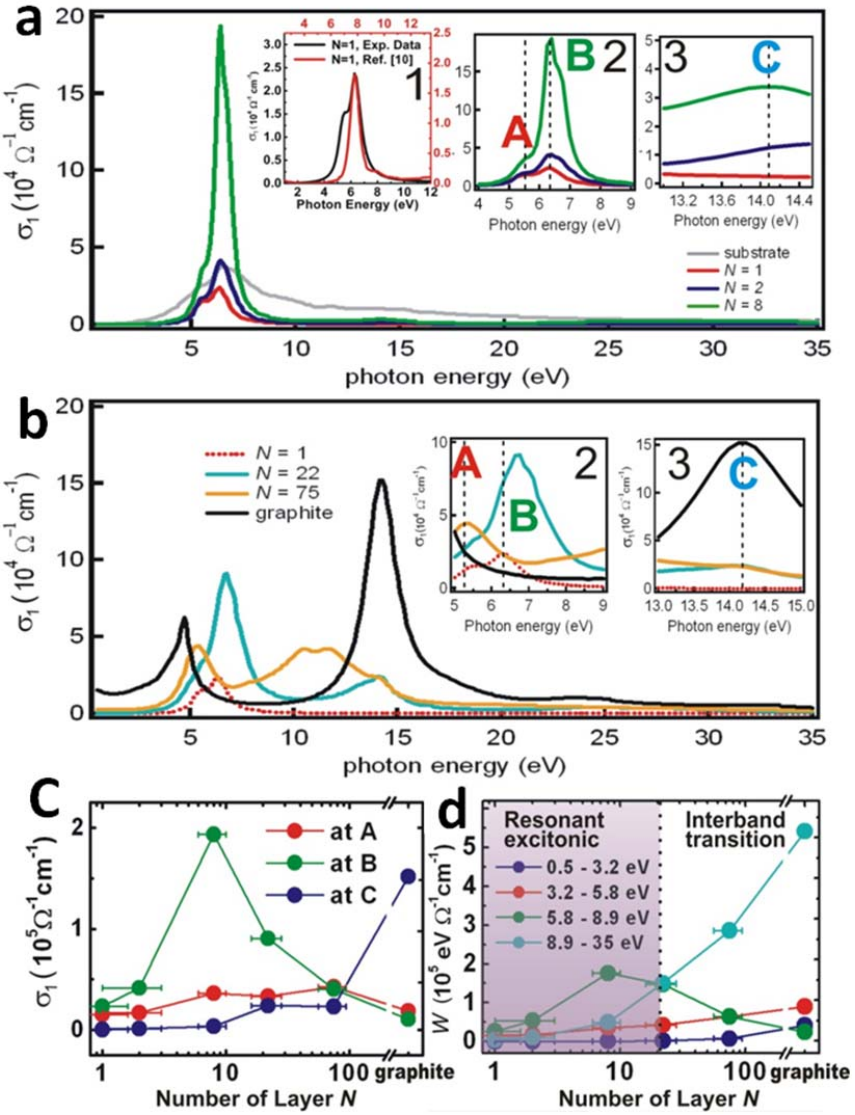

Figure 5.3 The optical conductivity (σ_1) of (a) substrate and graphene (N = 1,2,8) and (b) graphene (N = 22,75) and graphite shows three peaks at 5.4 eV (label A), 6.3 eV (label B), and 14.1 eV (label C). Inset 1 shows the comparison of $\sigma_{1,1}$ between experimental data and theoretical calculations. Insets 2 and 3 show the σ_1 on an expanded scale at various energy ranges. (c) The value of σ_1 at A, B, and C as a function of N. (d) The partial spectral weight (W) as a function of N [64].

structure at ~10 eV and a weak structure at 5.5 eV. These structures are from $\pi + \sigma$ and π

in-plane plasmon modes, respectively [163]. Based on the symmetry, the 5.5-eV plasmon peak structure is only visible for light polarization parallel to the *c* axis (**E**||*c*). In our measurement, the **E** was mixed between **E**||*c* and **E**⊥*c* with the main contribution from **E**⊥*c*; thus, the observed π plasmon is very weak. On the other hand, the $\pi + \sigma$ Plasmon mode is very strong in our geometry, which is consistent with electron-energy-loss spectroscopy (EELS) measurements [164]. As *N* increases, the $\pi + \sigma$ plasmon mode shifts toward higher energy and gets broader, while the structure at 5.5 eV is nearly *N* dependent. This *blue shift* may be due to strong effects of the interlayer Coulomb interaction on the total plasmon [162].

Based on Heisenberg's uncertainty principle a sharp peak corresponds to longer lifetime which essentially means the exciton has a higher binding energy. The narrow profile of the excitonic peak at 6.3 eV suggests a high binding energy as it has a long life time [62]. This narrow resonant exciton is unlike the broad resonant exciton predicted and observed in the lower energy range [57-61]. For this lower energy broad resonant exciton the life time is extremely small and no binding energy can be associated with it. However despite being resonant in character the prominent narrow feature of the 6.3 eV exciton implies a longer lifetime and higher binding energy. The observation of this sharp resonant exciton even at room temperature is a result of this high binding energy. The nearest absorption edge due to interband transitions could be estimated from considerations taken from other results. If one considers the angular-resolved

photoemission data, the distance of the σ band at the Γ point to the Fermi level is around 4.5 eV [165]. By assuming the distance of the σ^* band to the Fermi level to be similar to that of the σ band one will end up with 9 eV as the separation between the σ and σ^* bands. As evident the resonant excitonic peak position is far away from this energy (by 2.7 eV) and the position itself could be said as a dramatic manifestation of the resonant character of this exciton. As graphene is semi-metallic in character it is not expected to support bound excitons or at least excitons with long lifetimes. However such a prominent and narrow resonant exciton observed on graphene far away from the interband absorption edges is indeed remarkable and a direct consequence of its low dimensionality in conjunction with its intriguing electronic properties. This room temperature exciton could also lead to potential optoelectronic applications.

We next discuss peak A and its origin. As shown in Fig. 5.3(c), $\sigma_{1,N}$ (A) increases monotonically as a function of *N*. Interestingly, for $N > 8$ as well as for graphite the position of peak A shifts toward lower energies, as opposed to peak B, while the line shape is rather symmetric and the full width at half maximum (FWHM) is broader for larger *N*. Based on electronic band structure calculations [166], peak A is the result of interband transitions from the π to the π^* bands at the M point, where the van Hove singularity occurs. Furthermore, from analysis of energy-loss function [Fig. 5.1(b)] the $\mathrm{Im}(\varepsilon^{-1})$ shows a weak π-plasmon contribution. Thus, one can conclude that peak A is a mixture of interband transitions and a plasmonic excitation.

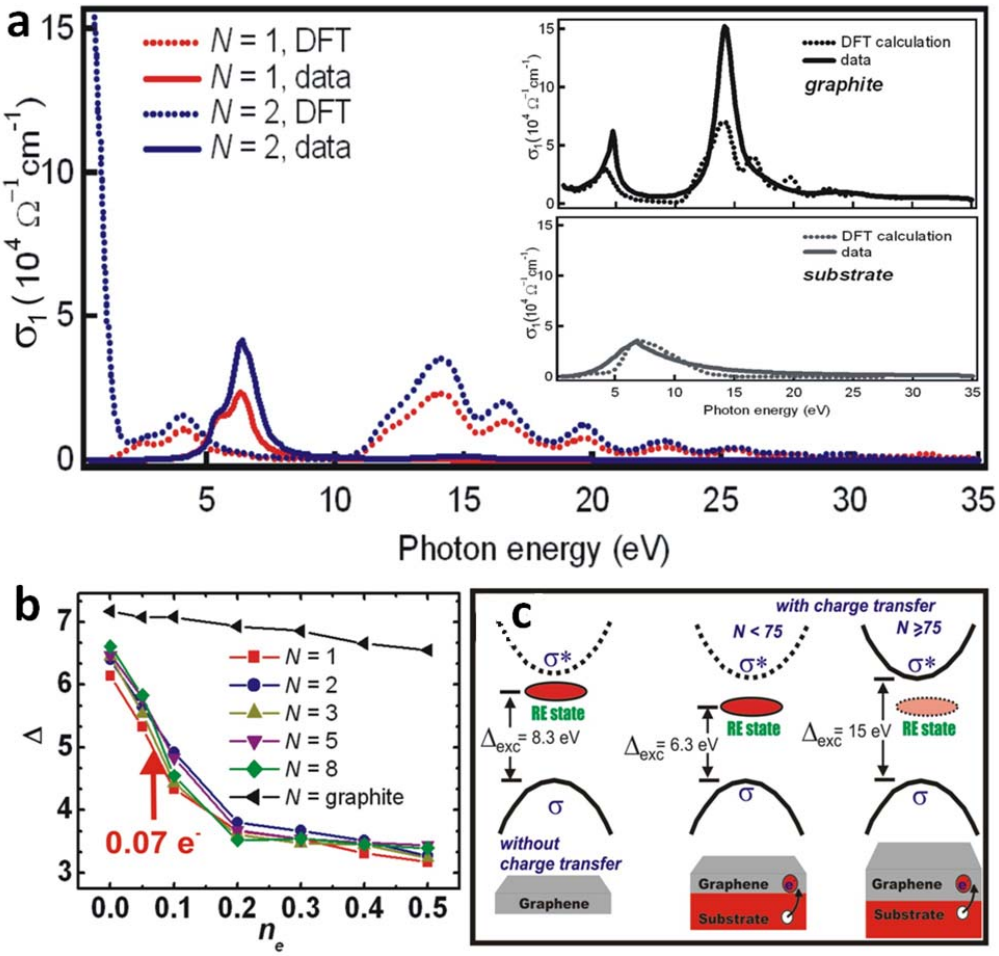

Figure 5.4 (a) Comparison between experimental data and calculated σ_1. (Top inset) σ_1 spectra of graphite. (Bottom inset) σ_1 spectra of the substrate. (b)The background single-particle continuum transitions (Δ) at the Γ point as a function of nominal charge transfer (ne) from substrate to graphene for various graphene layer (N). The red arrow shows the observed charge transfer in our sample. (c) A proposed model of optical absorption of exciton in graphene and graphene on substrate as function of N. RE stands for the resonant exciton and (Δ_{exc}) is excitation energy [64].

Another notable observation is a broad structure at 14.1 eV (peak C). The peak C is absent for $N = 1$ and $\sigma_{1,N}$ (C) increases dramatically for $N \geq 2$ [Fig. 5.3(c)]. Interestingly,

for graphite the σ_1 is dominated by peak C with symmetric lineshape. Based on electronic band structure calculations [63, 166, 167] this structure is from interband transitions from σ to σ^* bands at the Γ point. Peak C clearly has an intimate relationship with optical conductivity in graphite while peak B is a unique characteristic of graphene.

We next discuss partial spectral weight integral (W) because it describes the effective number of electrons excited by photons of respective energy. The σ_1 is restricted by the f-sum rule:

$$\int_0^\infty \sigma_1(E)dE = \frac{\pi n e^2}{2m^*} \qquad (5.4)$$

where n is the electron density, e is elementary charge and m^* is effective electron mass. Hence, one can extract the

$$W \equiv \int_{E_1}^{E_2} \sigma_1(E)dE \qquad (5.5)$$

for various energy ranges. Due to the f-sum rule and charge conservation, the W is constant, and thus one can study the spectral weight transfer and reveal interactions as well as the effect of N in the broad energy range of 0.5 to 35 eV. Figure 5.3(d) shows W for the different energy regions: 0.5 to 3.2 eV (region I, W_I), 3.2 to 5.8 eV (region II, W_{II}), 5.8 to 8.9 eV (region III, W_{III}), and 8.9 to 35.0 eV (region IV, W_{IV}). The W_I is mainly governed by the transition around the Dirac cone, that is, π to π^* around the K point in the Brillouin zone, which is consistent with previous publications [55, 89]. The W_{II}, W_{III} and W_{IV} show the main contribution from peaks A, B, and C, respectively. Interestingly, W_I and W_{II} show an almost similar trend in which the W increases

monotonically as function of N, while the W_{III} and W_{IV} show completely different behaviour. For $N \leq 8$ the W_{III} increases as N increases, while for $N > 8$ W_{III} decreases as N increases. On the other hand, W_{IV} increases rapidly for $N \geq 8$. In graphite, W_{IV} is maximum while W_{III} reaches its smallest value. We find a crossover between W_{III} and W_{IV} at $N \sim 28$ [see Fig. 5.3(d)]. Thus, we propose that for $N < 28$ the optical conductivity of epitaxial multilayer graphene is dominated by high-energy resonant excitonic effects, while for $N > 28$, the optical conductivity is dominated by interband transitions.

To gain further insight, we have calculated the optical conductivity ($\sigma_{1,calc}$) of graphene, graphite, and substrate using DFT. We have studied the role of interband transitions and have compared them with experimental results [see Fig. 5.4(a)]. Noting that our calculations do not include electron-hole (e-h) interactions, ($\sigma_{1,calc}$) is mainly driven by interband transitions and serves as a reference for the uncorrelated case.

The electronic structures and optical conductivity ($\sigma_{1,calc}$) are calculated within the framework of density functional theory (DFT), using the CASTEP code which is based on plane wave and ultrasoft pseudo potentials [168]. The Perdew-Burke-Ernzerhof form of generalized gradient approximation [169] is adopted for the exchange-correlation potential. Graphene is modeled by a slab of 1×1 unit cell (2.46 Å) with a 15 Å vacuum region between graphene planes in adjacent cells. The electron wave function is expanded in plane waves with a cutoff energy of 310 eV and a monkhorst-pack grid [170] is used for irreducible Brillouin zone sampling. For the calculation of electronic

properties, 15×15×1 k-point mesh is used while for the calculation of optical conductivity ($\sigma_{1,calc}$), a denser k-point mesh, 21×21×1 Perdew-Burke-Ernzerhof is used. The total energy is converged to within 5×10^{-7} eV/atom

Based on the DFT calculation, $\sigma_{1,calc}$ mimics reasonably well the σ_1 for graphite as well as for the 6H-SiC(0001)/buffer layer. For graphite, the peak at 4 eV is dominated by transitions from $\pi \rightarrow \pi^*$ bands while the peak at 14.1 eV is dominated by transitions from $\sigma \rightarrow \sigma^*$ bands. This is consistent with previous theoretical study [167].

On the other hand, the DFT calculations for graphene show that its optical conductivity cannot be explained with interband transitions. As shown in Fig. 5.4(a), the calculated optical conductivity for graphene shows a completely different result than the experimental data and thus our attempt to mimic σ_1 for N = 1 and 2 failed. Calculations based on DFT show that the $\sigma_{1,calc}$ for graphene (N = 1, 2) above 3 eV is very similar to that seen with graphite. This is in contrast to our experimental results. This further supports that the $\sigma_{1,N}$ is mainly driven by strong e-h interactions which lead to a high-energy resonant exciton and form an unusual electronic band structure while the optical conductivity of graphite is mainly driven by interband transitions. It is shown that for N = 1, once one turns on the e-h interactions, the peak around 4 eV and the peak around 14.1 eV [inset of Fig. 5.4(a)] vanish, resulting in a new and very strong peak in between [63].

To find out the origin of the redshift of the excitonic excitation, we have calculated the variation of the σ bands and the background single-particle continuum transitions (Δ) as functions of charge transfer (n_e) and strain. We find out that while the σ bands are nearly independent from these two effects, the background single-particle continuum transitions very much depend on the charge transfer n_e from substrate to the graphene layer [Fig. 5.4(b)]. Based on our DFT calculations, the charge transfer from substrate to graphene n_e is about ~0.07e (per graphene unit) and thus the background single particle continuum transitions reduce by ~1.4 eV compared to that of for $n_e = 0$. The strain in graphene due to the lattice mismatch with the substrate reduces the background single particle continuum transitions by 0.6 eV. These two effects altogether decrease the single-particle continuum transitions to about 2.0 eV in total. Thus, one may expect to see the exciton at a lower energy of ~6.3 eV. Our result may suggest that energy excitation of the exciton depends on the n_e and the strain.

Interestingly, our calculation shows that Δ does not dependent on N significantly [Fig. 5.4(b)]. This is, in fact, consistent with our experimental result. In contrast, the theoretical predictions in Ref. 63 show an energy shift between the exciton in graphene and bilayer graphene which is attributed to enhanced screening. Our experimental results show, however, that the position of the exciton does not depend on the N value until about N = 22. This can be reconciled with Ref. 63 only if one assumes that screening effects are significantly reduced. Thus, by comparing the experimental results and theoretical

calculations, one may conclude that screening effects in graphene are much weaker than one would expect.

Finally, based on our experimental results of high-energy optical conductivity, DFT calculations, and recent *ab initio* GW-BSE calculations [63], we have proposed the following, phase diagram [Fig. 5.3(c)– 5.3(d)] and a model for optical absorption which is proportional to σ_1 [Fig. 5.4(c)]. For free-standing graphene of N = 1, the optical absorption is dominated by high-energy resonant exciton effects which occur around 8.3 eV. However, in our case due to the charge transfer and lattice mismatch between graphene and the substrate, the resonant exciton occurs at 6.3 eV. For N <28, the optical absorption shows very strong resonant excitonic like structure and weak interband transitions. For 28 < N < 75 the optical absorption shows a mixture between exciton and interband transitions [Figs. 5.3(d) and 5.4(c)]. For N >75 as well as for graphite, the optical absorption is dominated by interband transitions.

5.4 Conclusion

In summary, we have observed a high-energy room temperature stable resonant exciton at ~6.3 eV redshifted far away from the absorption continuum (by ~2.7 eV suggested by the band structure) in the optical conductivity of multilayer epitaxial graphene revealing strong collective e-h interactions. The resonant exciton persists for very large N and thus dominates the electronic properties owing to the poor screening in graphene. Furthermore, the mixture of interband transition from π to π^* at the M point and weak π

plasmonic excitation gives rise to peak in the optical conductivity at 5.4 eV. These findings demonstrate the importance of high-energy optical conductivity and have strong implications on the understanding of the electronic structure of epitaxial graphene.

Chapter 6

Optical conductivity study of screening of many-body effects in graphene

Theoretical studies have shown that electron-electron (e-e) and electron-hole (e-h) interactions play important roles in many observed quantum properties of graphene making this an ideal system to study many-body effects. In this work we show that spectroscopic ellipsometry can enable us to measure these interactions quantitatively. We present spectroscopic data in two extreme systems of graphene on quartz (GOQ), an insulator, and graphene on copper (GOC), a metal which show that for GOQ, both e-e and e-h interactions dominate while for GOC e-h interactions are screened. The data further enables the estimation of the strength of the many body interactions through the effective fine structure constant, (α_g^*). The α_g^* for GOQ indicates a strong correlation with an almost energy independent value of about 1.37. In contrast, α_g^* value of GOC is photon energy dependent, is almost two orders of magnitude lower at low energies indicating very weak correlation.

My contributions in this work are in planning the experiment, sample preparation, data taking and analysis.

6.1 Introduction and motivation

In this chapter we discuss in detail our study of the optical conductivity of graphene in different dielectric environments- by using different substrates.

Tailoring the dielectric interface has been proposed as an immediate step to manipulate the electron-electron (e-e) and electron-hole (e-h) interactions in graphene [19] as it is two-dimensional in structure and also in almost all cases requires a substrate [58, 59, 88,171,172]. Experimental reports addressing questions whether graphene is a strongly or weakly interacting system have thrown light on the fact that the answer mostly depends

on the energy scale of interest [115,173]. Optical measurements from far infrared to deep ultraviolet (0.1–5.5 eV) have been performed on graphene on insulating substrates [58, 59] (with negligible screening effect) and on free-standing graphene [60] which show prominent contributions from both e-e and e-h interactions as predicted by theoretical calculations [57]. An extreme case of screening by a substrate dielectric interface is to use a metallic substrate, which has a huge supply of free electrons, in close proximity with the graphene layer. For example, metallic substrates have been used for one-dimensional systems like single-walled nanotubes (SWNT) to study the screening of many-body effects [87]. Optical-conductivity measurement is not only sensitive to interband transitions and intraband (e.g., Drude, e-e interactions) processes but it is also the most direct way to observe the effect of e-h interactions as in optical processes electron excitation creates a concomitant hole state.

The effects of different dielectric environments on the transport properties of graphene highlight the importance of the effective fine-structure constant (α_g^*) as one of the parameters of screening [125]. The fine-structure constant (α_g) is the ratio of potential energy to kinetic energy of electrons for free-standing graphene, and is $\frac{e^2}{\hbar v_F}$, where $\hbar$ is Planck constant and v_F is the renormalized Fermi velocity near the Dirac point, has the nominal value of 2.2 and it indicates that graphene is a strongly interacting system [19, 116]. However a recent study on highly oriented pyrolytic graphite [115] has elucidated the fact that the effective fine-structure constant (α_g^*) which is given by

$$\alpha_g^*(k,\omega) = \frac{\alpha_g}{\varepsilon(k,\omega)} \qquad (6.1)$$

where k and ω are momentum and energy, respectively, may deviate from the value of 2.2 to far lower magnitude indicating that graphene might be weakly interacting depending on k and ω. On the other hand, when the graphene layer is sandwiched between two dielectric media whose complex dielectric constants are ε^1 and ε^2 respectively, the effective fine-structure constant can be tuned and the new value is given by

$$\alpha_g^* = \frac{2e^2}{(\varepsilon^1 + \varepsilon^2)\hbar v_F} \qquad (6.2)$$

6.2 Experimental technique and data analysis

In this work, real part of the optical conductivity, $\sigma_1(\omega)$ of monolayer graphene has been extracted from measured ellipsometric parameters ψ and Δ. The energy range of measurement is 0.5- 5.3 eV.

6.2.1 Sample preparation and characterization

The details of samples preparation are explained in section 3.3.2 of this thesis in detail. Basically we use (monolayer) graphene samples prepared by CVD method on Cu foil asreported by Li et al. [24] for this study. For measurement of graphene on quartz substrate the transfer is performed (Section 3.3.2) using the three step process [27]. The graphene layer is placed on the substrate as shown schematically in fig. 3.12. The Raman

spectra (Figure 6.1) shows strong monolayer characteristic with negligible defect contributions [153]. This confirms high quality of the graphene samples prepared.

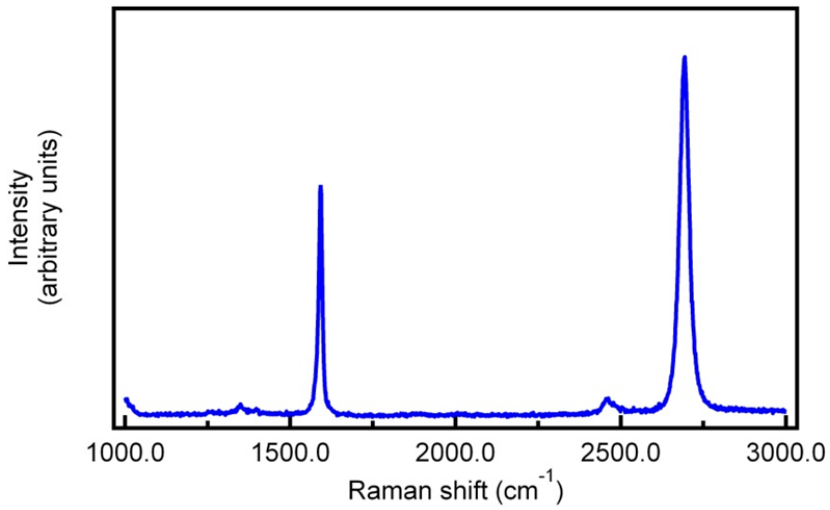

Figure 6.1 Raman Spectra of graphene on quartz with 514.5 nm laser [61].

From the same piece of copper foil with graphene (used for transfer to quartz substrate) 5 mm X 5 mm pieces are cut with a sharp blade. Half of those are treated with oxygen argon plasma to remove the graphene layers from their top. Generally in ambient condition copper is always covered with native oxides CuO and Cu_2O [174]. In our case treatment in oxygen environment has augmented the process of dominance of CuO with negligible presence of Cu_2O. (Also later, fitting procedure shows that the measured data requires only CuO contribution to fit with no contribution from Cu_2O to further confirm this.). The plasma-treated Cu foils are kept in ultrasonic bath for 30 minutes submerged in ethanol to remove the unwanted oxide layer of CuO from its surface [174]. We observe some systematic increase in the pseudo-dieletric functions upon spectroscopic

ellipsometry measurement of the copper foil during ultra-sonification with saturation values for 30 minutes and beyond. Spectroscopic ellipsometry data of (Ψ, Δ) are taken on these copper foils as well as on those with graphene on top. Graphene was grown on pure and clean copper. The dielectric function of pure copper is extracted by fitting the (Ψ,Δ) simultaneously (explained in following sections) with a multilayer model of a thin layer CuO (which remains even after ultrasonication in ethanol) on top of pure copper. This is later used for fitting of the (Ψ,Δ) data measured on graphene on top of copper.

6.2.2 Measurement and data analysis

The spectroscopic ellipsometer set up available in the laboratory [explained in section 3.1.5] is used for the measurements. We report data in the range from 0.5 – 5.3 eV.

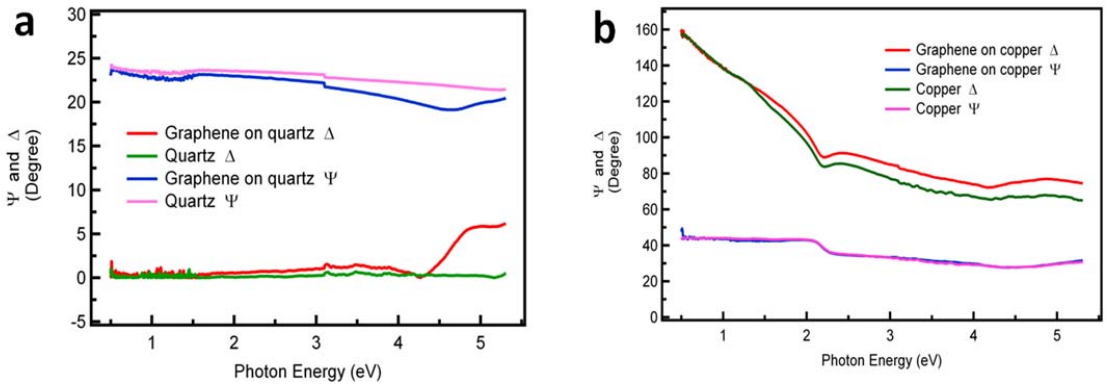

Figure 6.2: (a) Δ and ψ plots of graphene on quartz (GOQ) and pure quartz taken using spectroscopic ellipsometer at 70 degree incident angle. (b) Δ and ψ plots of graphene on copper (GOC) and copper foil taken using spectroscopic ellipsometer at 70 degree incident angle [61].

Spectroscopic ellipsometric data (Ψ, Δ) are taken at multiple incident angles and at several spots on the samples. The data at different spots are identical in almost all cases which show sample homogeneity. The multiple incident angle data is used for global fitting of data. In Figure 6.2 we show the measured (Ψ, Δ) values of samples with graphene and without graphene on substrate (quartz and copper respectively) at 70^0 incident angle. The spectra show the pronounced contrast due to the presence of graphene which is only ~3 angstrom thick. It may be mentioned that the copper (Ψ, Δ) plotted in Figure 6.2(b) also contain contribution from oxide layer on top.

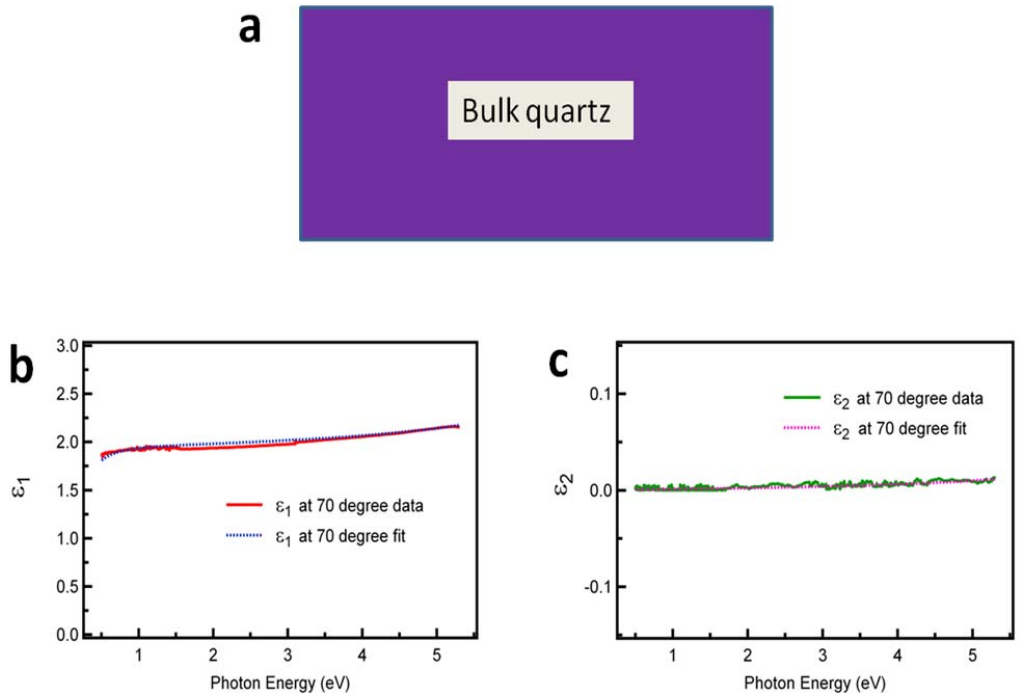

Figure 6.3: (a) Bulk substrate model for quartz. (b) Fitting of ε_1 at 70^0 incident angle for quartz. (c) Fitting of ε_2 at 70^0 incident angle for quartz [61].

Data analysis and fitting are performed using Reffit software as explained in detail in Chapter 4 (Sections 4.1-4.3). The graphene layer has been assumed to be flat and isotropic [158, 175]. Graphite is known to be uniaxial with out of plane ε_1 ~2.35 (for ≤ ~5 eV) which is lower than the in plane value and $\varepsilon_2 = 0$ ((for ≤ ~5 eV) [176]. As graphene is a single layer of graphite, the effect of c-axis anisotropy in graphene depends on the path length of the penetrating light. However as monolayer graphene is extremely thin the effect of such anisotropy is very small. Only in-plane contributions finally contribute almost fully to the optical conductivity. Our method of using isotropic model is in line of similar recent spectroscopic ellipsometric reports on graphene [158, 175]. However there has been report of use of uniaxial model also for graphene incorporating a Cauchy response for the c-axis [58].

We have used global fitting with simultaneous fitting of data for two incident angles (60^0 and 70^0 degrees) both for graphene on quartz and for graphene on copper to get the unique dielectric functions. The fitting is performed using Drude-Lorentz oscillator models in all cases.

Figure 6.3 above shows the plots of fitting for the ε_1 and ε_2 values found from the direct conversion of the Ψ and Δ values measured on the bulk quartz substrate. In all subsequent fittings multilayer models have to be used due to the presence of thin layers on top of the substrate- in which case the direct numerical inversion is not straightforward. Figure 6.4 shows the final (Ψ, Δ) fitting for the case of graphene on quartz (GOQ). From this fit the resultant dielectric function (ε) gives the optical conductivity $\sigma_1(\omega)$ as shown in Figure 6.8.

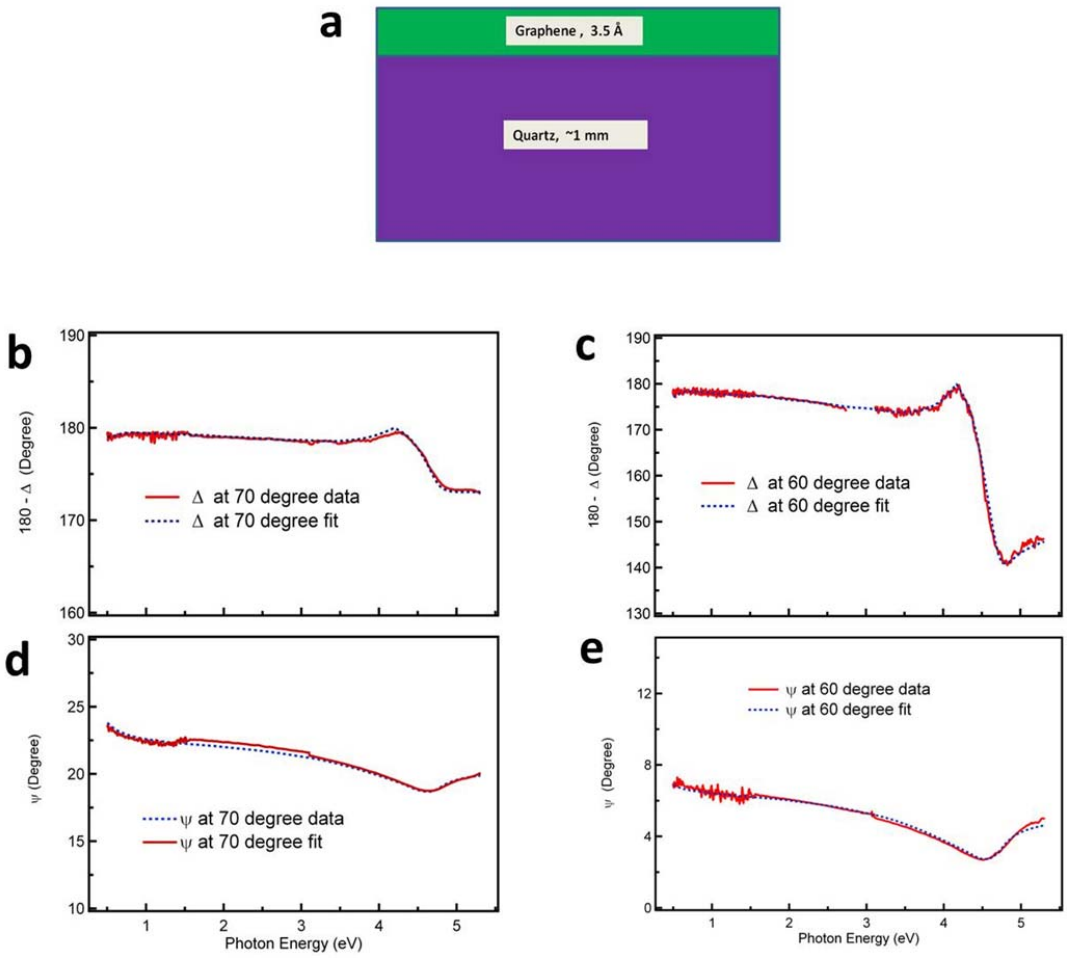

Figure 6.4: (a) Multilayer model for graphene on quartz (GOQ). (b) Fitting of Δ at 70^0 incident angle for graphene on quartz (GOQ). (c) Fitting of Δ at $60^0$for graphene on quartz (GOQ). The data around 3.2 eV are not reliable here due to the detector sensitivity issues. Therefore not shown from ~2.6 to 3.3 eV. (d) Fitting of ψ at 70^0 for graphene on quartz (GOQ). (e) Fitting of ψ at $60^0$for graphene on quartz (GOQ) [61].

To extract the $\sigma_1(\omega)$ of graphene layer on copper (GOC) we proceed similarly as in case of GOQ above. But here we have to extract the pure copper dielectric function first using the multilayer model for the copper substrate itself due to the presence of CuO layer. For

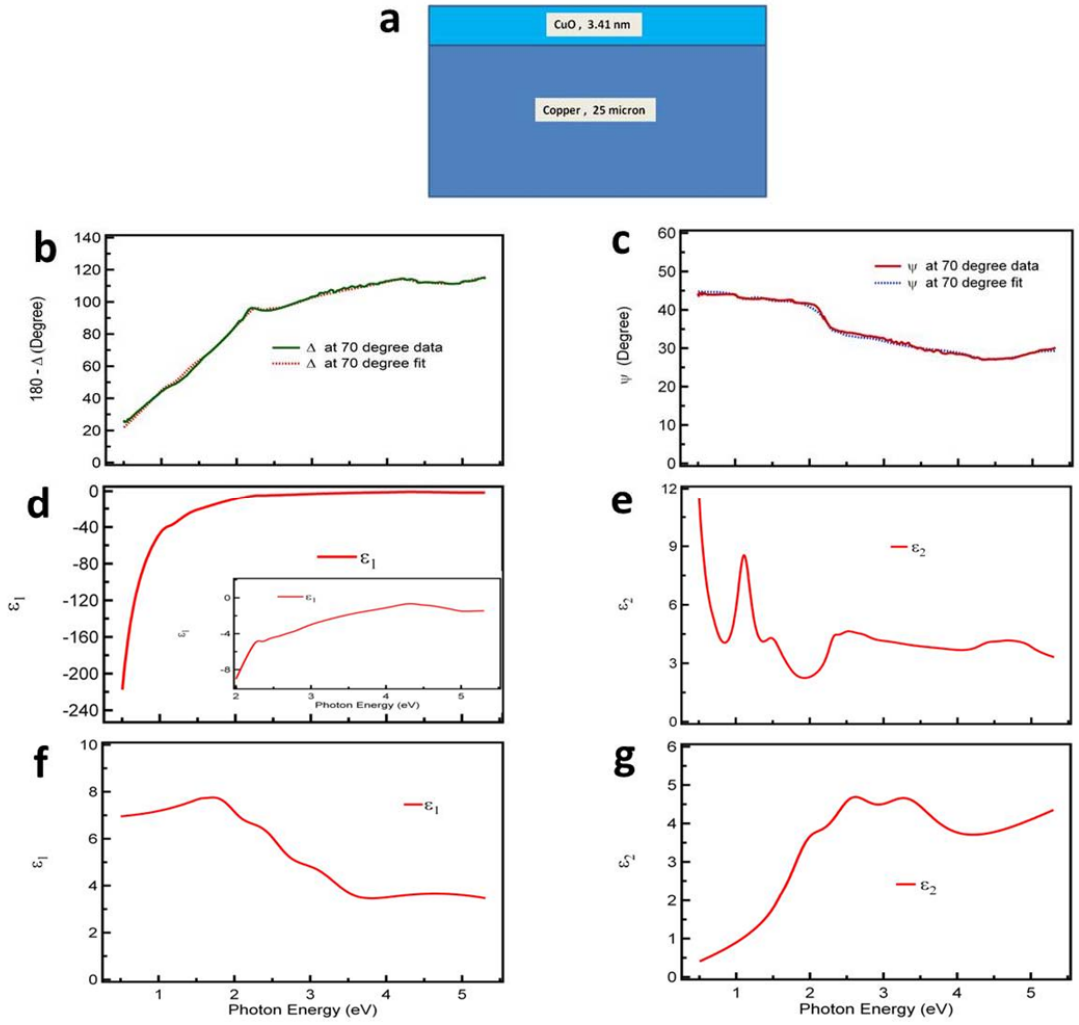

Figure 6.5: (a) Multilayer model of CuO on copper. (b) Fitting of Δ at 70^0 for copper. (c) Fitting of ψ at 70^0 for copper . (d) Extracted ε_1 for copper. (e) Extracted ε_2 for copper. (f) Extracted ε_1 for CuO. (g) Extracted ε_2 for CuO [61].

the dielectric function used for CuO we find that we can use the same oscillator positions as used by Ito et al. (1-5 eV) [177] with slightly different strengths but with similar overall final structure. The oscillators are listed in Table 1 below. In fact Palik et al. [178] has reported dielectric function for CuO which varies even more than reported by

Ito et al.. Differences in crystal structure, growth conditions and surface coverage may be the reasons for these variations. We get the best fit for our data using the results shown in Figure 6.5(f) and 6(g). Similarly our copper dielectric function result shown in Figure 6.5(e) and 6.5(f) is similar in structure to reported values [178, 179].

Serial number	W_0 (in cm^{-1})	W_p (in cm^{-1})	γ (in cm^{-1})
1	12900	907.22	1231.2
2	16120	11490	5572.3
3	20900	16783	6770.9
4	27000	21737	9214.5
5	64922	141240	61406

Table 6.1: Drude-Lorentz parameters for dielectric function of CuO. The parameters W_0, W_p and γ are the transverse frequency (eigenfrequency), the 'plasma' frequency and the linewidth (scattering rate) respectively [155].

It has to be mentioned that CuO surface layer is only used for modeling the ellipsometric data (Ψ, Δ) for copper foil (without graphene) measured in the ambient. From this analysis we extract the pure copper dielectric function. Subsequently this pure copper dielectric function is used for fitting (Ψ, Δ) data for graphene on copper (GOC). During a typical CVD growth of graphene, a high-temperature hydrogen annealing step is used to remove the surface oxide on copper. The formation of graphene on the copper protects the copper surface from re-oxidation thereafter. Hence we have only used a two layer system consisting of graphene layer on pure copper (without any CuO layer in between) for the fitting of (Ψ, Δ) data for GOC.

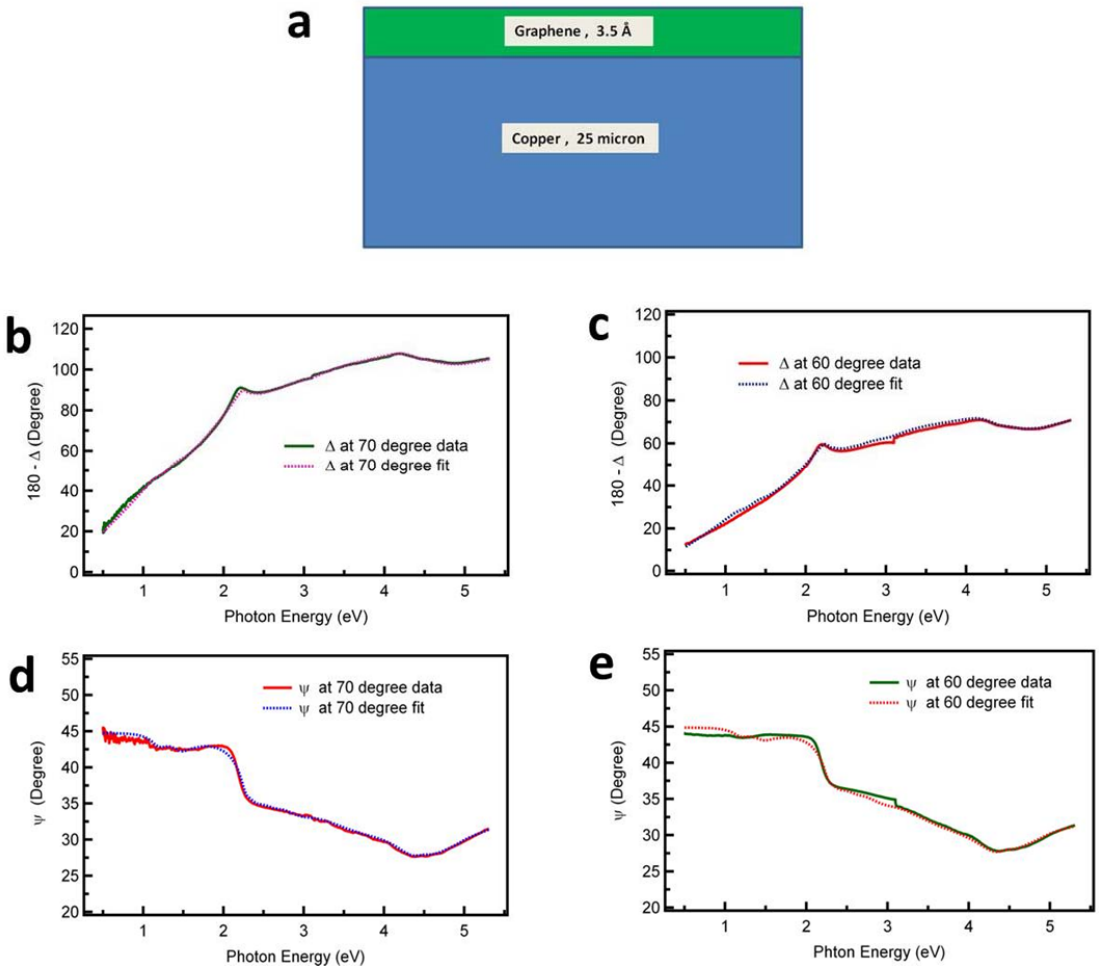

Figure 6.6: (a) Multilayer model of graphene on copper (GOC) (b) Fitting of Δ at 70^0 incident angle for graphene on copper (GOC). (c) Fitting of Δ at $60^0$for graphene on copper (GOC). (d) Fitting of ψ at 70^0 for graphene on copper (GOC). (e) Fitting of ψ at 60^0 for graphene on copper (GOC) [61].

Figure 6.6 above show the result of fitting of (Ψ, Δ) data for GOC. The extracted σ_1 (ω) for the graphene layer on copper is plotted in Figure 6.7.

6.4 Results and discussions

In Figure 6.7 below $\sigma_1(\omega)$ for the graphene layer for both GOQ and GOC have been plotted after extraction from fitting as explained in detail in the previous section. It is seen that $\sigma_1(\omega)$ of the graphene layer on quartz (GOQ) (shown in red) has behaviour akin to exfoliated monolayer graphene in different regions of the energy range of measurement. Beyond the infrared range ($\omega > 1.5$ eV) $\sigma_1(\omega)$ starts gradually increasing from the constant value $(\frac{\pi e^2}{2h})$. It may be mentioned that our observed constant value is consistent with other CVD grown graphene [180] which is slightly less than the universal value observed in case of pristine exfoliated graphene [56,59,60].

A prominent asymmetric peak in $\sigma_1(\omega)$ is observed at 4.6 eV which can be attributed to excitonic effects in the optical transitions at the M point in the Brillouin zone of graphene. This peak is a result of the interplay between interband transitions, e-e and e-h interactions [57]. If one considers only band to band transitions using local density approximation (LDA) approach the optical transition peak should occur at ~4.1 eV. By inclusion of the e-e interactions through GW approach the optical transition peak is predicted at 5.2 eV. By further incorporating the e-h interaction the optical transition peak is predicted to be red shifted by ~600 meV from 5.2 eV to 4.6 eV [57].

As shown in Figure 6.7(a), the most important observation of this study is that graphene on copper substrate (GOC, shown in black) has distinctively different trend of $\sigma_1(\omega)$ at the ultraviolet range. The peak for optical transitions for GOC is blue shifted to 4.96 eV

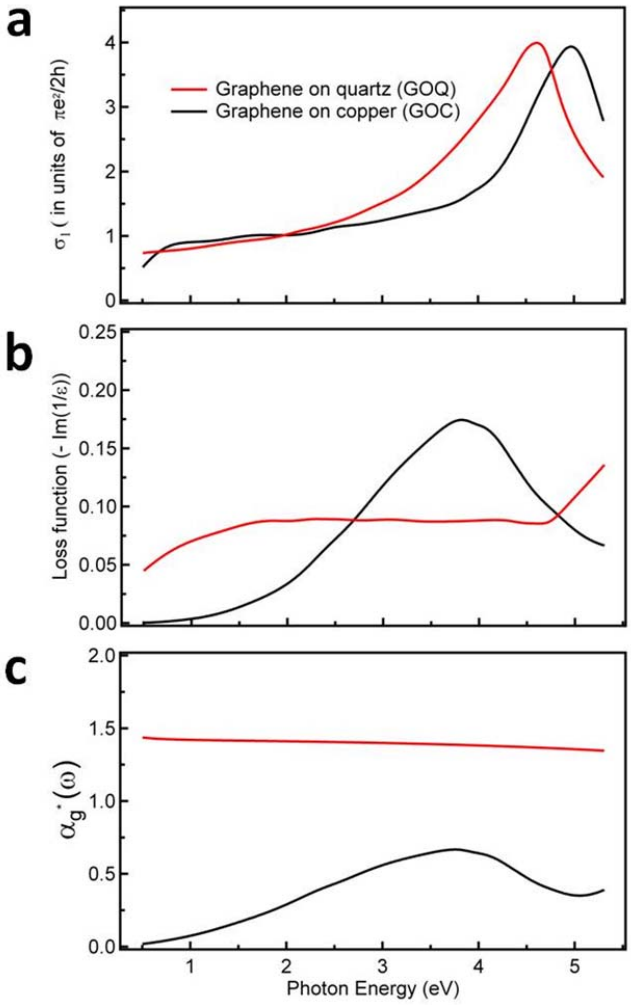

Figure 6.7: (a) Real part of optical conductivity, $\sigma_1(\omega)$ of graphene on quartz (graphene on copper) shown in red (black). (b) Loss function of graphene on quartz (graphene on copper) shown in red (black). (c) Energy dependence of effective fine structure constant, α_g^*, of graphene on quartz (graphene on copper) shown in red (black) [61].

compared to 4.60 eV as found in GOQ. Interestingly the line-shape of $\sigma_1(\omega)$ for GOC is symmetric unlike the line shape of $\sigma_1(\omega)$ for GOQ which possesses asymmetric profile.

These two aspects – red-shift of the optical transition peak and symmetric line-shape - are the key signatures of the different roles played by e-e and e-h interactions.

Figure 6.7(b) shows the Loss function ($-Im(1/\varepsilon)$) for both GOQ and GOC. We do not see any structure for GOQ at 4.6 eV as seen in $\sigma_1\,(\omega)$. This is an evidence of the absence of plasmonic contribution to the peak in $\sigma_1\,(\omega)$ at 4.6 eV. For GOC we observe a broad structure centered at 3.9 eV which may be attributed to plasmonic excitations. However this is far below the peak seen for $\sigma_1\,(\omega)$ at 4.96 eV. This again rules out plasmonic contribution.

This asymmetric line-shape of the $\sigma_1\,(\omega)$ can be interpreted using a phenomenological approach proposed by Fano [118-121], which takes into account e-h interactions. In Fano theory discrete excitonic states residing below an electronic continuum couple with the continuum states giving rise to considerable asymmetry in the optical transition strengths near a saddle point singularity. We fit our experimental data using Fano interference analysis by employing a phenomenological relationship where a dominant excitonic state is coupling with the continuum [119-121]. Figure 6.8 shows a detailed Fano analysis on the $\sigma_1\,(\omega)$ data for GOQ and GOC. The details of the Fano analysis is explained in section 4.5 of this thesis. For our data for GOQ in equation *(4.35)* we have used

$$\sigma_{1,cont}(\omega) = (-1.7)\,\log|1-\omega/\omega_0| + 0.68 \qquad (6.3)$$

giving the best fit for our data.

Similarly for our data for GOC we have used

$$\sigma_{1,cont}(\omega) = (-1.7)\,\log|1-\omega/\omega_0| + 0.76 \qquad (6.4)$$

giving the best fit for our data.

This unperturbed $\sigma_{cont}(\omega)$ is convoluted with a Gaussian of width 380 meV to account for the experimental broadening. The background constant values of 0.68 and 0.76 respectively for GOQ and GOC are added to account for the constant $\sigma_1(\omega)$ in the infrared and visible energy range (universal constant $\sigma_1(\omega)$ for the ideal graphene).

The results of the Fano fitting of $\sigma_1(\omega)$ for GOQ are plotted in Fig 6.8(a). The Fano parameters for GOQ are q = -1.16, Γ = 0.99 eV and $E_{res} = 4.90$ eV. These numbers are comparable to the reported values for exfoliated graphene . Particularly the large value Γ signifies a short life-time (~0.34 fs). Similar extremely short life-time has been inferred from reflectivity measurements on exfoliated graphene [59]. These lifetimes are far smaller than in case of conventional excitons (Frenkel and Wannier excitons). The resonant character as well as extremely short life-times need further studies to be elucidated in depth and clarity. The peak position and asymmetry of $\sigma_1(\omega)$ of GOQ can be fitted reasonably well using this approach. The slight mismatch at 1.5 – 3 eV may be due to inherent quality issues of CVD graphene. CVD graphene is known to be polycrystalline due to its growth on metals (Cu, Ni etc) which have polycrystalline grains. The most decisive factor in the reduction of the optical conductivity (particularly for this energy range) may be the preferential reduction of π electron density as observed in case of polycrystalline graphite [181]. Moreover using transmission measurements the absorption in the whole range in consideration here for similar CVD graphene has been reported [180] to be less than the predicted values [57]. On the other hand above 5 eV

the match discrepancy can be attributed to the use of unperturbed band to band transition result instead of exact GW result [59] as the starting point. Overall the reasonable fitting to Fano model signifies the presence of prominent excitonic effects in our graphene sample, GOQ.

On the contrary the peak position of $\sigma_1(\omega)$ for GOC is at 4.96 eV and with Fano parameters of q = -0.96, Γ = 0.98 eV and $E_{res} = 5.19$ eV we can account for the redshift from the unperturbed peak at 5.2 eV but the distinctively symmetric shape of our result cannot be fitted with this model as seen from Figure 6.8(b). Therefore it signifies the very weak strength, if any, of excitonic contribution in this redshift [121]. This further indicates strong screening of e-h interactions in GOC.

More generally screening effects can be quantified by analyzing the α_g^*. In figure 6.7(c) we show $\alpha_g^*(\omega)$ for GOQ and GOC. Here we find that for GOQ, $\alpha_g^*(\omega)$ has a value of 1.37 at 4.6 eV and it does not vary by more than 5% in the energy range of our interest (0.5- 5.3 eV). This dynamic $\alpha_g^*(\omega)$ is greater than the static $\alpha_g^*(\omega = 0)$= 0.81 which is regularly used to describe correlations in graphene (on quartz or SiO_2/Si substrate). This indicates that the dynamical screening in GOQ is weak and so the system can be categorized as a strongly interacting system for this energy range. In the case of GOC α_g^* at 4.96 eV is ~0.36. It is interesting to note that in contrast to GOQ, α_g^* varies from 0.02 to 0.67 in the energy range of 0.5 – 5.3 eV for GOC. This basically means that the dynamic screening is stronger than in the case of GOQ as indicated by the lower value of

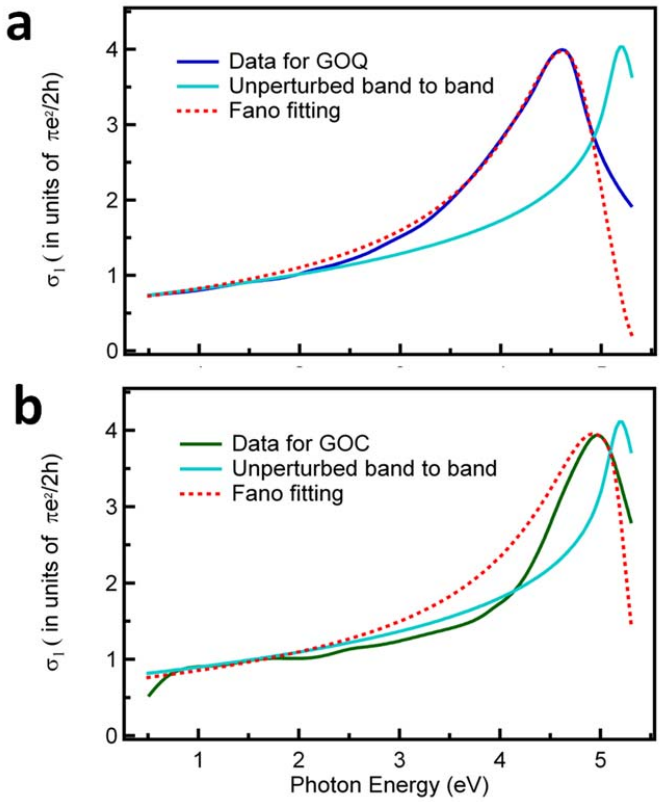

Figure 6.8: Fano line-shape analysis (a) for GOQ and (b) for GOC. Fit of GOQ and GOC experimental $\sigma_1(\omega)$ are shown in red dashed lines. The $\sigma_{cont}(\omega)$ is taken as the unperturbed band to band transition shown in cyan. (See section 4.5 for details of Fano line-shape analysis.) [61]

$\alpha_g^*(\omega)$. These results suggest that GOC is a weakly interacting system in comparison to GOQ.

The plasma frequency of Cu is known to be above 5 eV. Ordal *et al.* [185] reported it to be 7.389 eV, Zeman *et al.* [186] reported it to be 8.76 eV while Ehrenreich *et al.* [179] reported it to be ~7.5 eV etc. Our experimental range is till 5.2 eV. Therefore we cannot

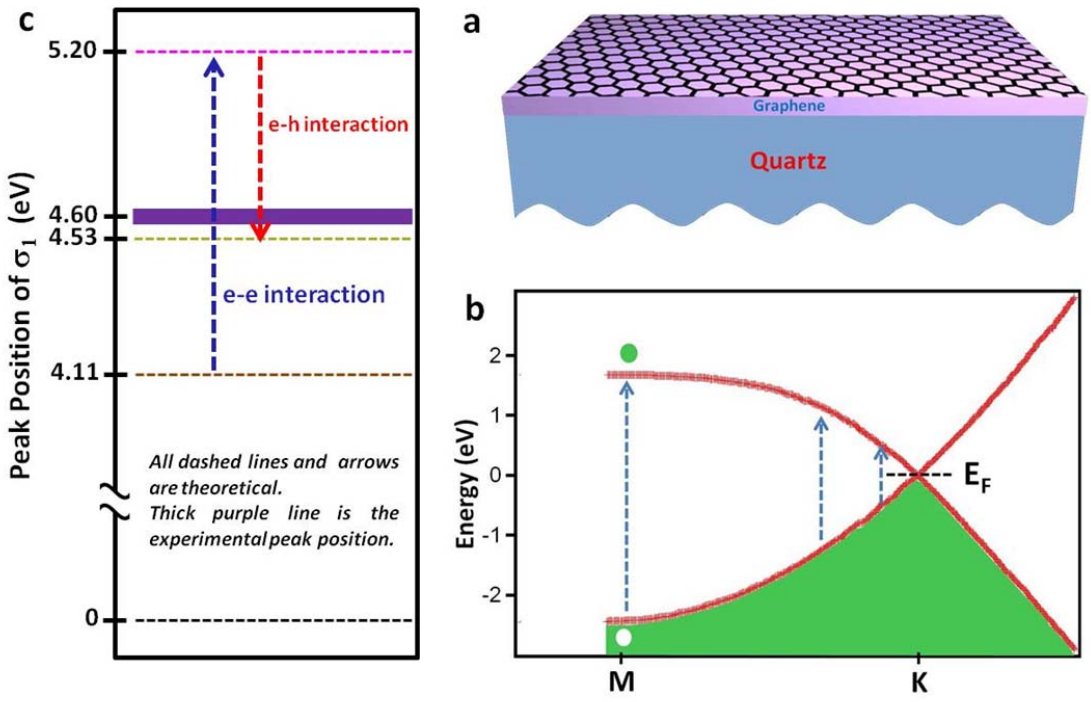

Figure 6.9: (a) Cartoon of graphene on quartz substrate (GOQ). (b) Schematic band diagram from Density functional theory (DFT) of graphene on quartz (GOQ) assuming no doping as in free-standing case. Possible optical transitions are shown where all states above the Dirac point are accessible. (c) Schematic energy values that represent the peak position in the optical transitions for GOQ. All dashed lines and arrows are representing theoretical predictions. The brown dashed line (----) at 4.11 eV represents the result from local density approximation (LDA) theory [94] which accounts only for band to band transitions. The pink dashed line (---) at 5.20 eV represents the result from GW calculations which takes into account many-body electron –electron (e-e) interactions [94]. The blue arrow (→) indicates the difference in energy of GW from LDA calculations. The green dashed line (---) at 4.53 eV represents the energy value predicted by GW- Bethe Salpeter Equation (GW-BSE) approach which includes also the electron – hole (e-h) interactions [94]. The red arrow (→) indicates the energy difference between GW and GWBSE calculations which is the contribution only from e-h interactions. The thick purple line (—) at 4.60 eV is representing the asymmetric peak position in our experimental result described in text for GOQ. The thickness is proportional to the error bar which is affected mostly by the fitting procedure. The closeness of our result with the GWBSE prediction indicates the presence of both e-e and e-h interactions in GOQ [94].

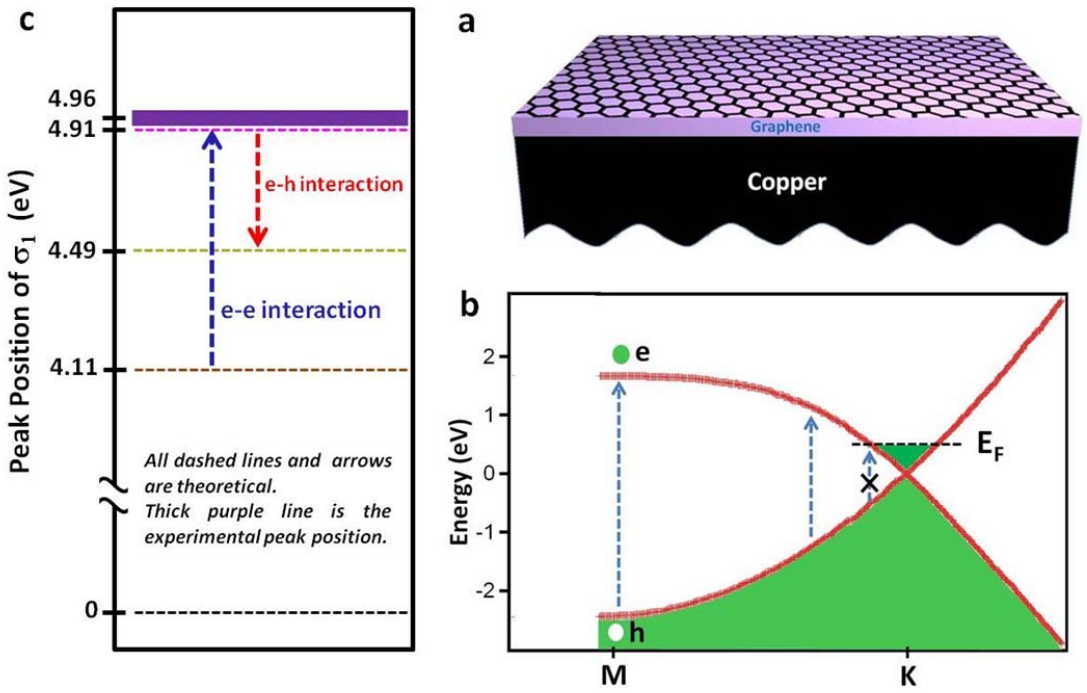

Figure 6.10: (a) Cartoon of graphene on copper substrate (GOC). (b) Schematic band diagram from Density functional theory (DFT) of graphene on copper (GOC) assuming considerable electron doping based on DFT calculations [127]. Possible transitions are shown with cyan arrows (→) to states above the Fermi level. States below the Fermi level but above the Dirac point are not accessible (represented by crossed cyan arrow). (c) Schematic energy values that represent the peak positions in the optical transitions for GOC. All dashed lines and arrows are representing theoretical predictions where electron doped graphene (0.01 electrons per unit cell of graphene) is considered. The brown dashed line (----) at 4.11 eV represents the result from local density approximation (LDA) theory which accounts only for band to band transitions [94]. The pink dashed line (---) at 4.91eV represents the result from GW calculations which takes into account many-body e-e interactions [94]. The blue arrow (→) indicates the difference in energy of GW from LDA calculations. The green dashed line (---) at 4.49 eV represents the energy value predicted by GW- Bethe Salpeter Equation (GW-BSE) approach which includes also the e-h interactions [94]. The red arrow (→) indicates the energy difference between GW and GWBSE calculations which is the contribution only from e-h interactions. The thick purple line (—) at 4.96 eV is representing the symmetric peak position in $\sigma_1(\omega)$ of our experimental result described in text for GOC. The thickness is proportional to the error bar which is affected mostly by fitting procedure. The fact that our experimental peak position is close to GW prediction indicates that e-h interactions are screened almost fully [61].

probe the plasma frequency region. However we do use a Drude term with plasma frequency of 7.56 eV for pure copper to model our data of the substrate (in the ambient) for best fit. Later on this same dielectric function model is used for fitting the data of graphene on copper (where the optical model is – graphene on pure copper).

In Figures 6.9 and 6.10 we present schematic energy diagrams and optical transition levels in order to explain the observed optical conductivity and possible scenarios for both GOQ and GOC respectively. For GOQ, $\sigma_1(\omega)$ peak is at 4.6 eV and it can be explained with the existence of both e-e and e-h interactions which are well supported by theoretical model [57]. This suggests that the interactions between graphene and the substrate are weak and the graphene layer behaves almost like free-standing graphene.

For GOC, $\sigma_1(\omega)$ peak is at 4.96 eV and this 360 meV blue shift (from the GOQ peak) is considerably large. This may involve two processes- firstly considerable electron transfer from the metal substrate [127] giving rise to electron doping influencing the optical conductivity [94] and secondly hybridization of graphene bands with that of substrate (copper) bands [126] which also will affect the optical conductivity. Theoretically, for graphene deposited on metal (like Cu, Ni) [127] the Fermi level shifts considerably depending on the work function of the metal as well as the separation between the metal substrate and the graphene layer. For our case, graphene is grown on copper without any other layer in between with a gap of ~ 0.3nm. This electron doping screens the e-h interactions while e-e interactions are dominant. The scenario depicted in

Figure 6.10 is from predictions using DFT calculations of a Fermi level shift of 0.5 eV above the Dirac point when graphene is in contact with copper substrate [127]. For the case of free standing doped graphene one would expect to see the excitonic peak at almost similar position like in GOQ at 4.49 eV [94] due to the presence of both e-e and e-h interactions even while doped.

Another noticeable aspect of our result is the absence of distinct signature of the coupling between the p_z orbital of the carbon atoms and d_{z^2} orbital of the copper atoms in the plots for $\sigma_1(\omega)$. Theoretical studies [126, 127] have predicted that metals can be broadly divided into two classes depending on the coupling strength of these orbitals. For example in case of graphene on nickel, graphene bandstructure is perturbed heavily due to strong coupling, whereas in case of graphene on copper (which belongs to the other class of metals) graphene still retains most of its intrinsic bandstructure features. However our result shows even smaller coupling in case of graphene on copper than predicted. Firstly we do not see any structure below 5 eV for the $\sigma_1(\omega)$. of GOC. This is in contrast to theoretical calculations which predicted presence of copper d_{z^2} bands at approximately 2 eV below the Fermi energy when the substrate is Cu (111) [126]. Secondly we do not see a Pauli blockade in $\sigma_1(\omega)$ for GOC at about 1 eV which translates into about 0.5 eV of Fermi level shift due to charge transfer. Rather we see a dip in the $\sigma_1(\omega)$ plot at about 0.5 eV which represents a Fermi level shift of less than 0.25 eV. These two aspects may be a signature of weak coupling between polycrystalline copper and graphene.

6.5 Conclusion

In conclusion, we observe that the dynamical screening in graphene on metallic substrate is stronger than in the case of graphene on quartz by as large as two orders of magnitude. We propose that the observed blue-shift in the peak position of optical conductivity at the van Hove singularity (at the M point) is the result of the fact that electron-electron interactions are still dominating but electron-hole interactions are strongly screened. Our result opens new paths to study the interplay of e-e and e-h interactions and their individual strengths in many-body physics. Furthermore it demonstrates the suitability of spectroscopic ellipsometry technique (along with theoretical calculations) to study the interactions in graphene interfaces.

Chapter 7

Ultraviolet transparency of graphene on $SrTiO_3$

Fano anti-resonance is often observed in the absorption spectra of materials which render the possibility of discrete excitonic states residing in a background continuum. Graphene, despite being a zero gap material, manifests prominent signatures of many-body effects in the form of excitonic Fano anti-resonance which redshifts its van Hove peak making it asymmetric. However in this work we report even a more dramatic renormalization of the optical conductivity of graphene making it almost fully transparent in the ultraviolet region due to excitonic Fano anti-resonance at a much lower energy (3.94 eV) where the excitons reside between graphene conduction bands and new hybridized valence bands originating from carbon p_z-orbital of graphene and oxygen p_z-orbital of $SrTiO_3$. Moreover its faster auto-ionization rate than the saddle point exciton is the signature of increased screening by the substrate. Ultrafast differential reflectance measurements and density functional theory calculations also indicate hybridization as well as give the positions of low lying substrate conductions bands and support the role of direct transitions from intrinsic graphene bands to these new bands which augments the optical conductivity further below the resonance energy.

My contributions in this work are in planning the experiment, sample preparation and characterization, data taking and analysis. Optical pum-probe experiments as well as data analysis thereof are performed together with Dr. Chan La-O-Vorakiat and Prof. Elbert E. M. Chia of Nanyang Technological University (NTU) in close collaboration. Dr. Ming Yang and Prof. Yuan Ping Feng from NUS performed the DFT calculations in collaboration.

7.1 Introduction and motivation

Graphene is two dimensional (2D) and the thinnest material known to be successfully isolated [1,2]. It is remarkable that the 2D structure as well as relatively straightforward transfer process to various substrates make it possible to manipulate the dielectric environment to finally control the correlation strengths in graphene [19,61,93,125]. Also

graphene is essentially an interface itself when we put it on a substrate unlike the case of putting together two dissimilar bulk materials where there can be reasonable distinction of bulk-interface-bulk regions. Till now the real part of the optical conductivity (σ_1) of graphene has been almost always measured either on substrates which have large band gaps (~9 eV; quartz, SiO_2/Si etc) or when freestanding [56, 58-61]. In this scenario because of the limitation of the energy range one can only probe that range of the band-structure which is intrinsically graphene-like because the substrate valence and conduction bands are energetically far away in the momentum space (or inevitably only the graphene bands in the case when it is freestanding). On the contrary when graphene is on an insulating substrate whose band-gap is intermediate (< 4 eV approximately) we can expect to see various interesting and novel effects due to the possible hybridization and also due to other processes in presence of energetically similar graphene bands as well as substrate valence and conduction bands.

This work shows evidence of striking new phenomena in the graphene layer due to substrate interaction when graphene is on $SrTiO_3$, which has a band gap ~3.2 eV, in the form of sustaining new excitonic states which lead to Fano anti-resonance and as a result makes graphene nearly transparent in the ultraviolet (UV) region. This is remarkable from the point of view of new optical phenomena in the graphene-substrate interface which has not been explored much yet and also this could lead to novel functionalities with important application potentials in the near future.

It has to be mentioned that $SrTiO_3$ and its interfaces with other materials are exciting systems themselves and of tremendous current interest as have been revealed by many recent reports [188]. Hence combined with the extraordinary properties of graphene a graphene-$SrTiO_3$ interface could be further expected to be the host of intriguing new physical processes in general.

7.2 Experimental technique and data analysis

In this work we perform spectroscopic ellipsometry (SE) [141-144] and ultrafast differential reflectivity (UDR) [189] measurements on the graphene samples prepared by low pressure Chemical Vapour Deposition (CVD). Basically graphene is transferred to bulk $SrTiO_3$ (100) substrates as well as SiO_2 (271.5 nm)/Si substrates and these two different types of samples are used for measurement and compared.

7.2.1 Sample preparation

The sample preparation process using wet transfer method is described in detail in section

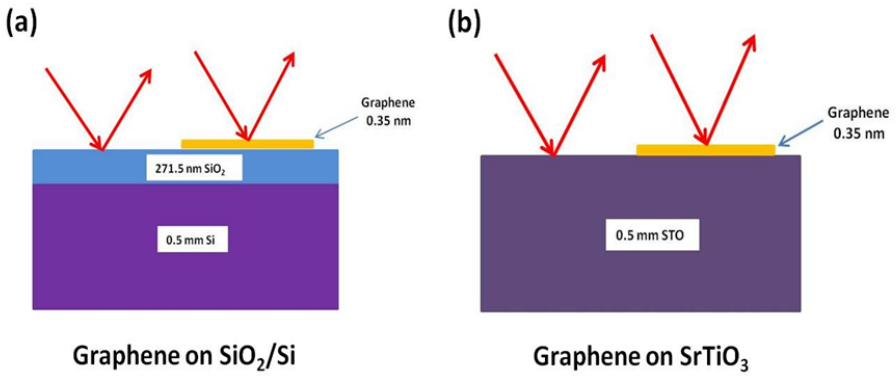

Figure 7.1: Schematic cross section of the graphene samples under study. The thicknesses are not to scale.

3.3 of this thesis. The graphene layers have been carefully positioned during transfer to the substrates such that they cover one side of the substrate as shown in Figure 7.1 below. This is to make sure that we get rid of the unwanted possible differences in optical parameters due to the use of different substrates (even when the material is same) as well as due to the fact that in this case both the substrate and the 'graphene on substrate' go through same treatment procedure which further reduces spurious contributions. This has been also explained in Section 3.3.2.1.

Raman measurement using a 514.5 nm laser performed on the graphene on SiO_2/Si sample shows distinct single layer characteristics [153] as well as negligible defects in the graphene layer as plotted in Fig. 3.13. Raman measurements performed on 'graphene

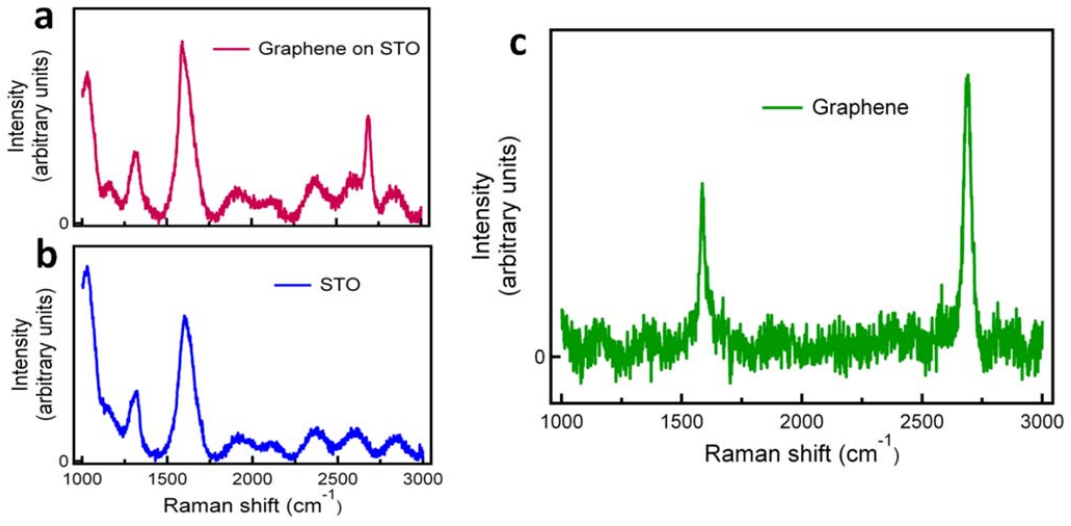

Figure 7.2 (a) Raman spectra of graphene on $SrTiO_3$ with 514.5 nm laser. (b) Raman spectra of $SrTiO_3$ with 514.5 nm laser. (c) (Normalized) Raman Spectra of only the graphene layer with 514.5 nm laser.

on $SrTiO_3$' and $SrTiO_3$ substrate part only are shown in Fig. 7.2 (a) and (b) respectively. Fig. 7.2 (c) shows the normalized Raman shift plot for the graphene layer only. This plot is obtained by subtracting the $SrTiO_3$ data from the 'graphene on $SrTiO_3$' data after normalizing the $SrTiO_3$ peak at 1616 cm^{-1} and the general background to same intensity for both.

The shape and relative intensities of G and 2D peaks in Fig. 7.2 (c) clearly show the single layer characteristics [153]. The noisy baseline is due to subtraction of comparable small numbers and as a result it is hard to resolve if there is any defect peak (D peak) present. However the defect contribution is known to be from the quality of graphene sample which is found to be with very negligible defect contribution from our Raman measurement of 'graphene on SiO_2/Si' as can be seen in Fig. 3.13. The same set of samples are used both for SE as well as UDR measurements.

7.2.2 Measurement and data analysis

SE measurements are performed as explained in detail in section 3.1 and also similarly as in other studies (Chapters 5,6,8) described in this thesis. The reliable data range is limited to 5.2 eV due to the limitation of the micro-focus probes. Here in this study we have reported data from 0.5 - 5.2 eV for all measurements.

The substrates used in this study – $SrTiO_3$ (100) and SiO_2/Si are homogeneous and isotropic and with atomically flat top surfaces. SE measurements of (Ψ, Δ) at different spots on the substrates are found to be identical for individual incident angles.

For modeling as well as extraction of optical parameters, (Ψ, Δ) measured at one spot for different incident angles are used. Use of simultaneous fitting of several incident angle data is crucial for the uniqueness of the final results. Figures 7.3 and 7.4 show the

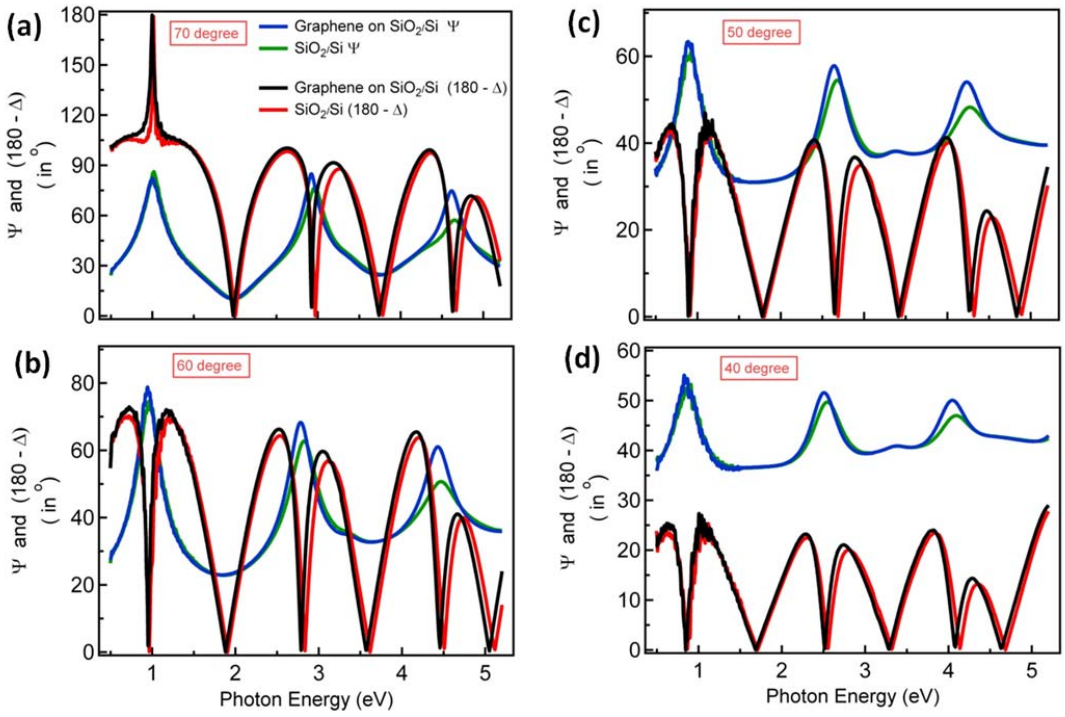

Figure 7.3 Comparison of Ψ,(180- Δ) data for 'graphene on SiO_2/Si' and only for SiO_2/Si for individual incident angles of (a) 70°, (b) 60°, (c) 50° and (d) 40°.

contrast when the graphene monolayer is resting on the SiO_2/Si and $SiTrO_3$ respectively. As can be seen, the contrast in (Ψ, Δ) measured by SE is considerable in almost all the angles. This further demonstrates the suitability of this technique (SE) for optical measurements of graphene on different substrates.

Multilayer modeling which takes into account reflections at each interface through Fresnel coefficients is used for simultaneous fitting of data measured at multiple incident angles. Graphical fitting of data has been performed using Reffit software [156] with

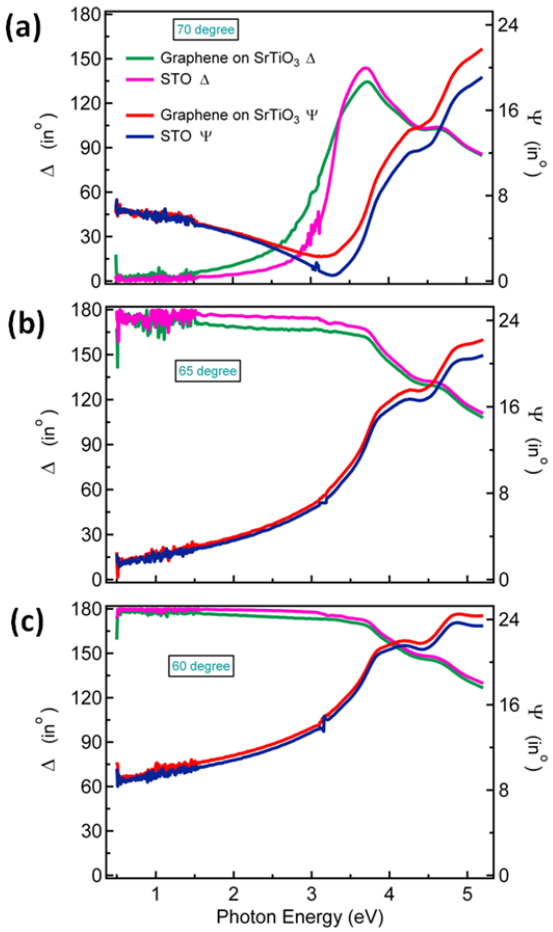

Figure 7.4 Comparison of (Ψ, Δ) data for 'graphene on $SrTiO_3$' and only for $SrTiO_3$ for individual incident angles (a) 70^o, (b) 65^o and (c) 60^o.

Drude- Lorentz oscillators as described in detail in Chapter 4. The graphene layer has been assumed to be flat and isotropic as reported in similar studies [158]. For 'graphene on SiO_2/Si' as well as for the substrate alone (SiO_2/Si) we have used 70^0, 60^0, 50^0, 40^0 incident angle data. For 'graphene on $SrTiO_3$' as well as the substrate alone ($SrTiO_3$) we have used 70^0, 65^0, 60^0 incident angle data.

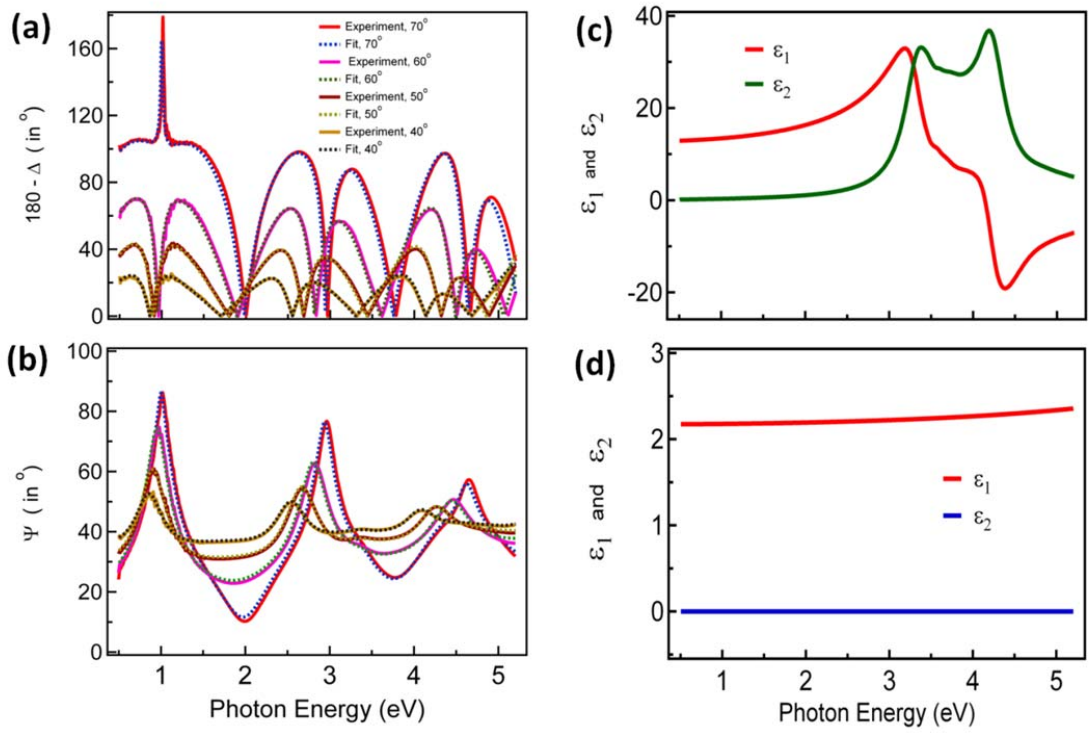

Figure 7.5 (a) (180 - Δ) data and fit for SiO_2/Si. (b) Ψ data and fit for SiO_2/Si. (c) Used values of (ε_1, ε_2) for Si layer after modeling of data from measurements of Si wafer not shown here. (d) Extracted (ε_1, ε_2) for the SiO_2 layer.

Fig. 7.5 (a) and (b) show the data and fit of 180-Δ and Ψ for SiO_2/Si respectively measured only on the substrate part (not covered with graphene) of the sample as shown

in Fig. 1 (a). Before this we have fitted measured values of (Ψ, Δ) on a silicon substrate to extract the (ε_1, ε_2) of Si which is plotted in Fig. 7.5(c). These (ε_1, ε_2) have been used to fit the (Ψ, Δ) for SiO_2/Si in turn in the present case. The extracted (ε_1, ε_2) of the SiO_2 layer have been shown in Fig. 7.5(d). This is similar to reported results [177] and expected of SiO_2 which is essentially transparent in the energy range of interest. The

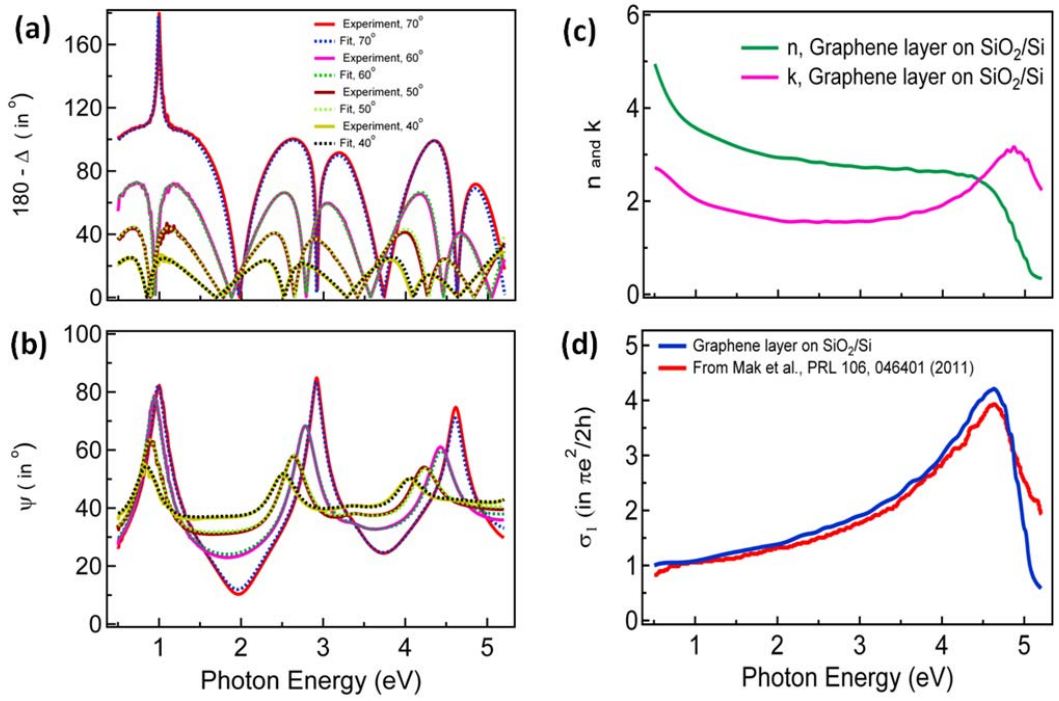

Figure 7.6 (a) (180 - Δ) data and fit for 'graphene on SiO_2/Si'. (b) Ψ data and fit for 'graphene on SiO_2/Si'. (c) Extracted (n, k) for graphene layer. (d) Extracted σ_1 for the graphene layer plotted with reported result from Mak et al. [59] measured on exfoliated graphene.

thickness of the SiO_2 layer is found to be 271.5 nm from the best fit (manufacturer's claim of thickness is 270 nm).

Figure 7.6 (a) and (b) above show the data and fit of 180- Δ and Ψ for graphene on SiO_2/Si measured on the graphene covered part of the substrate as shown in Fig 1(a). It may be mentioned that for the best fit we have to use a Cauchy layer of thickness 1 nm between graphene and the substrate similar to what has been reported by Kravets et al. [58]. The extracted (n, k) for the graphene layer is plotted in Fig 7.6 (c) which is similar

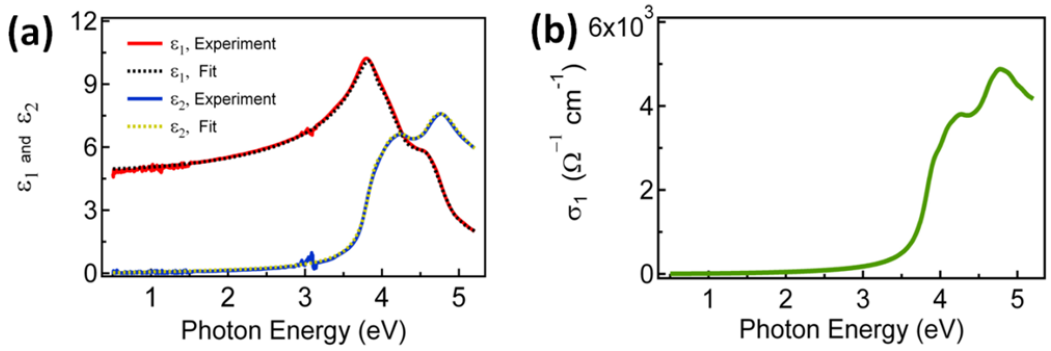

Figure 7.7 (a) Data and fit of (ε_1, ε_2) for $SrTiO_3$ substrate. **(b)** Extracted σ_1 (bulk) from the fit.

to many other reports on exfoliated as well as CVD graphene [58,158,175]. Fig 7.6 (d) shows the extracted σ_1 from our fitting and also the comparison with reported σ_1 for exfoliated graphene found using reflectivity measurements by Mak et al. [59]. The slightly higher value of σ_1 in our result may be attributed to the presence of some amount of bilayer areas (below 5%) in our CVD graphene (which is normally observed for CVD graphene [190]).

The $SrTiO_3$ (100) substrate has not been treated for any preferential termination [191]. So we expect both SrO and TiO terminations on the surface equally. The roughness of the

surface is found to be less than ~5Å by AFM measurements. This atomically flat substrate is reasonably modeled using a flat underlying substrate with graphene sitting on top in our analysis. The (Ψ, Δ) data measured on the substrate part of the sample as shown in Fig. 1(b) is directly converted to (ε_1, ε_2) which is possible for the case of a bulk substrate [141-144]. The (Ψ, Δ) measured for multiple incident angles give the same (ε_1,

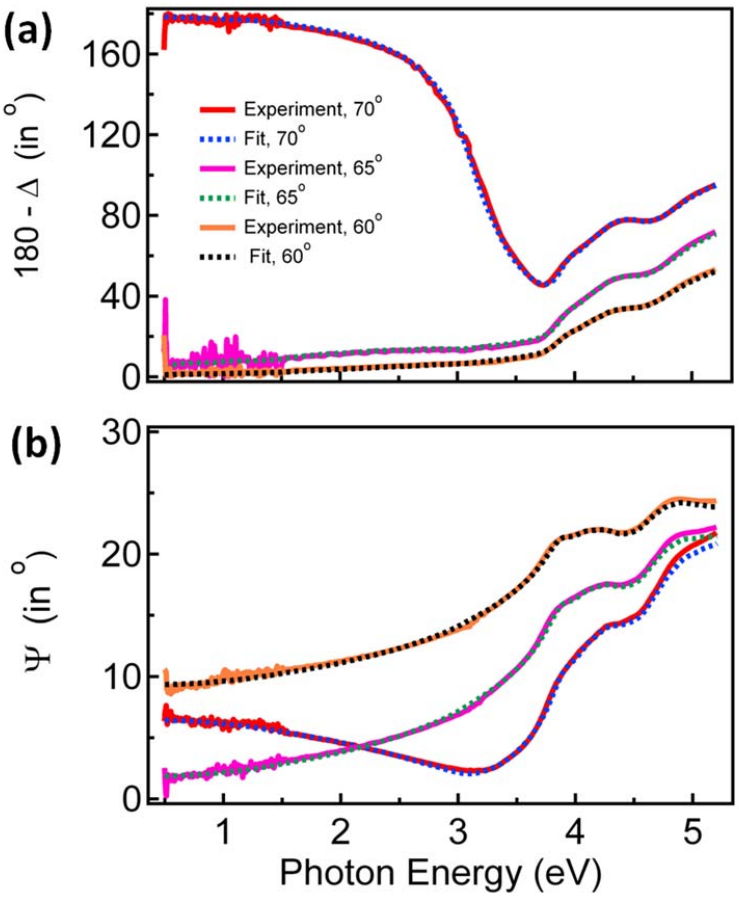

Figure 7.8 (a) (180 - Δ) data and fit for 'graphene on $SrTiO_3$'. (b) Ψ data and fit for 'graphene on $SrTiO_3$'.

ε_2) and therefore this (ε_1, ε_2) is used to model and extract the Drude-Lorentz oscillator parameters later to be used for further fitting of data measured on graphene layer supported on this substrate. Fig. 7.7(a) above shows this data and fit. From the model σ_1 (bulk) for $SrTiO_3$ is found to be as shown in Fig 7.7(b).

Fig. 7.8 above shows the (180- Δ) and Ψ data and fit respectively for 'graphene on $SrTiO_3$' . It may be mentioned that for the best fit a Cauchy layer of thickness 2 Å has to be used in this case in between graphene layer and $SrTiO_3$ substrate.

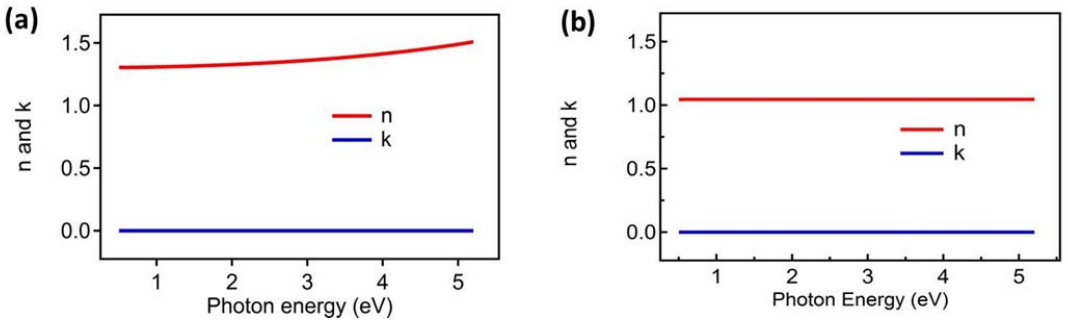

Figure 7.9 (a) Refractive index (n) and extinction coefficient (k) for the Cauchy layer in the case of graphene on SiO_2/Si. (b) Refractive index (n) and extinction coefficient (k) for the Cauchy layer in the case of graphene on $SrTiO_3$.

There has been report [192] of non-uniform coverage of water molecules underneath graphene on a substrate. The hydrophobic or hydrophilic nature of the substrate will also determine the amount of water molecules trapped. From our fitting it seems the contribution from water molecules could be larger in the case of graphene on SiO_2 as the refractive index of the Cauchy layer is (Fig. 7.9(a)) closer to water value for the visible

range. On the other hand the Cauchy layer for the graphene on $SrTiO_3$ case (Fig. 7.9(b)) seems to be coming mostly from air as the refractive index is close to 1. We have performed multiple incident angle data fit (at least 3 in each case) to account for the three unknowns- graphene (ε_1, ε_2) and Cauchy layer ε_1. It has to be mentioned that the Cauchy layer does not introduce any structure in the energy range of interest. Also we have used Drude –Lorentz oscillators for the Cauchy layer fit. Therefore we present the final fit results not in terms of explicit Cauchy form- whereas Drude-Lorentz representation is a better physical representation in general and desirable.

The extracted (n, k) and σ_1 are plotted in Fig. 7.10 and Fig. 7.11(b) respectively.

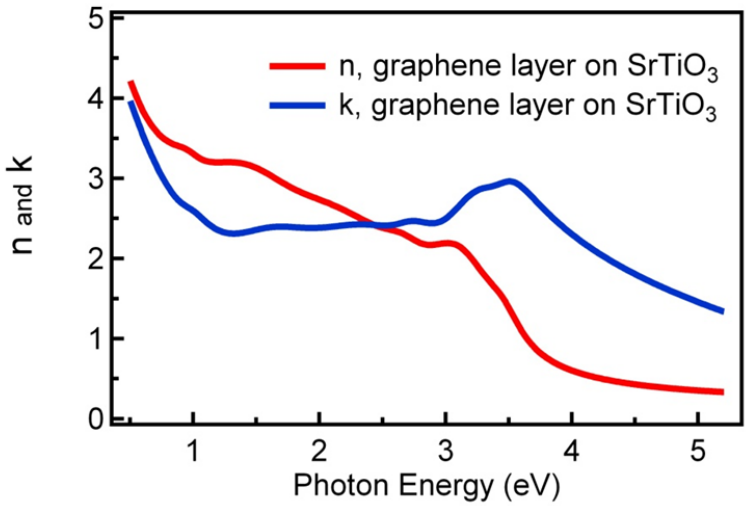

Figure 7.10: Extracted (n, k) for graphene layer (on $SrTiO_3$)

The experimental detail of the UDR measurements are explained in Appendix II. Here in this chapter we will only discuss the final results from these UDR measurements.

7.3 Results and discussions

Figure 7.3 show ψ and (180-Δ) for 'Graphene on SiO_2/Si' as well as for SiO_2/Si substrate alone for different incident angles. The changes in both ψ and (180-Δ) when the graphene layer is present are remarkably distinct; for example - the ψ values changing as much as by $\sim 20^0$ near 4.5 eV for 70^o incident angle data. Similarly, in case of 'graphene on $SrTiO_3$' we see large contrast particularly in the case of (180-Δ). For example in the case

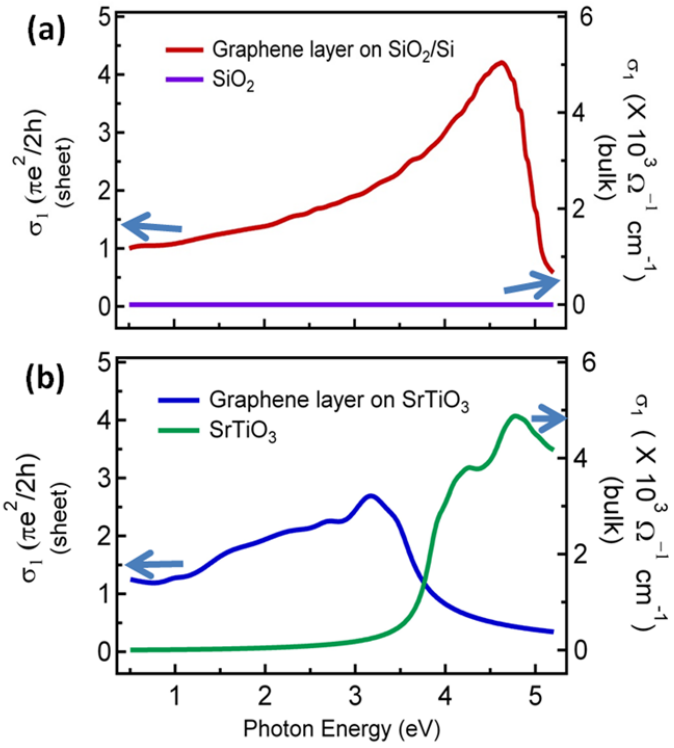

Figure 7.11 (a) Extracted sheet conductivity, σ_1 for graphene layer on SiO_2/Si and bulk conductivity, σ_1 of SiO_2 from fit**. (b)** Extracted sheet conductivity σ_1 for graphene layer on $SrTiO_3$ and bulk conductivity, σ_1 of $SrTiO_3$ from fit**.**

of 70^o incident angle data the (180-Δ) data for 'graphene on $SrTiO_3$' is higher in value than that of the $SrTiO_3$ substrate data below ~ 3.4 eV but considerably lower beyond that energy and gradually merging later on. For both the systems SE data are taken at multiple incident angles and fitted using Kramers –Kronigs compliant multiple Drude-Lorentz oscillators simultaneously. The extracted σ_1 (sheet) for the graphene layers in both cases are plotted in Figs. 7.11(a) and (b) which show some very remarkable differences explained next. The bulk optical conductivity of the substrates for each case is also plotted in Fig. 7.11. In Fig 7.11(a) it can be seen that there is no optical transitions in the substrate for this energy range. But as can be seen in Fig. 7.11(b) there are considerable optical transitions starting from ~3.5 eV.

In Fig 7.11(a), σ_1 for graphene layer on SiO_2/Si shows characteristic graphene features observed in case of exfoliated as well as CVD graphene on substrates like SiO_2/Si, quartz [58, 59, 61, 158, 175] and also in free standing graphene [56,60]. From 0.5 to ~1.5 eV the σ_1 is constant ($\pi e^2/2h$) which is attributed to the linear band-structure of graphene [19,57]. Beyond this range σ_1 starts to gradually increase and a prominent peak is observed at 4.6 eV. This peak is attributed to the optical transitions at the M point in Brillouin zone of graphene which has a Van Hove singularity. The asymmetric nature of the this peak and the red-shift from the position (5.2 eV) predicted by GW calculations which takes into account only e-e interactions are signatures of prominent excitonic effect present in graphene [57].

In case of graphene layer on $SrTiO_3$, as shown in Fig. 7.11(b), in contrast we see remarkably different σ_1 which has features very unlike that of graphene layer on SiO_2/Si or for that matter free standing graphene [56, 60]. The most dramatic change is the almost full quenching of σ_1 after a peak at ~3.2 eV. The next most important difference is the increase of σ_1 at lower energies (from 0.5 eV to ~ 3.2 eV). Also we observe some structures in this range whereas σ_1 for graphene layer on SiO_2/Si is found to be smoothly increasing gradually beyond ~1.5 eV.

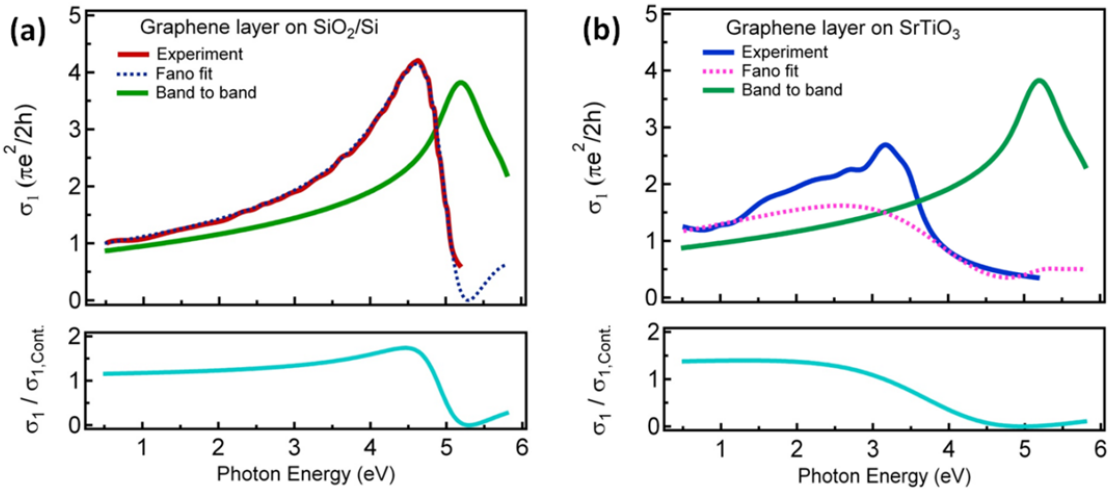

Figure 7.12 (a) Fano line-shape fitting for σ_1 of graphene layer on SiO_2/Si. **(b)** Fano line shape fitting for σ_1 of graphene layer on $SrTiO_3$. For both **(a)** and **(b)** the green curves represent the same σ_1 due to unperturbed band-to-band transitions (with a Gaussian broadening of 400 meV). The lower panels for both **(a)** and **(b)** show the respective Fano functions which are the ratios of the final σ_1 to the unperturbed band-to band σ_1 in each case.

Phenomenological Fano line-shape analysis beautifully captures the role of resonant excitonic effects in renormalizing graphene σ_1 giving it asymmetric shape and also in the red-shifting of the peak position [59,118-121] from the independent particle predictions. Furthermore it also provides insights into the position of the excitonic resonance energy as well as the auto-ionization time scales of the excitons. The essence of the Fano interference effect is that discrete auto-ionizing state(s) can couple with a continuum giving an asymmetric line shape to the final absorption with enhanced or reduced absorption below or above the resonance energy [189, 118-121]. The final σ_1 can be represented by equation *(4.34)*.

In Figure 7.12(a) we show the Fano line-shape analysis in the case of graphene layer on SiO_2/Si . We use a band to band $\sigma_{1,\mathrm{cont}}(\omega)$ of the form given by equation *(4.35)*.

	A	B	γ (eV)	ω_0 (eV)	q	Γ (eV)	ω_{res} (eV)	t_a (fs)
Graphene layer on SiO_2/Si	1.75	0.8	0.40	5.20	−0.86	0.83	4.94	0.44
Graphene layer on STO	1.75	0.8	0.40	5.20	−0.63	3.3	3.94	0.11

Table 7.1: Parameters used for estimation of unperturbed band –to- band $\sigma_{1,\mathrm{cont}}(\omega)$ as well as for final Fano line shape analysis.

The values of constants and parameters used in this analysis as shown in Table 7.1 give a $\sigma_{1,\mathrm{cont}}$ which matches closely in peak position and width used in other reports as well

with GWBS calculations [57, 59]. Particularly the final Fano fitting closely matches with our data for the resonance energy position of 4.94 eV with a Γ of 830 meV which is equivalent to an auto-ionization time of $\sim 0.44\, fs$ which shows the resonant nature of the excitonic state with fast dissociation.

However in comparison σ_1 for graphene layer on $SrTiO_3$ is of very different nature than that of graphene layer on SiO_2/Si. But surprisingly we could still account for the shape of σ_1 using Fano anti-resonance starting with the same $\sigma_{1,\mathrm{cont}}$ with plausible additional physical processes present. We claim that the two major observations - robust quenching of σ_1 beyond ~3.2 eV as well as enhanced σ_1 even below ~ 1.5 eV to be clear signature of this Fano anti-resonance. We report this particular observation to be the first evidence of a new phenomenon - an excitonic resonance state at much lower energy of 3.94 eV. This new exitonic state with a broadening of 3.3 eV explains the nearly full transparency of the graphene layer as well as other features of σ_1 in conjunction with the presence of new transitions from graphene valence bands to low lying hybrid conduction bands (due to strong substrate interaction).

As can be seen in Fig 7.12 (b) although almost fully quenched, σ_1 for graphene layer on $SrTiO_3$ does not go to zero exactly. However in case of Fano anti-resonance there should be a zero above (as we have negative q) the resonance energy. This suggests that when we start with the possible picture of Fano anti-resonance between the continuum of graphene transitions with that of the new excitonic state which we propose to be present in the hybridized graphene and substrate bands then there may be some fraction of

$\sigma_{1,\mathrm{cont}}$ which do not couple with the discrete states and hence contribute to the final optical conductivity as coming from 'intrinsic graphene transitions' and also possibly without any e-h interaction renormalization. Therefore we fit our data with the following modified Fano formula

$$\frac{\sigma_1(\omega)}{\sigma_{1,\mathrm{cont}}(\omega)} = x + (1-x)\frac{(q+\varepsilon)^2}{1+\varepsilon^2} \qquad (7.1)$$

where x represents the fraction of $\sigma_{1,\mathrm{cont}}$ which is not coupled by Fano anti-resonance. From our simulations we find the best fit to the features using a resonance energy of 3.94 eV for which we find the fraction x to be ≈ 0.12 if we compare the experimental σ_1 and $\sigma_{1,\mathrm{cont}}$ at the minimum of Fano anti-resonance which is at 4.97 eV. It may be mentioned that at this point it is not clear whether this fraction is nonzero because of interface quality or there is an intrinsic fundamental limit to the Fano coupling. Nevertheless the result of the Fano fit is shown in Fig. 7.12(b) where the main features- quenching of σ_1 above ~3.2, enhanced σ_1 below ~1.5 eV and also the slope of σ_1 around 4 eV can be accounted for well. The large broadening (~3.3 eV) is the cause of the enhanced σ_1 infrared and visible regions. However above ~1.5 eV the enhancement cannot be fully accounted for by the Fano resonance alone and there are additional interesting structures in σ_1. We attribute these to new transitions possible from intrinsic graphene like bands below the Fermi level to new hybrid bands or bands belonging fully to the substrate [135]. It is further supported by our ultrafast differential reflectivity (UDR) data to be explained next. In short the Fano resonance can account for the enhanced conductivity at

low energy (< ~1.5 eV) as well as the ultraviolet transparency and also the slope of the edge of σ_1 around 4 eV. These clearly indicate that the new hybrid bands support excitonic states around 3.94 eV with a broad line width. A width of 3.3 eV represents an auto-ionization time of ~0.11 fs which is four times faster than the case of graphene layer on SiO_2/Si. This could be due to the fact that $SrTiO_3$ has a high (~300) static dielectric constant which screens the quasi-particles reducing the excitonic strength and hence also their life-time considerably [59, 121].

Ultrafast differential reflectivity ($\Delta R/R$) for both 'graphene on SiO_2/Si' and 'graphene on $SrTiO_3$' are measured using a degenerate pump-probe set-up using Ti:sapphire mode-lock lasers with 80 MHz pulse repetition rate generating 40 fs pulses of 800 nm wavelength. The pump and probe pulses are of mutually orthogonal polarizations. The laser spot size for the pump pulse is of 50 micron diameter. The pump power is varied for different measurements from 3 milliwatt (mW) to 15 mW while the probe power is kept fixed at 0.5 mW. In our data we report the power level of the pump pulse in terms of fluence which is related to pump power by the following relation

$$\text{Fluence (J/cm}^2\text{)} = \text{Laser pulse energy (J)} / \text{focal spot area} \qquad (7.2)$$

Fig 7.13(a) shows the plots of $\Delta R/R$ measured at different pump fluence for 'graphene on SiO_2/Si'. For all the pump fluence there is almost a constant individual $\Delta R/R$ background which can be clearly attributed to the Si layer [194]. All of these $\Delta R/R$ data can be fitted with a bi-exponential decay consisting of a fast decay (~100 fs) and slow

decay (~ 1.5 ps) and an offset to account for the contribution from the silicon layer underneath as shown in Fig. 7.12(a).

$$\frac{\Delta R}{R} = -(A \times e^{-x/\tau_{fast}} + B \times e^{-x/\tau_{slow}} + C) \qquad (7.3)$$

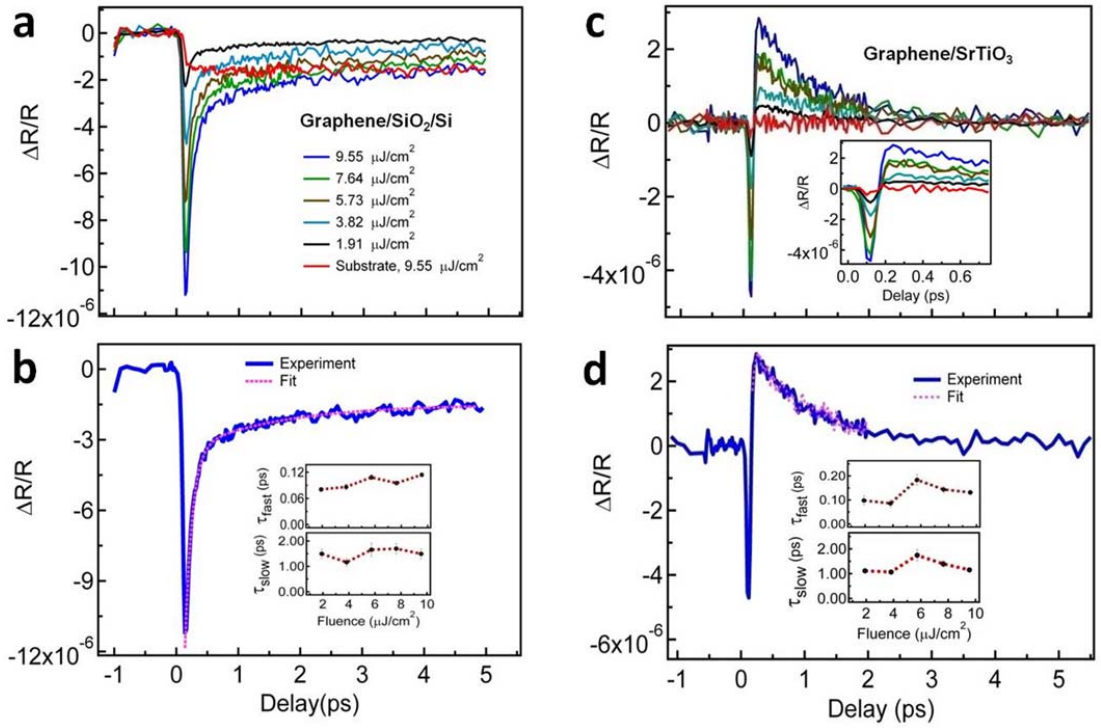

Figure 7.13 (a) Ultrafast differential reflectivity ($\Delta R/R$) for various pump powers for both Graphene/SiO_2/Si and substrate (SiO_2/Si). **(b)** Representative fitting of $\Delta R/R$ for pump fluence 9.55 μJ/cm^2 using bi-exponential model with an offset. Insets show the plots of τ_{fast} and τ_{slow} as functions of fluences. **(c)** $\Delta R/R$ for various pump powers for both Graphene/$SrTiO_3$ and substrate ($SrTiO_3$). **(d)** Representative fitting of $\Delta R/R$ for pump fluence 9.55 μJ/cm^2 using bi-exponential model and adding the contributions from 'intrinsic graphene like transitions' found from the graphene/SiO_2/Si data of same fluence. Insets show the plots of τ_{fast} and τ_{slow} as functions of fluences (after bi-exponential model fitting without offset).

These two decays can be attributed to hot electron-optical phonon coupling and optical phonon- acoustic phonon coupling processes [140, 191] respectively. However the $\Delta R/R$ for 'graphene on $SrTiO_3$' as shown in Fig 7.13 (c) are of very different character than that of 'graphene on SiO_2/Si'. It first becomes negative with a fast dip and then becomes positive with fast rise with gradual decay thereafter. We propose these features to be the signatures of new additional excitation paths possible in the system where electrons can be excited from the graphene bands below and starting from the Fermi level to the lowest conduction bands which have strong interaction with the substrate bands [128,135]. These hybridized bands are not present in the same energy range for the case of 'graphene on SiO_2/Si'. We employ an analysis scheme for these $\Delta R/R$ where we subtract the contribution of the intrinsic graphene like transitions obtained for each individual fluence (found from the 'graphene on SiO_2/Si' case) and then fit the data with a bi-exponential model with no offset [Fig.7.13(d)].

$$\frac{\Delta R}{R} = A \times e^{-x/\tau_{fast}} + B \times e^{-x/\tau_{slow}} \qquad (7.4)$$

The intrinsic graphene transitions have a faster rise time than the transitions from graphene bands to the new conduction band states which have strong substrate interaction in the hybrid structure and hence we see the two peaks of opposite sign. The negative $\Delta R/R$ for 'graphene on SiO_2/Si' is due to state- filling effects while in the case of 'graphene on $SrTiO_3$' the extrinsic transitions are such that the excited carriers could be again re-excited by the probe beam leading to a positive $\Delta R/R$ unlike the purely

intrinsic case [140]. Overall these features show that new transitions are possible to conduction bands interacting strongly with the substrate.

The various time scales involved as well as the other constants from the fit of $\Delta R/R$ for both the cases of 'graphene on SiO_2/Si' and 'graphene on $SrTiO_3$' give us further important new information. As can be seen in the inset of Fig. 7.13(b) the average τ_{fast} for graphene layer is ~100 fs while average τ_{slow} is 1.5 ps. These values are in agreement with literature values [195,140]. However our new results of 'graphene on $SrTiO_3$' have (Fig. 7.13 (d)) an average τ_{fast} of ~150 fs while average τ_{slow} of ~1.2 ps.

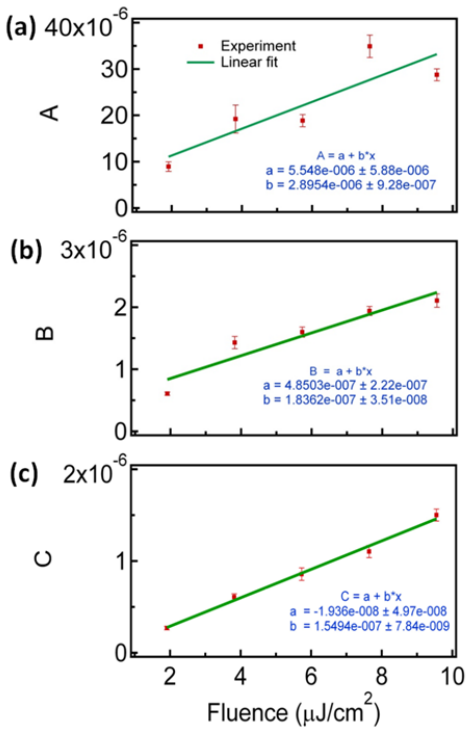

Figure 7.14 Pump fluence dependence of **(a)** constant *A*, **(b)** constant *B* and **(c)** constant *C* for 'graphene on SiO_2/Si' in equation *(7.1)*.

A slower relaxation of hot electrons through optical phonon coupling may be due to the fact that the new transitions are to the hybrid states having more contributions from the $SrTiO_3$ substrate which facilitates re-absorption of optical phonons (from the substrate) which slows the process [140]. Again the time scales are not too different which suggest that the bands may be indeed hybrid and not totally of pure $SrTO_3$ type which is the substrate. A faster τ_{slow} in case of 'graphene on $SrTiO_3$' may be due to increased decay channels of the optical phonons to acoustic phonons mediated by the $SrTiO_3$ substrate

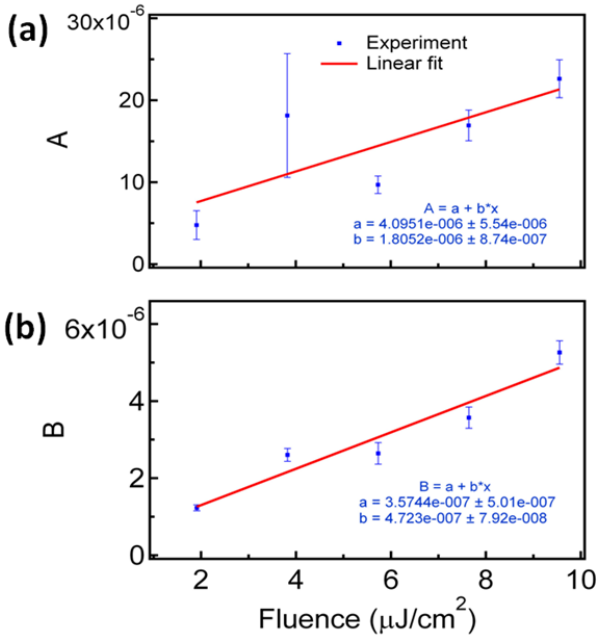

Figure 7.15 Pump fluence dependence of **(a)** constant *A* and **(b)** constant *B* for 'graphene on $SrTiO_3$' in equation *(7.2)*.

again. In Figure 7.14 we plot the pump fluence dependence of the constants *A*, *B* and *C* in equation *(7.1)* in case of 'graphene on SiO_2/Si'. The linear dependence of each of these amplitudes shows that the photogenerated carriers have not reached the saturation level. Similar linear nature of constants *A* and *B* of equation (7.2) in case of 'graphene on $SrTiO_3$' (Fig. 7.15) shows that in that system also the photogenerated carriers have not reached the saturation limit. It also shows that the photon absorption process is first order and linear and at low energy corresponding to 800 nm photon.

We further investigate the electronic structures of the 'graphene on $SrTiO_3$' system using ab initio density functional theory (DFT) calculations. All calculations were carried out by using DFT based Vienna *ab initio* simulation package (VASP) [196,197]. The frozen-core all-electron projector-augmented wave (PAW) [198] potential and Perdew–Burke–Ernzerhof (PBE) exchange-correlation functional were used, as well as the plane-wave basis with a kinetic energy cutoff of 400 eV.

Due to different lattice symmetry and lattice constant between pristine graphene and $SrTiO_3$, the strained $(\sqrt{3} \times 3)$ graphene supercell was used to match with (1×2) supercell of $SrTiO_3$ (001) surface with TiO_2 termination and 5 layers of thickness, in which 7.14% compressive and 7.19% tensile strains were applied along graphene a and b lattice directions respectively. The vacuum region in the interface model was set to 15 Å to minimize Coulomb interactions of neighbor surfaces, and 8×4×1 *k*-point meshes were used for the interface structures. The bottom two layers of $SrTiO_3$ substrate were fixed

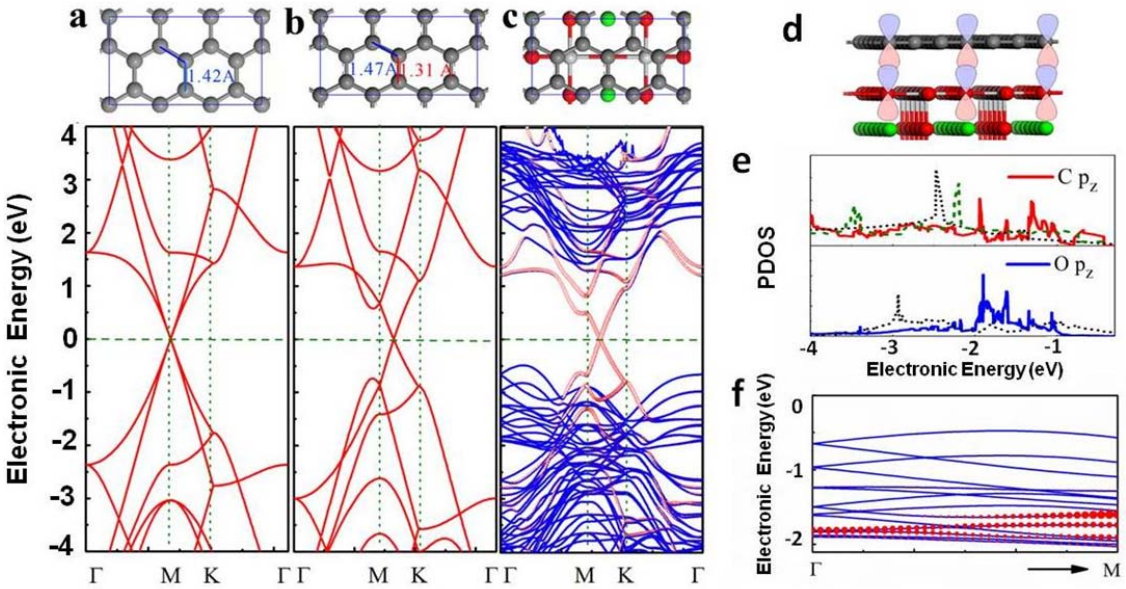

Figure 7.16 (a) Band-structure for free standing $(\sqrt{3} \times 3)$ graphene supercell (top view of the supercell is in the panel above). **(b)** Band-structure for strained $(\sqrt{3} \times 3)$ graphene supercell (top view of the supercell with strained graphene is in the panel above). **(c)** Band structure of Graphene/$SrTiO_3$ with strained monolayer graphene on top of 2.5 unit cells (5 layers) of $SrTiO_3$ substrate. The dotted red line in the band-structure (bottom panel) denotes the contribution of Cp_z bands of graphene. **(d)** Schematic of hybridization of Cp_z orbital of graphene with Op_z orbital of $SrTiO_3$ in Graphene/$SrTiO_3$. **(e)** The projected density of state (PDOS) of Cp_z orbital and Op_z orbital in the hybrid Graphene/$SrTiO_3$ system. The dotted black lines denote the corresponding PDOS for Cp_z in free-standing graphene and *O*p_z in isolated $SrTiO_3$ substrate. The dotted green line in the top panel shows the PDOS for strained graphene. **(f)** Zoomed in band-structure of Graphene/$SrTiO_3$ showing the new graphene Cp_z bands not seen in that energy range for the case of freestanding or strained graphene without $SrTiO_3$ substrate. The red dotted lines denote Cp_z bands.

during the relaxation process, and Van de Waals effect between $SrTiO_3$ and graphene [199] was included also. Figures 7.16(a) and (b) are the band structures of free and strained $(\sqrt{3} \times 3)$ graphene, respectively. The flat bands near M point in pristine graphene are mapped to Γ point in present case because of the band folding. Compared

with the band-structures of free standing and strained graphene, the Cp_z valence bands from stained graphene supported on $SrTiO_3$ substrate are lifted up significantly near Γ point, while the conduction band are pushed down slightly, indicating that the bands of $SrTiO_3$ substrate interact with the bands (shown in the schematic of Figure 7.16(d)) of supported graphene and cause the related change of the band-structure. This interaction is further confirmed by the PDOS of Fig. 7.16(e), in which strong hybridization is indicated between p_z orbital of carbon in graphene and oxygen in $SrTiO_3$ for Graphene/$SrTiO_3$ system, especially at the energy range of -2 eV to -1 eV from the Fermi level (see the zoomed in band-structure of Graphene/$SrTiO_3$ in Fig. 7.16(f).

In Fig. 7.17 we propose the fundamental mechanisms involved for both the systems 'graphene on SiO_2/Si' and 'graphene on $SrTiO_3$' using schematics. As monolayer graphene is a two dimensional (2D) material, the whole layer itself could have interfacial properties together with one or few layers of substrate. Electronic structures of the underlying substrate play the most crucial role in controlling the nature of this new hybrid system. Optical spectroscopic studies can probe the electronic structure and correlation effects in such a hybrid system including regions near and far away from Dirac point. However with conventional optical studies (as in our case till 5.2 eV) we are only in the intrinsic graphene like regimes as the substrate bands are far away for the substrate layer in contact SiO_2 which has a band gap of ~ 9 eV. Our results from SE as well as UDR

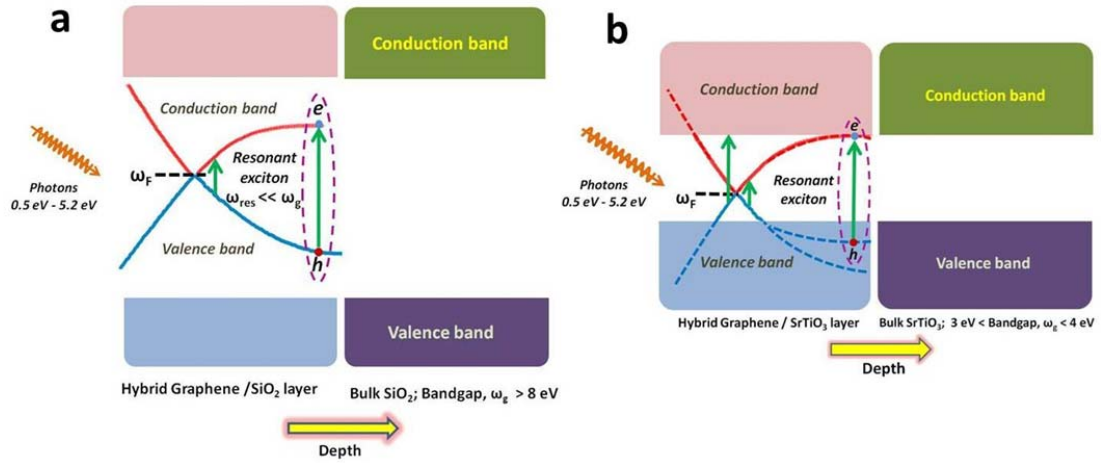

Figure 7.17 (a) Schematic band diagrams for the top layer (shown as hybrid Graphene/SiO_2) and the bulk substrate underneath for Graphene/SiO_2/Si system. The resonant exciton is in purely graphene bands. All transition possible are within purely graphene bands. **(b)** Schematic band diagrams for the top layer (shown as hybrid Graphene/$SrTiO_3$) and the bulk substrate underneath for Graphene/$SrTiO_3$ system. The resonant exciton resides between graphene conduction band and the hybrid bands formed by graphene valence bands with $SrTiO_3$ valence bands (more specifically hybridization of Cp_z with Op_z orbitals). Also transitions from graphene bands to states influenced and contributed mainly by the substrate in its lowest conduction bands are possible in this hybrid Graphene/$SrTiO_3$ system as indicated by the additional green arrow. These transitions are not present in Graphene/SiO_2/Si case.

also confirm that in this system the graphene layer (on SiO_2/Si) shows intrinsic graphene like character. On the other hand in Fig. 7.17 (b) we show the case of 'graphene on $SrTiO_3$'. Here the hybrid nature of the graphene layer due to the presence of bands of $SrTiO_3$ dramatically alters the scenario. First of all we have new excitonic states supported between graphene conduction band and the new valence bands coming from the hybridization of p_z orbitals of carbon in graphene and oxygen in $SrTiO_3$. This again couples with the continuum of the graphene transitions by Fano anti-resonance and

makes graphene almost fully transparent in the UV region. At the same time this Fano anti-resonance enhances the low energy (< ~3.2) σ_1. The hybrid nature of the graphene layer also supports new transitions from the graphene valence band to the conduction band states interacting strongly with the substrate. These transitions are only possible when the excitation energy is of the range ~1.5 eV or higher. This is a reasonable energy cut-off as the energy separation between the Fermi level to these bands is approximately of that value. Our data for σ_1 of 'graphene on $SrTiO_3$' also indicate such a threshold. Above ~1.5 eV the contributions of such transitions increase reaching the highest value for energy 3.2 eV after which the Fano anti-resonance induced transparency takes over.

7.4 Conclusion

To summarize -this work presents clear evidence of new physical processes in the 'graphene on $SrTiO_3$' system. First, the substrate electronic structure interacts strongly with the graphene bands which results in new hybrid bands. These hybrid bands generate excitonic states which lead to Fano anti-resonance with drastic renormalization of the optical conductivity inducing nearly full transparency of the graphene layer in the UV range. The large Fano broadening indicates an almost four times faster auto-ionization of the new resonant excitons. The optical conductivity further shows evidence of increased transition strength at energies below the resonance energy (< 3.2 eV) due to transitions from intrinsic graphene bands to bands influenced and contributed mainly by the substrate in the hybrid structure. Overall this work elucidates the new and important physics of a 'Graphene/intermediate band-gap insulator' system with evidence of

remarkable interactions of the substrate and graphene bands leading to quantum interference phenomena mediated by many body effects in the form of strong electron - hole interactions. Hence these systems are important from fundamental physics as well as application point of view as these also have the potential for new functionalities.

Chapter 8

Tunable optical absorption and interactions in graphene via oxygen plasma

We observe significant changes of optical conductivity (σ_1) in single layer graphene induced by mild oxygen plasma exposure, and explore the interplay between carrier doping, disorder, and many-body interactions from their signatures in the absorption spectrum. The first distinctive effect is the reduction of the excitonic binding energy that can be extracted from the renormalized saddle point resonance at 4.64 eV. Secondly, σ_1 is nearly completely suppressed ($\sigma_1 \ll \sigma_0$) below an exposure-dependent threshold in the near infrared range. The clear step-like suppression follows the Pauli blocking behaviour expected for doped monolayer graphene. The nearly zero residual conductivity below $\omega \sim 2E_F$ can be interpreted as arising from the weakening of the electronic self-energy. Our data shows that mild oxygen exposure can be used to controllably dope graphene without introducing the strong physical and chemical changes that are common in other approaches to oxidized graphene, allowing a controllable manipulation of the optical properties of graphene.

My contributions in this work are in data analysis, Fano fitting and interpretations.

8.1 Introduction and motivation

In the absence of disorder, the optical conductivity (σ_1) of graphene – two dimensional carbon atoms arranged in a hexagonal lattice – displays many remarkable optical properties, including a broadband universal optical conductivity ($\sigma_0 = \pi e^2/2h$) in the infrared-visible range [19,61,64,92]. In the visible–ultraviolet range the interplay between electron-electron (e-e) and electron-hole (e-h) interactions yields unique excitonic effects that renormalize and red shift the bare band structure saddle point resonance by ~0.6 eV.

These effects are clearly seen in the real part of the σ_1 of graphene [57-61,64,183], and highlight the importance of many-body interactions for an accurate description of the electronic properties of graphene. Recently, controlled disorder, such as defects, impurities, vacancies, and ad atoms, have been studied intensively and proposed to control the transport and optical properties of graphene [74,86,201-204]. Here we explore controlled disorder in graphene by oxygen plasma exposure.

Mild oxygen plasma exposure has been used widely to produce graphene oxide. This dry method has numerous advantages, namely: the oxidation can take place rapidly, and it does not strongly modify the transport properties of graphene. It is known that this method introduces structural defects and disorder due to the attachment of oxygen to carbon atoms, and to the reduction in the overall sp^2 order [205]. The fact that the oxygen arrives at the sample surface by a process of diffusion, makes remote oxygen plasma treatment a clean way to control the amount of disorder in graphene [205]. However, plasma exposure can have very different outcomes in the optical and transport properties of graphene, depending on the intensity of irradiation that directly translates into the degree of disorder and amorphization of the resulting carbon lattice. Increased carrier densities, semiconducting transport behaviour, and photoluminescence are frequently seen [205,206], but there is no consensus as to whether these features arise from a bulk band gap, or are due to disorder-induced localized states. Hence, it is of great interest to study directly the optical absorption spectrum of these systems, and analyse the interplay between carrier doping, disorder, and many-body interactions from their signatures in the optical absorption spectrum.

8.2 Experimental details

In this work, we study the evolution of σ_1 of monolayer graphene in the frequency range of 0.5–5.3 eV under mild (low power ~4 W) exposure to oxygen plasma. We perform Raman and spectroscopic ellipsometry (SE) after each consecutive 2-second (t_s) exposure of the graphene sample to oxygen plasma.

8.2.1 Sample preparation

Single layer graphene (SLG) was prepared on top of Copper foil via a low-pressure chemical vapour deposition (CVD) process and then transferred to the SiO_2(300 nm)/Si substrate (explained previously in chapter 3). One difference in this work from what has been explained in chapter 3 for sample preparation is that the copper etchant here is $FeCl_3$ instead of $(NH_4)_2S_2O_5$, while other procedures are same.

8.2.2 Oxygen plasma treatment and Raman measurement

The SLG sample was exposed to the mild oxygen plasma for three consecutive durations of 2 s, 4 s, and 6 s using a radio-frequency (rf) plasma system. The rf power was maintained at 4 W and chamber pressure at 50 mTorr. The pristine SLG and oxygen plasma exposed SLG were investigated using Raman and SE measurements. Raman spectra were recorded using a 514 nm laser excitation wavelength (Renishaw Raman measurement system). A low laser power of ~ 2 mW is employed to minimize laser heating effects. All the measurements were performed at room temperature, in ambient, and on the same sample. To check the stability of the sample we placed the sample into

dry box for one day after SE measurements. After that, we repeated the SE measurements and the SE data showed no significance change indicating that the sample is stable enough under the measurement in an ambient environment.

8.3.3 Spectroscopic Ellipsometry (SE) measurement and analysis

SE [141-144] measurements are performed on the graphene sample and substrate (SiO_2 (300 nm)/Si) using a SENTECH SE850 ellipsometer available in the laboratory. The details of this SE set-up is described in Chapter 3.

SE data for Ψ and Δ are taken at multiple incident angles and at several spots on the sample. The data at different spots are identical in almost all cases which show sample

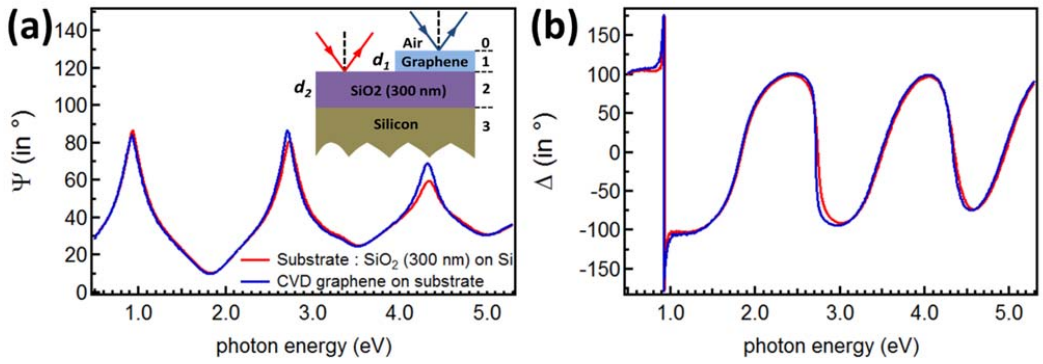

Figure 8.1 Spectroscopic ellipsometry data of single layer CVD (chemical vapor deposition) graphene on SiO_2 (300 nm)/Si substrate. (a) Ψ and (b) Δ for Substrate (CVD graphene) shown in red (blue). The inset in (a) shows the optical multilayer model used in extracting the Ψ and Δ. Medium 0,1,2,3 in the model denote air, a graphene layer with the thickness d_1 of 0.335 nm, a SiO_2 layer with the thickness d_2 of 300 nm, and silicon bulk, respectively.

homogeneity. The multiple incident angle data is required for global fitting of data. SE measurement is generally preferable because it gives both the real and imaginary parts of

the dielectric function directly whereas other measurement techniques such direct reflectivity require Kramers-Kronig transformation. Moreover in case of very thin films the change in phase of the incident light waves upon reflection is much more pronounced than the change in amplitude of the light of different polarizations. These two facts make

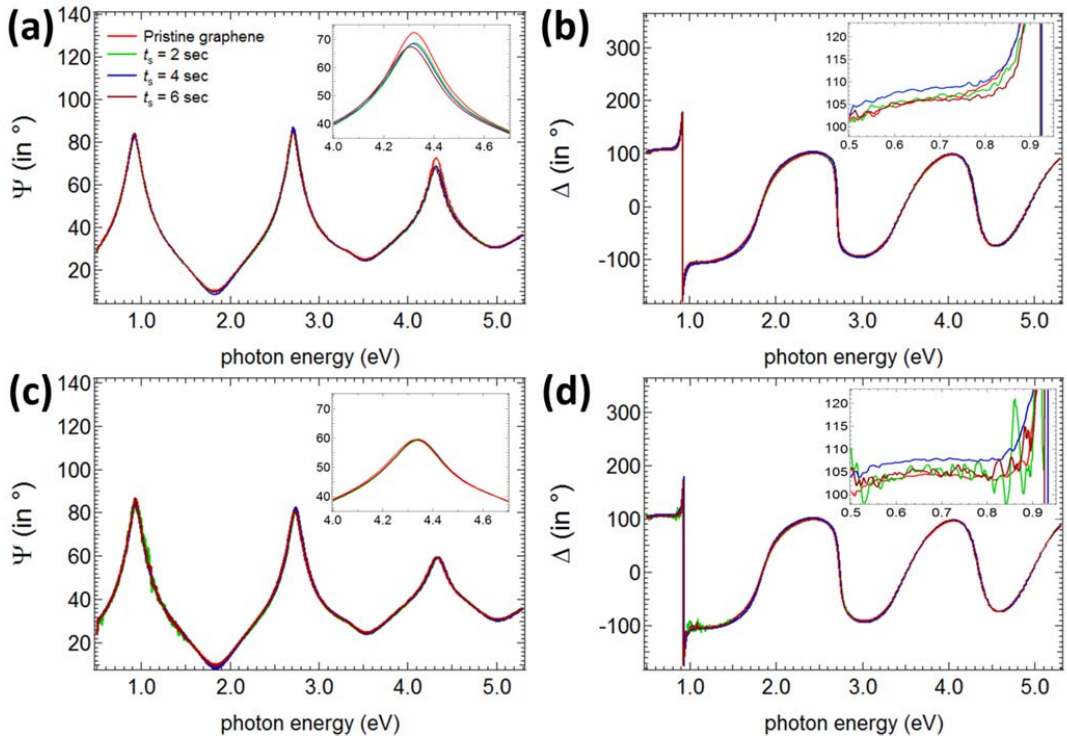

Figure 8.2 (a) and (b) are the experimental Ψ and Δ at an incident angles (θ_0) of 70^0 for pristine graphene on SiO_2 (300 nm)/Si substrate and after cumulative oxygen plasma exposure (t_s) in 2 seconds steps. (c) and (d) are the experimental Ψ and Δ at an incident angles (θ_0) of 70^0 for SiO_2 (300 nm)/Si substrate only. The insets show the zoom of Ψ and Δ at particular energy ranges.

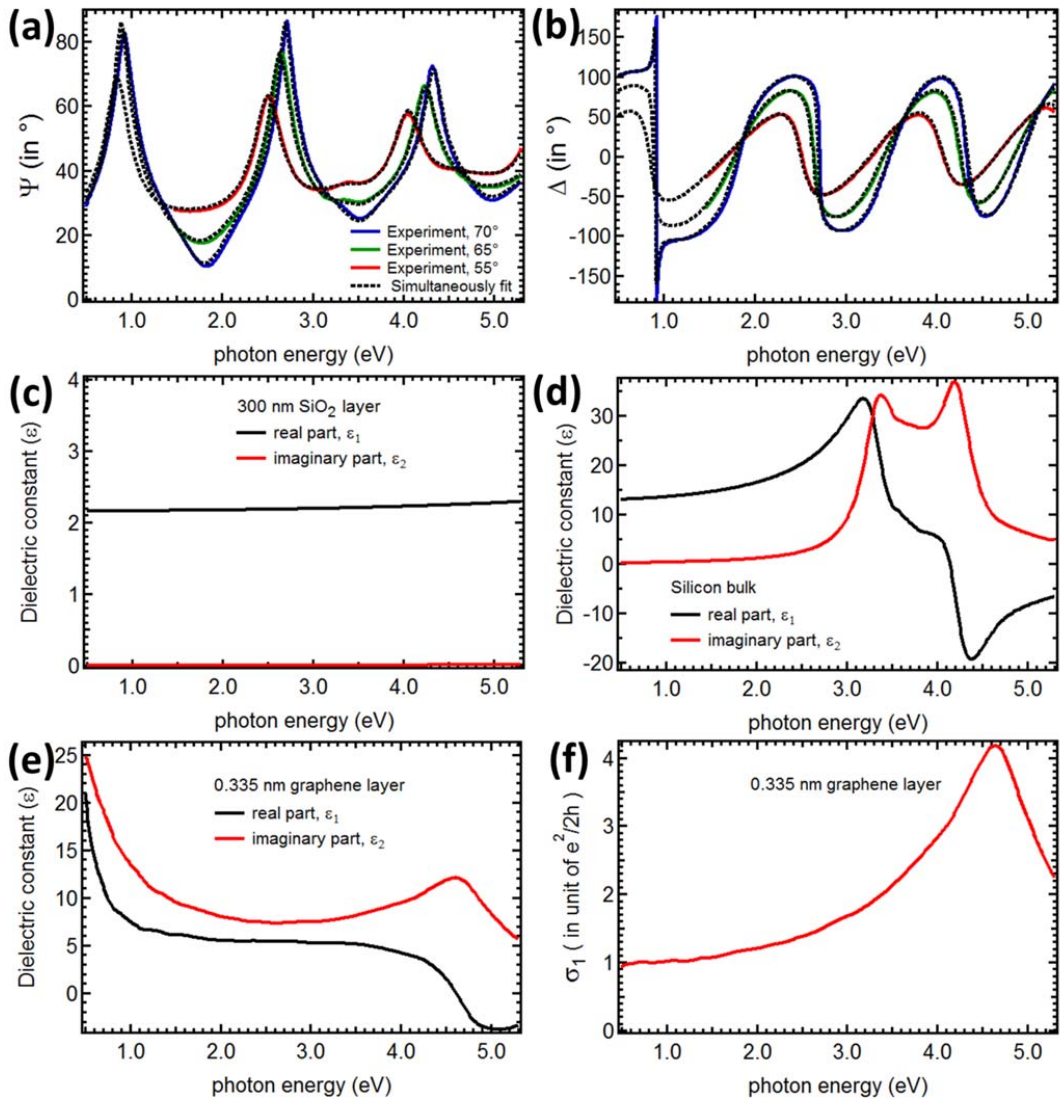

Figure 8.3 Detailed analysis of spectroscopic ellipsometry data for pristine graphene on SiO_2 (300 nm)/Si substrate. (a) and (b) are the experimental Ψ and Δ at different incident angles (θ_0) 70^o,65^o, and 55^o shown in solid blue, green, and red lines, respectively. The best match model extracted from the analysis shown in dashed black lines. (c) Model dielectric constant used in the optical model for 300 nm SiO_2 layer. (d) Model dielectric constant used in the optical model for silicon bulk. (e) Model dielectric constant extracted from the optical model for 0.335 nm graphene layer. (f) Corresponding optical conductivity of 0.335 nm graphene extracted from (e).

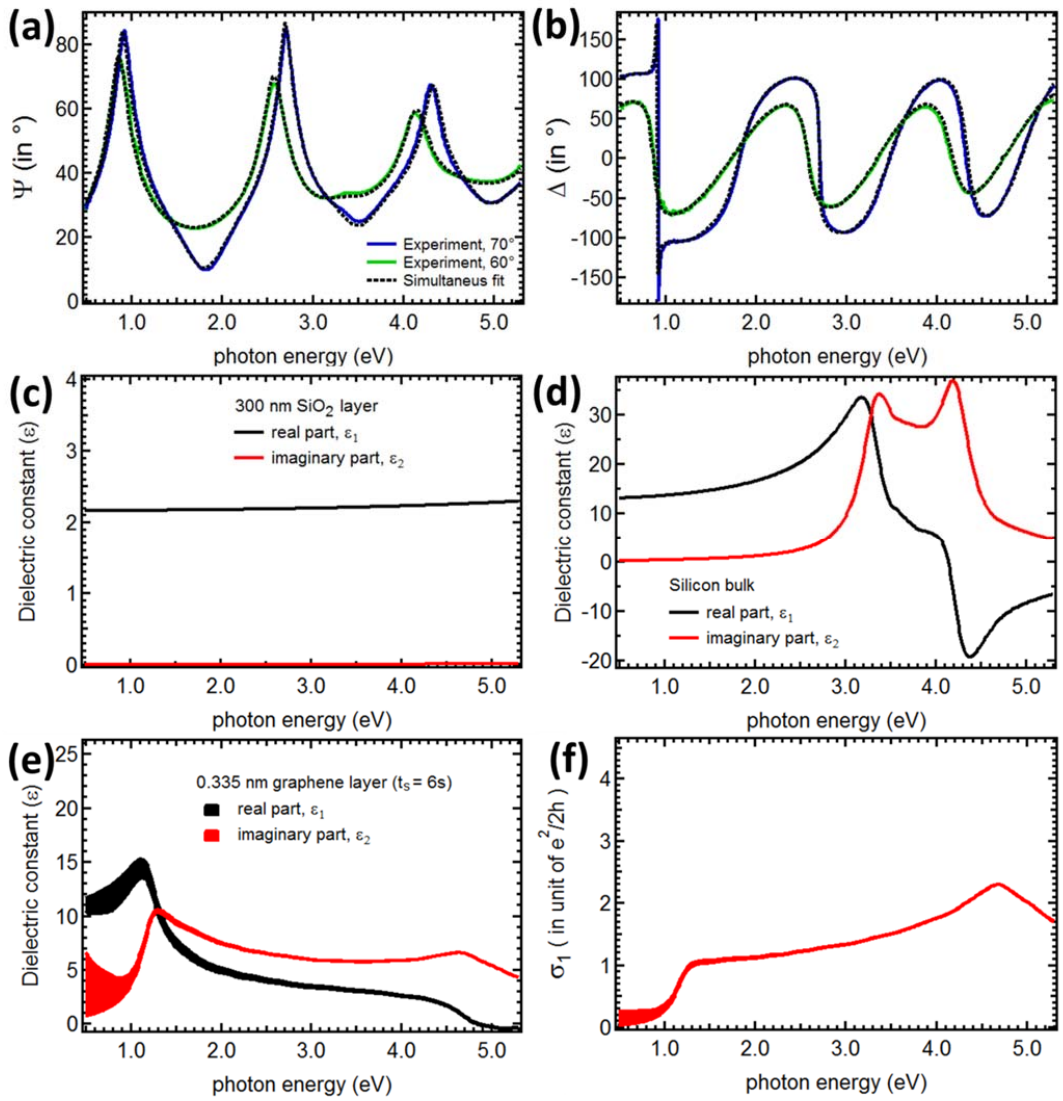

Figure 8.4 Detailed analysis of spectroscopic ellipsometry data for graphene on SiO_2 (300 nm)/Si substrate after 6s of oxygen plasma exposure time (t_s). (a) and (b) are the experimental Ψ and Δ at different incident angles (θ_0) 70° and 60° shown in solid blue and green lines, respectively. The best match model extracted from the analysis shown in dashed black lines. (c) Model dielectric constant used in the optical model for 300 nm SiO_2 layer. (d) Model dielectric constant used in the optical model for silicon bulk. (e) Model dielectric constant ε_1 extracted from the optical model for 0.335 nm graphene layer. (f) Corresponding optical conductivity σ_1 of 0.335 nm graphene extracted from (e). The shaded area in ε_1 and σ_1 indicates the range in which the model still can match the experimental Ψ and Δ (within the error bars).

SE an ideal method for analyzing systems like very thin monolayer of graphene on a substrate. In Figure 8.1 we show the measured Ψ and Δ values of samples with and without graphene on substrate at 70^{o} incident angle. The spectra show the pronounced contrast due to the presence of graphene which is only ~3 angstrom thick.

We depict the experimental Ψ and Δ of pristine graphene on SiO_2 (300 nm)/Si substrate and after cumulative oxygen plasma exposure (t_s) in 2 seconds steps in Figs. 8.2 (a) and (b). Due to oxygen plasma exposure, Ψ and Δ are slightly changed especially in the energy range indicated in inset of Figs. 8.2 (a) and (b). These facts shows that the optical constants (e.g. dielectric constant and hence optical conductivity) changed and care should be taken when the fitting procedure is applied in these particular energy ranges. In contrast, within the error bars of the measurements, there is no significance change of the measured Ψ and Δ of SiO_2 (300 nm)/Si substrate after cumulative oxygen plasma exposure (see Figs 2(c) and (d) as well as the insets).

For our case, the system is modeled with Fresnel coefficients for an optical multilayered film system (see inset of Fig. 8.1 (a)).The model composed of a silicon bulk (label 3), a 300 nm SiO_2 layer (label 2), a 0.335 nm graphene layer (label 1), and the air (label 0). The details of the fitting procedure is described in Chapter 4. In Figure 8.3, the data fitting for pristine graphene case is shown with all the individual dielectric functions of each layer of material. Similarly in Figure 8.4 the data fitting for the sample with 6s exposure is shown with the final dielectric function results. Similar data fitting is performed for all the different exposure times (but not shown here).

8.2.4 Fano line shape analysis

Fano line –shape analysis in this work is performed as described in Section 4.5 of this thesis. The vertical errors bars for Fano parameters (q, Γ, E_{res}, and E_0) that appear in Figure 8.7 (to be explained in detail in the next section) stem out from the consideration that within these error bars, one still can have the good match between Fano model and experimentally extracted σ_1 while doing the fitting. The horizontal error bars of these Fano parameters originated from the measurement error of oxygen exposure time in which the measurements are still reliable within one second range.

8.3 Results and discussions

From the results of Raman and SE taken after each consecutive 2-second (t_s) exposure of the graphene sample to oxygen plasma it is seen that with the increase of t_s two important effects develop: a significant reduction of the resonant saddle-point peak (or resonant excitonic peak) at 4.6 eV, and the dramatic suppression of σ_1 (close to zero) for photon energies below 1 eV.

In Figure 8.5(a) we show the Raman spectra for graphene on SiO_2 before (pristine) and after exposure to oxygen plasma for 2s, 4s, and 6s, respectively. The high quality of our pristine graphene is confirmed by the very sharp Raman G peak at 1593 cm^{-1} and no evidence of defect scattering (absent D peak). Furthermore, the ratio between the intensity of D peak and G peak (I_D/I_G) is about two and the 2D peak possess a symmetric single Lorentzian. These indicate that our graphene is indeed single layer graphene

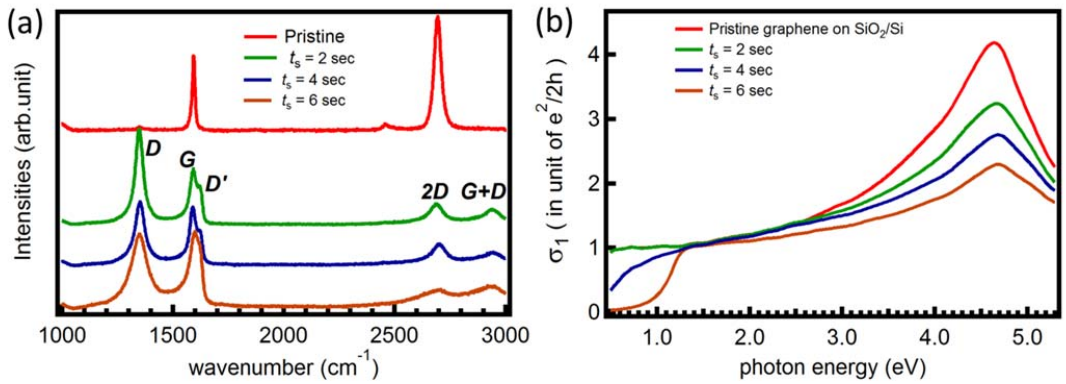

Figure 8.5 (a) Raman spectra (excitation wavelength of 514 nm) for pristine single layer graphene (SLG) on SiO_2 (300 nm)/Si, and after consecutive oxygen plasma exposure time, t_s = 2s, 4s, and 6s. (b) Corresponding real part of optical conductivity, $\sigma_1(\omega)$, extracted from spectroscopic ellipsometry measurements.

[153,207]. Upon exposure to oxygen plasma, the appearance of the D and D' peaks at ~1318 cm^{-1} and 1615 cm^{-1}, respectively, indicates pronounced inter and intravalley scattering [153, 206-208]. After the first exposure, we observe a decrease in the ratio between D and G peak intensities (I_D/I_G), which changes from 1.65 to 0.95 with growing t_s. The fact that D and D' peaks are very high and broad for t_s > 2s suggests relatively strong disorder. Furthermore, based on the three step model of structural disorder in graphitic materials [209], our oxidized samples are likely affected in stage two. In this stage the decrease of (I_D/I_G) is due to the decrease in the number of sp^2 ordered rings, and is related to the in plane crystalline grain size (L_a) through the empirical formula: $I_D/I_G = C'(\lambda)L_a^2$, where $C'(\lambda)$ denotes a constant at the particular excitation wavelength (λ) used in Raman measurements. Here we use $C'(514\ nm)$ = 0.55 nm^{-2} [205, 209].

Figure 8.5(b) displays the evolution of σ_1 as function of t_s. The two main effects are: (1) a significant reduction (more than 50 %) of the van Hove peak at 4.64 eV in the ultraviolet (UV) range; (2) σ_1 is gradually suppressed to zero in a step-like fashion as t_s increases in the near infrared (NIR) range. We now discuss these two observations in more detail.

A prominent asymmetric peak in σ_1 at 4.64 eV can be attributed to excitonic renormalization of the independent particle optical transitions at the M point (i.e. Van Hove singularity (VHS)) in the Brillouin zone of the graphene band structure. If one considers only direct band to band transitions using a local density approximation (LDA) the optical transition peak should occur at ~4.1 eV. By accounting for e-e interactions within a GW approach the optical transition peak is predicted to lie at 5.2 eV. By further incorporating e-h interactions, the peak is red shifted by ~600 meV from 5.2 eV to 4.6 eV [57-61].

In order to quantify the interplay between e-e and e-h interactions in our controlled disordered graphene, we employ the Fano phenomenological approach since, as seen previously, the asymmetric peak measured here at 4.64 eV resembles a Fano profile. Following Fano's model, the asymmetric lineshape in optical spectra originates from the coupling of the continuum electronic states near the saddle point singularity (M point) to discrete sharp excitonic states residing below that continuum [118,121] (Details of the Fano resonance can be found in Section 4.5).

Figure 8.6(a) shows the best fit of σ_1 for pristine single layer graphene using the phenomenological Fano analysis with the parameters q = -1.12, Γ = 0.94 eV, $E_{res} = 4.96$ eV, and $E_0 = 5.25$ eV. The fitting result in energy range of 0.5 to 5.0 eV captures

the asymmetric line shape at 4.64 eV and the universal σ_1 at lower energy very well. However, above 5.0 eV there is discrepancy which may come from the fact that we used the logarithmic function to represent the continuum (unperturbed band to band transition that includes the electron-electron interaction). Figure 8.6(b) shows the separate contributions of σ_{cont} (upper panel) and Fano resonance (lower panel) to the resultant σ_1, as a function of the oxygen exposure time. Figures 8.7(a), (b), and (c) show the dependence of Fano parameters q, Γ, E_{res}, and E_0, respectively, on the amount of disorder. The symmetric peak at 5.25 eV in σ_{cont} coming from the unperturbed band to band transitions (see Fig. 8.6(b)) decreases significantly to 50% without any shift in energy, as quantified in Figure 8.7(c). As for the contribution of the Fano resonance, it shows no significant change in shape as inferred from their q and Γ values, which barely change within the error bars (Figures 8.6(a) and 6(b)). This suggests that after oxygen plasma exposure, our sample remains having intrinsic properties of graphene. If doping changes the electron-hole interaction via screening effects then one would expect to observe the change of energy of resonance excitonic effects as well as the lineshape (see [61]). However, a gradual blue shift as high as 120 meV is observed in the energy of the Fano resonance, as seen clearly from Figure 8.7(c). This suggests a considerable reduction of the excitonic binding energy by 120 meV.

We consider now the dramatic suppression observed in σ_1 at frequencies below 1eV. Oxygen plasma hole-dopes graphene and might, or might-not, introduce strong

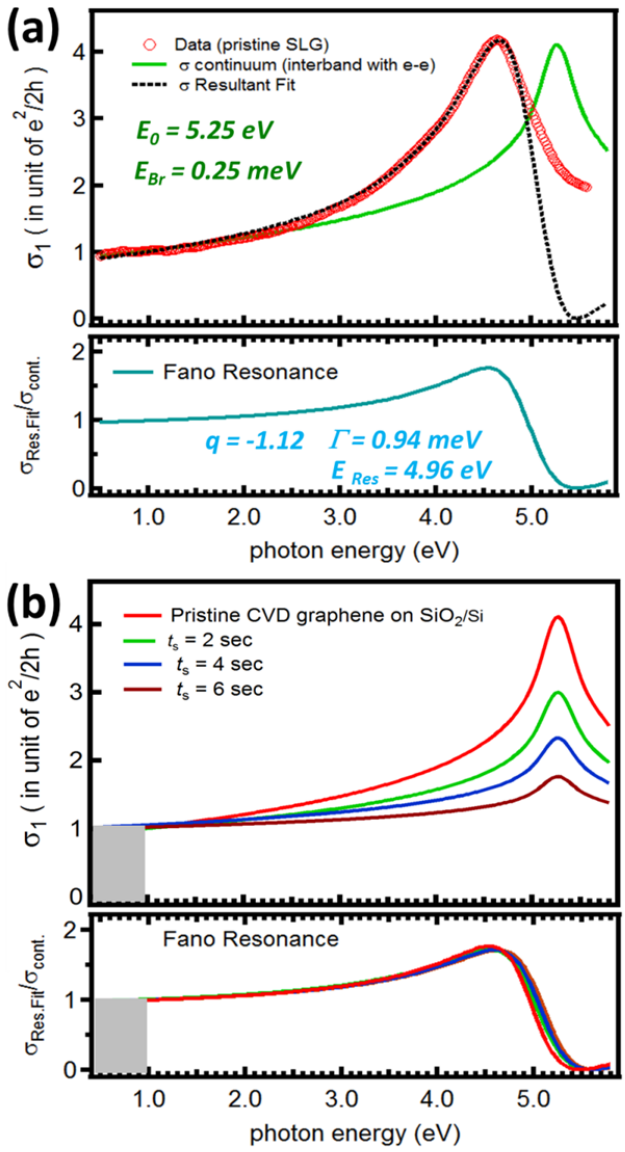

Figure 8.6 (a) Fit of experimental data using phenomenological Fano line shape analysis for pristine single layer graphene on SiO_2 (300nm)/Si. Upper panel: the optical conductivity σ_1 extracted from spectroscopic ellipsometry is shown as red circles, and the total fit is the dashed line; the unperturbed band to band component, σ_{cont}, is shown in green/solid. Lower panel: Fano resonance profile from eq. (3). (b) Comparison of the unperturbed band to band transitions (upper panel) and Fano resonance profile (lower panel) as the oxygen plasma exposure time increased. The grey area denotes the region where σ_1 is suppressed, which is not captured by the Fano approach.

renormalization of the band structure, depending on the amount of disorder, and how the oxidation affects the graphene lattice. Given that the overall profile of σ_1 retains all the features of pristine graphene, we interpret the suppression of σ_1 at low frequencies as due to simple Pauli blocking, which excludes interband transitions for frequencies below

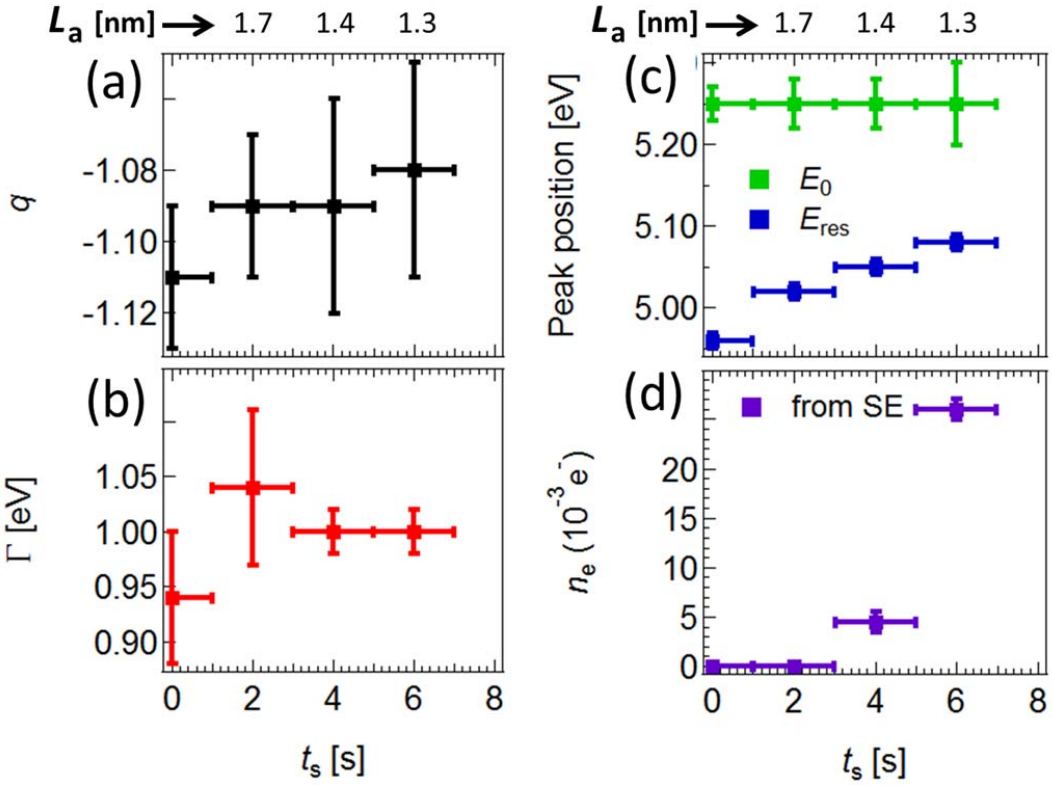

Figure 8.7 Fano parameters extracted from the fit of σ_1 as function of oxygen plasma exposure time t_s. The corresponding disorder parameter L_a (the in-plane crystalline grain size) derived from t_s is depicted on top of the graphs. (a) The lineshape parameters q. (b) The exciton lifetime. (c) The peak position of unperturbed band to band transition (E_0) and Fano Resonance (E_{res}). The number of charge carriers (n_e) extracted directly from the onset of the Pauli blocking in the experimental traces of $\sigma_1(\omega)$.

$2E_F$, where E_F is the Fermi Energy (see Figure 8.8(b) and (c)). The presence of a spectral gap is unlikely, as it would lead to strong rearrangement of the JDOS in the entire spectral range [205], which we do not detect here. Hence we attribute the effect to simple Pauli blocking, which suppresses σ_1 below $\omega = E_F$ from its universal value σ_0 [92]. Assuming that the graphene dispersion remains linear after oxygen exposure, we can estimate the number of charge carriers (n_e) per unit cell as $n_e = A\,\frac{|E_F|^2}{\pi(\hbar v_F)^2}$, where A is the area of the graphene unit cell, and E_F can be extracted directly from fitting the NIR conductivity to the theoretical intraband contribution to σ_1. Figure 8.7(d) shows the dependence of n_e on oxygen exposure. Moreover, in graphene the integrated spectral weight (W) in the NIR is conserved, and density independent: $\int_0^{\omega_M} \sigma(\omega)d\omega \simeq \sigma_0\omega_M$, when the integration limit ω_M is beyond $2E_F$. This integrated spectral weight is shown in Figure 8.8(a), and allows us to check the consistency of the extracted E_F directly from the relative changes in optical spectral weight with different exposure times. The doping scenario is also consistent with the exposure-induced shift of the Raman G peak in our Raman data in Figure 8.5(a) [205,210].

What is striking in our optical data in this region is the apparent complete suppression of σ_1 below $2E_F$ (Figure 1(b), t_s = 6s), when the optical response of doped graphene in the Pauli-blocked region is usually characterized by a residual conductivity ~0.2-0.4σ_0 [54]. Such a residual conductivity can be justified theoretically on the basis of a finite

electronic self-energy whose imaginary part is linear in ω [211]. The self-energy contributions can arise from the marginal Fermi liquid character of the electron-electron interactions in graphene, as well as optical phonons or disorder [98,108]. Our Raman data

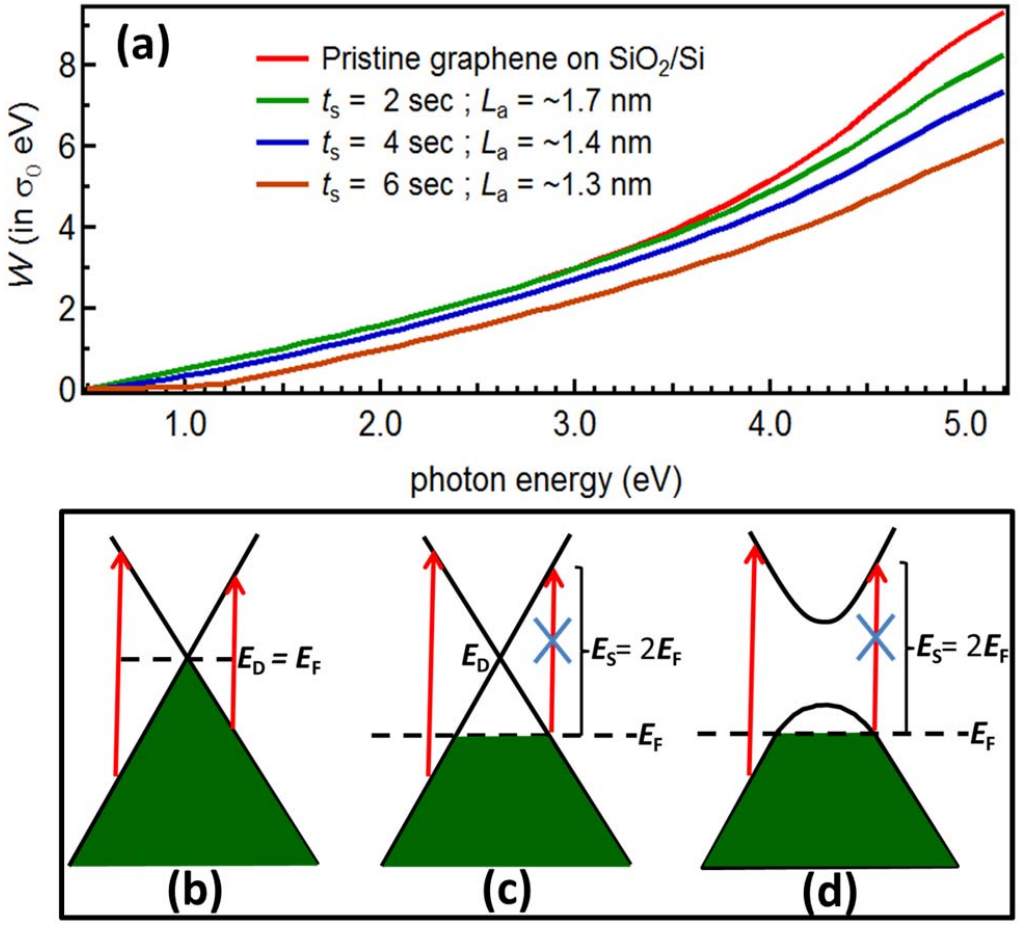

Figure 8.8 (a) The integrated optical spectral weight (W) up to the photon energies in the horizontal axis. (b) Allowed optical transitions (vertical red arrow) in pristine graphene. E_d and E_F denotes the Dirac point and Fermi energy, respectively. (c) Likewise, for hole-doped graphene. Optical transitions below E_F are disallowed due to Pauli's exclusion principle. (d) In hole-doped and gapped graphene.

shows that the optical phonons are clearly affected by the oxygen exposure, and the Fano analysis of the optical data around the VHS reveals the clear suppression of the exciton binding energy, thus hinting at reduced interactions with increased exposure times. Together these effects can lead to the suppression of the marginal Fermi liquid self-energy, thus explaining the nearly zero optical absorption below $2E_F$. Since our samples are disordered, it would also imply that the dominant mechanism for the residual optical conductivity in the Pauli-blocked region might indeed lie in the interaction effects, rather than disorder.

Finally, we underline that our plasma exposure is much milder than the intensities employed in recent reports, which reveal pristine graphene transitioning from ambipolar metallic to insulating behaviour upon treatment with oxygen plasma [205,206].

8.4 Conclusion

In conclusion, we perform spectroscopy ellipsometry and Raman measurements on graphene with disorder induced by *mild* oxygen plasma exposure. We see that it affects the magnitude of electronic interactions from the reduction of the excitonic binding energy in the UV range, and from the nearly zero residual optical conductivity in the Pauli-blocked NIR range, which is consistent with the weakening of the electronic self-energy. Our data suggests, in addition, that low levels of oxygen plasma exposure can be used as a controllable means to tune the optical absorption in graphene, without disrupting the overall graphene optical response, as happens in other oxygenation and doping strategies.

Chapter 9

Summary and future directions

In this final chapter we summarize all the important findings of this thesis from a united perspective. As described in detail in the initial chapters, the main aim of this thesis is to investigate the electronic structures of graphene and understand the various optical processes therein with special focus on electronic correlations. With different optical spectroscopic techniques we have not only obtained a detailed and deeper understanding of the graphene electronic structures in the lower energy range (< 5 eV) in various circumstances but also explored high energy range (<35 eV) which was never studied experimentally before. Similarly using various substrates as well as controlled disorder we have been able to manipulate the electronic correlation strengths and doping levels etc. We conclude the chapter with important immediate future directions underway as extensions of the works in this thesis.

9.1 Summary

Understanding the various features of the electronic spectrum of graphene encompassing different regions of the Brillouin zone *per se* is an essential requirement for a deeper grasp of graphene physics. SE measurements from mid infrared to deep UV (~ 0.5 eV to ~5 eV) performed in various studies [61,187,200] give us detailed insight into graphene electronic structures in this particular energy range. It is seen that graphene (prepared by CVD method) on substrates like SiO_2/Si, quartz (which are used more frequently for various studies found in literature [58, 59]) exhibit optical properties quite similar to those predicted for freestanding graphene [57] (and also measured on exfoliated graphene

[58,59]). This essentially represents weak graphene-substrate interactions, in terms of affecting optical properties, most likely due to the fact that these substrates are wide band gap materials (~ 9 eV). At the same time optical conductivity of graphene at higher energies (till ~ 35 eV) measured in epitaxial graphene [64] shows features very different from what is predicted only using band - to - band transitions (and for that matter even different from what is predicted incorporating e-e interactions as well). In our results we report [64] the first such experimental study and it definitely underlies the unique physics graphene offers for electronic correlation effects (particularly e-h interactions) in the form of huge resonant excitonic effect.

Graphene optical conductivity is predicted [57,62] and observed [58-61] to be renormalized at the deep UV region due to excitonic effects for freestanding as well graphene supported on substrates like SiO_2/Si, quartz. Our results [61,196] from graphene on those substrates (SiO_2/Si, quartz) show similar effects. However we have used these results as 'references' in these studies involving substrate dependent optical conductivity measurements. New results [61, 187,200] from graphene measured on various substrates show that indeed we see considerable and dramatic changes in the optical conductivity due to correlation effects. SE measurements reveal that for graphene on a metallic substrate (Cu) optical conductivity peak is blue shifted by about 400 meV and also its line-shape becomes more symmetric [61]. This is a clear signature of screening of e-h interactions. However even more dramatic effects are observed in case of graphene on $SrTiO_3$ substrate. The optical conductivity goes through a huge renormalization due to

the substrate assisted new excitonic states in graphene which couple to the band-to- band continuum [187] through Fano-anti-resonance. This also signifies the strong electronic coupling between the graphene layer with the low-band gap insulating substrates allowing such new e-h states to exist. Similarly in the case of graphene studied after mild oxygen plasma treatment we observe a Pauli blockade like quenching of optical conductivity in the mid infrared range [200]. This is exciting because the higher energy region (till 5.3 eV) shows very much graphene like signatures negating the possibility that it is due to a gap opening. At the same time, near zero optical conductivity seen at the Pauli blocking region (unlike other reports [54,66]) could be the signature of the reduced correlation effects.

Overall these studies demonstrate the importance of correlation effects as well as the new paradigm of electronic coupling scenarios graphene offer with different substrates resulting in small to very large renormalization of optical conductivity. Its 2D nature with the added advantage of smallest thickness makes it convenient for such substrate effects to be observed relatively easily. The works in this thesis suggest in general that planer graphene-substrate structures could be the host of very interesting physics as well functionalities worthy to be explored extensively in the near future. It could be said that these functionalities might lead to important application prospect in tuning opto-electronic properties of graphene in a controllable way.

One other aspect which is appealing regarding these studies is that the conventional correlation studies in graphene use local probes [212] and also extremely high quality

graphene (say freestanding exfoliated samples) samples [90]. On the contrary our studies use graphene samples prepared by CVD method mostly (also epitaxial in one study [64]) and the effects are not exactly local as the light spot is generally of ~200 micron size. Despite these our results prove that the spectroscopic techniques used in this thesis are adequately powerful to elucidate graphene electronic structures revealing robust signatures of correlation effects in it. Nevertheless higher quality samples are always desirable to eliminate spurious effects but preparing large area (few hundred micron size) single crystalline suspended sample is still a huge experimental challenge. At the same time these techniques (used in this thesis) probe regions of the spectrum which are not very close to charge neutrality point and so are complementary to reports of correlation effects using transport studies for a complete and richer picture. On the whole various optical spectroscopic techniques have been used as a powerful technique to investigate rich graphene physics and all the various results in this thesis are testimonies to it.

9.2 Future Directions

The various studies undertaken in this thesis naturally open the prospects of a whole new set of further studies as extension of the ideas and techniques with the motivation of bringing out a very complete picture of graphene optical properties modulated by substrates due to correlation effects, electronic coupling etc. It is also worth mentioning that although the studies undertaken in this thesis are not with the immediate motivation of application but rather with the motivation of understanding fundamental physics, the

interface optical physics could be studied extensively from potential application perspective in say photovoltaics, photodetectors etc. immediately. Below we briefly describe a few such directions –some of which have more fundamental physics implications while others have application oriented focus.

9.2.1 Gate dependent optical conductivity

With the inherent high sensitivity of SE, even a slight change in dielectric function could be detected [141-144]. At the same time gate-tuning (or field effect tuning) is a very 'clean' way to dope graphene. Both of these aspects make it possible to study graphene optical conductivity in a broad range from ~0.5 eV to ~5 eV with the existing set-up. Although there have been reports of gate-tuning of graphene optical conductivity the reports are mostly focused in the far to near infrared regions [54,66]. Therefore this region (~0.5 eV – ~5 eV) of the spectrum is still unexplored with gate-tuning. Moreover all those studies used reflectivity measurements which have inherent limitations in comparison to SE studies. All these facts make it an exciting immediate study to be undertaken as there has been interesting predictions of manifestation of correlation effects with doping [93] in this spectral range. However it has to be mentioned that the effects are small and it is an experimental challenge to observe such effects reproducibly and controllably. Availability of good quality large area graphene samples and challenges related to gating large area graphene are other issues to be resolved in this case. Measurements have already been performed with the device structures explained in Section 3.3.3, and reproducibility is the major issue now with gate induced changes

being very small. Refinements of the measurement set-up and geometry as well as using a vacuum chamber are the next steps planned.

9.2.2 Graphene on TiO_2 and other substrates

As has been seen in the case of graphene on $SrTiO_3$ substrate [187], graphene on rutile TiO_2 (110) could be a very interesting system to study using SE as well as pump-probe technique. We expect to see electronic coupling as well Fano resonance as TiO_2 has somewhat similar band dispersions and bandgap as that of $SrTiO_3$. Moreover rutile TiO_2 (110) is anisotropic in character which may lead to further interesting anisotropic effects on the optical conductivity.

Similarly availability of a set of substrates like GaAs, $LAlO_3$, Al_2O_3 etc. with atomically flat top surface makes it possible to study the effect of electronic coupling between graphene and substrate as a function of bandgap as well as varying electronic structures of the substrate. This could lead to a very complete general picture of the physical processes and interactions in such interfaces which affect the optical properties directly.

9.2.3 Photoconductivity and light induced charge transfer

As seen from the differential ultrafast reflectivity study of graphene on $SrTiO_3$ [187] there is photo-induced transitions from graphene valence band to conduction band states coming from the SrTiO3 substrate (or also might be to the new hybrid bands formed). These show that these system could be a potential material for photovoltaics, photodetectors or photocatalysis. We propose integrating field effect device structures in

such interfaces (as explained in Sections 3.3.4 and 3.4) using lithographic techniques, which will not only give the wavelength resolved photo-response but also the interplay of gate-tuned carrier concentration change in graphene with it. For this gate-dependent study 300 nm films of $SrTiO_3$ is deposited on Nb-doped $SrTiO_3$ films (by pulsed laser deposition technique) and then graphene has been transferred to such a substrate as explained in Section 3.3.2. Optimization of such device fabrication is underway for better performance. Similarly rutile TiO_2(110) films grown on Nb-doped $SrTiO_3$ substrates could be another such interesting substrate where graphene could be transferred and studied under photo-illumination with gate – dependence. It may be mentioned that there have been reports of enhanced photo-response in the UV-Vis region for graphene-TiO_2 interfacial systems [128,130,131] but these reports are not for planner structures. Rather they use lesser quality reduced graphene oxide and TiO_2 in a composite form. Our planner structure could lead to the understanding and realization of the electronically superior CVD graphene planner structures on substrates with better performance.

9.2.4 High energy optical conductivity of graphene on $SrTiO_3$

As we have seen the optical conductivity of graphene on $SrTiO_3$ is renormalized drastically by the electronic coupling between the graphene and the underlying substrate. The spectral weight of graphene's optical conductivity could be shifted to higher energies due to correlation effects which could be observed in a similar study like in the case of epitaxial graphene [64] in this thesis (Chapter 5), where we measure the optical

conductivity in the range of 0.5- 35 eV, and this could lead to further insight into these systems with important new findings. Work is in progress in this regard where the main challenge is in the analysis of the reflectivity data with proper normalization using SE data.

9.2.5 Infrared studies

Substrate dependent optical conductivity using reflectivity as well as transmission measurements in the infrared region of the spectrum could lead to very important results related to the interplay of electronic coupling and correlation effects in graphene near the charge neutrality point due to the substrate. This is further important because there have been predictions of charge transfer of large magnitudes for such systems (e. g., TiO_2 substrates or metal substrates) [127-129]. Doping of graphene due to charge transfer from the substrates could be revealed as Pauli blocking in the optical conductivity. So, a study till far infrared region can be assumed to be adequate to show the presence and nature of such charge transfer. Similarly it will be interesting to see how the threshold [54,66] in the Pauli blockade region is affected in case of variation of the substrate. Furthermore the shape of the Drude tail could tell us about the scattering rates etc. of charge carriers giving deeper insight into the graphene-substrate coupling.

List of Publications

[1] *Observation of room-temperature high-energy resonant excitonic effects in graphene,* I. Santoso, **P. K. Gogoi**, H. B. Su, H. Huang, Y. Lu, D. Qi, W. Chen, M. A. Majidi, Y. P. Feng, A. T. S. Wee, K. P. Loh, T. Venkatesan, R. P. Saichu, A. Goos, A. Kotlov, M. Rübhausen and A. Rusydi, Phys. Rev. B 84, 081403(R) (2011).

[2] *Optical conductivity study of screening of many-body effects in graphene interfaces,* **Pranjal Kumar Gogoi**, Iman Santoso, Surajit Saha, Sihao Wang, Antonio H. Castro Neto, Kian Ping Loh, T. Venkatesan, Andrivo Rusydi. EPL (Europhysics Letters), 99, 67009 (2012).

[3] *Temperature-dependent and anisotropic properties of layered Pr0:5Ca1:5MnO4 probed by spectroscopic ellipsometry*, M. A. Majidi, E. Thoeng, **P. K. Gogoi**, F.Wendt, S. H. Wang, I. Santoso, T. C. Asmara, I. P. Handayani, A. A. Nugroho, M. Rübhausen, A. Rusydi, Phys. Rev. B 87, 235135 (2013).

[4] *Optical Signatures of Controlled Perturbation of Excitonic Effects and Suppression of Optical Conductivity in Graphene*, Iman Santoso, Ram Sevak Singh, **Pranjal Kumar Gogoi**, Teguh Citra Asmara, Wei Chen, Andrew Thye Shen Wee, Vitor Manuel Perreira, Andrivo Rusydi. (*Accepted for publication in* Phys. Rev. B.).

[5] *Evidence of near perfect ultraviolet transparency of graphene on SrTiO3 induced by Excitonic Fano resonance,* **Pranjal Kumar Gogoi**, Chan La-O-Vorakiat, Ming Yang, Iman Santoso, Teguh Citra Asmara, Antonio H. Castro Neto, Yuan Ping Feng, Elbert E. M. Chia, Kian Ping Loh, T. Venkatesan, Andrivo Rusydi (*under preparation*)

Bibliography

[1] K. S. Novoselov, A. K. Geim, S. V. Morozov, D. Jiang, Y. Zhang, S. V. Dubonos, I. V. Gregorieva, and A. A. Firsov, Science 306, 666 (2004).

[2] K. S. Novoselov, D. Jiang, F. Schedin, T. J. Booth, V. V. Khotkevich, S. V. Morozov, A. K. Geim, PNAS, 102, 10451 (2005).

[3] K. S. Novoselov, Rev. Mod. Phys. 83, 837 (2011).

[4] B. C. Brodie, Phil. Trans. R. Soc. London 149, 249 (1859).

[5] P. R. Wallace, Phys. Rev. 71, 622 (1947).

[6] P. R. Schroeder, M. S. Dresselhaus, A. Javan, Phys. Rev. Lett. 20, 1292 (1968).

[7] W. Andreoni, *The Physics of Fullerene-Based and Fullerene-Related Materials* (Springer, Berlin , 2000).

[8] R. Saito, G. Dresselhaus, M. S. Dresselhaus, *Physical Properties of Carbon Nanotubes* (Imperial College Press, London 1998).

[9] J.-C. Charlier, X. Blase, S. Roche, Rev. Mod. Phys. 79, 677 (2007).

[10] S. Mouras, A. Hamm, D. Djurado, J.-C. Cousseins, Revue de Chimie Minerale, 24, 572 (1987).

[11] R. E. Peierls, Helv. Phys. Acta 7, 81 (1934).

[12] R. E. Peierls, Ann. Inst. Henri Poincare´ 5, 177 (1935).

[13] L. D. Landau, Phys. Z. Sowjetunion 11, 26 (1937).

[14] L. D. Landau, E. M. Lifshitz, *Statistical Physics, Part I* (Pergamon, Oxford, UK), Vol. 1(1980).

[15] N. D. Mermin, H. Wagner, Phys. Rev. Lett. 17, 1133 (1966).

[16] K. S. Novoselov, A. K. Geim, S. V. Morozov, D. Jiang, M. I. Katsnelson, I. V. Grigorieva, S. V. Dubonos, A. A. Firsov, Nature (London) 438, 197(2005).

[17]Y. Zhang, Yan-Wen Tan, Horst L. Stormer, P. Kim, Nature (London) 438, 201(2005).

[18] A. K. Geim, K. S. Novoselov, Nature Mater. 6, 183 (2007).

[19] A. H. Castro Neto, F. Guinea, N. M. R. Peres, K. S. Novoselov, A. K. Geim, Rev. Mod. Phys. 81, 109 (2009).

[20] A. K. Geim, Science 324, 1530 (2009).

[21] Ph. Avouris, Nano Lett. 10, 4285 (2010).

[22] A. H. Castro Neto, K. S. Novoselov, Mater. Express, 1, 10 (2011).

[23] C. Berger, Z. Song, T. Li, X. Li, A. Y. Ogbazghi, R. Feng, Z. Dai, A. N. Marchenkov, E. H. Conrad, P. N. First, W. A. de Heer, J. Phys. Chem. B, 108 (52), 19912 (2004).

[24] X. Li, W. Cai, J. An, S. Kim, J. Nah, D. Yang, R. Piner, A. Velamakanni, I. Jung, E. Tutuc, S. K. Banerjee, L. Colombo, R. S. Ruoff, Science 324, 1312 (2009).

[25] S. Stankovich, D. A. Dikin, G. H. B. Dommett, K. M. Kohlhaas, E. J. Zimney, E. A. Stach, R. D. Piner, S. T. Nguyen, R. S. Ruoff, Nature, 442, 282(2006).

[26] R. Ruoff, Nature Nanotech. 3, 10 (2008).

[27] S. Bae, K. Hyeongkeun, Y. Lee, X. Xiangfan, J. S. Park, Z. Yi, J. Balakrishnan, T. Lei, H. R. Kim, Y. Song, Y. J. Kim, K. S. Kim, B. Oezyilmaz, J. H. Ahn, B. H. Hong, S. Iijima, Nature Nanotech. 5, 574 (2010).

[28] K. F. Mak, C. Lee, J. Hone, J. Shan, and T. F. Heinz, Phys. Rev. Lett. 105, 136805 (2010).

[29] L. Britnell, R. V. Gorbachev, R. Jalil, B. D. Belle, F. Schedin, A. Mishchenko, T. Georgiou, M. I. Katsnelson, L. Eaves, S. V. Morozov, N. M. R. Peres, J. Leist, A. K. Geim, K. S. Novoselov, L. A. Ponomarenko, Science 335, 947(2012).

[30] L. A. Ponomarenko, A. K. Geim, A. A. Zhukov, R. Jalil, S. V. Morozov, K. S. Novoselov, I. V. Grigorieva, E. H. Hill, V. V. Cheianov, V. I. Falko, K.Watanabe, T. Taniguchi & R. V. Gorbachev, Nature Physics Letters 7, 958(2011).

[31] C. R. Dean, L. Wang, P. Maher, C. Forsythe, F. Ghahari, Y. Gao, J. Katoch, M. Ishigami, P. Moon, M. Koshino, T. Taniguchi, K. Watanabe, K. L. Shepard, J. Hone, P. Kim, arXiv:1212.4783 (19 Dec, 2012).

[32] C. Lee, X. Wei, J. W. Kysar, J. Hone, Science 321,385 (2008).

[33] I. Meric, M. Y. Han, A. F. Young, B. Ozyilmaz, P. Kim, K. L. Shepard, Nature Nanotech, **3**, 654 (2008).

[34] A. A. Balandin, S. Ghosh, W. Bao, I. Calizo, D. Teweldebrhan, F. Miao , C. N. Lau, Nano Lett. 8, 902(2008).

[35] J. S. Bunch, A. M. van der Zande, S. Verbridge, I. W. Frank, D. M. Tanenbaum, J. M. Parpia, H. G. Craighead, P. L. McEuen, Science 315, 490 (2007).

[36] J. C. Slonczewski, P. R. Weiss, Phys. Rev. 109, 272 (1958).

[37] J.W. McClure, Phys. Rev. 119, 606 (1960).

[38] N. H. Shon, T. Ando, J. Phys. Soc. Jpn. 67, 2421 (1998).

[39] V.V. Cheianov, V. I. Fal'ko, Phys. Rev. B 74, 041403(R) (2006a).

[40] D. Allor, T. D. Chen, D. A. McGady, Phys. Rev. D 78,096009 (2008).

[41] A. V. Shytov, M. I. Katsnelson, L. S. Levitov, Phys. Rev. Lett. 99, 246802 (2007).

[42] A. Shytov, D. Abanin, L. Levitov, Phys. Rev. Lett. 103, 016806 (2009).

[43] A. F. Young, P. Kim, Nat. Phys. 5, 222 (2009).

[44] N. Stander, B. Huard, D. Goldhaber-Gordon, Phys. Rev. Lett. 102, 026807 (2009).

[45] A. J. M. Giesbers, G. Rietveld, E. Houtzager, U. Zeitler, R. Yang, K. S. Novoselov, A. K. Geim, J. C. Maan, Appl. Phys. Lett. 93, 222109 (2008).

[46]A. Tzalenchuk, S. Lara-Avila, A. Kalaboukhov, S. Paolillo, M. Syväjärvi, R. Yakimova, O. Kazakova, T. J. B. M. Janssen, V. Fal'ko, S. Kubatkin, Nature Nanotech. 5, 186 (2010).

[47] K. I. Bolotin, F. Ghahari, M. D. Shulman, H. L. Stormer, P. Kim, Nature 462, 196 (2009).

[48] D. Hofstadter, Phys. Rev. B 14, 2239(1976).

[49] K.I. Bolotin, K.J. Sikes, Z. Jiang, M. Klima, G. Fudenberg, J. Hone, P. Kim, H.L. Stormer, Solid State Comm. 146 351 (2008).

[50] C. R. Dean, A. F. Young, I.Meric, C. Lee, L. Wang, S. Sorgenfrei, K. Watanabe, T. Taniguchi, P. Kim, K. L. Shepard , J. Hone, Nature Nanotech. 5, 722 (2010).

[51] D. Pesin, A. H. MacDonald, Nature Materials, 11, 409 (2012).

[52] W. Gannett, W. Regan, K. Watanabe, T. Taniguchi, M. F. Crommie, A. Zettl, Appl. Phys. Lett. 98, 242105 (2011)

[53] A. B. Kuzmenko, E. van Heumen, F. Carbone, D. van der Marel, Phys. Rev. Lett. 100, 117401 (2008).

[54] Z. Q. Li, E. A. Henriksen, Z. Jian, Z. Hao, M. C. Martin, P. Kim, H. L. Stormer, D. N. Basov, Nature Phys. 4, 532 (2008).

[55] K.F. Mak, M.Y. Sfeir, Y. Wu, C.H. Lui, J.A. Misewich, T.F. Heinz, Phys. Rev. Lett. 101, 196405 (2008).

[56] R. R. Nair, P. Blake, A. N. Grigorenko, K. S. Novoselov, T. J. Booth, T. Stauber, N. M. R. Peres, A. K. Geim, Science 320, 1308 (2008).

[57] L. Yang, J. Deslippe, C.-H. Park, M. L. Cohen, S. G. Louie, Phys. Rev. Lett. 103, 186802 (2009).

[58] V. G. Kravets, A. N. Grigorenko, R. R. Nair, P. Blake, S. Anissimova, K. S. Novoselov, A. K. Geim, Phys. Rev. B 81, 155413 (2010).

[59] K. F. Mak, J. Shan, T. F. Heinz, Phys. Rev. Lett. 106, 046401 (2011).

[60] D. H. Chae, T. Utikal, S. Weisenburger, H. Giessen, K. v. Klitzing, M. Lippitz, J. Smet, Nano. Lett. 11, 1379 (2011).

[61] P. K. Gogoi, I. Santoso, S. Saha, S. Wang, A. H. Castro Neto, K. P. Loh, T. Venkatesan, A. Rusydi, EPL, 99, 67009 (2012).

[62] L. Yang, Phys. Rev. B 83, 085405 (2011).

[63] P. E. Trevisanutto, M. Holzmann, M. Côté, and V. Olevano, Phys. Rev. B 81, 121405(R) (2010).

[64] I. Santoso, P. K. Gogoi, H. B. Su, H. Huang, Y. Lu, D. Qi,W. Chen, M. A. Majidi, Y. P. Feng, A. T. S. Wee, K. P. Loh, T. Venkatesan, R. P. Saichu, A. Goos, A. Kotlov, M. R¨ubhausen, and A. Rusydi, Phys. Rev. B 84, 081403 (2011).

[65] A. Boosalis, T. Hofmann, V. Darakchieva, R. Yakimova, M. Schubert, Appl. Phys. Lett. 101, 011912 (2012).

[66] J. Horng, C.-F. Chen, B. Geng, C. Girit, Y. Zhang, Z. Hao, H.A. Bechtel, M. Martin, A. Zettl, M.F. Crommie, Y.R. Shen, F. Wang, Phys. Rev. B 83, 165113 (2011).

[67] A. B. Kuzmenko, E. van Heumen, and D. van der Marel, P. Lerch, P. Blake, K. S. Novoselov, and A. K. Geim, Phys. Rev. B 79, 115441 (2009).

[68] H. T. Chen, W. J. Padilla, J. M. O. Zide, A. C. Gossard, A. J. Taylor, R. D. Averitt, Nature 444, 597 (2006).

[69] T. J. Yen, W. J. Padilla, N. Fang, D. C. Vier, D. R. Smith, J. B. Pendry, D. N. Basov, X. Zhang, Science 303, 1494 (2004).

[70] J. Chen, M. Badioli, P. Alonso-Gonza´lez, S. Thongrattanasiri, F. Huth, J. Osmond, M. Spasenovic, A. Centeno, A. Pesquera, P. Godignon, A. Z. Elorza, N. Camara, F. J. Garcı´a de Abajo, R. Hillenbrand, F. H. L. Koppens, Nature doi: 10.1038/nature11254 (2012).

[71] Z. Fei, A. S. Rodin, G. O. Andreev, W. Bao, A. S. McLeod, M. Wagner, L. M. Zhang, Z. Zhao, M. Thiemens, G. Dominguez, M. M. Fogler, A. H. Castro Neto, C. N. Lau, F. Keilmann, D. N. Basov, Nature, doi:10.1038/nature11253 (2012).

[72] V. M. Pereira, A. H. Castro Neto, Phys. Rev. Lett. 103, 046801 (2009).

[73] N. Levy, S. A. Burke, K. L. Meaker, M. Panlasigui, A. Zettl, F. Guinea, A. H. Castro Neto, M. F. Crommie, Science 329, 544 (2010).

[74] D. C. Elias, R. R. Nair, T. M. G. Mohiuddin, S. V. Morozov, P. Blake, M. P. Halsall, A. C. Ferrari, D. W. Boukhvalov, M. I. Katsnelson, A. K. Geim, K. S. Novoselov, Science 323, 610 (2009).

[75] J. T. Robinson, J. S. Burgess, C. E. Junkermeier, S. C. Badescu, T. L. Reinecke, F. K. Perkins, M. K. Zalalutdniov, J. W. Baldwin, J. C. Culbertson, P. E. Sheehan,E. S. Snow, Nano Lett.10,3001 (2010).

[76] Y.-M. Lin, C. Dimitrakopoulos, K. A. Jenkins, D. B. Farmer, H.-Y. Chiu, A. Grill, Ph. Avouris, Science 327, 662 (2010).

[77] M. Y. Han, B. Özyilmaz, Y. Zhang, P. Kim, Phys. Rev. Lett. 98, 206805 (2007).

[78] L. A. Chernozatonskii, P. B. Sorokin, J.W. Bruning, Appl. Phys. Lett. 91, 183103 (2007).

[79] X. Li, Y. Zhu, W. Cai, M. Borysiak, B. Han, D. Chen, R. D. Piner, L. Colombo, R. S. Ruoff, Nano Lett. 9, 4359 (2009).

[80] S. Stankovich, D. A. Dikin, G. H. B. Dommett, K. M. Kohlhaas, E. J. Zimney,E. A. Stach, R.D. Piner, S. T. Nguyen, R. S. Ruoff, Nature 442, 282 (2006).

[81] L. Gong, I. A. Kinloch, R. J. Young, I. Riaz, R. Jalil, K. S. Novoselov, Adv. Mater. 22, 2694 (2010).

[82] N. R. Wilson, P. A. Pandey, R. Beanland, R. J. Young, I. A. Kinloch, L. Gong, Z Liu, K. Suenaga, J. P. Rourke, S. J. York, J. Sloan, ACS Nano 3, 2547 (2009).

[83] F. Schedin, A. K. Geim, S. V. Morozov, E. W. Hill, P. Blake, M. I. Katsnelson, K. S. Novoselov, Nature Materials 6, 652 (2007).

[84] F. Xia, T. Mueller, Y. Lin, A. Valdes-Garcia, Ph. Avouris, Nature Nanotech. 4, 839 (2009).

[85] H. Zhang, D. Y. Tang, L. M. Zhao, Q. L. Bao, K. P. Loh, Optics Express 17, 17630 (2009).

[86] J.-H. Chen, C. Jang, S. Adam, M. S. Fuhrer, E. D. Williams, M. Ishigami, Nature Physics 4, 377 (2008).

[87] H. Lin, H. Lin, J. Lagoute, V. Repain, C. Chacon, Y. Girard, J.-S. Lauret, F. Ducastelle, A. Loiseau, S. Rousset, Nature Mat. 9, 235 (2010).

[88] B. E. Feldman, J. Martin, and A. Yacoby, Nature Phys. 5, 889 (2009).

[89] A. Bostwick, T. Ohta, T. Seyller, K. Horn, E. Rotenberg, Nature Phys. 3, 36 (2007).

[90] D. C. Elias, R. V. Gorbachev, A. S. Mayorov, S. V. Morozov, A. A. Zhukov, P. Blake, L. A. Ponomarenko, I. V. Grigorieva, K. S. Novoselov, F. Guinea, A. K. Geim, Nature Phys. 7, 701 (2011).

[91] D. A. Siegel, C.-H. Park, C. Hwang, J. Deslippe, A. V. Fedorov, S. G. Louie, A. Lanzara, PNAS 108 ,11365 (2011).

[92] N. M. R. Peres, Rev. Mod. Phys. 82, 2673 (2010).

[93] N. M. R. Peres, R. M. Ribeiro, A. H. Castro Neto, Phys. Rev. Lett. 105, 055501 (2010).

[94] L. Yang, Nano. Lett. 11, 3844 (2011).

[95] Dresselhaus, M. S., and G. Dresselhaus, Adv. Phys. 51, 1 (2002).

[96] P. Hohenberg, W. Kohn, Phys. Rev. 1964, 136, B864.

[97] W. Kohn, L. J. Sham, Phys. Rev. 1965, 140, A1133.

[98] T. Ando, Y.S. Zheng, H. Suzuura, J. Phys. Soc. Jpn. 71, 1318 (2002).

[99] N.M.R. Peres, F. Guinea, A.H.Castro Neto, Phys. Rev. B 73, 125411 (2006).

[100] L A Falkovsky, Journal of Physics: Conference Series 129**,** 012004 (2008).

[101] D.S.L. Abergel, V.I. Fal'ko, Phys. Rev. B 75, 155430 (2007).

[102] H.T. Chen, W.J. Padilla, J.M.O. Zide, A.C. Gossard, A.J. Taylor, R.D. Averitt, Nature 444, 597 (2006).

[103] S. Das Sarma, S. Adam, E.H. Hwang, E. Rossi, Rev. Mod. Phys. 83, 407 (2011).

[104]N.M.R. Peres, J.M.B.L. dos Santos, T. Stauber, Phys. Rev. B 76, 073412 (2007).

[105] E.H. Hwang, S. Adam, S. Das Sarma, Phys. Rev. Lett. 98, 186806 (2007).

[106]V.P. Gusynin, S.G. Sharapov, J.P. Carbotte, Phys. Rev. Lett. 96, 256802 (2006).

[107] D.N. Basov, R.D. Averitt, D. van der Marel, M. Dressel, K. Haule, Rev. Mod. Phys. 83, 471 (2011).

[108] T. Stauber, N.M.R. Peres, A.K. Geim, Phys. Rev. B 78, 085432 (2008).

[109] M. Mecklenburg, J. Woo, B.C. Regan, Phys. Rev. B 81, 245401 (2010).

[110] C.F. Chen, C.H. Park, B.W. Boudouris, J. Horng, B.S. Geng, C. Girit, A. Zettl, M.F. Crommie, R.A. Segalman, S.G. Louie, F. Wang, Nature 471, 617 (2011).

[111] M. Liu, X.B. Yin, E. Ulin-Avila, B.S. Geng, T. Zentgraf, L. Ju, F. Wang, X. Zhang, Nature 474, 64 (2011).

[112] F. Wang, Y.B. Zhang, C.S. Tian, C. Girit, A. Zettl, M. Crommie, Y.R. Shen, Science 320, 206 (2008).

[113] E.G. Mishchenko, Phys. Rev. Lett. 98, 216801 (2007).

[114] S.H. Abedinpour, G. Vignale, A. Principi, M. Polini, W.-K. Tse, A.H. MacDonald, Phys. Rev. B 84, 045429 (2011).

[115] J. P. Reed, B. Uchoa, Y. I. Joe, Y. Gan, D. Casa, E. Fradkin, P. Abbamonte, Science 330, 805 (2010).

[116] T. O. Wehling, E. Sasioglu, C. Friedrich, A. I. Lichtenstein, M. I. Katsnelson, S. Blugel, Phys. Rev. Lett. 106, 236805 (2011).

[117] F. Bassani, G.P. Parravincini, *Electronic States and Optical Transitions in Solids* (Pergamon Press, Oxford, 1975).

[118] U. Fano, Phys. Rev. 124, 1866 (1961).

[119] J. C. Phillips, Phys. Rev. 136, A1705 (1964).

[120] P.Y. Yu and M. Cardona, *Fundamentals of Semiconductors: Physics and Materials Properties* (Springer, Berlin, 1996).

[121] J. C. Phillips, *Excitons. In The Optical Properties of Solids, Editor: J. Tauc* (Academic Press, New York, 1966).

[122] L. A. Ponomarenko, R. Yang, T. M. Mohiuddin, M. I. Katsnelson, K. S. Novoselov, S. V. Morozov, A. A. Zhukov, F. Schedin, E. W. Hill, and A. K. Geim, Phys. Rev. Lett. 102, 206603 (2009)

[123] S. D. Sarma, Q. Li, Solid State Commun. 152, 1795 (2012).

[124] J. Y. Kim, C. L. Sukang Bae, K. S. Kim, B. H. Hong, E. J. Choi, Appl. Phys. Lett. **98**, 201907 (2011).

[125] C. Jang, S. Adam, J.-H. Chen, E. D. Williams, S. Das Sarma, M. S. Fuhrer, Phys. Rev. Lett. 101, 146805 (2008).

[126] X. Zhiping M. J Buehler, J. Phys.: Condens. Matter 22, 485301 (2010).

[127] G. Giovannetti, P. A. Khomyakov, G. Brocks, V. M. Karpan, J. van den Brink, and P. J. Kelly, Phys. Rev. Lett. 101, 026803 (2008).

[128] A. Du, Y. H. Ng, N. J. Bell, Z. Zhu, R. Amal, S. C. Smith, J. Phys. Chem. Lett. 2, 894 (2011).

[129] A. Du, S. Sanvito, Z. Li, D. Wang, Y. Jiao, T. Liao, Q. Sun, Y. H. Ng, Z. Zhu, R. Amal, S. C. Smith, J. Am. Chem. Soc. 134, 4393 (2012).

[130] K. K. Manga , S. Wang , M. Jaiswal , Q. Bao, K. P. Loh, Adv. Mater. 22, 5265 (2010).

[131] K. K. Manga, Y. Zhou, Y. Yan, K. P. Loh, Adv. Funct. Mater. 19, 3638 (2009).

[132] Tung, V. C.; Kim, J.; Cote, L. J.; Huang, J. J. Am. Chem. Soc. 133, 9262 (2011).

[133] Li, Q.; Guo, B.; Yu, J.; Ran, J.; Zhang, B.; Yan, H.; Gong, J. R. J. Am. Chem. Soc. 133, 10878 (2011).

[134] Iwase, A.; Ng, Y. H.; Ishiguro, Y.; Kudo, A.; Amal, R. J. Am. Chem. Soc. 133, 11054 (2011).

[135] R. Long, N. J. English, O. V. Prezhdo, J. Am. Chem. Soc. 134, 14238 (2012).

[136] C.H. Lui, K.F. Mak, J. Shan, T.F. Heinz, Phys. Rev. Lett. 105, 127404 (2010).

[137] D. Sun, Z.-K. Wu, C. Divin, X. Li, C. Berger, W.A. de Heer, P.N. First, T.B. Norris, Phys. Rev. Lett. 101, 157402 (2008).

[138] P.A. George, J. Strait, J. Dawlaty, S. Shivaraman, M. Chandrashekhar, F. Rana, M.G. Spencer, Nano Lett. 8, 4248 (2008).

[139] W.-T. Liu, S.W. Wu, P.J. Schuck, M. Salmeron, Y.R. Shen, F. Wang, Phys. Rev. B 82, 081408 (2010).

[140] X. Zou, D. Zhan, X. Fan, D. Lee, S. K. Nair, L. Sun, Z. Ni, Z. Luo, Lei Liu, T. Yu, Z. Shen, E. E. M. Chia, Appl. Phys. Lett. 97, 141910 (2010).

[141] R. M. A. Azzam and N. M. Bashara, *Ellipsometry and Polarized Light* (North-Holland, Amsterdam, 1977).

[142] H. G. Tomkins and W. A. McGahan, *Spctroscopic Ellipsometry and Reflectomertry: A User's Guide* (John Wiley & Sons, Inc., New York ,1999).

[143] H. G. Tomkins and E. A. Irene, ed, *Handbook of Ellipsometry* (William Andrew, New York, 2005).

[144] H. Fujiwara, *Spectroscopic Ellipsometry- Principles and Applications* (John Wiley & Sons, Ltd, England, 2007)

[145] P. Drude, Ann. Phy. 32, 584 (1887); Ann.Phys. 34, 489 (1888).

[146] E. Hecht, *Optics* (Addision Wesley, San Fransisco, 2002).

[147] M. Born and E. Wolf, *Principles of Optics* (Cambridge University Press, Cambridge, 1999).

[148] W. Chen, H. Xu, L. Liu, X. Y. Gao, D. C. Qi, G. W. Peng, S. C. Tan, Y. P. Feng, K. P. Loh, A. T. S. Wee, Surf. Sci. 596, 176 *(*2005).

[149] H. Huang, W. Chen, S. Chen, A. T. S. Wee, ACS Nano. 2, 2513 (2008).

[150] H. Huang**,** S. Chen, X. Y. Gao, W. Chen, A. T. S. Wee, ACS Nano, 3, 3431(2009).

[151] C. Berger, Z. Song, L. Xuebin, W. Xiaosong, N. Brown, C. Naud, D. Mayou, L. Tianbo J. Hass, A. N. Marchenkov, E. H. Conrad, P. N. First, W. A. de Heer Science 312, 1191 (2006).

[152] S. Shivaraman, M. V. S. Chandrashekhar, J. J. Boeckl, M. G. Spencer, J. Elec.Mat. 38, 725 (2009).

[153] A. C. Ferrari, J. C. Meyer, V. Scardaci, C. Casiraghi, M. Lazzeri, F. Mauri, S. Piscanec, D. Jiang, K. S. Novoselov, S. Roth, A. K. Geim, Phys. Rev. Lett. 97, 187401 (2006).

[154] M. Fox, *Optical properties of solids* (Oxford University Press, New York, 2007).

[155] N. W. Aschroft, N. D. Mermin, *Solid state Physics* (Thomson Learning, 1976)

[156] Reffit manual *http://optics.unige.ch/alexey/reffit_files/Manual.pdf*

[157] A. B. Kuzmenko, Rev. Sci. Instrum. 76, 083108 (2005).

[158] F. J. Nelson, V. K. Kamineni, T. Zhang, E. S. Comfort, J. U. Lee, and A. C. Diebold, Appl. Phys. Lett. 97, 253110 (2010).

[159] A. Rusydi, R. Rauer, G. Neuber, M. Bastjan, I. Mahns, S. Müller, P. Saichu, B. Schulz, S. G. Singer, A. I. Lichtenstein, D. Qi, X. Gao, X. Yu, A. T. S. Wee, G. Stryganyuk, K. Dörr, G. A. Sawatzky, S. L. Cooper, M. Rübhausen, Phys. Rev. B 78, 125110 (2008).

[160] G. Zimmerer, Nucl. Instrum. Methods Phys. Res. A 308, 178 (1991).

[161] E. A. Taft and H. R. Philipp, Phys. Rev. A 138, 197 (1965).

[162] A. G. Marinopolous, L. Reining, V. Olevano, A. Rubio, Phys. Rev. Lett. 89, 076402 (2002).

[163] T. Eberlein, U. Bangert, R. R. Nair, R. Jones, M. Gass, A. L. Bleloch, K. S. Novoselov, A. Geim, P. R. Briddon, Phys. Rev. B 77, 233406 (2008).

[164] J. Lu, K. P. Loh, H. Huang, W. Chen, A. T. S. Wee, Phys. Rev. B 80, 113410 (2009).

[165] K. V. Emtsev, F. Speck, Th. Seyller, L. Ley, J. D. Riley, Phys. Rev. B 77, 155303 (2008).

[166] S. Latil and L. Henrard, Phys. Rev. Lett. 97, 036803 (2006).

[167] R. Ahuja, S. Auluck , J. M. Wills, M. Alouani, B. Johansson, O. Eriksson, Phys. Rev. B 55, 4999 (1997).

[168] D. Vanderbilt, Phys. Rev. B 41, 7892 (1990).

[169] J. P. Perdew, K. Burke, M. Ernzerhof, Phys. Rev. Lett. 77, 3865 (1996).

[170] H. J. Monkhorst, J. D. Pack, Phys. Rev. B. 13, 5188 (1976).

[171] R. T. Weitz, M. T. Allen, B. E. Feldman, J. Martin, A. Yacoby, Science 330, 812 (2010).

[172] K. I. Bolotin, F. Ghahari, M. D. Shulman, H. L. Stormer, P. Kim, Nature 462, 196 (2009).

[173] A. Bostwick, F. Speck, T. Seyller, K. Horn, M. Polini, R. Asgari, A. H. MacDonald, E. Rotenberg, Science 328, 999 (2010).

[174] A. Satta, D. Shamiryan, M. R. Baklanov, C. M. Whelan, Q. T. Le, G. P. Beyer, A. Vantomme, K. Maex, J. Electrochem. Soc. 150, 5, G300-G306 (2003).

[175] J. W. Weber, V. E. Calado, M. C. M. van de Sanden, Appl. Phys. Lett. 97, 091904 (2010).

[176] D. L. Greenaway, G. Harbeke, F. Bassani, E. Tosatti, Phys. Rev. 178, 1340 (1969).

[177] T. Ito, H. Yamguchi, T. Masumi, S. Adachi, J. Phys. Soc. of Japan, 67, 9, 3304-3309 (1998).

[178] E. D. Palik, Editor, *Handbook of Optical Constants of Solids II,* Academic Press, New York (1991).

[179] H. Ehrenreich, H. R. Philipp, Phys. Rev. 128, 4, 1622 (1962).

[180] C. Lee, J. Y. Kim, S. Bae, K. S. Kim, B. H. Hong, E. J. Choi, Appl. Phys. Lett. 98, 071905 (2011).

[181] H. Hashimoto, S. Nishiuma, K. Takada, K. Nakamura, R. Ueno, T. Den, Jpn. J. Appl. Phys. 38, 4136 (1999).

[182] V. N. Kotov, B. Uchoa, V. M. Pereira, F. Guinea, A. H. Castro Neto, Rev. Mod. Phys. 84, 1067 (2012)

[183] T. O. Wehling, I. Grigorenko, A. I. Lichtenstein, A. V. Balatsky, Phys. Rev. Lett. 101, 216803 (2008).

[184] E. E. Salpeter, H.A. Bethe, Phys. Rev. 84, 1232 (1951).

[185] M. A. Ordal, R. J. Bell, R. W. Alexander, Jr, L. L. Long, M. R. Querry, Applied Optics, 24, 4493(1985).

[186] E. J. Zeman, G. C. Schatz, J. Phys. Chem. 91, 634 (1987).

[187] Manuscript under preparation- *Evidence of near perfect ultraviolet transparency of graphene on SrTiO3 induced by excitonic Fano resonance.*

[188] H. Y. Hwang ,Y. Iwasa, M. Kawasaki, B. Keimer, N. Nagaosa, Y. Tokura, *Nat. Mater.* 11, 103 (2012).

[189] A. Othonos, J. Appl. Phys. 83, 1789 (1998).

[190] Y. Zhang, L. Zhang, C, Zhou, Articles ASAP, Accounts of Chemical Research (2013).

[191] G. Koster, B. L. Kropman, G. J. H. M. Rijnders, D. H. A. Blank, and H. Rogalla, Appl. Phys. Lett. 73, 2920 (1998).

[192] K. Xu, P. Cao, J. R. Heath, Science 329, 1188 (2010).

[193] A. E. Miroshnichenko, S. Flach, Y. S. Kivshar, Rev. Mod. Phys., 82, 2257 (2010).

[194] A. J. Sabbah, D. M. Riffe, Phys. Rev. B. 66, 165217 (2002).

[195] M. Breusing, C. Ropers, and T. Elsaesser, Phys. Rev. Lett. 102, 086809 (2009).

[196] G. Kresse, H. Hafner, Phys. Rev. B 47, 558 (1993).

[197] G. Kresse, H. Hafner, Phys. Rev. B. 48, 13115(1994).

[198] P. E. Blochl, Phys. Rev. B. 50, 17953 (1994).

[199] S. Grimme, J. Comp. Chem. 27, 1787 (2006).

[200] Manuscript accepted for publication in Phys. Rev. B. *Tunable optical absorption and interactions in graphene via oxygen plasma.*

[201] J. H. Chen, W.G. Cullen, C. Jang, M.S. Fuhrer, and E.D. Williams, Phys. Rev. Lett. 102, 236805 (2009).

[202] T.O. Wehling, S. Yuan, A.I. Lichtenstein, A.K. Geim, and M. I. Katsnelson, Phys. Rev. Lett. 105, 056802 (2010).

[203] S. Yuan, R. Roldan, H. de Raedt, and M.I. Katsnelson, Phys. Rev. *B* 84, 195418 (2011).

[204] V.M. Pereira, F. Guinea, J. M. B. Lopes dos Santos, N. M. R. Peres, A. H. Castro Neto Phys. Rev. Lett. 96, 036801 (2006).

[205] D.C. Kim, D.Y. Jeon, H.J. Chung, Y.S. Woo, J.K. Shin and S. Seo, Nanotechnology 20, 375703 (2009).

[206] A. Nourbakhsh, M. Cantoro, T. Vosch, G. Pourtois, F. Clemente, M. H van der Veen, J. Hofkens, M. M. Heyns, S. D. Gendt, B. F Sels, Nanotechnology 21, 435203 (2010).

[207] L. G. Cancado, M. A. Pimenta, B. R. A. Neves, M. S. S. Dantas, and A. Jorio,

Phys. Rev. Lett. 93, 247401 (2004).

[208] M. A. Pimenta, G. Dresselhaus, M. S. Dresselhaus, L. G. Canc¸ado, A. Jorio, R. Saito, Phys. Chem. Chem. Phys. 9, 1276 (2007).

[209] A. C. Ferrari, J. Robertson, Phys. Rev. B 61, 14095 (2000).

[210] J. Yan, Y. Zhang, P. Kim, and A. Pinczuk, Phys. Rev Lett. 98, 166802 (2007).

[211] A.G. Grushin, B. Valenzuela, and M.A.H. Vozmediano, Phys. Rev. B 80, 155417 (2009).

[212] Y. Wang, V. W. Brar, A. V. Shytov, Q. Wu, W. Regan, H.Z. Tsai, A. Zettl, L. S. Levitov, M. F. Crommie, Nature Phys. 8, 653 (2012).

[213] Z. Xingquan, *PhD Thesis* (2012).

Appendix A

Optical pump-probe set-up

Optical pump-probe data presented in this work have been taken in the degenerate pump-probe set up available in the laboratory of Assistant Professor Chia Ee Min Elbert from Nanyang Technological University. The schematic of the set-up is shown in Figure A1 (a) and an image of the set-up is shown in Figure A1 (b).

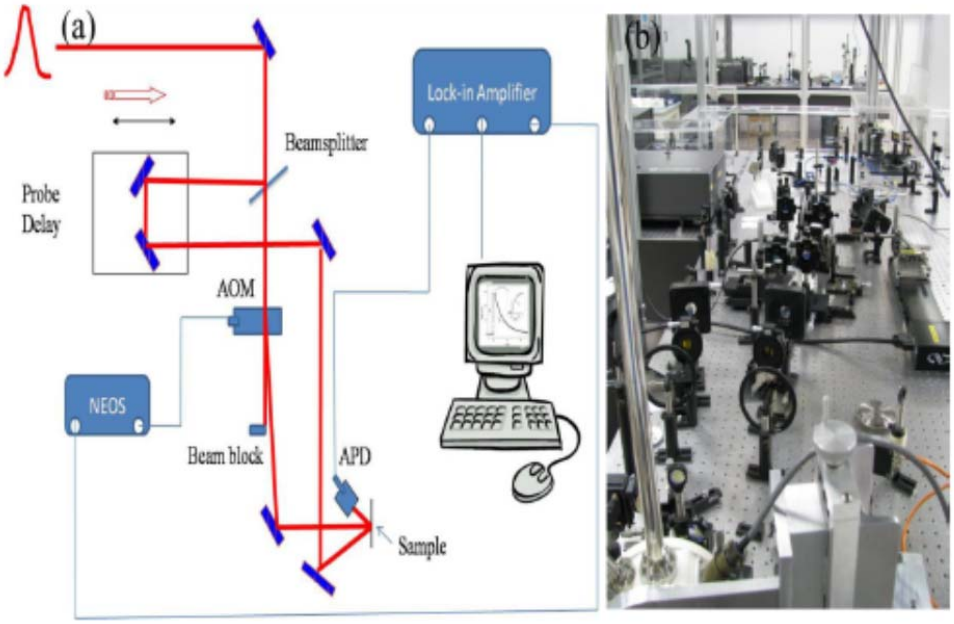

Figure A1 (a) Schematic of the lab set-up. (b) An image of the set-up. [213]

In a typical optical pump-probe set up an ultrafast pulse is first split by a beam splitter into two pulses- called pump and probe. By the use of various optical elements the two pulses are made to arrive in different times at the same sample position. In this current set-up the pump probe time delay can be made as small as 10 fs. The pump beam is typically more intense then the probe beam and also the probe beam diameter is generally smaller while it overlaps on top of the pump beam spot in the sample. When the intense pump beam falls on the sample it increases the electronic temperature of the sample creating hot carriers. Subsequently the probe beam is used to investigate the relaxation of these hot carriers as a function of the delay. Normalized differential reflectance ($\Delta R/R$) is measured in the present case for the probe beam. As the energy of both the pump and the probe beam is same it is called a degenerate set-up. The normalized differential reflectance ($\Delta R/R$) can be written as

$$\frac{\Delta R}{R} = \frac{R_E - R_0}{R_0}$$

where R_E is the reflectance of the probe beam after pump excitation and R_0 is the reflectance before pump excitation. The pump beam is modulated with an acoustic-optical modulator (AOM) which is also connected to a lock-in amplifier. Avalanche photodetector (APD) is used to record both the pump and probe signal with the help of the lock-in amplifier.

The pulsed laser used for the generation of the pump and probe beams is a Ti:sapphire mode-lock lasers with 80 MHz pulse repetition rate. It generates 40 fs pulses of 800 nm wavelength.

Appendix B

The Igor pro macro routine for Fano fitting

```
Function oa_SE2fromfano(coef)  // individual epsilon 2 Fano)
	wave coef
	//Variable,x

	Wave wguess=root:OpticsAnalysis:Fit:wguess // added only for Pranjal
	Variable Er,E0,y,Ebr
	Variable dT = deltax(wguess)
	Variable pG
	wave wtest2=root:OpticsAnalysis:Fit:wtest2
	Er=coef[2]//[1]
	E0=coef[3]//[1]

	EBr=0.4//coef[1]//0.5//0.01*E0
	//wave ResGaussian=root:OpticsAnalysis:Fit:ResGaussian
	pG=abs(6*EBr/dT)
	//Make/O/N=201 ResGaussian
	Make/O/N=(pG) ResGaussian
	//SetScale/I x ,-(dT*100),(dT*100),ResGaussian
	SetScale/I x,Er-(pG-1)/2*dT,Er+(pG-1)/2*dT,ResGaussian
	ResGaussian = exp(-((x-Er)*2*sqrt(ln(2))/(EBr))^2)
	//SetScale/I x,0*dT,1*pG*dT,ResGaussian
```

```
	//ResGaussian = exp(-(x-Er)^2/(EBr)^2)

	Variable sumexp
	//sumexp = sum(ResGaussian,-(dT*100),(dT*100))
	//sumexp = sum(ResGaussian,Er-(pG-1)/2*dT,Er+(pG-1)/2*dT)
	sumexp=sqrt(pi/((4*ln(2))/(Ebr^2)))/dT
	ResGaussian/=sumexp
	Wguess+=oa_SE2fromfano2(coef,x)//Interband transition
	//Wguess+=wtest2


	convolve/A  ResGaussian,Wguess
	duplicate/O wguess wfano
	wguess*=1.75
	wguess+=0.8
	duplicate/O wguess  w_inter
	wfano=oa_SE2fromfano1(coef,x)
	Wguess*=oa_SE2fromfano1(coef,x) //actual Fano lineshape
	//convolve/A ResGaussian,Wguess
End


Function oa_SE2fromfano1(coef,x)  // individual epsilon 2 Fano)
	wave coef
	Variable x
	Variable i,y,q,G,Er,E0,eps
	q=coef[0]//[1]
```

```
	G=coef[1]//[1]
	Er=coef[2]//[1]
	E0=coef[3]//[1]
	eps=2*(x-Er)/G
	//y=0
	//for(i=1;i<=n;i+=1)
	  // y=(q*G/1 + (x-Er))^2/((G/1)^2 + (x-Er)^2)
	   //y=(q+x)^2/(1+x^2)
	   y=(q+eps)^2/(1+eps^2)
	//endfor
	//for(i=1;i<=n;i+=1)
	//   y+=(coef[i]*coef[i+1]/2 + (x-coef[i+2]))^2/((coef[i+1]/2)^2 + (x-coef[i+2])^2)
	//endfor
	return y
End

Function oa_SE2fromfano2(coef,x)  // individual epsilon 2 for interband
	wave coef
	Variable x
	Variable E0,y,Er,Ebr,pG,dT

	E0=coef[3]
	//Er=coef[2]
	y=-log(abs(1-(x/E0)))
	//y=0.9*(-ln(abs(x-Er)))
	return y
End
```

Appendix C

Preliminary transport results for CVD graphene on SiO_2 and $SrTiO_3$

As explained in Chapter 2 and Chapter 3, we also want to investigate the photo-induced effects in graphene. One such directions is to fabricate graphene field- effect devices on a the substrate of interest and study transport behaviour when illuminated with light of varying wavelength as well as intensity. With such an aim graphene devices are fabricated both on SiO_2 (300 nm) /n-Si as well as on $SrTiO_3$ (300 nm)/ Nb-$SrTiO_3$ (deposited using pulsed laser deposition). The plan is to first fabricate working devices and then go for illuminated transport measurements later. Particularly these plans have immediate relevance to our important results explained in Chapter 7 which could shed more light on some important points .

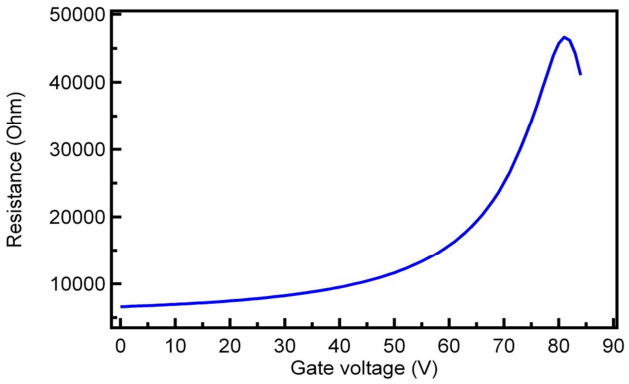

Figure C1: Resistance vs gate voltage for graphene on SiO_2 (300 nm) /n-Si

In Figure C1 we present our preliminary transport data for graphene device on SiO_2 (300 nm) /n-Si measured in ambient using techniques explained in Chapter 3. We see clear gate dependence but the graphene seem to be hole doped considerably. This may be due to (unintentional doping from) the processing steps or may be partially due to the fact that the measurement is performed in ambient (which dopes graphene). We see similar trend

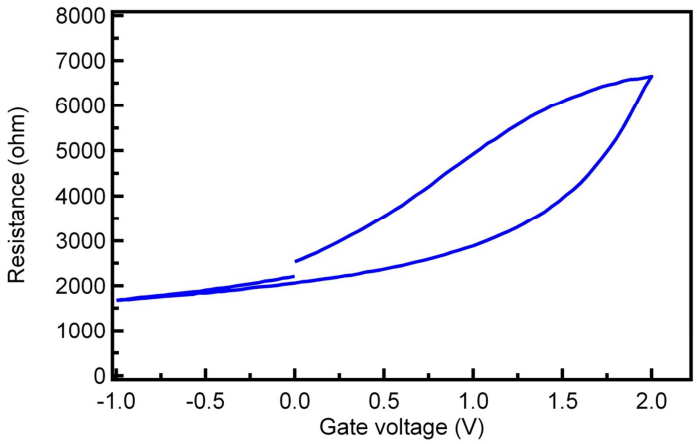

Figure C2: Resistance vs gate voltage for graphene on $SrTiO_3$ (300 nm)/ Nb-$SrTiO_3$ for a one full cycle gate voltage sweep.

in the case of the device fabricated on $SrTiO_3$ (in Figure C2). However again we see clear gate dependent resistance change and the smaller gate voltages required (in comparison to the previous case) is an indication that our device works with proper contact. The smaller gate voltage required in comparison to graphene on SiO_2 (300 nm) /Si is due to the fact that $SrTiO_3$ has a dielectric constant ~300 in room temperature which makes the field effect larger.

For reliable analysis and rigorous study better device performance is required- specially when we want to move to the next step of illuminated transport. Tuning the carrier concentration across the Dirac point is the desirable next step (or in other words the charge neutrality point should be observable as close as possible to zero applied gate voltage). But it has to be mentioned that these devices are fabricated using electron beam lithography (EBL) technique and the clear gate tuning shows that in fact working devices can be fabricated at present and it is an important step forward.